

# SANDIA REPORT

SAND2025-01826

Printed February 2025



Sandia  
National  
Laboratories

# Basin & Range Investigations for Developing Geothermal Energy

Christine Downs<sup>1</sup>, Carmen Winn<sup>2</sup>, Kurt Kraal<sup>1</sup>, Matthew Folsom<sup>2</sup>, Paul Schwering<sup>1\*</sup>,  
Nicholas Hinz<sup>2</sup>, Jade Zimmerman<sup>3</sup>, Steven Sewell<sup>4</sup>, William Cumming<sup>5</sup>, Alex Milton<sup>2</sup>,  
Andrew Sabin<sup>3</sup>, Janice Lopeman<sup>2</sup>

<sup>1</sup>Sandia National Laboratories

<sup>2</sup>Geologica Geothermal Group

<sup>3</sup>Navy Geothermal Program Office

<sup>4</sup>Australis Geoscience Ltd.

<sup>5</sup>Cumming Geoscience

\*Current affiliation: Pacific Northwest National Laboratory

Prepared by  
Sandia National Laboratories  
Albuquerque, New Mexico  
87185 and Livermore,  
California 94550

Issued by Sandia National Laboratories, operated for the United States Department of Energy by National Technology & Engineering Solutions of Sandia, LLC.

**NOTICE:** This report was prepared as an account of work sponsored by an agency of the United States Government. Neither the United States Government, nor any agency thereof, nor any of their employees, nor any of their contractors, subcontractors, or their employees, make any warranty, express or implied, or assume any legal liability or responsibility for the accuracy, completeness, or usefulness of any information, apparatus, product, or process disclosed, or represent that its use would not infringe privately owned rights. Reference herein to any specific commercial product, process, or service by trade name, trademark, manufacturer, or otherwise, does not necessarily constitute or imply its endorsement, recommendation, or favoring by the United States Government, any agency thereof, or any of their contractors or subcontractors. The views and opinions expressed herein do not necessarily state or reflect those of the United States Government, any agency thereof, or any of their contractors.

Printed in the United States of America. This report has been reproduced directly from the best available copy.

Available to DOE and DOE contractors from

U.S. Department of Energy  
Office of Scientific and Technical Information  
P.O. Box 62  
Oak Ridge, TN 37831

Telephone: (865) 576-8401  
Facsimile: (865) 576-5728  
E-Mail: [reports@osti.gov](mailto:reports@osti.gov)  
Online ordering: <http://www.osti.gov/scitech>

Available to the public from

U.S. Department of Commerce  
National Technical Information Service  
5301 Shawnee Rd  
Alexandria, VA 22312

Telephone: (800) 553-6847  
Facsimile: (703) 605-6900  
E-Mail: [orders@ntis.gov](mailto:orders@ntis.gov)  
Online order: <https://classic.ntis.gov/help/order-methods/>



## **ABSTRACT**

Hidden geothermal systems represent a potentially prolific energy resource that could support critical U.S. public and government energy priorities. Basin and Range Investigations for Developing Geothermal Energy (BRIDGE) addressed some the challenges associated with hidden system exploration by prioritizing cost-effective exploration early on through strategic workflow and informed decision-making that mitigates early risk and shifts resources to later exploration stages (e.g., drilling). Sandia National Laboratories partnered with U.S. Navy Geothermal Office, Geologic Geothermal Group, and independent consultants, with additional collaboration with U.S. Geological Survey and private industry. The primary tool of the BRIDGE project was to deploy a regional-scale airborne electromagnetic method to investigate the shallow resistivity structure in areas with high prospectivity. This was followed up at several prospects by a multidisciplinary exploration approach, including additional geologic, geophysical, and geochemical studies. A central tenet to the BRIDGE methodology is that zones of low resistivity frequently occur over geothermal systems in the Basin and Range, and when paired with other data constraints, imaging these zones can enable discovery of these systems. In addition to exploring greenfield areas (i.e., Grover Point), the BRIDGE project also flew HTEM resistivity surveys over known geothermal systems including those with established power plants (Don A. Campbell and Salt Wells) and prospects that are known to the literature but remain undeveloped, at least in part, due to a lack of understanding on the location of their producible reservoirs. BRIDGE produced a comprehensive set of data from prospects identified in the Nevada Play Fairway Analysis along with conceptual models for top ranking prospects, wherein all the observations are used to inform an interpreted model of the system. These models present a range of possible system parameters such as temperature and size, and they are further informed by system analogues in the Basin and Range province and elsewhere. The results of this work leave space for further exploration that may now occur at prospects ‘down the list’ rather than distribution exploration resources evenly across all prospects.

## **ACKNOWLEDGEMENTS**

Sandia National Laboratories is a multimission laboratory managed and operated by National Technology & Engineering Solutions of Sandia, LLC, a wholly owned subsidiary of Honeywell International Inc., for the U.S. Department of Energy's National Nuclear Security Administration under contract DE-NA0003525. This report describes objective technical results and analysis. Any subjective views or opinions that might be expressed in the paper do not necessarily represent the views of the U.S. Department of Energy or the United States Government. This report has been authored by an employee of National Technology & Engineering Solutions of Sandia, LLC under Contract No. DE-NA0003525 with the U.S. Department of Energy (DOE). The employee owns all right, title and interest in and to the article and is solely responsible for its contents. The United States Government retains and the publisher, by accepting the article for publication, acknowledges that the United States Government retains a non-exclusive, paid-up, irrevocable, world-wide license to publish or reproduce the published form of this article or allow others to do so, for United States Government purposes. The DOE will provide public access to these results of federally sponsored research in accordance with the DOE Public Access Plan <https://www.energy.gov/downloads/doe-public-access-plan>.

# CONTENTS

Abstract .....	3
Acknowledgements.....	4
Executive Summary.....	13
Acronyms and Terms.....	15
1. Introduction.....	16
2. Airborne Resistivity Imaging.....	21
2.1. Justification .....	21
2.2. Survey & Data Specifications.....	22
2.3. Geothermal Indicators & Strategy.....	25
3. Shallow temperature exploration .....	31
3.1. Background.....	31
3.2. BRIDGE Data Collection and Processing .....	31
4. Project Outcomes .....	35
4.1. Prospect Portfolio.....	35
4.2. Grover Point Prospect.....	38
4.2.1. Background .....	38
4.2.2. Geology.....	38
4.2.3. Hydrothermal Data .....	39
4.2.4. HTEM.....	42
4.2.5. 2-m Temperature Survey.....	44
4.2.6. Potential Fields .....	45
4.2.7. Preliminary Interpretation and Conceptual Model .....	49
4.2.8. Conclusion.....	53
4.3. Lee Allen Prospect.....	55
4.3.1. Background .....	55
4.3.2. Wells.....	64
4.3.3. Fluid Geochemistry.....	66
4.3.4. Geophysics .....	70
4.3.5. Geoscientific Interpretations.....	72
4.3.6. Conceptual Model.....	74
4.3.7. Power Capacity Estimates.....	80
4.3.8. Recommendations for Future Work .....	80
4.4. East Hawthorne Prospect.....	82
4.4.1. Background .....	82
4.4.2. Geology.....	82
4.4.3. Fluid Geochemistry.....	90
4.4.4. Wells.....	96
4.4.5. Geophysics .....	98
4.4.6. Geologic Interpretations .....	104
4.4.7. Conceptual Model.....	106
4.4.8. Recommendations for Future Work.....	110
4.5. Geothermal Exploration Data and Data Products.....	113
4.6. Conference Proceedings .....	113
References.....	115

Appendix A.	HTEM and 3D MT Resistivity Model for Lee-Allen .....	124
Appendix B.	3D Joint Inversion Resistivity Model at East Hawthorne (HTEM + MT).....	130
Appendix C.	Public Data Compilation.....	135
Appendix D.	Data Repository Summary.....	139
Distribution.....		145

## LIST OF FIGURES

Figure 1	Project cost and risk profile at various stages of development. BRIDGE prioritized cost-effective exploration early on (blue box) through strategic workflow and informed decision-making. Such as approach mitigates early risk (blue dashed line) and increases the rate of discovery success while shifting resources to later stages (e.g., drilling).....	17
Figure 2	The BRIDGE "prospecting" exploration workflow. Phase 1 identifies and initially ranks prospects. Phase 2 identifies priority data gaps. Phase 3 closes those data gaps. Phase 4 develops conceptual models and executes targeted TGH drilling. Phase 5 executes targeted slim hole drilling.....	18
Figure 3	Selected BRIDGE prospects and favorable structural targets identified in Nevada PFA. ....	19
Figure 4	BRIDGE acquired a regional-scale helicopter-borne transient electromagnetic survey (HTEM) as part of its early-stage reconnaissance effort.....	22
Figure 5	Comparison of the different inversions carried out on the data (a-d) and comparison to 1D (TE mode) MT inversion (e) for a cross-section through the Dixie Valley area. Depths below the DOI have been made opaque.....	25
Figure 6	Depth to the Top of Conductor (ToC, <10 Ohm-m) in the Gabbs Valley area and known shallow thermal anomalies identified by 2-meter temperature and/or thermal gradient wells. Where the HTEM profiles are black, there is a <10 Ohm-m conductor that is greater than 150 meters depth, where green there is no <10 Ohm-m conductor.....	26
Figure 7	Examples of HTEM resistivity profiles and their "favorability" ranking. Panels organize low resistivity structures by high, medium, or low ranking in terms of how indicative they are of a hidden system. This considers only HTEM and historic geologic mapping data and acknowledge other datasets (e.g., gravity, geochemistry, shallow or downhole temperature measurements) can change a prospect's ranking.....	30
Figure 8	Shallow temperature collected by the BRIDGE team (squares) at or near Gabbs Valley, NV. Also shown are existing 2-m temperature points (circles) and the HTEM top of conductor (ToC) map of Gabbs Valley from Figure 6.....	33
Figure 9	Two-meter temperature data collected by the BRIDGE team at Bell Flat, NV. Below is HTEM line T59010, which runs along the western margin of Bell Flat. A shallow low resistivity zone is visible in the HTEM data along line T59010 beneath the positive 2-m temperature anomaly. ....	34
Figure 10	Location of Dixie Valley including known and prospective geothermal systems including Quaternary faults [1], <b>black lines</b> , and physiographic locations mentioned in the text. DVFZ is Dixie Valley Fault Zone, MGFZ is Middlegate Fault Zone, GP is Grover Point, DVPP is Dixie Valley geothermal power plant, DM is Dixie Meadows, B is the Bend, TM is Tungsten Mountain, PM is Pirouette Mountain, and EMC is Eleven Mile Canyon. HTEM lines collected as part of the BRIDGE project are shown as blue lines. Top left insert: Location of map relative to Nevada state boundary.....	39

Figure 11 TGH map near Grover Point (triangles) and geochemistry samples (circles) with HTEM flight lines for reference. Note the greenery in the imagery, indicating the presence of springs and artesian wells. ....40

Figure 12 Geochemical ternary diagrams of the anions (left) and cations (right) of samples from artesian wells near Grover Point. Note that all samples are relatively Calcium (Ca) rich and relatively rich in bicarbonate ( $\text{HCO}_3$ ) and sulphate ( $\text{SO}_4$ ).....41

Figure 13 Location of HTEM lines in the Grover Point area (white lines) with portions of select cross-sections shown in this paper (black lines). A map of the depth to the top of conductor (ToC), defined as the top of a 12 Ohm-m surface, is shown with colored contours. ....42

Figure 14 Shallow temperature survey results near Grover Point in Dixie Valley are shown as small colored circles. Quaternary faults identified from new analysis of LiDAR data are shown as black lines. HTEM line locations are shown as blue lines. TGH data from the SMU database are shown as larger colored circles. ....43

Figure 15 Shallow temperature survey probe installation (left and top right), Resistive temperature device insertion (middle right), and probe retrieval (bottom right). ....44

Figure 16 Gravity survey and results. LiDAR fault scarps are shown as solid black lines and the hot SMU wellhead location is shown as a black cross. HTEM flight lines (white lines) are shown for reference. Gravity stations are shown as inverted black triangles in Panels A and B. Panel A: Imagery. Panel B: CBA reduced at 2.45 g/cc, gridded at 150 m cell size. Panel C: Horizontal gradient magnitude (HGM) of the CBA. Panel D: First vertical derivative (1VD) of the CBA, first upward continued by 25 m. ....46

Figure 17 A subset of an aeromagnetic survey, flight lines not shown, over the Clan Alpine Mountains (**Water Resources Division, 1985**). On each map, LiDAR fault scarps are shown as solid black lines and the hot SMU well 903-2 is shown as a black cross. HTEM flight lines (white lines) are shown for reference. Panel A: Topographic map; Panel B: Reduced-to-Pole (RTP) magnetic anomaly, Panel C: Horizontal gradient of the RTP anomaly, Panel D: vertical derivative of the RTP anomaly.....46

Figure 18 Preliminary structural interpretations from the gravity and magnetic datasets at Grover Point. Colored grid is the HGM of the gravity CBA. Contours are from the RTP magnetic data. HTEM lines shown as white lines, for reference. A zone of elevated 2M temperatures is highlighted with a dashed white polygon. ....48

Figure 19 HTEM resistivity, residual magnetic intensity (RMI) and gravity horizontal gradient magnitude (HGM) extracted along profiles 10100, 10130 and 19020. Zones of elevated 2M temperatures are shown as black lines (solid or dashed) below each resistivity profile. Well names and bottom hole temperatures are shown above each resistivity profile. HTEM lines that cross each profile are noted with the line name. ....50

Figure 20 Map view of the conceptual model, with select HTEM lines, temperature data, fault interpretations from gravity, and the inferred outflow.....52

Figure 21 Conceptual model cross-section along HTEM profile 10100. HTEM resistivity values are shown as the background colors. The basement – alluvial contact was derived from a 2D gravity model using a density contrast of 0.55 g/cc.....53

Figure 22 Lee-Allen location and overview, with HTEM flight Lines (black lines), MT stations (grey triangles) land ownership boundaries and model results along HTEM line T49020. Thermal gradients calculated from each TG well are listed below the well name. ....56

Figure 23 Simplified regional geologic context of the Lee-Allen prospect area, modified from Carlson (2017, 2018) and Hinz and others [42]. Faults shown on this map vary in certainty of location and exposure. Lee-Allen hot springs are marked by the red star. Note the NNE- and

NE-striking normal faults between the NW-striking major strike-slip faults. APHF = Agai Pai Hills Fault, GDHF = Gumdrop Hills Fault, BSF = Benton Springs Fault, RPF = Russell Pass fault. The blue line on the map shows the approximate contact between the 13.8 Ma rhyolite (shown in purple)/11.6 Ma basaltic andesite (shown in orange) that is the basis for inferring ~5 km of dextral offset on the Russell Pass fault. ....59

Figure 24 Geologic map of the Lee-Allen geothermal area from Hinz and others [42] highlighting distribution and kinematic characterization of NW-striking faults. Annotations on top of the map for reference in this report. Black lines over NW-striking faults with inferred stratigraphic offset and/or fault surface data which supports dextral motion. Purple lines over NW-striking faults with stratigraphic offset, but uncertain kinematics (normal vs strike-slip). ....61

Figure 25 Temperature-depth plots of the five US Navy thermal gradient holes near HTEM line T49020. Thermal gradients increase to the north. ....66

Figure 26 Chloride vs. SiO<sub>2</sub> for water samples near Lee-Allen. Note that due to the very high salinity of Stinking and Coyote Springs relative to all other waters, they plot far off the x-axis of this chart, despite relatively low SiO<sub>2</sub> concentrations near ~50 mg/kg). This likely indicates that these waters are not related to those near Lee-Allen hot springs. ....67

Figure 27 Map and ternary diagrams of water samples from near Lee-Allen. Above: anion trilinear. Below: cation trilinear. Several samples are missing key anion data and thus are missing from the top trilinear. ....68

Figure 28 Giggenbach cation geothermometer trilinear. Note that the samples near Lee-Allen hot springs plot approximately along a 180-200 °C trend, which is relatively consistent with the quartz and average Na/K geothermometer estimates. ....69

Figure 29 Depth slices through the 3D MT model at 100, 200, 300 and 500 meters below sea level. Maps include 2-m temperature points, wells, springs, silicified sediments, and an interpreted fault layer that is modified from Hinz et al., 2010a. ....71

Figure 30 Gravity and aeromagnetic data over the Lee-Allen Prospect, with springs, wells and interpreted fault layer modified from Hinz and others [42]. Note these maps show a more regional extent than other figures in this report. Upper left: Gravity CBA with gravity station locations (black triangles); upper right: Horizontal gradient magnitude of the CBA; lower left: Reduced-to-pole magnetic anomaly (RTP); lower right: Horizontal gradient magnitude of the pseudo-gravity transform of the aeromagnetic RTP. ....73

Figure 31 Geologic interpretations at the Lee-Allen prospect (modified from Hinz et al., 2010a) with 2-meter temperature points, wells, and surface alteration. A NW-striking strike-slip fault (The Russell Pass fault) has been interpreted from Geophysics. Along profile CM3 (white line) a cross-section from the 3D MT model is annotated with geologic interpretations. Above the cross section, values extracted from the gravity CBA and horizontal gradient of the CBA are shown for reference. ....75

Figure 32 Conceptual model figure for Lee-Allen. Reservoir area estimates (P90, P50, P10) are shown in map view on top of the horizontal gradient magnitude of the gravity complete Bouguer anomaly. Inferred isotherms of the P50 conceptual model are shown on the 3D .....77

Figure 33 Lee-Allen conceptual model along profiles CM2 and NW1 that intersect the interpreted outflow path of the geothermal system. ....78

Figure 34 Analogous Geothermal Fields in terms of power density (MWe/km<sup>2</sup>) and average temperature (°C), based on Wilmarth and others (2020). The red box denotes the range of these parameter applied to Lee-Allen. ....79

Figure 35 Overview map of East Hawthorne study area. Geologic map simplified from Hinz and others (2010c). Map includes wells (white circles), MT stations (black and blue triangles),

HTEM flight lines and contours of the 2-meter temperature probe degrees above background.....	83
Figure 36 Map from Faulds and Henry (2008) showing location of the East Hawthorne geothermal area (black box) relative to major active faults and Walker Lane structural domains. ....	85
Figure 37: Map and cross-section from Hinz and others (2010a): Semi-transparent geologic map draped over shaded relief image. Faults: highlighted red, Holocene; highlighted orange, Pleistocene; highlighted yellow, Quaternary undivided; dashed, inferred from subsurface and geophysical data.....	88
Figure 38 Field photos of the Pamlico fault in the Garfield Hills. ....	89
Figure 39 Map (above), anion trilinear (bottom left), and cation trilinear (bottom right) for water samples from near the tufa outcrops in the central part of the valley, East Hawthorne, and samples from two select wells in West Hawthorne for comparison. ....	90
Figure 40 Giggenbach cation geothermometer trilinear for samples in the Hawthorne area. Note that HWAD-5 plots outside of the partial equilibration zone and the majority of other samples plot in the “immature waters” zone. ....	92
Figure 41 Exploration wells drilled to date at the East Hawthorne geothermal prospect. 2-m degrees above background (DAB) is contoured, and geologic units are shown from Hinz and others (2010a). The background hill shade is from LiDAR and shows the locations of HAD infrastructure.....	93
Figure 42 Select well data observed from cuttings at well HAD-1. Left column: geology, inferred faults and lost circulation zones. Middle column: Qualitative degree of brecciation/shearing. Right column: Clay mineralogy from XRD, with equilibrated well temperature (red line). Figure includes content from Blake and others (2017) and Sewell and others (2023). ....	94
Figure 43 Temperature-depth plots for East Hawthorne wells. 30 °C/km and 45 °C/km gradients are shown as black and grey dashed lines, as a reference to potential background values here.....	95
Figure 44 Gravity and magnetic data over East Hawthorne. Panel A: Complete Bouguer anomaly (CBA) reduced at 2.45 g/cc and gridded at 150 m, with gravity station locations shown as small triangles. Panel B: Horizontal gradient (HGM) magnitude of the CBA. Panel C: First vertical derivative (1VD) of the CBA. Panel D: Reduced-to-pole magnetic anomaly (RTP) from the GeoDAWN dataset (Glen & Earney, 2024). ....	99
Figure 45 A comparison of the modelled resistivity results from 1D inversions of HTEM data, a 3D MT inversion, and a fully 3D joint inversion of MT and HTEM data. ....	100
Figure 46 Structural interpretation shown on different geophysical data layers. Panel A: HGM of the gravity CBA. Panel B: Reduced-to-pole aeromagnetic data. Panels C and D: Depth slices through the joint inversion resistivity models at 150 and 500 meters below surface, respectfully. ....	102
Figure 47 Geologic Interpretations of East Hawthorne using geological, gravity, magnetic and MT data. Along each profile, magnetic data and the horizontal gradient magnitude of the gravity have been extracted and are shown above slices through the 3D MT-HTEM joint inversion resistivity model. ....	103
Figure 48 Conceptual Model 1, with upflow hosted near the intersection of the Pamlico Fault and inferred NNE-striking, NW-dipping normal faults. ....	107
Figure 49 Conceptual Model 2, with upflow hosted on NNE-striking, NW-dipping normal faults that occur down-dip of the inferred fault contact intercepted by well HAD-1.....	108

Figure 50 Proposed TGH well target locations, with existing wells, relevant components of the fault model, 2-m temperature anomalies and reservoir area estimates for Models 1 and 2.....	111
Figure 51: Cross sections NE1 and NE2 through the 3D MT resistivity model. Layered 1D models of the MT data are shown as model bars on top of the 3D model, and are cut off at an arbitrary depth 2000 m.....	124
Figure 52: Cross sections NE3 and NE4 through the 3D MT resistivity model. Layered 1D models of the MT data are shown as model bars on top of the 3D model, and are cut off at an arbitrary depth 2000 m.....	125
Figure 53: Cross sections NW1 and NW2 through the 3D MT resistivity model. Layered 1D models of the MT data are shown as model bars on top of the 3D model, and are cut off at an arbitrary depth 2000 m.....	125
Figure 54 Cross sections along HTEM flight lines L40010 and L40020 through the 3D MT resistivity model. Layered 1D models of the MT data are shown as model bars on top of the 3D model.....	126
Figure 55 Resistivity models for HTEM flight lines L40010 and L40020. The transition to a transparent background denotes the likely depth of investigation, which is variable. MT stations are shown at black triangles for reference. ....	126
Figure 56 Cross sections along HTEM flight lines L40030 and L40040 through the 3D MT resistivity model. Layered 1D models of the MT data are shown as model bars on top of the 3D model.....	127
Figure 57 Resistivity models for HTEM flight lines L40030 and L40040. The transition to a transparent background denotes the likely depth of investigation, which is variable. MT stations are shown at black triangles for reference. ....	127
Figure 58 Cross sections along HTEM flight lines L49020 and L49030 through the 3D MT resistivity model. Layered 1D models of the MT data are shown as model bars on top of the 3D model.....	128
Figure 59 Resistivity models for HTEM flight lines L49020 and L49030. The transition to a transparent background denotes the likely depth of investigation, which is variable. MT stations are shown at black triangles for reference. ....	128
Figure 60 Depth slices through the 3D MT model at 100, 150, 200, 300 400 and 800 meters below surface. MT station locations are shown as black triangles for reference.....	129
Figure 61 Depth slices through the 3D joint inversion resistivity model (HTEM + MT) at 75, 150, 200 and 300 meters below surface. Each map includes key interpreted fault layer, wells, 2-m temperature contours and reservoir area estimates for Model 1 and Model 2, as discussed in the text.....	130
Figure 62 Depth slices through the 3D joint inversion resistivity model (HTEM + MT) at 450, 500, 600 and 700 meters below surface. Each map includes key interpreted fault layer, wells, 2-m temperature contours and reservoir area estimates for Model 1 and Model 2, as discussed in the text.....	131
Figure 63 Cross-sections through the 3D joint inversion model. Each section includes wells (existing = black, proposed = red), MT stations (small black circles) and 1D layered models of the MT shown as model bars. 1D models are arbitrarily clipped at 2 km deep and may include portions of data that are not 1D in nature. ....	132
Figure 64 Cross-sections through the 3D joint inversion model. Each section includes wells (existing = black, proposed = red), MT stations (small black circles) and 1D layered models of the MT shown as model bars. 1D models are arbitrarily clipped at 2 km deep and may include portions of data that are not 1D in nature. ....	133

Figure 65 Cross-sections through the 3D joint inversion model. Each section includes wells (existing = black, proposed = red), MT stations (small black circles) and 1D layered models of the MT shown as model bars. 1D models are arbitrarily clipped at 2 km deep and may include portions of data that are not 1D in nature. .... 134

**LIST OF TABLES**

Table 1 Technical specifications of the HTEM system .....24

Table 2 Two-meter temperature anomaly data acquired by BRIDGE or existing data from BRIDGE prospect locations with comparison TG data from select sites. DAB refers to Degrees Above Background.....32

Table 3 BRIDGE prospect portfolio and final status and assessment at the project end.....36

Table 4 Summary table of available well data at Lee-Allen. ....65

Table 5 Water sample temperatures, applicable geothermometers, and notes for samples from the Lee-Allen area. Colors correspond to the sample point colors in the other figures, e.g. red = “spring” samples from near Lee-Allen Hot Springs, light blue = wells, and dark blue = spring samples from Stinking and Coyote Springs.....70

Table 6 Lee-Allen conceptual model estimates of reservoir area and resource temperature. ....76

Table 7: Power capacity estimates for Lee-Allen .....80

Table 8: Select water sample temperatures, applicable geothermometers, and notes for waters samples from the Hawthorne Valley. Table colors correspond to the colors used in other figures in this section; red is East Hawthorne, light blue is West Hawthorne, and dark blue is the Tufa Area. ....91

Table 9 Well summary table for East Hawthorne.....96

Table 10 East Hawthorne conceptual model estimates of reservoir area and temperature. .... 106

Table 11 Recommended exploration drilling targets at East Hawthorne ..... 110

Table 12 Summary of BRIDGE published data. .... 139

This page left blank

## EXECUTIVE SUMMARY

As the opportunities to discover new power-capable hydrothermal reservoirs associated with surface manifestations diminish, geothermal resource exploration is increasingly focused on “blind” or hidden systems, enhanced geothermal systems, and other types of resources. Hidden geothermal systems – i.e., hydrothermal reservoirs lacking typical surface manifestations – represent a potentially prolific energy resource that could support critical U.S. public and government energy needs. It is estimated that about 70% of the convective hydrothermal systems in the Basin and Range province of the western U.S. are hidden resources, and that only about half of these resources have been discovered. Traditional exploration approaches start with the identification of warm-hot fluid flow indicators at the surface (i.e., hot springs, fumaroles, steaming ground, recent sinter depositions, and alternation zones). Hidden systems, however, have historically been identified by chance (i.e., unintentionally) from shallow wells drilled for other purposes such as groundwater or mineral exploration. Over the past couple of decades, exploration strategies for hidden systems in the Basin and Range have evolved towards a unified methodology. Recent contributions include identifying favorable structural settings, Play Fairway Analysis (PFA), machine learning, and regional surveying.

Basin and Range Investigations for Developing Geothermal Energy (BRIDGE), funded under DOE Contract Number NA0003525, was an applied research project proposed in response to the FY2020 Hydrothermal and Low Temperature Multi-Topic Funding Opportunity Announcement (DE-FOA-0002219) issued by the U.S. Department of Energy’s Geothermal Technologies Office (GTO). The research was conducted to address the GTO Hydrothermal Resource Program priorities of stimulating the discovery and development of hidden geothermal resources through pre-survey reconnaissance, pre-drilling exploration, conceptual modeling, and drilling. Specifically, GTO’s Hidden System Initiative aims to drive down the costs and risks associated with discovery of hidden systems in the Basin and Range region. Efficient methods in subsurface characterization are needed to reduce uncertainty and mitigate risk during the early exploration phase of resource development (where uncertainty and risk are highest). Thus, BRIDGE prioritized cost-effective exploration through strategic workflow and informed decision-making driven by a conceptual modeling philosophy, as opposed to the always tempting but routinely ineffective/risky “anomaly targeting” and “gut instinct” approaches. This methodology reduces uncertainty, increases the rate of discovery success, and enables de-risked investment in the more expensive stages of exploration (e.g., drilling). The workflow was applied to the project’s geothermal prospect portfolio, initially informed by the Nevada PFA, to yield a publicly available exploration portfolio and prospect ranking ready for public and industry utilization. This report presents the results of a scaled, multidisciplinary exploration workflow that drives down exploration costs and risks associated specifically with identifying and characterizing hidden, power-capable geothermal resources with the objective of improving exploration approaches for discovering hidden geothermal systems.

A primary focus of the project was conceptual modeling to guide prospect exploration in a phased workflow. In Phase 1, selected areas of interest in the Nevada PFA were identified and ranked in terms of being confirmed or possible power capable resources. During this phase, the team compiled geology data from maps and drilling, geochemistry and temperature data from springs and wells, and geophysics data from public sources. The team identified twenty-four (24) prospects based on these data, previous PFA studies, and a 3,000 km<sup>2</sup> helicopter-borne time-domain electromagnetic (HTEM) survey specifically designed to cover these prospects. HTEM imaged subsurface resistivity patterns typically up to 300 meters below ground surface. Favorable prospects were advanced to Phase 2 based on resource temperature inferences and land access considerations. Phase 2 identified priority geoscience data gaps (e.g., geophysics, geochemistry, shallow temperature

surveying) that, if closed, would advance the prospect forward. Emphasis was put on surface exploration approaches that can provide valuable information needed to build initial conceptual model elements. As data gaps were identified and closed in Phase 2, the high-ranking prospects were advanced to Phase 3 geophysics (e.g., detailed magnetotellurics geophysical surveying). Conceptual models informed by Phase 3 were updated with more information at reservoir depths. Phase 3 prospects were primed for drilling confirmation, starting with strategic temperature gradient hole (TGH) drilling (Phase 4) and, if there is sufficient evidence to pursue it, slim hole drilling (Phase 5).

Phase 1 HTEM data proved an exceptional reconnaissance tool that a) made subsequent Phases 2 & 3 more efficient, b) informed conceptual models, and c) appear to support clay cap / hydrothermal alteration models for Basin & Range hidden hydrothermal systems. A central finding was that zones of low resistivity frequently occur over geothermal systems in the Basin and Range and, when paired with other data constraints, imaging these zones can enable discovery of these systems. Calibrated interpretation of two producing hydrothermal systems supported these findings. Notably, the ability of HTEM to resolve shallow resource indicators proved strategic for targeting, and complementary for interpretation, of the deeper imaging but more expensive magnetotelluric survey method. In addition to exploring greenfield areas, BRIDGE also collected HTEM resistivity data over known geothermal systems including those with established power plants and prospects known to the literature but that remain undeveloped, at least in part, due to a lack of understanding on the location of their producible reservoirs.

The BRIDGE prospect portfolio and exploration workflow are testaments to the efficacy of the BRIDGE methodology. The team identified 24 prospects and created decision space to pursue the most viable based on technical and non-technical context. BRIDGE advanced conceptual models, and provided recommendations for Phase 4 temperature confirmation, of three top-ranking prospects. Phase 2 data gaps, and Phase 3 imaging, are primed to be pursued at many other prospects. It's important to note that land access barriers prevented several prospects from being advanced beyond Phase 2. Should access and/or economic constraints change, these and other prospects may be revisited in the future. The BRIDGE Project developed a scalable exploration workflow that furthers PFA, drives down exploration costs and risks associated with identifying hidden power-capable geothermal resources, and shift costs to finance drilling. The resulting portfolio and workflow provided crucial new resources for efficient exploration and more informed decision-making to facilitate the pursuit of economically viable U.S. geothermal power production.

## ACRONYMS AND TERMS

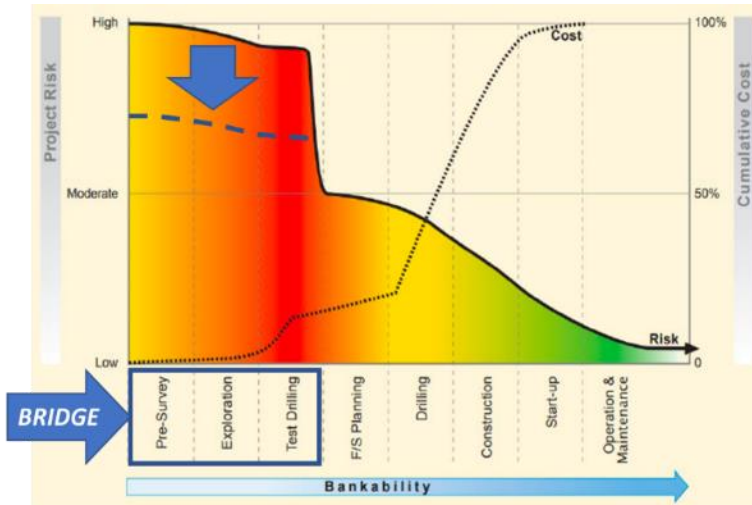
Acronym/Term	Definition
1VD	first vertical derivative
BHT	bottom hole temperature
BRIDGE	Basin & Range Investigations for Developing Geothermal Energy
CBA	complete Bouguer anomaly
DAB	degrees above background
DOE	Department of Energy
DOI	depth of investigation
GBCGE	Great Basin Center for Geothermal Energy
GDR	Geothermal Data Repository
GPO	[Navy] Geothermal Program Office
GTO	Geothermal Technologies Office
HGM	horizontal gradient magnitude
HTEM	helicopter-borne transient electromagnetics
IGRF	International Geomagnetic Reference Field
INGENIOUS	Innovative Geothermal Exploration through Novel Investigations of Undiscovered Systems
kya	thousand years ago
masl	meters about sea level
MT	magnetotellurics
MW	megawatt
NBMG	Nevada Bureau of Mines and Geology
NDWR	Nevada Division of Water Resources
PFA	Play Fairway Analysis
RMI	residual magnetic intensity
RMS	root mean squared
RPF	Russell Pass Fault
RTP	reduction to pole
SMU	Southern Methodist University
TDS	total dissolved solids
TEM	Time-domain electromagnetics
TG(H)	temperature gradient (hole)
USGS	United State Geological Survey
WSA	Wilderness Study Areas

## 1. INTRODUCTION

As the opportunities for discovering new power-capable hydrothermal reservoirs associated with surface manifestations diminish, geothermal resource exploration is increasingly focused on “blind” or hidden systems, enhanced geothermal systems, and lower temperature systems. This is related to both non-technical barriers, such as public opinion and regulatory priorities, and industry’s need for more opportunities for discovery that do not seriously impact uses of the surface of greater societal value. Blind geothermal systems – hydrothermal energy reservoirs lacking typical surface manifestations like hot springs, fumaroles, recent sinter deposition, and alteration zones – represent a potentially prolific energy resource that could support critical U.S. public and government energy priorities. Some have estimated that about 70% of the convective geothermal resources in the Basin and Range province are hidden resources and that only about half of these hidden resources have been discovered thus far e.g., [1]. The search for hidden systems, however, is typically time- and resource-intensive because of the scale of exploration (i.e., the upflow and outflow of a geothermal system may span only several km<sup>2</sup> and so may easily be missed amongst the 1000s of km<sup>2</sup> expanse of potentially prospective basins).

It is very likely that all power capable geothermal systems with surface expressions in the Basin & Range have been explored and that most have been developed, leaving little opportunity for expanding geothermal utilization based on these types of resources. Because hidden geothermal systems lack surface manifestations, they have been discovered mainly by chance (i.e., unintentionally) when anomalously high temperature was noticed in wells drilled for other purposes such as groundwater or mineral exploration [2]. Where a natural thermal manifestation or a fortuitously placed mining core hole indicate that some types of geothermal system exist, exploration approaches like detailed local geology and magnetotelluric (MT) surveys can be cost-effectively focused to locate temperature gradient (TG) and/or slim hole wells that reduce risk prior to targeting more expensive exploration production wells. However, conducting MT surveys at a regional scale to detect resistivity patterns potentially indicative of hidden geothermal systems would either have stations too widely spaced to provide reliable detection of hidden systems or would be far too expensive. Over the past decade, research projects directed at the exploration of hidden systems in the Basin and Range have investigated methods to reduce exploration risk more cost-effectively. These include the identification of key structural settings for follow-up surveys (e.g., [3], [4]), Play Fairway Analysis (e.g., [5], [6]), the use of machine learning [7], [8] and the BRIDGE project’s approach to integrating airborne electromagnetic resistivity methods at regional scale with a sequence of increasingly expensive local geoscience surveys to build geothermal conceptual models that support drilling decisions [9], [10], [11], [12].

The Geothermal Technologies Office Hidden System Initiative aims to drive down the costs and risks associated with the discovery of hidden geothermal systems in the Basin and Range region of the western U.S. and elsewhere. This initiative builds on the Play Fairway Analysis (PFA), adapted from petroleum and mining exploration, which identifies the potential locations of hydrothermal systems and qualifies geothermal opportunities. PFA incorporated regional to basin-wide distributions of geochemical, geophysical, and geological factors indicative of heat, permeability, and fluid characteristics into a favorability model with the primary focus on modeling permeability and combining data with regional heat flow data (e.g., [5]). The Nevada PFA has proven to be successful in targeting hidden systems in the Basin & Range. Initiatives such as the BRIDGE project and the Innovative Geothermal Exploration through Novel Investigations of Undiscovered Systems (INGENIOUS) project have followed up the PFA studies by developing and demonstrating



*Adapted from Gehringer & Loksha, 2012*

**Figure 1 Project cost and risk profile at various stages of development. BRIDGE prioritized cost-effective exploration early on (blue box) through strategic workflow and informed decision-making. Such as approach mitigates early risk (blue dashed line) and increases the rate of discovery success while shifting resources to later stages (e.g., drilling).**

technology and workflows to further identify and characterize geothermal resource targets suitable for drilling.

INGENIOUS builds on the Nevada PFA by developing regional to local scale play fairway exploration workflows and demonstrating them at new hidden system prospects. The INGENIOUS workflow combines a variety of advanced exploration tools (e.g., conceptual modeling, machine-learning, advanced geostatistics, value of information analysis) into candidate best practice options for exploring broad regions. The INGENIOUS study includes northeast California through central Nevada to western Utah to accelerate the discovery of commercially viable hidden systems across a broader Great Basin region.

BRIDGE developed an exploration workflow for hidden, power-capable geothermal resources that leverages regional airborne surveys, especially helicopter-borne time-domain electromagnetic (HTEM) resistivity survey data, to focus local geoscience surveys in a more cost-effective manner. The approach was tested on U.S. Department of Defense lands and adjacent areas in southern Nevada as well as at two developed geothermal fields to provide validation. The cost of mobilizing an HTEM system makes it unlikely that such a survey would be used to explore a single geothermal prospect. However, for most of the US Great Basin that is prospective for hidden geothermal systems, a regional HTEM survey similar to the data acquired for BRIDGE will become publicly available as part of the USGS Earth Mapping Resource Initiative [13]. In addition to HTEM, this initiative includes LiDAR, magnetic and gamma ray surveys like those utilized by BRIDGE. The reconnaissance geoscience data and analyses were integrated with the HTEM resistivity survey data to focus follow-up geoscience methods and identify contexts where heat can be detected using successively more costly 2-m temperature holes, 3D MT surveys, < 150-meter TG wells and slim hole wells to discover a geothermal reservoir. The approach prioritizes cost-effective exploration early on through strategic workflow and informed decision-making that mitigates early risk and shifts resources to later exploration stages (Figure 1 adapted from [14]).

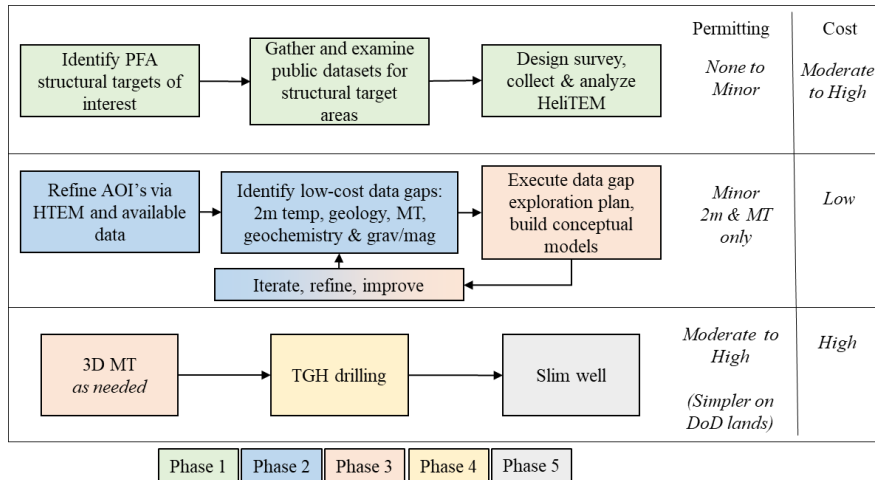


**Figure 2 The BRIDGE "prospecting" exploration workflow. Phase 1 identifies and initially ranks prospects. Phase 2 identifies priority data gaps. Phase 3 closes those data gaps. Phase 4 develops conceptual models and executes targeted TGH drilling. Phase 5 executes targeted slim hole drilling.**

The primary approach of the project is the identification of those data sets that can most cost-effectively support building conceptual models to guide drilling and discovery of economically viable geothermal reservoirs e.g., [15]. The tasks included in the project include demonstrating the utility of airborne and surface methods in developing conceptual models for hidden systems, demonstrating joint inversion of geophysical datasets, developing a ranking system; building a hidden systems portfolio complete with conceptual models, resource capacity estimates, and recommended next steps. The workflow is characterized by reconnaissance, exploration, modeling, and testing steps and organized into five (5) iterative phases (Figure 2):

- Phase 1 Identify and initially rank prospects based on data from Nevada PFA, existing geoscience datasets, and a project-acquired airborne resistivity survey and an assessment of the likelihood of developing a resource conceptual model that can be tested with 150 m temperature gradient wells and/or 500 m slim hole wells.
- Phase 2 Identify priority data gaps (geologic mapping, LiDAR analysis, geochemical sampling, 2-m temperature surveys, gravity, aeromagnetics and MT surveys) that, if closed, will advance a prospect forward/
- Phase 3 Conduct follow-up surface exploration studies to close high-priority data gaps.
- *Phase 4* Develop initial conceptual models, rank prospects, and design temperature gradient hole (TGH) campaigns.
- *Phase 5* Rank prospects and verify resource(s) with targeted deep slim wells and update conceptual models.

Phase 1 of BRIDGE selected areas of interest in the Nevada PFA (Figure 3) and ranked them relative to their likelihood of being identified using the planned program as being possible power capable resources. BRIDGE compiled geology data from maps and drilling, geochemistry and temperature data from springs and wells, and geophysics data from public sources and previous PFA studies. Well temperature and depth, temperature gradient, spring temperature, geochemistry, well logs came from the South Methodist University's (SMU) node of the National Geothermal Data System, Great Basin Center for Geothermal Energy, Nevada Division of Water Resources. Records

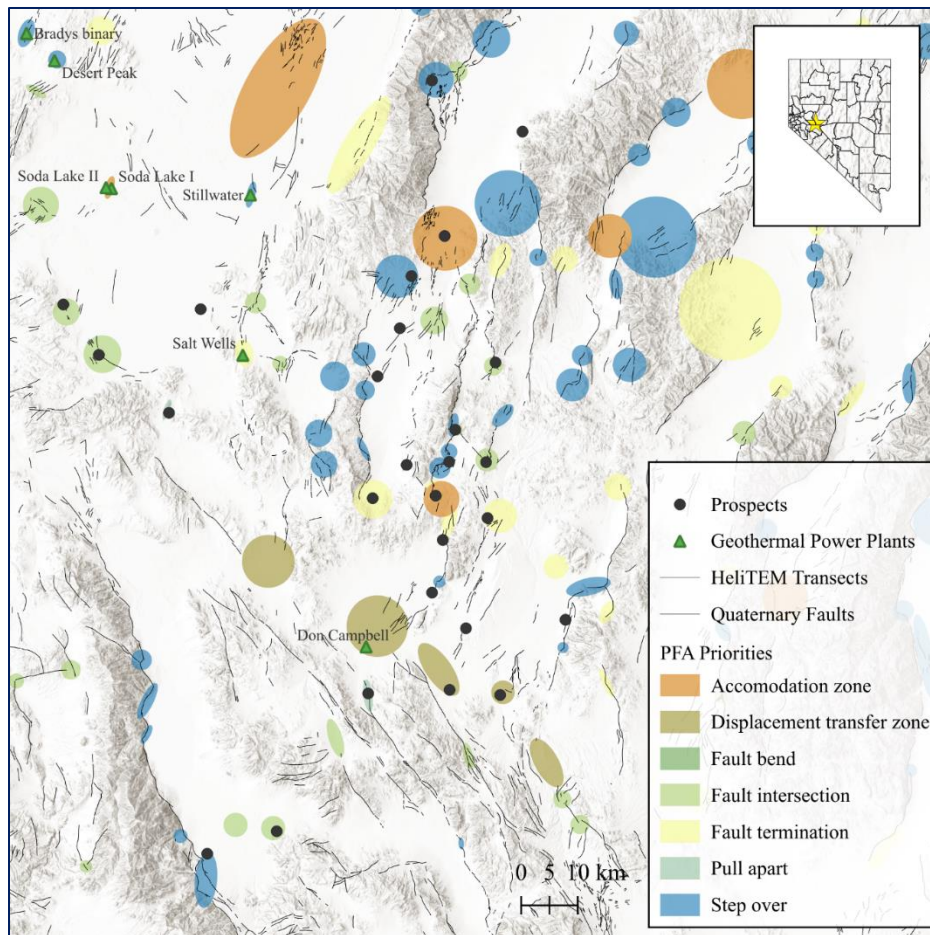


**Figure 3 Selected BRIDGE prospects and favorable structural targets identified in Nevada PFA.**

and data for geothermal and oil & gas wells came from the Nevada Division of Mines and Geology. Geologic maps came from the USGS's National Geologic Map Database. Two-meter temperature data came from published studies, the U.S. Navy Geothermal Program, and the U.S. Department of Energy's Geothermal Data Repository (GDR). Potential fields and MT datasets and maps come from the Navy (unpublished), GDR, and published studies. Twenty-four (24) prospects in and near Department of Defense lands in southern Nevada were identified based on these data, and by a 3,000 km<sup>2</sup> HTEM survey, specifically designed to cover potential prospects that could be assessed by resistivity imaging to ~300 meters, on average, below ground surface.

Prospects were judged favorable to move on to Phase 2 based on possible resource temperatures and land access. Phase 2 identified priority data gaps that, if closed, would advance the prospect from Phase 3 to drilling. Emphasis was put on surface exploration approaches that can provide valuable information needed to build a conceptual model ahead of exploration drilling. Surface exploration included geologic mapping informed by LiDAR analysis, geochemical sampling of springs and existing wells, 2-meter temperature and MT surveys (full surveys or in-fill), and focused gravity surveys. The novelty here was not in the exploration tools themselves but the way in which our data gap analysis and ranking guided our targeting approach.

- Geologic mapping is needed to provide better characterization of structural settings that could host upflow-outflow pathways and provide a basis for planning and interpreting other surface exploration (i.e., MT). Prior to field mapping, a LiDAR analysis was completed for some of the active prospect areas using the Geophysical Data Acquisition on Western Nevada (GeoDAWN) 1-meter resolution LiDAR data [16]. These analyses identified possible structural targets that mapping campaigns can confirm or reject.
- Geochemistry provides key indirect temperature data through geothermometry and inputs to conceptual model options.
- The 2-meter temperature surveys are an effective approach for identifying thermal anomalies in areas that are otherwise all or mostly unexplored e.g., [17]. Many prospects have limited surface temperature data, but what does exist often suggests a thermal anomaly. Infill or new 2-m temperature measurements is a low-cost tool for further defining thermal anomalies, adding context to HTEM interpretations, and informing TGH placement.
- The MT and HTEM data help characterize and map out the smectite caps that are common over these types of resources. (More on clay caps later in this report.)

As data gaps were identified, prospects shifted between Phase 2 and 3. The costliest exploration done in Phase 3 were an MT surveys that supported resistivity imaging using 3D inversions. MT surveys were done for high-ranking prospects to provide resistivity imaging below the depth of investigation of the HTEM. Strategic station layouts were based on initial conceptual modeling and HTEM data. Conceptual models were updated based on what was resolved in MT and HTEM models. MT data from one prospect, East Hawthorne, was jointly inverted with HTEM— an approach not used in a geothermal context prior to BRIDGE. The joint inversion provided superior imaging of resistivity structures through a larger depth range than the HTEM or MT on their own and has played an important role in developing proposed well targets at East Hawthorne. The BRIDGE workflow was ultimately organized not only by the planned phases but also by permitting and cost limitations. Permitting and cost demands are a critical consideration since minimizing overall risk, not just geoscience risk, was the overarching objective of BRIDGE. High demands are shifting to later phases, leaving space to prioritize prospect ranking and low-moderate cost surface exploration. The exception here is the HTEM survey, which is a large initial cost, but provides shallow subsurface imaging over approximately 3,000 km<sup>2</sup>.

High-ranking prospects would have moved to Phase 4, temperature gradient hole drilling. Since a conceptual modeling was developed in Phase 3, TGH targets are strategically positioned, as detailed for each high priority prospect, such that gradient data will further inform the conceptual model and potentially provide evidence to move forward to the final exploration phase (Phase 5) and drill one or more slim wells.

## 2. AIRBORNE RESISTIVITY IMAGING

### 2.1. Justification

Resistivity imaging is a particularly useful method in geothermal resource exploration (hidden or non-hidden systems) because of its sensitivity to key geothermal system attributes, primarily the smectite clay content of the aquicludes that cap the geothermal upflow and outflow zones. In the geothermal context of the Basin and Range, porosity, salinity, and temperature have important secondary effects on resistivity since smectite clays that have higher water or salt content or that are at higher temperature (up to 200 °C) are lower resistivity. However, rocks such as sandstones or crystalline metamorphic rocks that have low smectite clay content will typically be relatively resistive in comparison to smectite-rich rocks, even if they are hotter or more porous. Although the dominant effect on resistivity interpretations in an oil and gas context related to pore water saturation versus hydrocarbon saturation, this has little or no relevance to conventional geothermal resistivity interpretation. However, pore water saturation as it relates to the water table has a profound effect on smectite clay diagenesis and so the relationship of the resistivity pattern to the water table is important to geothermal interpretation, and low resistivity above the water table can be indicative of hydrothermal alteration related to an underlying geothermal reservoir. The relative ranges of resistivity values within a dataset are typically more useful than associating specific values with, for example, a clay cap since the water table, an increase in salinity or geothermal alteration can all reduce resistivity. That is, resistivity imaging is sensitive to multiple attributes of geothermal systems.

Clay mineral resistivities behave non-linearly with pore water content (e.g., [18], [19]) and so discriminating the influence of these attributes is a major data interpretation challenge. Rather than approach resistivity imaging from a quantitative petrophysical perspective, BRIDGE utilizes the HTEM data to resolve local, shallow low resistivity structures in the context of what is known about the geology and typical Basin & Range hydrothermal systems, their spatial relationship to the integrated geology, hydrology, and structural interpretation. Relatively low resistivity zones in the upper 2 to 3 km of the subsurface in western Basin & Range geothermal systems are mostly related to smectite clays, either sedimentary clay, hydrothermal alteration clay or both (e.g., [15], [20], [21]). Smectite clay has low electrical resistivity [18], [22] and forms layers with low vertical permeability that cap the flow path of the higher temperature upflow of the geothermal system and diverts it to a similarly capped outflow aquifer, eventually emerging at the surface or mixing with meteoric water. Low vertical permeability clay layers also prevent the downflow of cooler and, depending on salinity of hotter fluids, typically denser meteoric water. The smectite clay cap promotes the accumulation of hot water in relatively shallow permeability zones above upflows associated with deeply penetrating fault zones. Smectite-rich zones in Basin & Range systems are most found within Quaternary sedimentary shales but are also found as hydrothermal alteration zones in non-sedimentary volcanic, metamorphic, and intrusive rocks. Clays mixed with saline water associated with evaporites form particularly low resistivity zones unrelated to geothermal systems, particularly in the middle of basins. Basement rocks on the range side of basin-bounding faults are commonly high resistivity.

The resistivity pattern associated with a geothermal upflow might include a shallow dome in the base of the low resistivity cap at its apex and a deeply dipping interface of low resistivity basin-filling clay-rich sediments contrasting against the higher resistivity rocks associated with the hot upflow. The resistivity pattern associated with a geothermal outflow is typically a tabular zone that is particularly low resistivity over the outflow with a base dipping up in the direction of flow, with a very slight

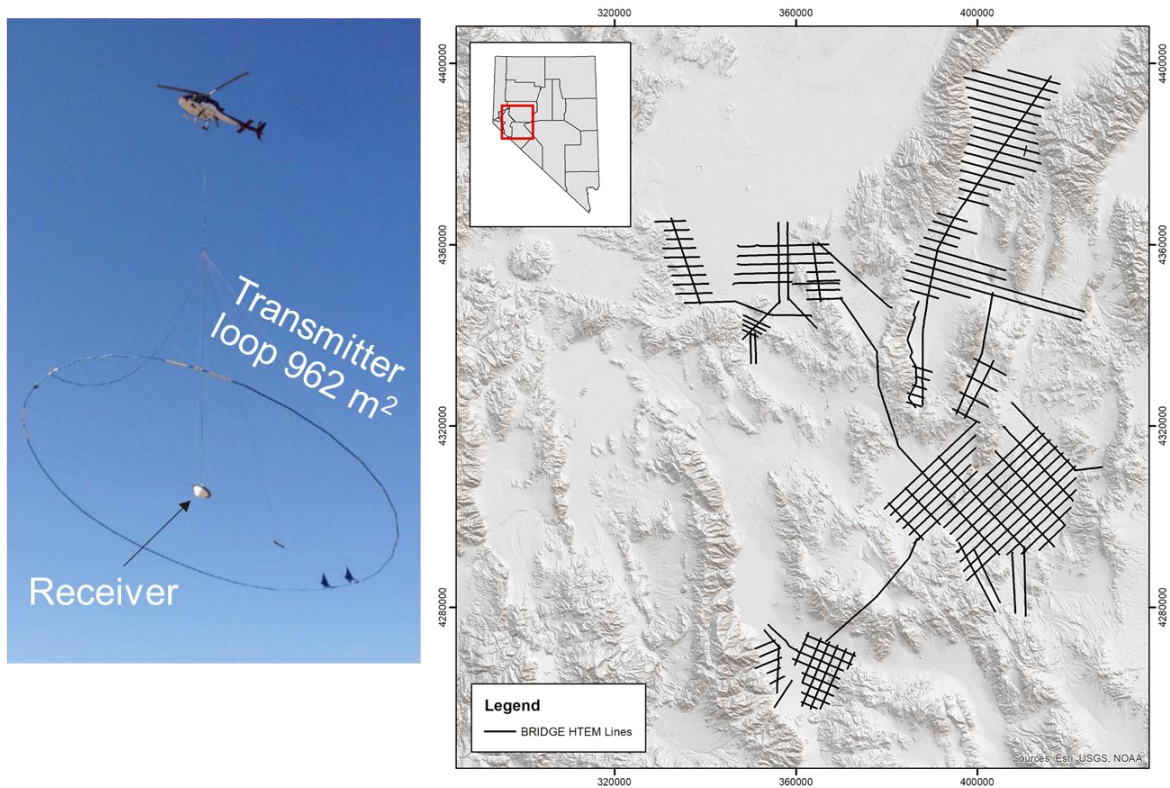


**Figure 4 BRIDGE acquired a regional-scale helicopter-borne transient electromagnetic survey (HTEM) as part of its early-stage reconnaissance effort.**

angle of dip that does not reach the surface, in the case of a hidden system. A high resistivity layer from the surface to the top of the clay cap is likely to be cooled by meteoric water, probably above the water table.

With this overall understanding of expected resistivity structures based on common geological features in Basin & Range systems, we can characterize prospects at a reconnaissance level ahead of complementary, detailed exploration approaches. BRIDGE focused on identifying low resistivity zones interpreted as potential clay caps over underlying permeable fractured rock or possible smectite zones that cap shallower outflows that are commonly associated with very shallow thermal anomalies that could be explored using 2-m temperature surveys that could prove the existence of a geothermal system at low cost [20].

## 2.2. Survey & Data Specifications

For Phase 1, a HTEM survey was flown over more than a dozen prospective basins in western Nevada with Xcalibur's HELITEM™ system (Figure 4). The 7.5 Hz-base frequency HELITEM™ system can detect conductive targets within moderately resistive rocks at depths of over 500 meters [23]. HTEM surveys have been conducted over several geothermal fields in Japan and they effectively imaged smectite clay alteration in the near surface with good matches between low resistivity areas and mapped occurrences of surface hydrothermal alteration e.g., [24], [25], [26], [27]. BRIDGE aims to test the efficacy of HTEM to image shallow conductive targets in typical Basin & Range settings (via its comparison with MT data and existing well logs) and thus identify potential new hidden systems.

The survey was designed to both test the HTEM method at producing geothermal power sites (the hidden Don A. Campbell and the Salt Wells systems), known but undeveloped systems (e.g. East Hawthorne) on DoD lands as well as to identify potential new hidden systems within and near the DoD lands in the study area, including highly prospective areas identified in the Nevada PFA. Lines were flown over known wells and MT surveys such that direct comparisons between the HTEM resistivity, MT resistivity and well temperature, geologic and alteration data could be made. Lines were spaced approximately two kilometers apart for lines perpendicular to basin boundaries with larger spacing for lines or single tie-lines parallel to the basin boundaries for most of the areas. The two-kilometer spacing was considered adequate for the purpose of identifying new potential hidden systems based on typical B&R systems having geophysical and thermal expressions of several km<sup>2</sup>. Closer line spacing of 1 km was flown over the East Hawthorne area where there is abundant well data and a known hidden geothermal system exists. Areas of high and rugged topography were avoided as these are difficult to fly when acquiring data. The survey plan also considered future accessibility of sites for TG and slim well drilling and potential electromagnetic noise sources (e.g. standoff of several hundred meters from high voltage powerlines, townships, and power plants). These considerations minimize the effects of electromagnetic noise sources on the acquired data.

The technical specifications of the HTEM system are listed in Table 1. A total of 1,877 line-km of HTEM was flown over 12 days of acquisition in March-April of 2022. Soundings were made approximately every 30 meters along flight paths to provide high horizontal resolution imaging along profiles.

The contractor delivered preliminary processing of the data within a day of the data being acquired in several forms, but the most useful for preliminary interpretation proved to be the differential resistivity cross-sections and maps. The differential resistivity inversion method is described in Huang & Fraser [28]. Comparison of the differential resistivity to the final inversion products and MT soundings in Figure 5 indicates that it provides a rapid, low cost and robust initial subsurface resistivity image. The differential resistivity cross-sections and maps were used to monitor data quality and depth of investigation and to adjust survey flight lines during the survey. For example, differential resistivity from several initial flight lines adjacent to the Fallon geothermal area indicated very low near-surface resistivity related to high salt content playas. As a result, the survey in the center of the basins around Fallon and other areas associated with evaporites was curtailed and more valuable data were collected at other BRIDGE areas of interest.

Three inversions of the HTEM were carried out – the differential resistivity inversion (as described previously), an inversion carried out by Xcalibur using their GALEI (GALEISBSTDEM) code and an inversion carried out by USGS using Aarhus Workbench (AarhusInv). The depth of investigation (DOI), an estimate of the depth to which resistivity is resolved, was computed by both Xcalibur and the USGS. The AarhusInv models provided both a ‘standard’ and ‘conservative’ DOI estimate. A comparison of the different inversions and DOI’s and how these compared to MT is shown in Figure 5. All inversions produced similar resistivity images above about 200 meters depth but deviate below this. The differential resistivity and the AarhusInv inversion produced the best results below 200 meters when compared to the MT. This, again, supports utility of on-the-fly differential resistivity imaging. The GALEI inversion consistently placed the base of low resistivity layers at depths inconsistent with MT observations. At depth, AarhusInv models were more in agreement with MT observations, and thus was chosen as the more acceptable model. Both the AarhusInv DOI estimates provided good estimates of the depth resolution based on comparison to MT data at several locations and where the deep resistivity became more variable laterally along cross-sections.

**Table 1 Technical specifications of the HTEM system**

<b>Parameter</b>	
Surveying speed	110 km/h
EM system	HELITEM™ 25 channel multicoil
Transmitter	Vertical axis loop
Transmitter loop area	962 m <sup>2</sup>
Number of transmitter loops	4
Transmitter height	35 m above ground, nominally
Receiver	Multicoil X, Y, Z
Receiver sampling rate	10 samples per second
Base frequency	7.5 Hz
Pulse width	33.3 ms
Pulse off-time	33.34 ms
Transmitted current	146 Amp
Dipole moment	5.6 x 10 <sup>5</sup> A m <sup>2</sup>

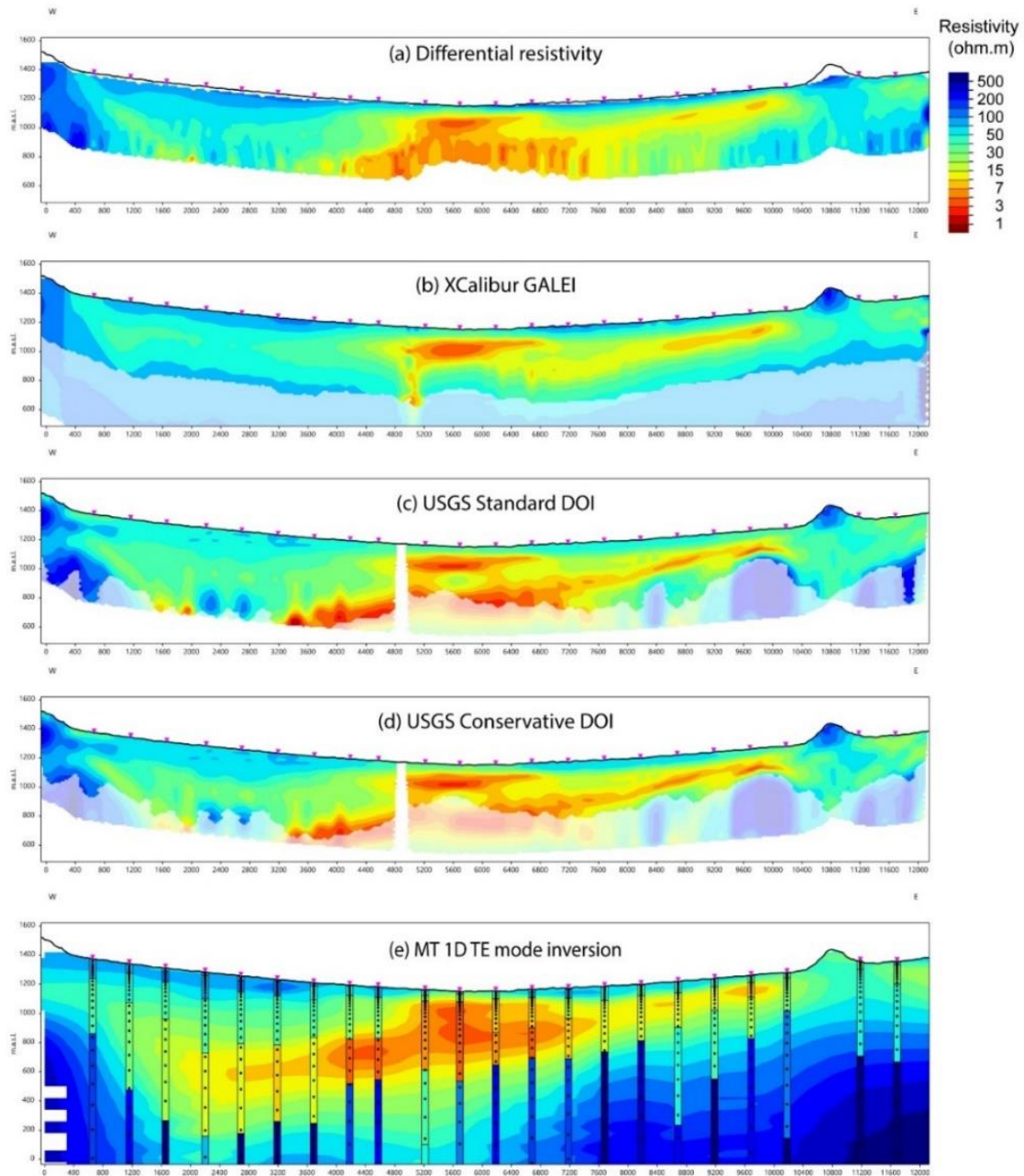


**Figure 5 Comparison of the different inversions carried out on the data (a-d) and comparison to 1D (TE mode) MT inversion (e) for a cross-section through the Dixie Valley area. Depths below the DOI have been made opaque.**

### 2.3. Geothermal Indicators & Strategy

HTEM data proved to be an important reconnaissance tool that made detailed surface exploration more efficient in the Basin and Range context and supported the development of geothermal conceptual models. Notably, HTEM data complements MT data by resolving shallow resource indications associated with smectite clay content (i.e., within 300 meters of the ground surface) while

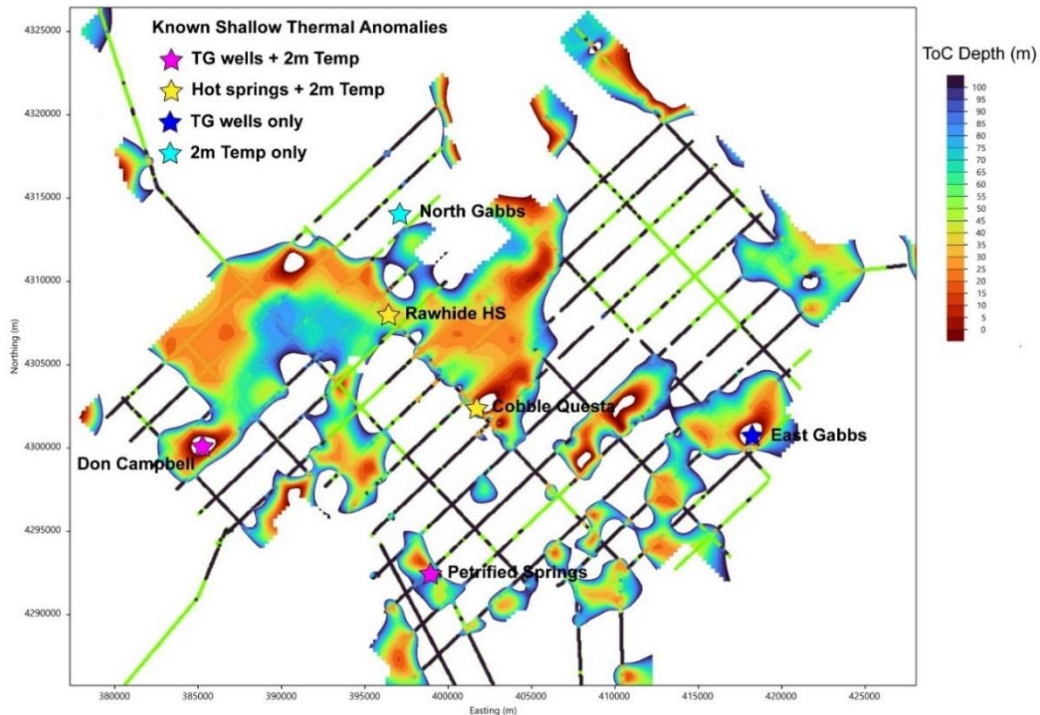


**Figure 6 Depth to the Top of Conductor (ToC, <10 Ohm-m) in the Gabbs Valley area and known shallow thermal anomalies identified by 2-meter temperature and/or thermal gradient wells. Where the HTEM profiles are black, there is a <10 Ohm-m conductor that is greater than 150 meters depth, where green there is no <10 Ohm-m conductor.**

MT resolves deeper resistivity patterns associated with hydrothermal reservoirs (e.g., up to 3,000 meters below the ground surface)

There is good spatial correlation between near-surface, low resistivities (upper 100 m, <10 Ohm-m) and previously identified near-surface thermal anomalies. In Gabbs Valley, for example, most of the identified shallow thermal anomalies in the area, as defined by 2m temperature surveys and drilling (e.g. thermal gradient wells), are associated with low resistivity (<10 Ohm-m) in the upper 100 meters (Figure 6). The North Gabbs thermal anomaly, which is based on 2m temperature surveying, does not have a large <10 Ohm-m near-surface resistivity feature, however it does have a deeper, <15 Ohm-m layer associated with it. This demonstrates the need to utilize other maps and cross-sections when examining the HTEM resistivity for possible hidden system resistivity signatures.

Several components of a geothermal conceptual model may contribute to a geothermal reservoir remaining hidden even though it is hot and permeable enough to be of economic interest. The low vertical permeability clay cap can prevent hot, buoyant, fracture-driven upflow from reaching the surface and forming hot springs if the water table is at the surface or fumaroles if the water table is below the surface and the upflow is above the boiling point. These caps typically consist of smectite clay-rich sediment, smectite-clay alteration, or a combination of the two. To dissipate the heat from the upflow, the upflow must be diverted up-dip below the cap to an outflow, which conductively dissipates heat, cooling outflow to <100 °C. Minor pathways through the cap are possible. For the system to remain hidden, the unconfined cold meteoric aquifer above the cap must be sufficiently thick and extensive to dilute any leakage and cool the top of the cap so that no hot water or steam

reach the surface. Cold meteoric water in the upper few hundred meters cool the top of the conductively heated cap and directly mixes with the geothermal outflow fluid, diluting its chemistry and reducing its temperature (Dobson, 2016). Key conceptual model elements include hot upflow, cooler outflow, a low vertical permeability cap, and mechanisms that “hide” the system from the surface (e.g., conductive heat loss and mixing with meteoric water). Where low resistivity smectite clay caps and/or laterally divert upflow, low resistivity zones ( $<10$  Ohm-m and as low as 2 Ohm-m) imaged by HTEM or MT are spatially correlated with the geometry of a clay cap. Low resistivity zones that extend above the water table are interpreted to be smectite alteration due to an underlying geothermal system. More resistive features or zones ( $\geq 10$  Ohm-m) below the interpreted cap may be associated with aquifers and may potentially host buoyant hot fluid of a geothermal system, although this is ambiguous since low permeability crystalline rocks will also be high resistivity. Medium to high resistivities ( $>10$  Ohm-m) above the low resistivity clay cap (and so not counting resistive basement rock on the range side of a basin-bounding fault), are interpreted as likely influenced by cold meteoric downflow and so have low prospectivity. This HTEM dataset generally was unable to resolve deeper than 300 meters. A geothermal system in the Basin and Range with a clay cap deeper than 300 meter is often masked by cold meteoric water penetrating to at least that depth and so such a system would remain hidden to an exploration approach based on HTEM. However, based on the conceptual patterns expected for hidden systems outlined here, it is expected that the great majority that could be economically developed at this time could be effectively explored using HTEM to detect at least their outflows, if not there upflows.

Figure 7 presents a series of resistivity structures captured in BRIDGE’s HTEM survey organized first by the presence or absence of favorable low resistivity patterns and then by their depth, lateral extent, and apparent dip. This series together with previously available geologic mapping and geoscience data, informed the initial BRIDGE prospect ranking process though the follow-up data acquisition including detailed LiDAR-geology, gravity, geochemistry, aeromagnetic, 2-m temperatures, downhole temperature logs, and MT, data) was expected to change the ranking of prospects.

High ranking resistivity structures are those interpreted as smectite clay caps. Herein we will use “feature” to refer to a low resistivity feature or pattern relative to its surroundings. Shallow features adjacent to a mapped fault (such as low resistivity in a basin and adjacent to a basin-bounding fault) and shallow local features in a favorable structural target setting (e.g., step-over or fault intersection) are two indicators to highly rank a prospect. Low-high-low features (i.e., low resistivity above and below a very local zone of medium to high resistivity) may be indicative of alteration and outflow and is also a high rank indicator.

Medium ranking resistivity structures include features on the range side of a basin-bounding fault, thin features grading into the basin, or a low-high-low feature that extends over a large area of a basin. Range side features may be the result of alteration but unlikely to be indicative of upflow. Features grading into a basin could potentially be deeper outflow. And low-high-low feature extending across a basin may be a thermal outflow aquifer.

Resistivity zones that are  $\leq 10$  Ohm-m but are situated such that it is unlikely that are associated with a smectite clay cap are low-ranked. Near-surface features within a basin, for example, in the Basin & Range are likely water-saturated evaporite-clay deposits. Dipping features within a basin are likely dipping strata (especially clear with low, medium, and high resistivity structures are all dipping together). Finally, large, prominent features on the range side of a fault are most likely old alternation and not indicative of a present-day system.

BRIDGE demonstrates the utility of airborne resistivity, when integrated with supporting geoscience data, is an effective and efficient method for characterizing potential hidden systems, guiding detailed surface exploration, and informing geothermal conceptual models. HTEM data complements MT data by resolving shallow resource indicators (e.g., within 300 meters of the ground surface) while MT resolves the deeper extent of the smectite pattern associated with hydrothermal reservoirs (e.g., up to 3,000 meters below the ground surface). The data summaries and conceptual models of BRIDGE's top ranked prospects discussed in this report will illustrate how these datasets are complementary.

If one or more of the ranking indicators above correspond to a clay zone at or near the surface, a 2-meter temperature survey has a high likelihood of detecting the thermal anomaly if an outflow or upflow underlies the cap. This is because impermeable clay reaching close to the surface likely prevents surface meteoric water from cooling the conductive heat transport from an underlying system, allowing a very shallow temperature anomaly to manifest a hidden system. Later in this report, we delve into shallow temperature surveying and individual prospect summaries show how 2-meter temperature data has been integrated into conceptual models.

One or more indicators of a clay zone capping a geothermal system could be confirmed if a TGH can be drilled at least 50 meters into the low resistivity clay zone so that a temperature pattern can be measured above and within the clay zone and extrapolated to the base of the clay zone. The temperature gradient within the clay is induced by the cold meteoric zone overlying the clay zone and the underlying geothermal system. Therefore, providing that the clay zone hosts no unresolved aquifers, the temperature gradient measured within the clay zone can be extrapolated to the base of the low resistivity clay zone resolved by HTEM or MT data.

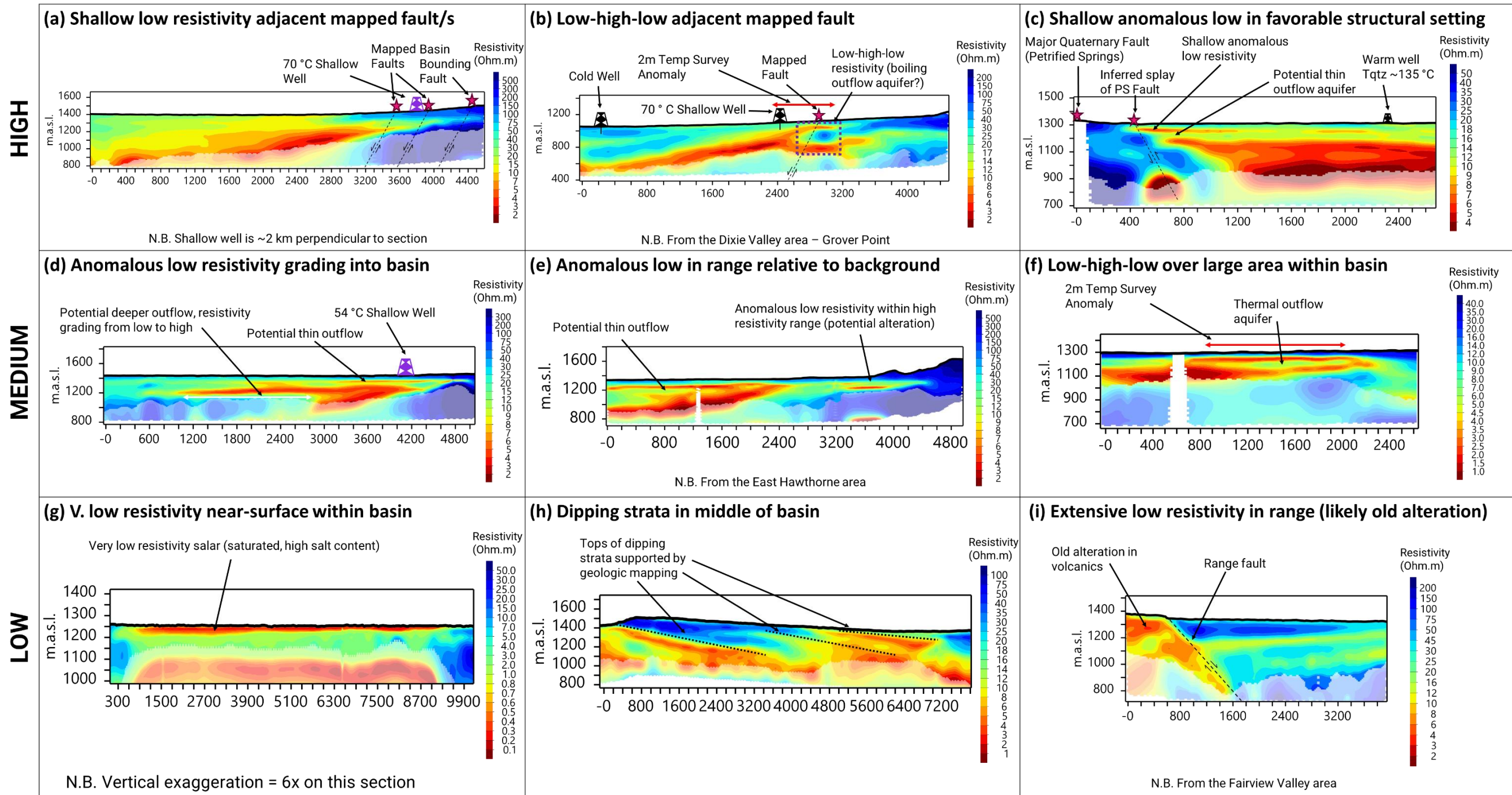
A major challenge in exploration geophysics, in general, is the temptation to “anomaly hunt”, which focuses on data targets rather than fully integrating geophysical observations with physical observations [15]. As a result, assumed correlations between geophysical measurements and physical justifications goes unchecked. Our solution to this is to prioritize a more disciplined conceptual modeling approach. Each exploration tool complements the others, and each exploration step prompts a decision-point; what is next, where, or walk away?

Strategy for using HTEM to explore prospects that are hidden but have shallow (2-150 meter) subsurface manifestation.

1. Assess the pre-survey likelihood of geothermal systems in the study area based on PFA reviews and a conceptual model reanalysis of existing information to constrain subsurface temperature, structure, hydrology, and thermal manifestations. Known resources (i.e., resources that have already been discovered and developed for geothermal power production) are also of interest for calibration and as analogues for generating conceptual models.
2. Check USGS, DOE and other sources for suitable existing HTEM resistivity surveying to image the depth to the low resistivity and low permeability clay cap, within which a thermally conductive (linear) temperature gradient could be targeted for drilling, and potentially image the underlying higher resistivity associated with shallow aquifers hosting outflows from deeper geothermal systems.
3. Analyze new or existing Lidar to assess favorable geology and assess new aeromagnetic data to support geological interpretation integrated with HTEM and other data.
4. Conduct 2m temperature surveys to establish if other data sets were correlated with elevated temperature that might be conceptually extrapolated to a deeper source.

5. In areas where the 2m or existing TG wells detect a prospective temperature gradient but where the HTEM did not penetrate to the base of the cap, conduct surface MT resistivity surveys to image the base of the cap to identify the depth to which the linear TG well gradient could be reliably extrapolated. Conduct surface gravity surveys to map sedimentary basin structural geometry and shallow sinter.
6. Drill temperature gradient (TG) wells that penetrate a thick enough section of the clay cap detected by HTEM and MT to provide a linear thermal gradient that could be reliably extrapolated to the base of the cap.
7. On the most prospective target(s), drill at least one testable slim hole well to discover the resource associated with the interpreted geothermal reservoir upflow source.

## Examples of HTEM Resistivity Structure and their Ranking as Potential Blind Geothermal Systems



N.B. Transparent part of resistivity cross-sections is below the estimate depth of investigation

Figure 7 Examples of HTEM resistivity profiles and their “favorability” ranking. Panels organize low resistivity structures by high, medium, or low ranking in terms of how indicative they are of a hidden system. This considers only HTEM and historic geologic mapping data and acknowledge other datasets (e.g., gravity, geochemistry, shallow or downhole temperature measurements) can change a prospect’s ranking.

### **3. SHALLOW TEMPERATURE EXPLORATION**

#### **3.1. Background**

Shallow temperature surveys have been deployed for geothermal exploration and site characterization for ~40 years in the Great Basin region of the western United States, with greenfield exploration use of 2-m temperature probes in the last ~20 years [29], [30], [31], [17], [32], [33], [34], [35], [36], [37], [38], [39], [40], [41], [11]. 2-m temperature surveys have been shown to be effective at mapping the extent of shallow outflow (0-500 m depth) at several geothermal resources and prospects [42]. Shallow temperature surveys are especially effective in the Great Basin region due to several geologic and climatic factors, such as overall low precipitation preventing concealing of thermal anomalies by cold groundwaters in many locations, and low thermal conductivity unconsolidated sediments near the surface that can increase shallow temperature gradients [43].

Recent DOE-GTO funded work on shallow temperature surveys as part of the INGENIOUS and BRIDGE projects include the compilation of existing publicly available 2-m temperature data [7], a review of equipment and data processing methodologies developed by the Great Basin Center for Geothermal Energy since ~2005 (BRIDGE-INGENIOUS Collaboration [44]; included here as supplemental text), a review of 2-m temperature survey case studies and their contribution to resource conceptual models (BRIDGE-INGENIOUS collaboration, [42]), and a forthcoming python-based workbook for processing 2-m data (INGENIOUS-BRIDGE collaboration, planned to be part of INGENIOUS project final deliverables).

#### **3.2. BRIDGE Data Collection and Processing**

Because 2-m temperature surveys can detect shallow hot outflow between 0-500 m depth, the BRIDGE team utilized the technique to evaluate prospects identified using the HTEM methodologies described above. The BRIDGE team acquired 2-m temperature data at five geothermal prospects (East Hawthorne, Grover Point, Dead Cow Splay, Kaiser, Bell Flat). The data was collected by personnel from the Navy Geothermal Program Office using the standard procedures outlined in Kraal and others (2024). For the East Hawthorne and Grover Point surveys, the effects of seasonal temperature oscillations have been removed to compare with existing 2-m temperature data at or near these locations (i.e. multi-survey correction). Background conditions for each of the five survey areas were removed to plot the data relative to background conditions (2-m DAB). The survey at East Hawthorne was conducted in 2022 to fill a gap between pre-existing 2-m data points. The survey at Grover Point was conducted around several existing warm TGH as well as a favorable HTEM geometry. The 2-m temperature data acquired by the BRIDGE team at East Hawthorne and Grover Point are discussed in their sections below. The 2-m temperature surveys conducted at Dead Cow Splay, Kaiser, and Bell Flat were performed in completely greenfield areas with no existing temperature data available, targeting favorable HTEM geometries hosted in favorable structural settings (Figure 8). All three surveys were limited to locations directly adjacent to existing roads. The Dead Cow Splay and Kaiser surveys did not identify any significant temperature anomaly (~2 °C above background or greater). The Dead Cow Splay survey crossed strike of a mapped quaternary fault scarp into a zone underlain by a shallow low resistivity zone. The Kaiser survey crossed several mapped Quaternary or younger fault scarps but did not cover the shallow low resistivity zone at this location due to lack of road access. The Bell Flat survey, however, did discover a previously unknown shallow temperature anomaly (~3.3 °C above background) that overlies a shallow low resistivity zone (Figure 9). Several favorable structural settings are around the shallow temperature anomaly, including several step-overs in the range bounding faults, fault

intersections, and a fault termination zone to the south. Further work is required to determine the complete geometry of the shallow outflow plume detected by the 2-m temperature and HTEM data, and to determine the most likely upflow location for these hot fluids. The case study examples shown above (as well as those below, with complete conceptual models) demonstrate an exploration workflow utilizing structural analysis and HTEM data to plan shallow temperature surveys, and the use of shallow temperature surveys to down select sites for future work, such as detailed geophysics and/or TG drilling.

**Table 2 Two-meter temperature anomaly data acquired by BRIDGE or existing data from BRIDGE prospect locations with comparison TG data from select sites. DAB refers to Degrees Above Background.**

<i>Location</i>	<b>Max Measured T °C</b>	<b>Max DAB (°C)</b>	<b>Mean DAB (°C)</b>	<b>Length (km)</b>	<b>Width (km)</b>	<b>Area (km<sup>2</sup>)</b>	<b>Excess Heat Loss (MW)</b>	<b>Depth to Isothermal (TG)</b>	<b>Outflow T (TG)</b>	<b>Citation</b>
<i>Gabbs (Don A. Campbell)</i>	37	19.3	9	3.4	1.7	6	16.9	150	128 °C	[45]
<i>Gabbs (Cobble Cuesta)</i>	19	6	1.9	3.7	1.4	2	1.2	NA	NA	[46]
<i>Gabbs (North)</i>	18	3.7	3.3	3.2	1.6	4	4.6	NA	NA	[46]
<i>Gabbs (Petriified Springs)</i>	24.8	5.3	3.7	2	2.2	6	7.0	110 m	124.9 °C	[40]
<i>Grover Point</i>	30.2	4.7	2.4	5.0	1.5	7.7	9.4	NA	NA	[12]
<i>Hawthorne East</i>	21.5	8.4	5.1	1.4	0.5	1.3	2.1	185 m	98 °C	[47]
<i>Gabbs (Kaiser)</i>	17.8	1.3	NA	NA	NA	NA	NA	NA	NA	BRIDGE
<i>Gabbs (Dead Cow Splay)</i>	17.7	1.2	NA	NA	NA	NA	NA	NA	NA	BRIDGE
<i>Bell Flat</i>	19.8	3.3	NA	1.2	NA	NA	NA	NA	NA	BRIDGE

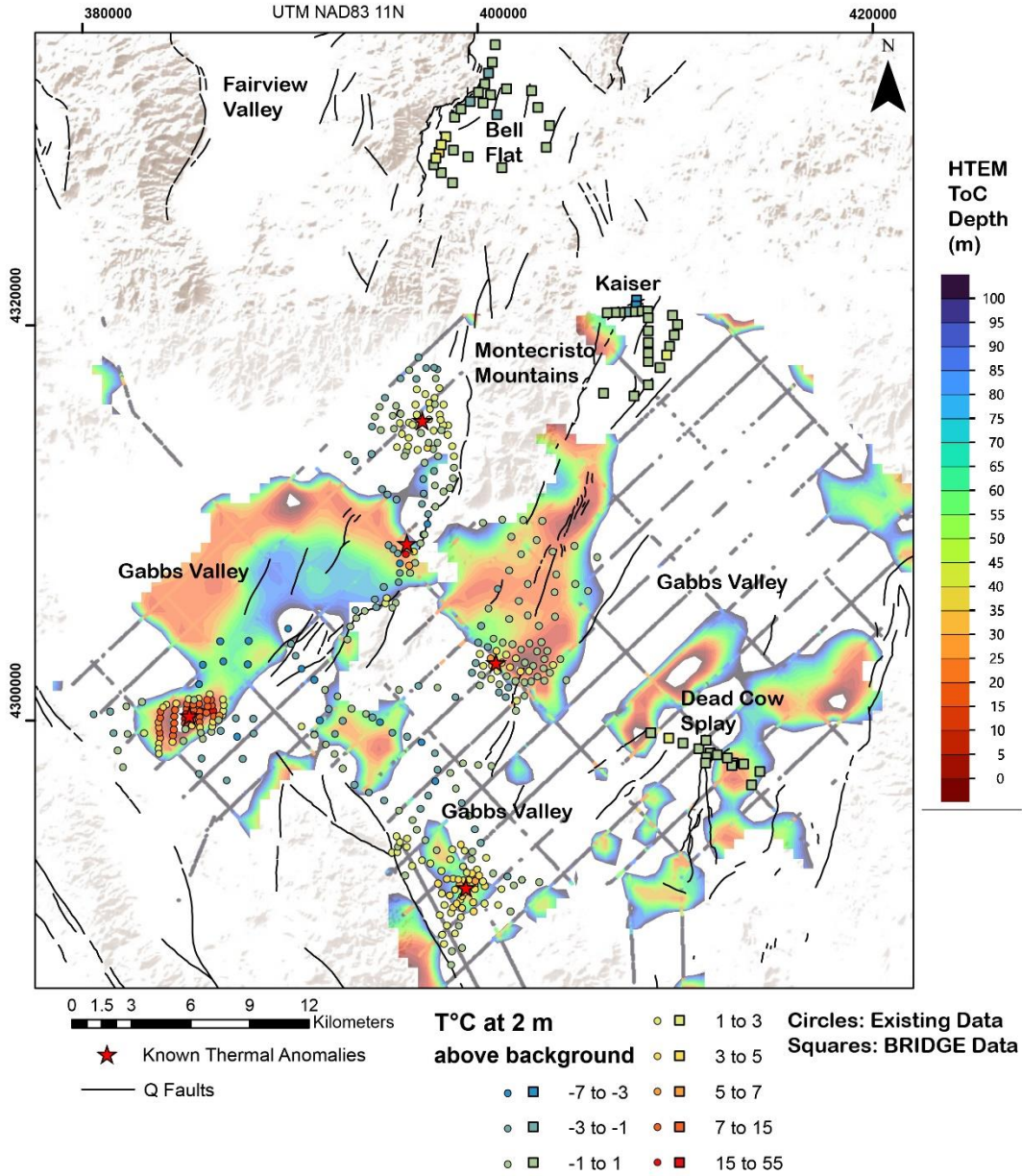


**Figure 8 Shallow temperature collected by the BRIDGE team (squares) at or near Gabbs Valley, NV. Also shown are existing 2-m temperature points (circles) and the HTEM top of conductor (ToC) map of Gabbs Valley from Figure 6.**

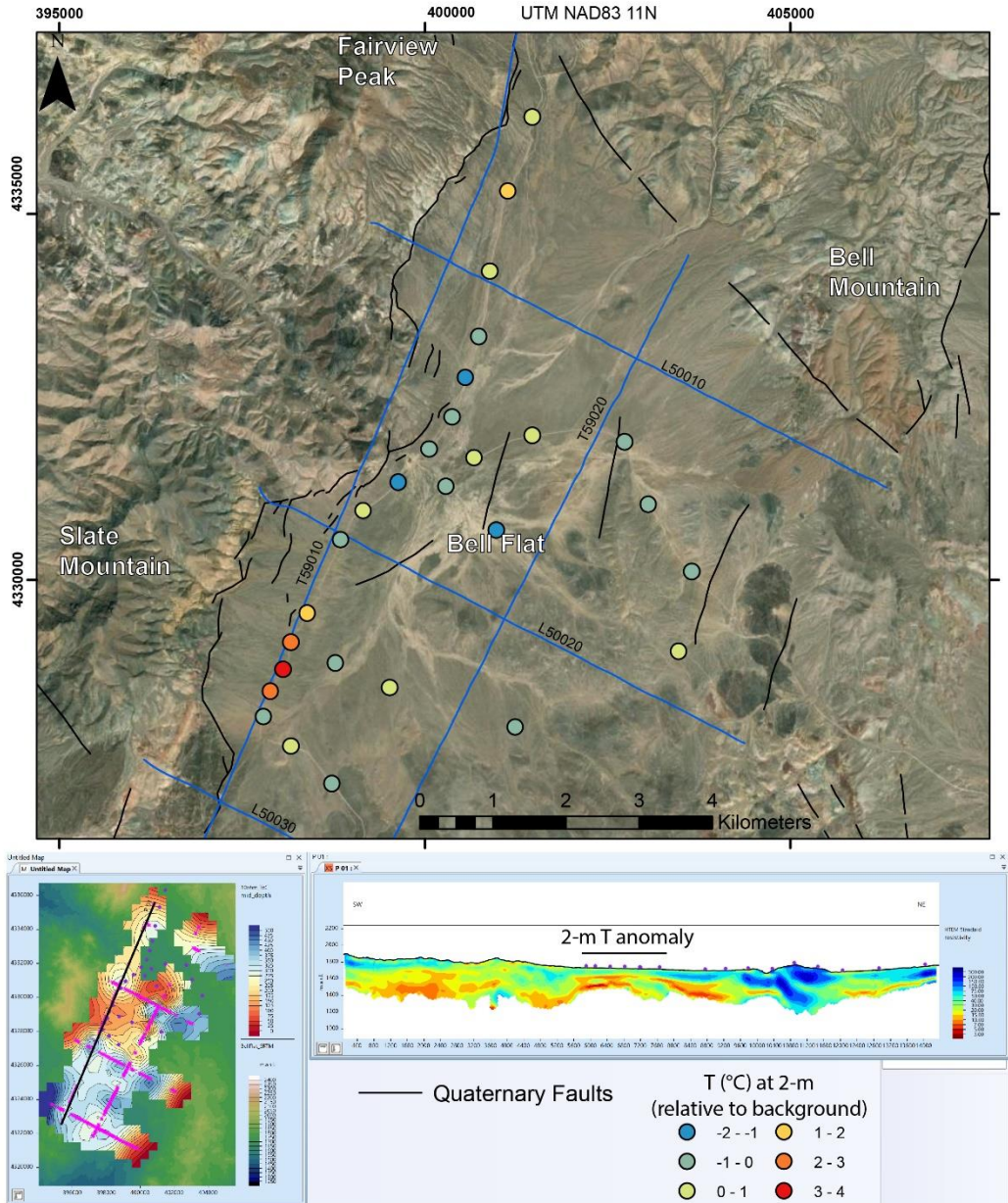


**Figure 9** Two-meter temperature data collected by the BRIDGE team at Bell Flat, NV. Below is HTEM line T59010, which runs along the western margin of Bell Flat. A shallow low resistivity zone is visible in the HTEM data along line T59010 beneath the positive 2-m temperature anomaly.

## **4. PROJECT OUTCOMES**

### **4.1. Prospect Portfolio**

Table 3 presents the BRIDGE prospect portfolio and final, as of the end of the project, assessment. Finalists are prospects in which exploration data provided positive justification for targeting TGH drilling. This BRIDGE report provides detailed data reviews and conceptual models for three finalists: Lee Allen, Grover Point, and East Hawthorne. The next step for these three areas is TGH drilling so that conceptual models may be updated and top prospects for resource confirmation drilling may be identified.

Non-finalists are not necessarily unfavorable areas. In several instances, for example, problems with timely land access prevented prospects from being advanced beyond Phase 2. The project also operated on a finite budget and timeline and, therefore, priority was given to prospects that were more favorable based on evolving geoscience assessments of likely success within the context of the budget and time available. This approach leaves room for further exploration to occur at other prospects based on the resource indicators tabulated.

**Table 3 BRIDGE prospect portfolio and final status and assessment at the project end.**

Prospect Name	Category	Eliminated?	Reasoning	Characteristics/Preliminary CM Components	Available data	BRIDGE contributions	Basin
Lee Allen	Finalist	No	HTEM signature, high temperature indications	Explored greenfield, likely pull-apart, sinter deposits, 140-180+ °C, hot wells, 2m anomaly	1:24k Geologic mapping, 2m, exploration wells, geochemistry, gravity, magnetics	HTEM, MT survey, Lidar analysis	Carson Sink
Grover Point	Finalist	No	HTEM signature, high temperature indications	Greenfield, likely displacement transfer zone, 70 °C in a 90m deep TGH	TGH (SMU), nearby geochemistry (cold wells), magnetics	HTEM, Lidar analysis, gravity survey, 2m, MT survey, geochemistry, geologic mapping	Dixie Valley
East Hawthorne	Finalist	No	Access to drilling, HTEM signature, >100 °C indications	Explored greenfield, likely displacement transfer zone or pull-apart, 2m thermal anomaly and 100 °C deep well temp.	1:24k Geologic mapping, 2m, TGH (GPO), sparse gravity (check w/ Matt)	HTEM, Lidar analysis, 2m, MT survey (joint inversion w/ HTEM), gravity re-processing	Walker Lake Valley
Bell Flat	Prospect	Phase 3	HTEM signature, good structural setting, ease of access	Greenfield, multiple PFA structural targets (stepovers, accommodation zone, fault intersection), no known thermal anomaly	1:24k Geologic mapping	HTEM, Lidar analysis, gravity survey, 2m survey	Bell Flat Valley
BR-16 North	Prospect	Phase 2	No clear HTEM signature; limited temperature indications	Greenfield, PFA structural target (fault intersection), no known thermal anomaly	1:24k Geologic mapping, 2m, TGH (gradient only; SMU/GPO), magnetics, gravity	HTEM	Carson Sink
BR-16 South	Prospect	Phase 2	No clear HTEM signature; limited temperature indications	Greenfield, PFA structural target (fault intersection), no known thermal anomaly	1:24k Geologic mapping, 2m, single TGH (gradient only; SMU/GPO), magnetics, gravity	HTEM	Carson Sink
Chalk Mountain	Prospect	Phase 2	Unclear HTEM signature, no high temperature indications	Greenfield, stepover, fault intersection, no known thermal anomaly	1:24k Geologic mapping, 2m, ~3 TGH (GPO), gravity, magnetics	HTEM, Lidar analysis	Dixie Valley
The Bend	Prospect	Phase 2	No access - WSA	Greenfield, stepover, 2m temperature anomaly	2m, ~TGH (SMU), gravity	HTEM, Lidar analysis	Dixie Valley
Bell Flat Hot Spring	Prospect	Phase 2	No access - active bombing range	Greenfield, no PFA target but likely fault termination, hot spring (~37 °C?)	1:24k Geologic mapping (limited coverage), TGH (GPO)	Lidar analysis	Fairview Valley
Big Kasock	Prospect	Phase 2	No access - active bombing range	Greenfield, fault termination, no known thermal anomaly	1:24k Geologic mapping (limited coverage), TGH (GPO)	HTEM, Lidar analysis	Fairview Valley
Labou Flat	Prospect	Phase 2	No access - active bombing range	Greenfield, stepover, no known thermal anomaly	Gravity, shallow cold well	HTEM, Lidar analysis	Fairview Valley
Rawhide Hot Springs	Prospect	Phase 3	Not a hidden system	Explored greenfield, likely fault termination or stepover, hot spring (62 °C; 160 °C qtz geothermometry), 2m temp. anomaly	1:24k Geologic mapping, 2m, geochemistry, regional gravity	HTEM, Lidar analysis, geochemistry	Gabbs Valley
North Gabbs	Prospect	Phase 3	Unclear HTEM (limited coverage) but good temp. indication	Greenfield, stepover, 2m temperature anomaly	1:24k Geologic mapping (partial coverage), 2m, TGH (SMU), single warm well (GBCGE, NWIS)	HTEM, Lidar analysis, MT survey	Gabbs Valley
Kaiser	Prospect	Phase 3	Interesting HTEM geometry without temperature data	Greenfield, fault termination (horsetail splay), no known temperature anomaly	1:24k Geologic mapping, TGH (SMU)	HTEM, Lidar analysis, MT survey, 2m survey	Gabbs Valley

Prospect Name	Category	Eliminated?	Reasoning	Characteristics/Preliminary CM Components	Available data	BRIDGE contributions	Basin
Cobble Cuesta	Prospect	Phase 3	Unclear HTEM (interference with conductive strata) but good temp. indication	Explored greenfield, pull-apart, 2m temperature and TGH anomaly	1:24k Geologic mapping, 2m, TGH (SMU), gravity	HTEM, Lidar analysis, MT survey, geochemistry	Gabbs Valley
Dead Cow Splay	Prospect	Phase 3	Interesting HTEM geometry without temperature data	Greenfield, likely fault termination or stepover, no known thermal anomaly	1:24 Geologic mapping, sparse gravity	HTEM, Lidar analysis, MT survey, 2m reconnaissance	Gabbs Valley
Town of Gabbs	Prospect	Phase 3	Unclear HTEM (interference with town infrastructure) but good temp. indication	Greenfield, likely stepover (complex zone), hot shallow wells (~70 °C)	1:24k Geologic mapping, hot shallow wells, geochemistry	HTEM, Lidar analysis, MT survey	Gabbs Valley
Gene Sawyer	Prospect	Phase 3	Interesting HTEM geometry with limited but good temp. indication	Greenfield, likely fault termination or stepover, warm shallow well (54 °C w/ 113 °C qtz geothermometry)	1:24k Geologic mapping, single warm shallow well, geochemistry	HTEM, Lidar analysis, MT survey	Gabbs Valley
Finger Rock	Prospect	Phase 2	No clear HTEM signature	Greenfield, likely displacement transfer zone and/or fault intersection, no known thermal anomaly	1:24k Geologic mapping, sparse gravity, partial coverage magnetics	HTEM	Gabbs Valley
Benton Springs	Prospect	Phase 2	No clear HTEM signature	Greenfield, PFA pull-apart target, no known thermal anomaly	1:24k Geologic mapping, sparse gravity	HTEM	Gabbs Valley
Middlegate	Prospect	Phase 2	Interesting HTEM geometry but limited coverage with no temp. anomaly	Greenfield, no PFA target but likely stepover, no known thermal anomaly	1:24k Geologic mapping (partial coverage), gravity (partial coverage)	HTEM	Middlegate Valley
Salt Wells	Control	N/A	N/A	Developed, horsetail splay, sinter deposits, 130-180 °C, 2m anomaly	1:24k Geologic mapping, 2m, TGH, production wells,	HTEM	Carson Sink
Don A. Campbell	Control	N/A	N/A	Developed field (25 MW), displacement transfer zone, 120-125 °C high flow fluid production, 2m anomaly	1:24k Geologic mapping, 2m, geochemistry, deep wells (check w/Kurt and Matt)	HTEM	Gabbs Valley
Carson Lake/Fallon	Calibration	N/A	N/A	Explored greenfield, likely stepover, hot springs, 100-140 °C, shallow temp. anomaly, low permeability in deep wells	1:24k Geologic mapping, 2m, TGH (GPO, FORGE), deep wells, geochemistry, gravity	HTEM	Carson Sink
Pirouette Mountain	Calibration	N/A	N/A	Explored greenfield, accommodation zone; 2m, TGH, and slim well temperature anomaly (~85 °C)	1:24k Geologic mapping, 2m, TGH (SMU, GPO), single geochemistry, deep well, gravity, magnetics, MT, seismic	HTEM, Lidar analysis, Leapfrog model	Dixie Valley
Elevenmile Canyon	Calibration	N/A	N/A	Explored greenfield, stepover; 2m and TGH temperature anomaly (>80 °C)	1:24k Geologic mapping, 2m, TGH (SMU, Hunt), gravity, magnetics, MT, seismic	HTEM, Lidar analysis, Leapfrog model, geochemistry	Dixie Valley
Petrified Springs	Calibration	N/A	N/A	Explored greenfield, displacement transfer zone, 2m and TGH anomaly	1:24k Geologic mapping, 2m, TGH (SMU and Craig), MT, gravity, magnetics	HTEM	Gabbs Valley
West Hawthorne	Calibration	N/A	N/A	Explored greenfield, stepover, 2m temp anomaly, high deep well temps. (~115 °C w/ >120 °C qtz geothermometry)	1:24k Geologic mapping, 2m, TGH (GPO), geochemistry, gravity, 3D seismic	HTEM	Walker Lake Valley

## **4.2. Grover Point Prospect**

Data gap analysis, exploration, and conceptual modeling for Grover Point in Dixie Valley, NV was presented at the 49th Workshop on Geothermal Reservoir Engineering at Stanford University, CA [12]. A 3D MT survey was acquired after this proceeding. The data, 3D model, and summary slides are available on GDR [9].

### **4.2.1. Background**

The Grover Point prospect is on the eastern side of Dixie Valley and was first identified by temperature gradient hole (TGH) drilling in the late 1970s. The hottest of these wells recorded a bottom hole temperature (BHT) of 72.6 °C at 88 m depth, but several wells contributed to a larger region of elevated thermal gradients referred to as the Clan Alpine Ranch [48]. The geothermal system at Grover Point is one of several systems found in Dixie Valley (DV) [49]. These include the Dixie Valley Geothermal Power Plant (DVPP), A drilled and commercially ready prospect at Dixie Meadows, and prospects in various stages of exploration such as Elevenmile Canyon, Pirouette Mountain, Dixie Comstock, and The Bend (Figure 10). Geothermal systems are found throughout Dixie Valley and the Basin and Range at fault terminations and stepovers [50], [51]. The Tungsten Mountain geothermal power plant is found 25 km to the east of Grover Point and is the closest commercially operational field.

A large portion of DV was covered by the airborne electromagnetic (AEM) survey designed and commissioned by BRIDGE (Figure 10). There are many configurations available for AEM surveying. To optimally meet the objectives for this terrain and application, a helicopter-borne transient electromagnetic (HTEM) system was deployed. The HTEM dataset was considered alongside existing public data to help identify prospects for further characterization. Out of several BRIDGE portfolio prospects covered by the HTEM survey in DV, Grover Point was selected for further studies based largely on interpretations of the low-resistivity anomalies imaged by HTEM.

### **4.2.2. Geology**

Dixie Valley is bounded to the south by an accommodation zone between DV and Fairview Valley, to the west by the Dixie Valley Fault system (east-dipping, dextral-normal slip) along the Stillwater Range, and to the east by a west-dipping fault system along the Clan Alpine Mountains [52]. Moderate local strain rates for the region 10-9/yr, [53] coincide with the extensional regional stress regime and, locally, 0.3-0.5 mm/yr extension rates for Dixie Valley [54]. The Stratigraphic sequence includes middle Miocene to present sedimentary and volcanic deposits filling the basin which overlays early to middle Tertiary volcanic rocks and Mesozoic metasedimentary and metavolcanic basement e.g., [55].

The Grover Point thermal anomaly is located roughly at the projected intersection of the north-striking, west-dipping Middlegate Fault Zone (MGFZ) and a series of the north-east striking, west-dipping normal faults that lie along the eastern margin of Dixie Valley. Although neither of these fault zones are shown to extend to the thermal anomaly proper (Figure 10), new LiDAR analysis and other work in this report suggests that both zones may extend into this area. Exactly how they interact in the context of the geothermal prospect remains largely unknown.

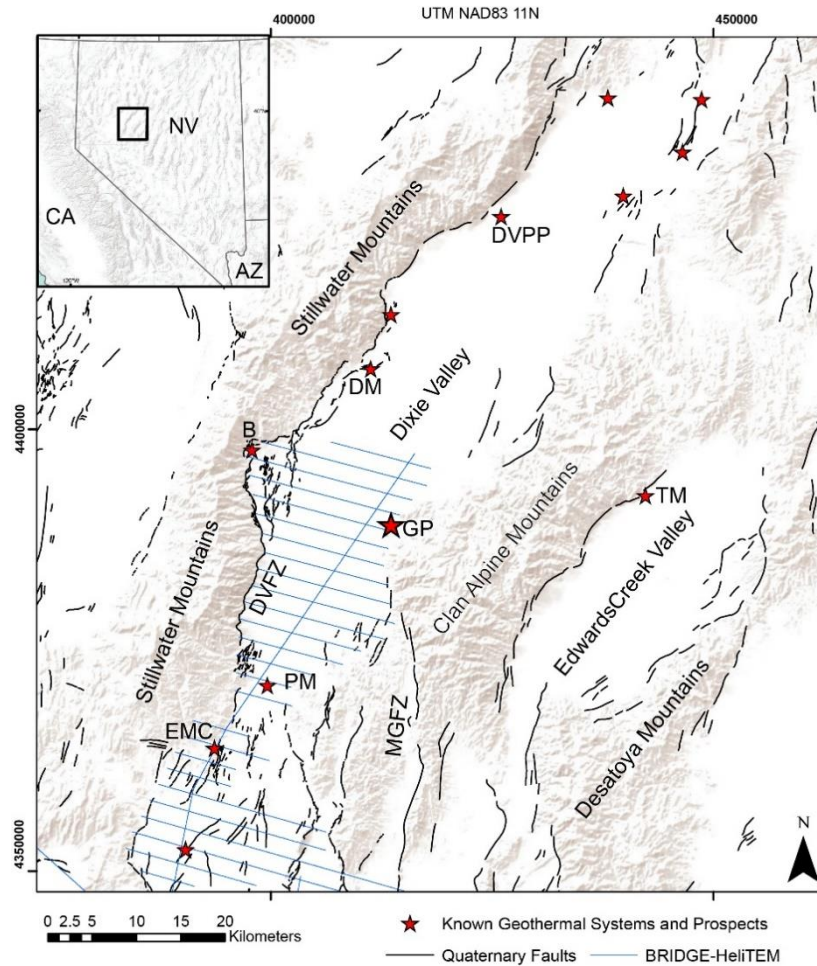


**Figure 10 Location of Dixie Valley including known and prospective geothermal systems including Quaternary faults [1], black lines, and physiographic locations mentioned in the text. DVFZ is Dixie Valley Fault Zone, MGFZ is Middlegate Fault Zone, GP is Grover Point, DVPP is Dixie Valley geothermal power plant, DM is Dixie Meadows, B is the Bend, TM is Tungsten Mountain, PM is Pirouette Mountain, and EMC is Eleven Mile Canyon. HTEM lines collected as part of the BRIDGE project are shown as blue lines. Top left insert: Location of map relative to Nevada state boundary.**

### 4.2.3. Hydrothermal Data

There are numerous shallow wells and springs near Grover Point that have been logged/sampled for hydrothermal characterization purposes. This section describes the thermal and geochemical data from these sources.

#### 4.2.3.1. Thermal Data

Shallow artesian wells in the middle of the basin, drilled to depths less than 200 m (although several are deeper), and are associated with an abandoned settlement in the area. Shallow TGH exploration drilling was conducted in 1978 - 1979 and can be found in the SMU Heat Flow and Well Data

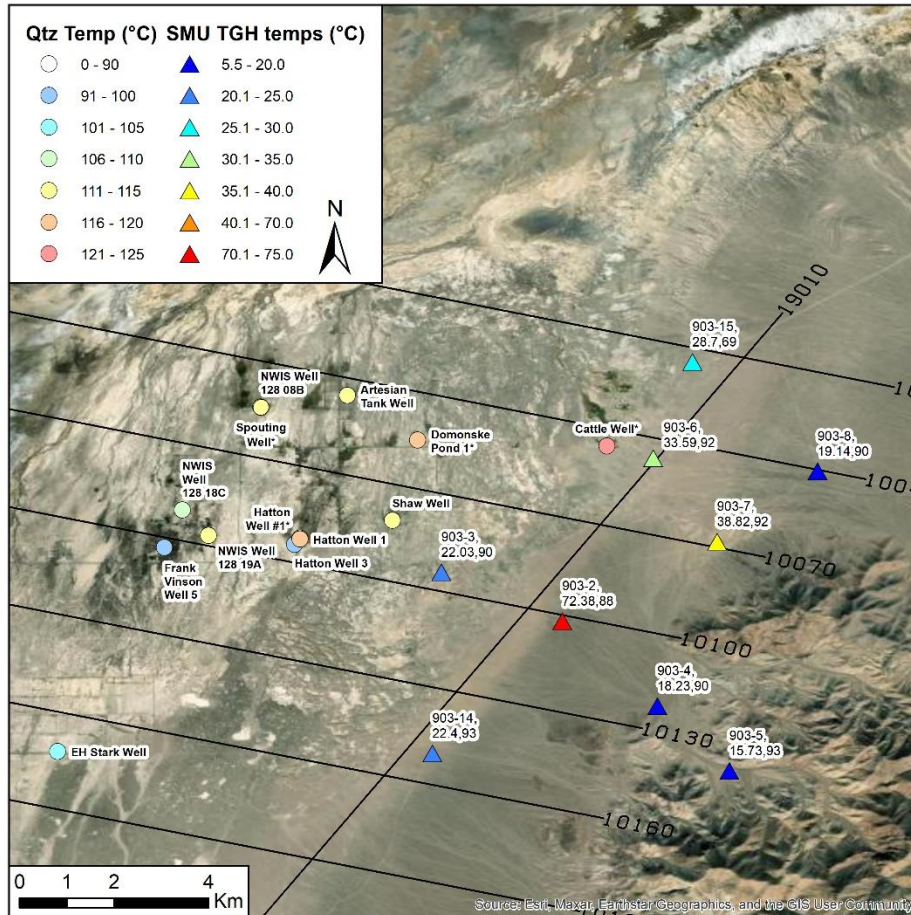


**Figure 11 TGH map near Grover Point (triangles) and geochemistry samples (circles) with HTEM flight lines for reference. Note the greenery in the imagery, indicating the presence of springs and artesian wells.**

database. Temperature data from the SMU database includes BHT measurements from 19 wells in the vicinity of the so-called ‘Grover Point well’ on USGS topographic quads, which became the namesake for this prospect (Figure 11 The Grover Point well is labelled as 903-7 in Figure 11 and has the second highest BHT in the area at 38.82 °C at 92 m deep. The hottest well, 903-2, reached a BHT of 72.38 °C at 88 m depth. A third warm well, 903-6, has a BHT of 33.59 °C at 92 m deep. The remaining wells have BHT values below 30 °C, and most of them are below 20 °C.

Temperature gradients in many of these wells are significantly elevated above background values in Dixie Valley, which averages  $54 \pm 5$  °C/km [48]. Contoured thermal gradient values indicate an anomalous zone with gradients  $> 500$  °C/km at Grover Point, which is caused by well 903-2. Several other wells in this study area have thermal gradients  $> 250$  °C/km [48]. These elevated gradients may be influenced by the shallow outflow of geothermal fluids, which are common in the Basin and Range. If so, it would not be appropriate to project them to great depths. For instance, at Tungsten Mountain, also a hidden system, some shallow wells there intercept 124 °C outflow and a thermal roll-over at 152 m deep [56]. This rollover is located at a contact between alluvial cover and

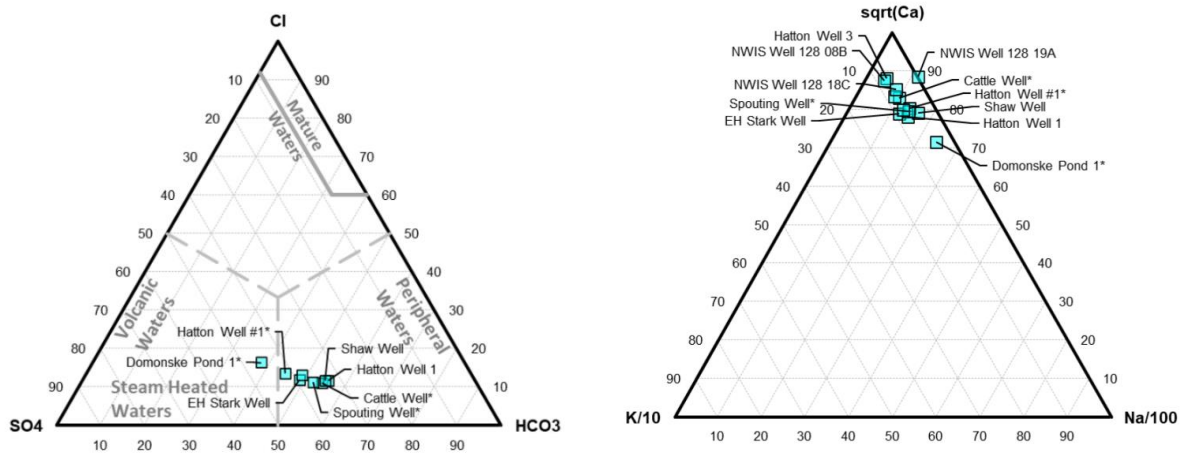


**Figure 12 Geochemical ternary diagrams of the anions (left) and cations (right) of samples from artesian wells near Grover Point. Note that all samples are relatively Calcium (Ca) rich and relatively rich in bicarbonate ( $\text{HCO}_3$ ) and sulphate ( $\text{SO}_4$ ).**

underlying tuffs. Temperature-depth profiles are not available at Grover Point, and so it is not possible to assess if and how advective effects are playing a role.

Flowing temperatures from artesian wells in the settlement area to the west of Grover Point are between 15 °C and 22 °C, with warmer temperatures generally found in the eastern portion of the settlement. Of temperature measurements taken in June of 2023 as part of the BRIDGE project (well names with a \* at the end of the name), there is a clear trend of warming temperatures towards the Grover Point thermal anomaly. The Cattle Well measured 20.6 °C and the Spouting Well 18°C; wells in between have temperatures between the two.

#### 4.2.3.2. Geochemical Data

Geochemical data from approximately ten samples are available near Grover Point in databases like Great Basin Center for Geothermal Energy and Argonne National Laboratory. Of these, only 4 have full analyses of major analytes including bicarbonate. The BRIDGE team collected an additional 4 samples for analysis, including the Cattle Well, Domonske Pond #1, Hatton Well #1, and Spouting Well samples (Figure 11). These waters are Calcium-bicarbonate-sulphate type waters, which are representative of meteoric groundwater in the Basin and Range (Figure 12). While sulphate is commonly found in steam-heated waters from geothermal systems, in the Basin and Range it is also common for the sulphate to be picked up from evaporite-rich basin fill. Chloride concentrations are low (<60 ppm), however, silica concentrations are anomalously high for 20 °C water, with quartz geothermometers conductive, [57] ranging between 92 and 123 °C. Similar to the trend with measured temperatures, there is a noticeable trend in the quartz geothermometers of warmer temperatures to the northeast and cooler temperatures to the west and south as distance increases from the thermal anomaly. The Cattle Well sample, which is near well 903-6 (33.59 °C), has the highest quartz geothermometry temperature of 123 °C. Domonske Pond and Hatton Well 1 both have geothermometry temperatures of 117 °C, while samples to the south (such as the EH Stark Well) have temperatures below 100 °C. This trend may indicate that trace amounts of geothermal fluid is intermixing with the meteoric groundwater in the region and is consistent with the trend of warmer TGH to the north.

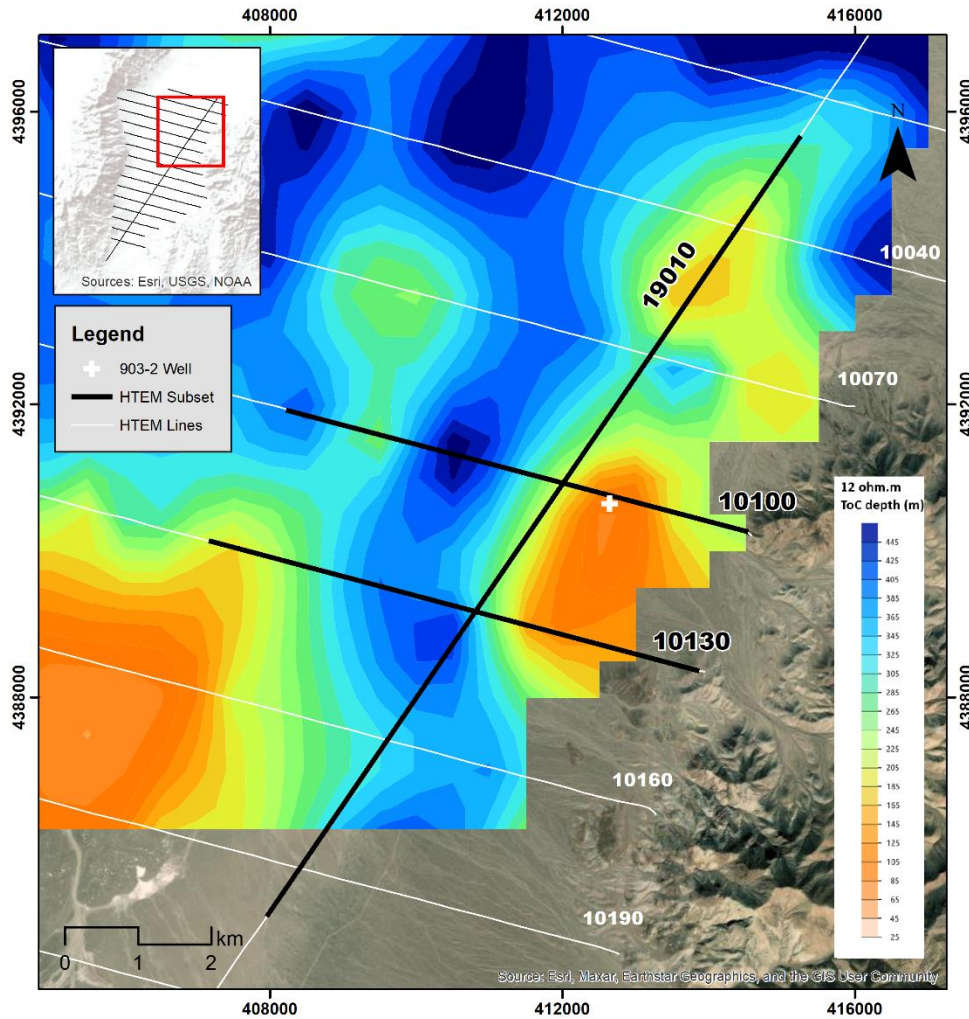


**Figure 13 Location of HTEM lines in the Grover Point area (white lines) with portions of select cross-sections shown in this paper (black lines). A map of the depth to the top of conductor (ToC), defined as the top of a 12 Ohm-m surface, is shown with colored contours.**

#### **4.2.4. HTEM**

The HTEM resistivity surveying method is typically used for relatively shallow (<500 m depth) mineral exploration and groundwater mapping. The method operates in a similar way to ground-based central loop transient electromagnetic (TEM) surveys. Current is passed through a large wire transmitter loop; the current is turned off and the decay in voltage over time is measured in a small multicoil receiver (X, Y, and Z). The decay in voltage over time is influenced by the subsurface resistivity and hence can be inverted to obtain resistivity with depth information.

As part of the BRIDGE project, HTEM was flown over more than a dozen prospective basins in western Nevada by Xcalibur using their HELITEM™ system [10]. The 7.5 Hz HELITEM™ system was the most powerful airborne electromagnetic surveying system available to BRIDGE and has been shown to be capable of detecting conductive targets within moderately resistive rocks at depths

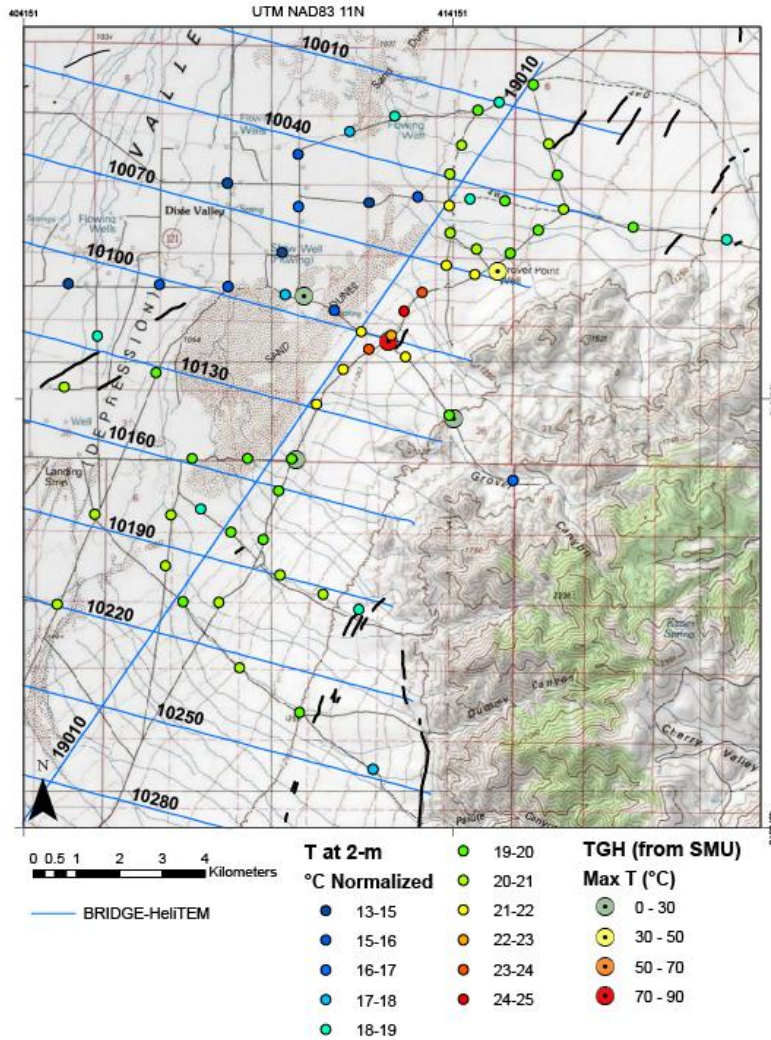


**Figure 14** Shallow temperature survey results near Grover Point in Dixie Valley are shown as small colored circles. Quaternary faults identified from new analysis of LiDAR data are shown as black lines. HTEM line locations are shown as blue lines. TGH data from the SMU database are shown as larger colored circles.

of over 500 m [23]. This survey deployed a transmitter loop with an area 962 m<sup>2</sup>, suspended 35 m above ground, and traveling at an average speed of 110 km/hr. The receiver collected data samples at roughly 10 samples/second, which results in higher lateral resolution than is possible using ground-based methods. The lines and selected segments are shown in map view in Figure 13.

One insightful way to view the HTEM results is to construct a top-of-conductor surface (ToC). The BRIDGE project has separately demonstrated that the elevation of the top of such shallow conductors are correlated with known geothermal prospects in Gabbs Valley and elsewhere. Here we have constructed a ToC grid from the HTEM lines by manually picking the 12 Ohm-m contours and gridding the results (Figure 13, colored grid). We note that the ToC is the shallowest in a zone between lines 10100 and 10130, and to the east of tie line 19010.

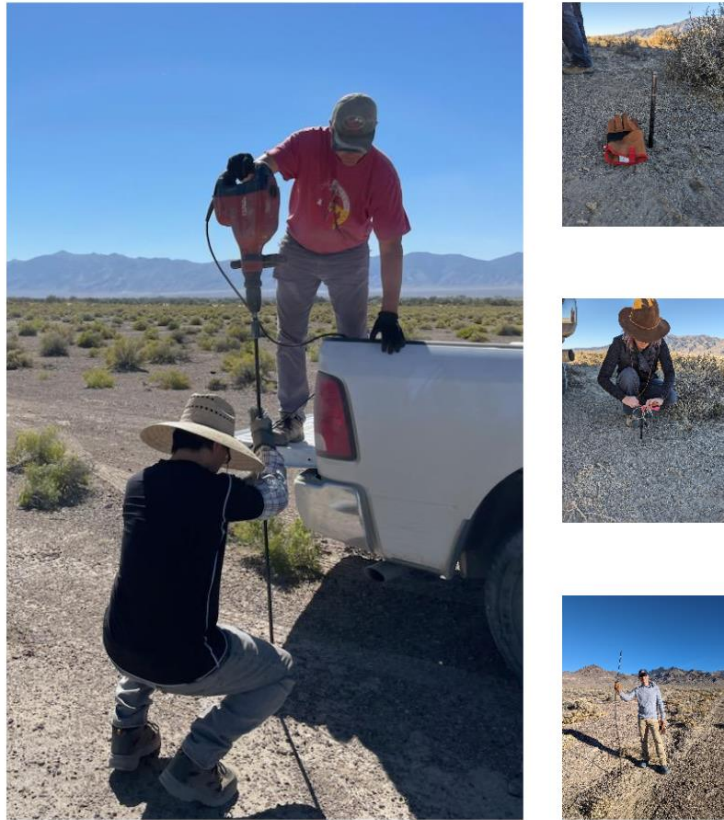


**Figure 15 Shallow temperature survey probe installation (left and top right), Resistive temperature device insertion (middle right), and probe retrieval (bottom right).**

#### **4.2.5. 2-m Temperature Survey**

The 2-meter (2M) temperature survey at Grover Point consists of 64 points collected in one phase in August 2023 and another phase in November 2023 using standard procedures [17], [58]. Data was collected by the U.S. Navy’s Geothermal Program Office. Probes 2.04 m in length were driven into the ground using an electric demolition hammer and temperatures were measured at 1, 1.5 and 2-m depth after they were allowed to equilibrate for a minimum of 1 hour. All point were collected on the shoulders of roadways to minimize the impact of the survey, and the survey design was influenced largely by the distribution of dirt roads. shows images of the survey operations.

Once all the data points were collected, the temperatures were checked for outliers using a z-score test. No outliers were present in the Grover Point data. Next, these data were corrected for elevation as the survey covered an area with >100 m of elevation change. A datum of 1040 m was chosen for calculating the elevation correction. This was the lowest elevation of all the probe locations in the dataset. The elevation correction factor ( $Y_t$ ) was calculated using the adiabatic lapse rate of 1 °C/100m where  $X_z$  is the elevation of the probe’s location at the ground surface. See Equation 1.

$$Y_t = (1040 \text{ m} - X_z) (-1 \text{ } ^\circ\text{C}/100 \text{ m}) \quad (1)$$

Equation (1) is applied to each probe location. Calculated  $Y_t$  values were then added to the measured 2M temperature values. Slope and albedo corrections were not applied to these data. To

account for the possible seasonal temperature differences between the August and November sampling phases, all data were normalized. To accomplish this, the average background temperature of each phase was calculated. This value was subtracted from the regional background temperature of 20 °C, as determined for the Basin and Range by [58], to obtain the normalization factor for each phase. The calculated normalization factors are -6.08 °C for the August dataset and -0.54 °C for the November dataset. These normalization factors were added to the elevation-corrected values in their respective datasets to generate the final normalized temperatures (Figure 15).

The 2M survey at Grover Point identified a prominent positive temperature anomaly ~5 °C above background, with adjusted background temperatures of 20 °C. The anomaly is centered near the hot well 903-2. It is roughly 2 km long and 1 km wide in size however, its width east-to-west is poorly constrained.

#### **4.2.6. Potential Fields**

To better understand the structural setting at Grover Point, a new 110-station gravity survey was commissioned and a legacy airborne magnetic dataset was re-examined [55], [59].

##### **4.2.6.1. Gravity**

A total of 110 new gravity stations were collected by Zonge International Inc. in the fall of 2023 (Figure 16a). Station spacing varied between 400 m and 800 m to cover a sufficiently large area with the resolution needed for prospect-scale investigation. The survey was designed to characterize the northeast-striking fault zone. The eastern margin of DV is by bound west dipping structures, but they have not been mapped in this area. A subtle and short (~500 m) Quaternary LiDAR fault scarp was also picked in this vicinity.

Using a reduction density of 2.45 g/cc, the complete Bouguer anomaly (CBA) was at gridded at 150 m using a minimum curvature algorithm (Figure 16b). An assessment of a suitable reduction density for this area was carried out qualitatively, and an intermediate value of 2.45 g/cc was chosen as a compromise between low-density basin fill and higher-density Paleogene volcanic rocks that comprise the Clan Alpine range. This choice may amplify the gravity values over topographic highs, but it is suitable for investigations under alluvial fans and piedmont slopes where the bulk of Basin and Range geothermal systems are found. Horizontal gradient magnitude (HGM) and first vertical derivative (1VD) grids were produced from the CBA (Figure 16c, d, respectively). The CBA was upward continued by 25 m prior to generating the 1VD grid for smoothing purposes.

The gravity data were modelled in 2D using the GM-SYS profile modeling program, a component of Oasis Montaj software package. The forward gravity response is calculated using methods described by Talwani and others [60]. A simple, 2-layer model was constructed along HTEM line 10100, which is perpendicular to gravity contours. Densities of 2.12 g/cc and 2.67 g/cc were assigned to the alluvial cover and basement, respectively. No actual measurements of rock densities were taken. The basement contact was modelled dipping gently from an outcrop on the east to a maximum depth of ~1 km on its western side. Two steep contacts with offsets of ~200 m each helped fit the data where the horizontal gradients were highest. The model fit the data with a root mean square error of ~0.05.

##### **4.2.6.2. Magnetics**

The USGS commissioned an aeromagnetic survey over the Clan Alpine Mountains in 1985 [59]. The survey was flown along east-west Lines at a survey height of ~300 m, with 800 m line spacing. This

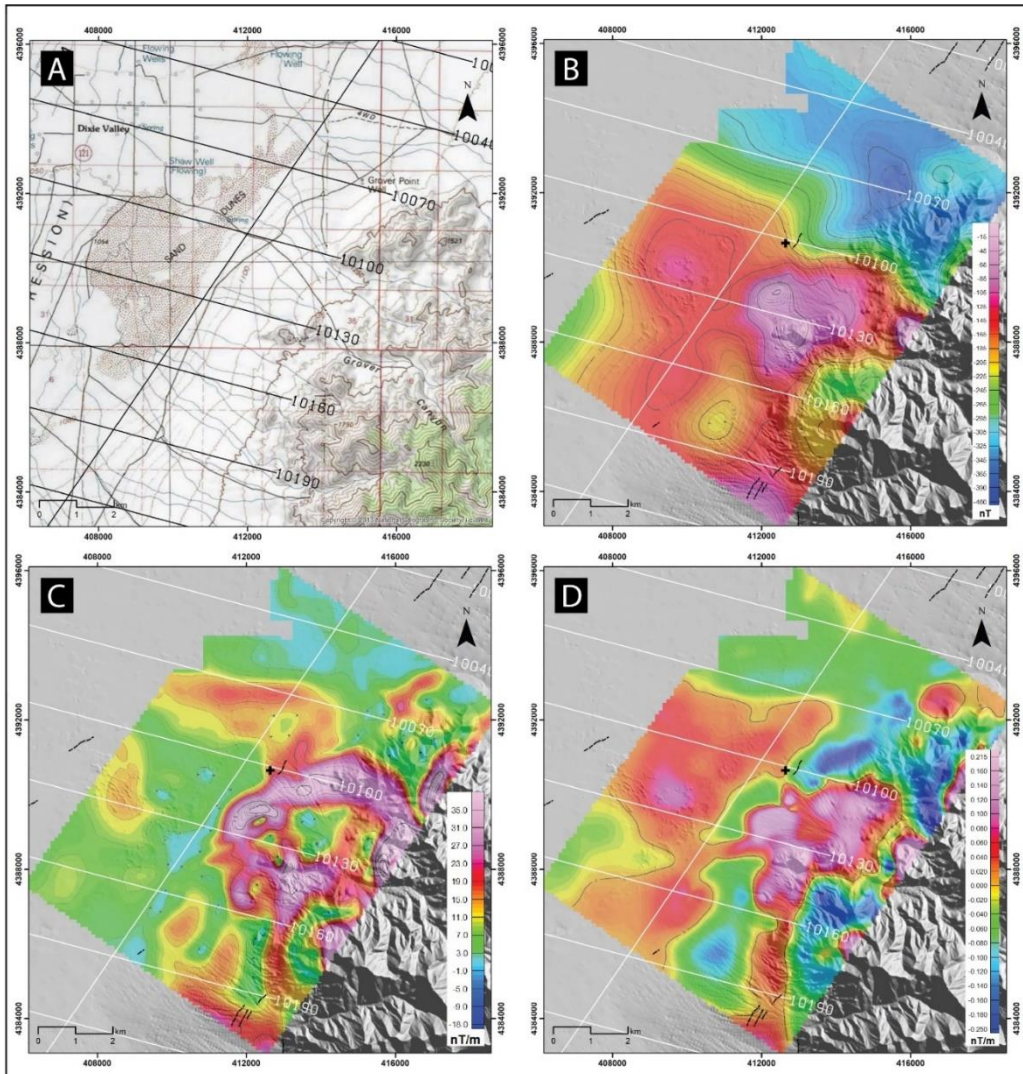


**Figure 16 Gravity survey and results. LiDAR fault scarps are shown as solid black lines and the hot SMU wellhead location is shown as a black cross. HTEM flight lines (white lines) are shown. Figure 17 A subset of an aeromagnetic survey, flight lines not shown, over the A and B. PaiClan Alpine Mountains (Water Resources Division, 1985). On each map, LiDAR fault nel C: Horziscarps are shown as solid black lines and the hot SMU well 903-2 is shown as a/D) of black cross. HTEM flight lines (white lines) are shown for reference. Panel A: Topographic map; Panel B: Reduced-to-Pole (RTP) magnetic anomaly, Panel C: Horizontal gradient of the RTP anomaly, Panel D: vertical derivative of the RTP anomaly.**

data  
later

was  
re-

processed and incorporated with a 2012 aeromagnetic survey commissioned by the U.S. Navy over southern Dixie Valley, using a grid cell size of 100 m. For this study, we clipped out a small subset from these grids and re-applied color scales suitable for this smaller area (Figure 17).

Magnetic data were also collected along each HTEM line, using an in-loop cesium vapor sensor mounted aft of the EM receiver. The nominal height of the sensor was 35 m, much closer to the ground than the 1985 USGS survey. With line spacing of 2 km, however, this survey geometry is suboptimal for gridding the data. This dataset was primarily used for QA/QC of the HTEM data where it is an independent and effective tool for identifying cultural noise. These data were diurnally

corrected using a base station and the IGRF removed to provide a residual magnetic intensity (RMI) data channel.

#### **4.2.6.3. Potential Fields Interpretations**

A preliminary structural interpretation has been developed using the gravity and magnetic datasets with context provided by the LiDAR interpretation and the HTEM results (Figure 18). As with many hidden geothermal systems in the Basin and Range, some faults at Grover Point may be concealed. In this section we discuss these preliminary geologic interpretations from these potential field datasets.

Gravity data can be used to delineate the edges of buried, near-vertical contacts using the horizontal gradient method [61], [62]. which takes advantage of the fact that the steepest horizontal gradients in gravity data occur directly over such contacts. We have applied this technique to the Grover Point dataset and made several picks of inferred steeply dipping fault locations. The colored grid in Figure

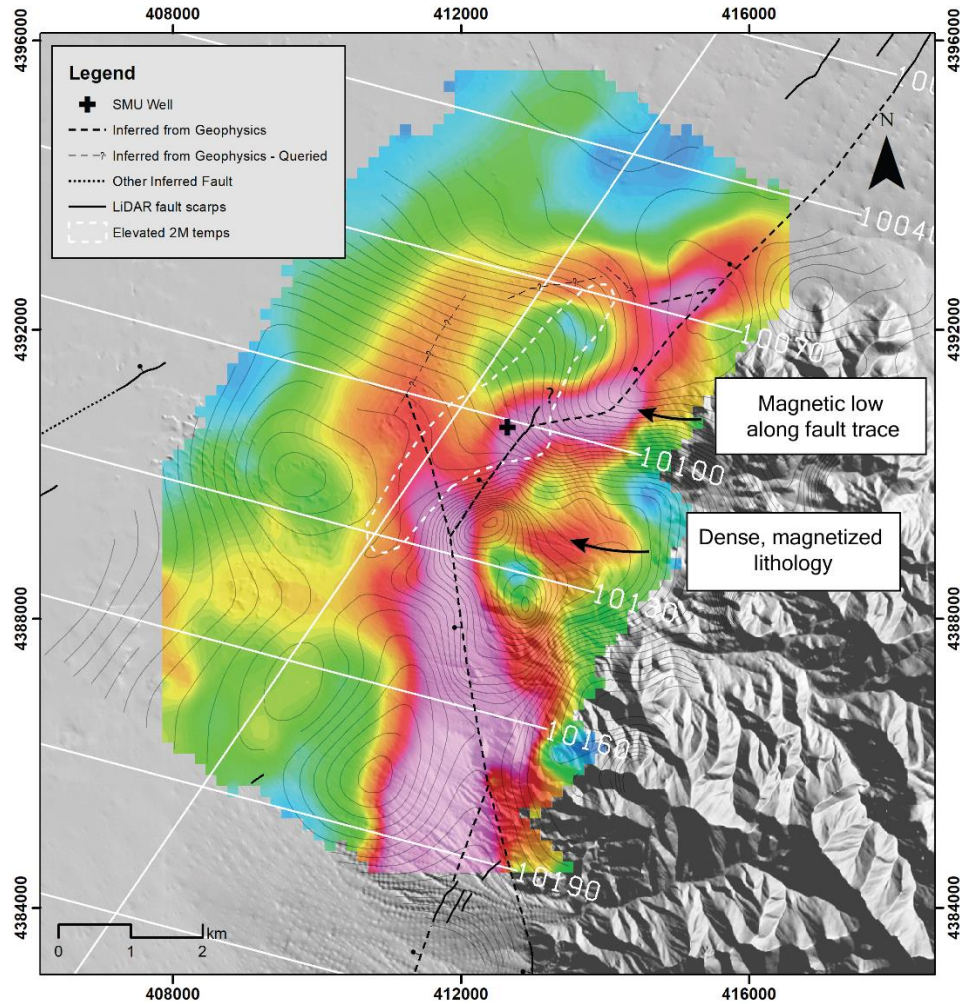


**Figure 18 Preliminary structural interpretations from the gravity and magnetic datasets at Grover Point. Colored grid is the HGM of the gravity CBA. Contours are from the RTP magnetic data. HTEM lines shown as white lines, for reference. A zone of elevated 2M temperatures is highlighted with a dashed white polygon.**

16 shows the gravity HGM of the CBA along with inferred normal fault contacts (black dashed lines). The contours are from the RTP magnetic dataset for comparison purposes. The strongest HGM gradients run north-south before taking a sharp bend to the northeast roughly between HTEM lines 10100 and 10130. This north striking lineament also extends past the bend before also turning northeast and re-connecting to the main HGM lineament. We have less confidence in these more basin-ward features and display them as queried faults in Figure 18. Overall, the patterns suggest that a fault intersection and sharp  $\sim 45^\circ$  bend in faulting is located near the shallow 2M thermal anomaly. It should be noted that the gravity data is only sensitive to faults that host a lateral change in density, and other features would not be detected.

The first vertical derivative (1VD) of potential field data removes regional trends and emphasizes shallower features, as shown by the higher values of the 1VD of the gravity in Figure 16d and the magnetic data in Figure 17d. On the foot-wall side of the fault bend, it is apparent that a high-

density and highly magnetized body lies buried at relatively shallow depths and may also outcrop in the range.

The 1VD of the gravity data also suggests that a more basin-ward, near-surface dense body lies ~1.5 km northeast of well 903-2 (Figure 16d). This zone lies between the two inferred northeast-striking normal fault zones. It may be locally caused by a shallowly buried and down dropped bench in the basement rocks, or possibly by a transition from unwelded to welded tuffs which are both common in this part of the Clan Alpine Range. Given its proximity to inferred geothermal outflow, it is also possible that it results from silicification and densification of sediments, which has been observed at other geothermal fields including San Emidio [63], Don A. Campbell e.g., [45], [64]. Some types of epithermal silicification processes can occur at shallow depths where geothermal outflow is at the water table e.g., [65] and many others.

Evidence for faulting is suggested from a short-wavelength lineament of low magnetic intensity with a northeast strike, which is co-located with the strong gravity HGM lineament picked as a normal fault. This zone is best seen in the RTP of the magnetic data (Figure 17b, contours in Figure 18), and also, in the vertical derivative of the RTP where this feature is emphasized (Figure 17c).

Identification of faults buried under alluvial cover using magnetic methods is well documented in Dixie Valley and in other extensional environments [66], [67]. Alternatively, zones of low magnetic intensity are sometimes observed over parts of geothermal systems and have been attributed to the destruction of magnetic minerals through geothermal processes [68]. This has been observed at some Basin and Range geothermal systems including Dixie Meadows [69], the Don A. Campbell operating field [45] and at a hidden geothermal prospect in South Gabbs Valley [40]. In addition to these possible explanations, the magnetic low lineament may also be explained by edge-effect from the adjacency of a highly magnetized, shallowly buried lithology, or simply from terrain effects.

A long wavelength trend is also apparent from the magnetic data. This is seen in the RTP grid where magnetization values are lower to the north and higher to the south, separated along a southeastern trend. This entire dataset [55] shows that this zone of low magnetization extends over the entire Clan Alpine Range. This is likely caused by rock units of lower or reverse remnant magnetization that are regionally extensive.

#### **4.2.7. Preliminary Interpretation and Conceptual Model**

This section describes the preliminary interpretations and conceptual model for the Grover Point geothermal prospect.

##### **4.2.7.1. Preliminary Interpretation**

Figure 19 shows HTEM results in cross-section view along with the RMI collected from an independent magnetometer inside the HTEM loop, and the HGM of the ground-based gravity data, extracted along each line. Also noted on each cross-section is the approximate extent of two-meter temperature (2m) anomalies, the HTEM lines that cross it, and shallow TGH data listing the well name and bottom hole temperature.

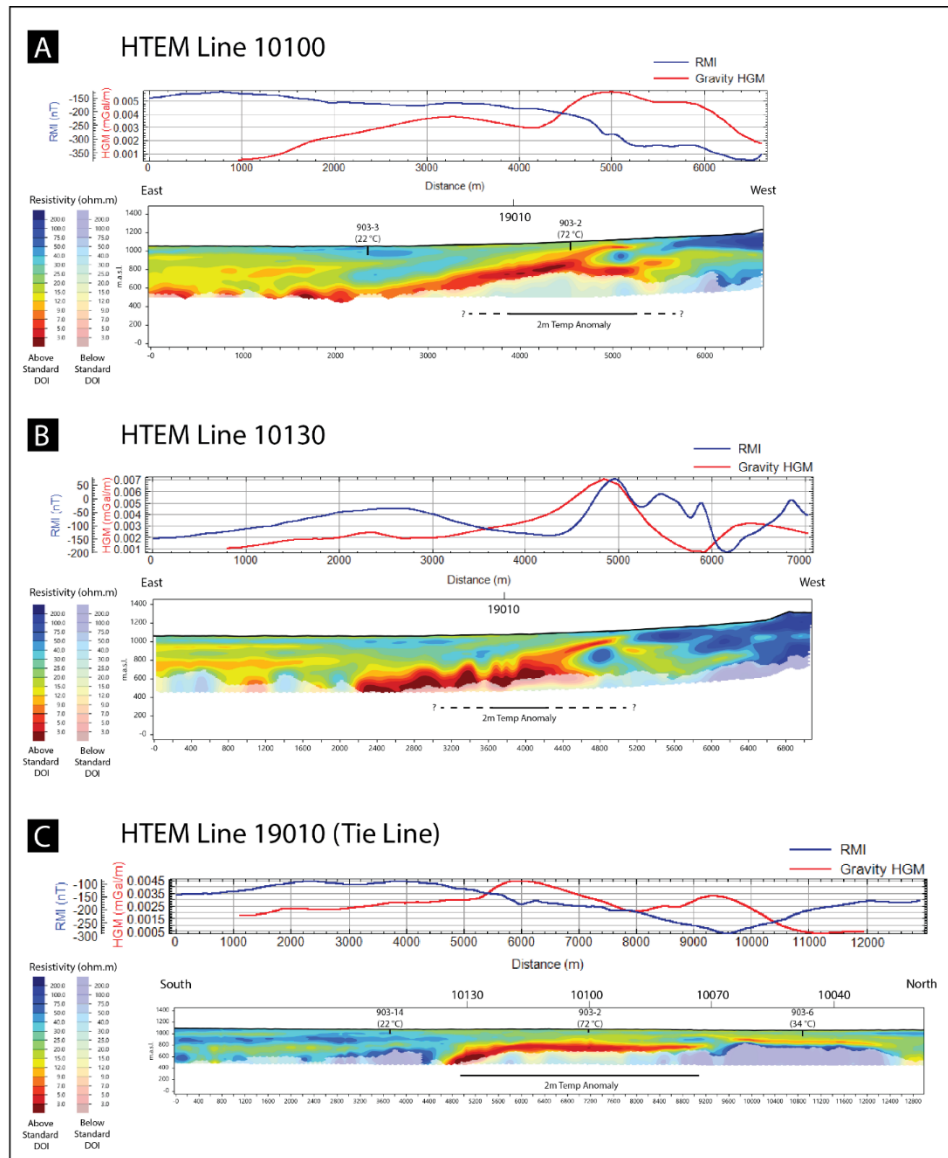


**Figure 19 HTEM resistivity, residual magnetic intensity (RMI) and gravity horizontal gradient magnitude (HGM) extracted along profiles 10100, 10130 and 19020. Zones of elevated 2M temperatures are shown as black lines (solid or dashed) below each resistivity profile. Well names and bottom hole temperatures are shown above each resistivity profile. HTEM lines that cross each profile are noted with the line name.**

Analysis of the BRIDGE HTEM data indicates typical depths of resolution of 300-500 m throughout the basins except where near-surface evaporite deposits and high salinity waters lower resistivity to <1 Ohm-m which limits the depth of penetration to <100 m [10]. We show the modeling results using a 'standard depth-of-investigation', which is a depth cut-off determined by the inversion program. This cutoff can be seen in the cross sections of Figure 19 where the resistivity colors change from opaque to transparent. HTEM models above this depth cut-off has proven to agree with resistivity models from MT data, and with wells at other locations. Below the

computed standard depth of investigation, the resistivity is shown to a constant depth of ~600 m. Inverse results in this portion of the models may not be well constrained.

The HTEM surveying at Grover Point identified a low resistivity zone (<15 Ohm-m) that encompasses the shallow thermal anomaly identified from well 903-2 and 2M temperature surveying (Figure 19). The top of this low resistivity zone shallows from west to east with near constant dip, consistent with deepening sediments to the west. Where the zone of low resistivity is at its shallowest, it overlies a resistive lens-shaped feature seen on lines 10100 and 10130. The shallow low resistivity zone terminates abruptly on both lines on their eastern sides.

We interpret this thin, near-surface conductor co-located with a shallow thermal anomaly as clay alteration within sediments that caps a shallow outflow plume of hot water hosted in the underlying resistive lens. A deeper conductor below the resistive lens is observed on profiles 10100 and 10130. On the easternmost sections of profiles 10100 and 10130, resistivity is mostly high (>50 Ohm-m) consistent with basement rocks in the footwall of a basin-bounding fault. Where the resistivities are the lowest on these profiles, (<5 Ohm-m) the DOI is reduced, and the base of these contacts cannot be imaged with HTEM. Along line 10130, in particular, the strong deep conductor has an undulating shape, which may not represent the true structure.

HTEM tie line 19010 shows a strong zone of low resistivity at a constant depth and ~4 km in length. This zone truncates sharply to the southwest of line 10130 but extends for nearly 2 km northeast of line 10100 and thins in this direction. One possible explanation for this flat-topped geometry is that this profile is parallel to the strike of controlling faults.

#### **4.2.7.2. Preliminary Conceptual Model**

The overall interpretation is that Grover Point lies at the intersection and possible termination of the north-striking MGFZ with northeast-striking normal faults that bound the eastern side of Dixie Valley. This forms a complex structural zone where these two zones meet, which likely influences the presence of a hidden geothermal system hosted along a northeast-striking, northwest-dipping normal fault system. Figure 20 shows the conceptual model in map view, noting the extent of an inferred low-resistivity clay 'cap', a possible zone of up-flow, and the direction of inferred outflow. The conceptual model is shown in cross section view in Figure 21 and along HTEM line 10100. The depth to basement was calculated from a 2D model of the gravity data.

Key conceptual model elements identified from these data include:

The HTEM identified a pattern of resistivity analogous to other producing geothermal systems throughout the Basin and Range (e.g., San Emidio, Brady's, Desert Peak, Dixie Meadows, Tungsten Mountain) with zones of low resistivity smectite clay alteration in basin-fill sediments capping hot, relatively resistive aquifers. The geometry of the resistivity patterns supports that the system is hosted along northeast-striking faults. The low resistivity zones appear to cap both a deeper semi-confined reservoir and a shallow, northeast-trending outflow plume. A resistive lens seen best in HTEM line 10100 may indicate a silicified and permeable zone of sediments that helps channelize fluid flow along-strike, as similar features do at other fields. HTEM tie-line 19010 supports an along-strike length of the system potentially up to ~4 km, which is similar to many other Basin and Range fields.

The gravity survey has identified likely fault geometries and can estimate the depth of basin fill. The data is the strongest evidence for the termination of a north-striking, west-dipping fault zone into northeast-striking, northwest-dipping normal faults that bound the eastern margin of DV. These observations are supported by the newly analyzed LiDAR and the legacy aeromagnetic datasets.

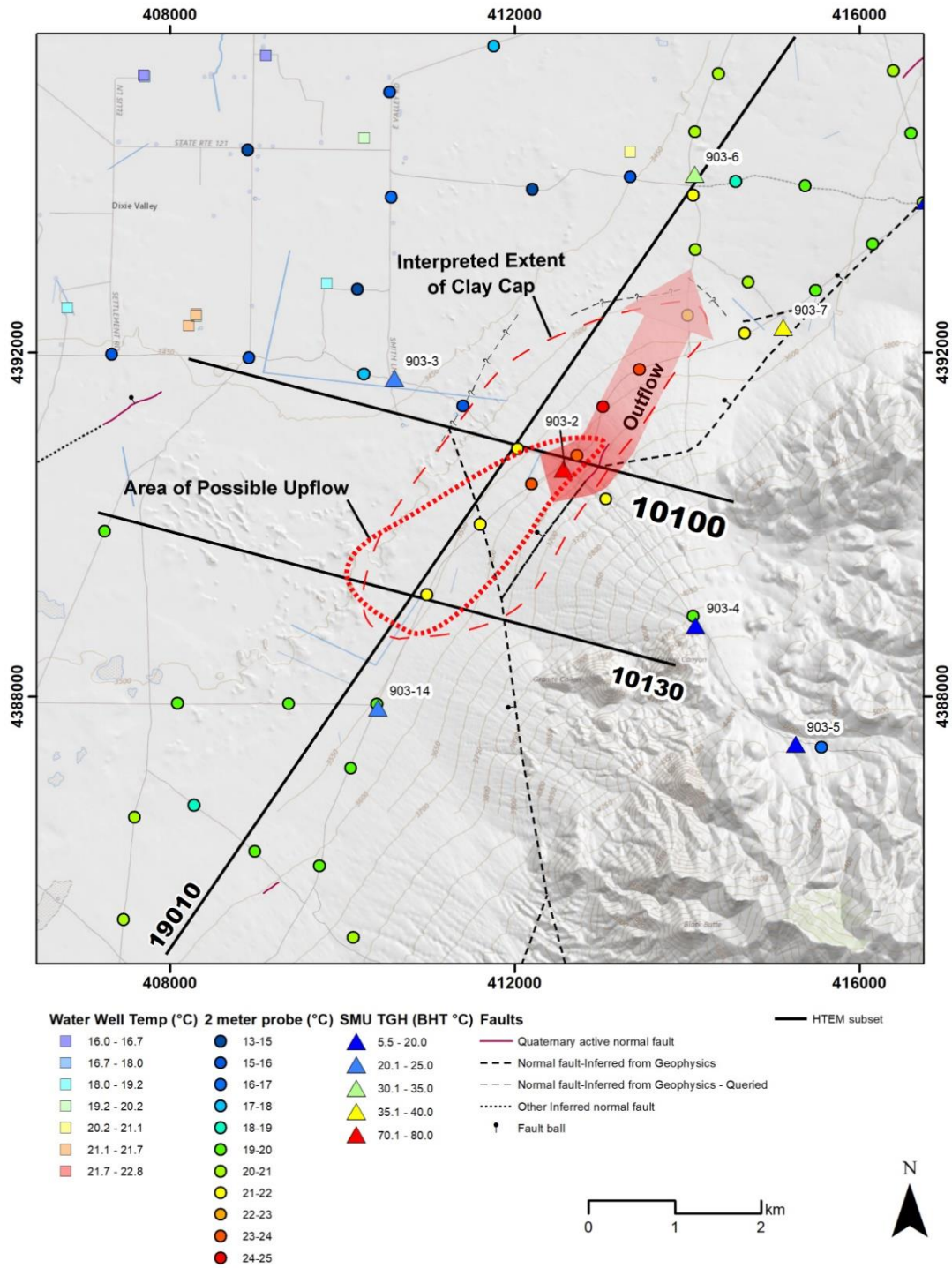


**Figure 20** Map view of the conceptual model, with select HTEM lines, temperature data, fault interpretations from gravity, and the inferred outflow.

Geochemical analysis identified dilute geothermal fluids with silica geothermometry of 120 °C to the north and west of the thermal anomaly. These samples are mixed with meteoric waters which

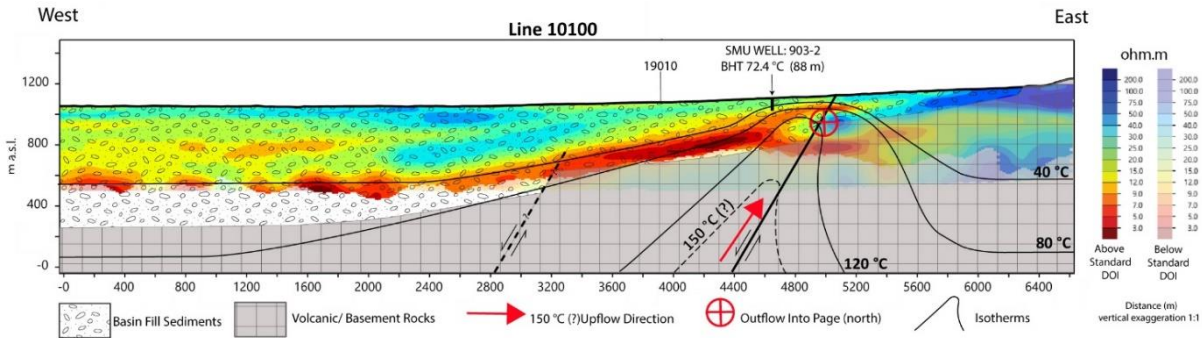


**Figure 21 Conceptual model cross-section along HTEM profile 10100. HTEM resistivity values are shown as the background colors. The basement – alluvial contact was derived from a 2D gravity model using a density contrast of 0.55 g/cc.**

reduces the geothermometry estimates of the maximum temperature of water-rock equilibrium. Maximum reservoir temperatures are unconstrained; however, the patterns of resistivity are similar to other geothermal systems with proven reservoir temperatures in the range of 135-165 °C.

Well 903-2 has a BHT of 72.4 °C at a depth of 88 m, and a thermal gradient > 500 °C/km. Given these observations, we assume this well is likely near the hot geothermal up-flow; alternatively, it may be associated with outflow. Additional anomalously warm TGH wells (903-6, 903-7, and 903-15) support outflow to the northeast. The 2M temperature probe survey identified a northeast-trending anomaly directly over inferred faults. Zones with anomalous 2M temperatures are common over shallow outflow plumes but can be difficult to observe directly over up-flow zones and productive reservoirs where the cap is thicker. We interpret the 2M anomaly at this prospect to represent where these fluids rise to their shallowest depths, along a northeast-flowing outflow path. Limited outflow may move westward where it interacts with shallow groundwaters and provides a geochemical influence, but a limited thermal influence.

#### **4.2.8. Conclusion**

The Grover Point case study presented here provides an example of the BRIDGE methodology being developed to identify and characterize hidden geothermal systems. Work done thus far at Grover Point has progressed the prospect from a limited thermal anomaly to a conceptual model that supports the existence of a potentially power capable resource. Further work is needed to prove this system, particularly TGH drilling to indicate that resource temperatures >120 °C may exist here. An MT survey and additional geologic mapping, not included in this report, was completed to better characterize the deeper resistivity structure in the area of interest. These data are published on GDR and will help further refine the conceptual model and guide the targeting of a future TGH drilling program.

Geologica Geothermal Group Inc. (Geologica) has prepared the following written conceptual model report in accordance with our contract with Sandia National Laboratories to provide technical support services. This report presents the results of the investigation completed by Geologica as defined in the BRIDGE project Statement of Work (SOW) titled “Advancing Geothermal Play Fairway Analysis to Identify and Assess Hidden Geothermal Energy Resources in the Basin and Range”, USA, dated January 4th, 2022.

The primary tool of the BRIDGE project was to deploy a regional-scale airborne electromagnetic method to investigate the shallow resistivity structure in areas with high prospectivity. This was followed up at several prospects by a multidisciplinary exploration approach, including additional geologic, geophysical and geochemical studies [10], [11], [12]. A central tenet to the BRIDGE methodology is that zones of low resistivity frequently occur over geothermal systems in the Basin and Range, and when paired with other data constraints, imaging these zones can enable discovery of these systems as shown in [11], [10], [70], [15], [22] and others.

In addition to exploring greenfield areas, the BRIDGE project also flew HTEM resistivity surveys over known geothermal systems including those with established power plants (Don A. Campbell and Salt Wells) and prospects that are known to the literature but remain undeveloped, at least in part, due to a lack of understanding on the location of their producible reservoirs. Two examples that fall into this latter category include the prospects of Lee-Allen and East Hawthorne. Despite both being explored to some extent in the past, neither prospect has deployed a resistivity-based exploration technique until now. This paper presents the multidisciplinary results that the BRIDGE project has developed over these fields. These efforts include the development of conceptual models for each prospect, wherein all of the observations are used to inform an interpreted model of the system (e.g., [15]). These models present a range of possible system parameters such as temperature and size, and they are further informed by system analogues in the Basin and Range province and elsewhere.

### 4.3. Lee Allen Prospect

#### 4.3.1. Background

The Lee-Allen geothermal prospect lies ~30 km south of Fallon NV, near the border between BLM and Department of Defense lands, which are known locally as Bombing Range 19 (BR-19) (Figure 22). Hot fluids were not reported to be present at the surface when first observed by workers of European decent and in the first geological reports on this area [71]. At that time the geothermal system could have been classified as a hidden system, since it lacked active surface manifestations but had ample evidence of Pleistocene and younger geothermal activity in the form of sinter deposits and silicified sediments at the surface. Allen Springs, along one of the sinter terraces, discharges < 1 gallons per minute of flow with reported temperatures of 15 °C [72], 24 °C [73], 26.2 °C (Nick Hinz, unpublished).

Thermal waters were first reported in shallow diggings by [74]. In 1932, a 10” well was drilled and encountered boiling water and steam, with frequent geysering activity [72]. Between 1951 and 1978 approximately a dozen shallow wells were drilled in this small area, mostly 10-50 m in depth, with the deepest at 177 m. All of the wells drilled near the springs encountered boiling artesian conditions and moderate flows up to 60 lpm [72]. The fluids produced from these wells were used for a variety of direct use applications. The modern-day Lee Hot Springs is a relic of these drilling activities, with reported temperatures of 88-100 °C flowing from a well, likely the first well drilled here in 1932 [73], [75], [76]. Also in 1978, Oxy Geothermal Inc. drilled well 72-33 to 914 m between Allen and Lee Hot springs. This well was not full-sized and was designed as a deep temperature gradient/observation hole, but few details about this well are available in public reports and databases. Some available details include that boiling water was encountered at about 13 m deep and the bottom hole temperature is reported at 119 °C [72]. However, it is unknown under what conditions this temperature was measured and if it represents a fully heated up temperature, either static or flowing. The limited geology log for this well based on public records indicate that alluvium was encountered from ground surface to either 80 or 250 ft, the result of variations in historical notes provided in online databases by the Nevada Bureau of Mines and Geology (NBMG), and then altered Mesozoic metamorphic rocks to bottom.

Between 1978 and exploration work completed as part of the BRIDGE project, leases changed hands multiple times and additional exploration work was completed, however none of these data are publicly available. The only publicly available work that was completed between 1978 and the BRIDGE project was geologic and gravity surveys completed by NBMG and University of Nevada Reno (UNR) with funding from the Great Basin Center for Geothermal Energy (GBCGE) and DOE [36], [77], [78].

The study by Hinz and others [78] focused on the structural controls of the geothermal system e.g., [3] and involved geologic mapping, geochronology, acquisition of new gravity data, gravity modelling, and integrating the results of geologic mapping with observations and interpretations from the gravity models. Lee-Allen is located near the western margin of the Walker Lane; a tectonic zone marked by NW-striking dextral strike-slip faults. These authors noted that evidence for NW-striking features is abundant in gravity and aeromagnetic datasets, and these structures intersect NE-striking, SE-dipping normal faults, the most prominent of which cuts near the hot springs and along the southeastern margin of an outcrop of Mesozoic diorite referred to as Allen Ridge. This work concluded that the geothermal system was hosted on a small right step or pull-apart on NE-striking normal faults where they intersected NW-striking dextral strike-slip faults. In 2010 a detailed geologic map was published over Lee-Allen that included many of these insights [77].

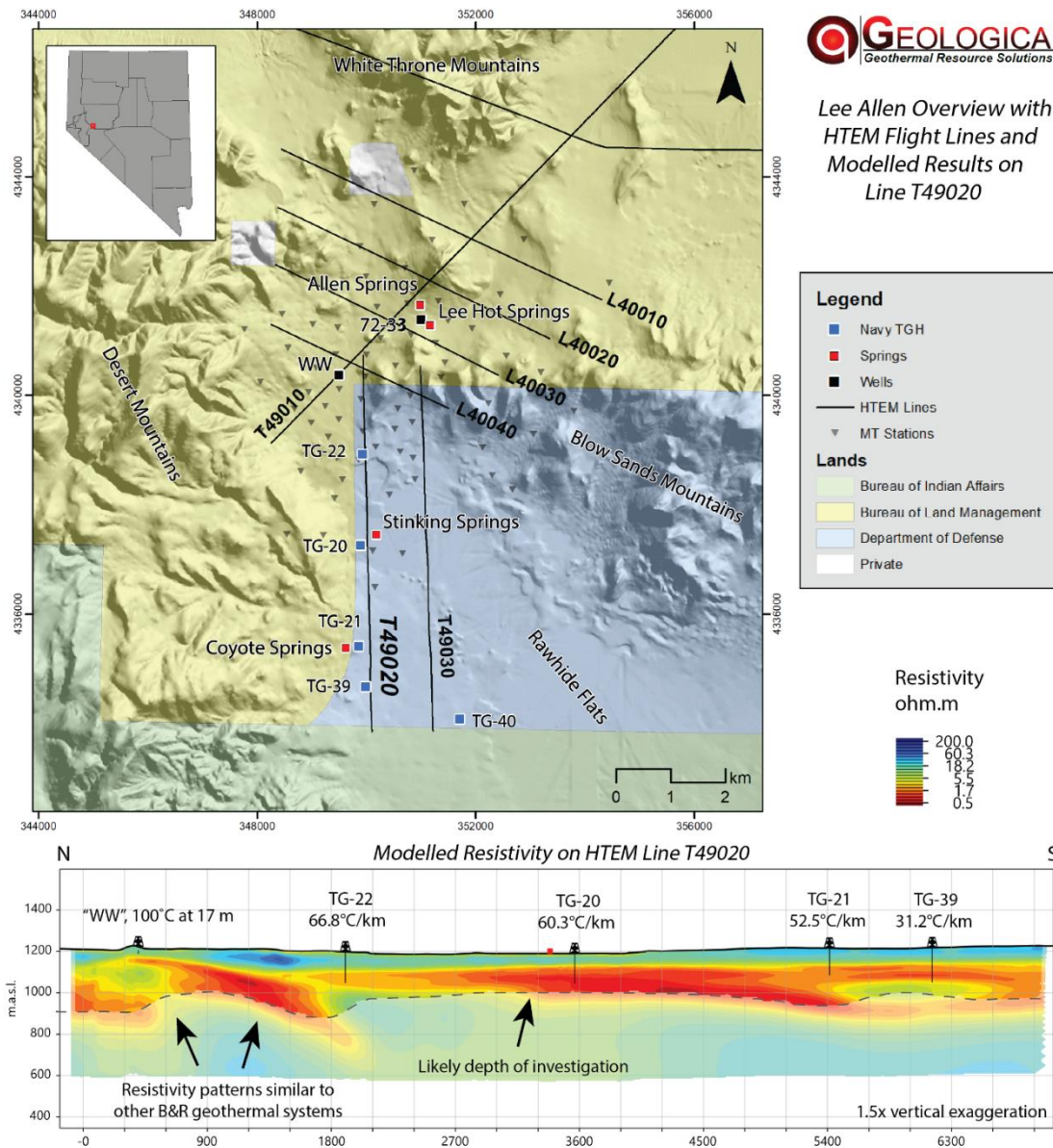


**Figure 22 Lee-Allen location and overview, with HTEM flight Lines (black lines), MT stations (grey triangles) land ownership boundaries and model results along HTEM line T49020. Thermal gradients calculated from each TG well are listed below the well name.**

Shallow probe temperature surveys were conducted by both Miller at 1.5 m deep [72] and Skord and others [79] at 2-m deep. Results from both surveys indicated a roughly oval shaped thermal anomaly centered over the modern springs and elongated slightly in an east-west direction. The magnitude of the 2-m thermal anomaly is large in comparison with other fields, with the hottest point at 67.9 °C and several points greater than 40 °C. In contrast, the area which includes temperatures above 26 °C is perhaps ~0.5 km<sup>2</sup>, which is much smaller than at other fields see [43] for a comparison. The points from Skord and others [79] are shown as colored circles in many of the maps in this report.

The main contributions from the BRIDGE Project were the addition of modern resistivity datasets, first with HTEM and later with magnetotellurics (MT). The BRIDGE project flew seven HTEM lines over the Lee-Allen prospect along NE, NW and NS striking azimuths (Figure 22). Line spacing is roughly 2 km. One NS-striking HTEM line, T49020, exhibited patterns of low resistivity similar to those observed over other geothermal upflow or outflow zones. Specifically, these features include: (1) A very near-surface shallow conductor that rises above what appears to be a continuous low-resistivity stratigraphy. (2) A generally dome-shaped top and bottom of the low-resistivity zone, although the lower portion may be below the depth of investigation here. (3) An embedded resistive lens below the shallowest low resistivity unit. Similar embedded resistors have been imaged along outflow paths at the operating field of San Emidio [63] and at a greenfield prospect called Grover Point [12], and in shallow zones over the producing fields of Don A. Campbell and Salt Wells. The mechanisms behind the patterns of resistivity at Don A. Campbell in particular have been investigated by the BRIDGE program [80]. Above the embedded resistor, the low resistivity units are often caused by smectite-clay alteration of unconsolidated sediments. The increase of resistivity within the embedded resistor can be caused by enhanced silicification by cooling, near-boiling fluids, and they tend to occur in strata with elevated permeability such as beach deposits or fanglomerate sands and gravels. These resistors have also been shown to correlate with a transition from smectite-dominated clays to mixed smectite-illite species at temperatures as low as  $\sim 100$  °C. Conspicuously absent from the resistivity patterns at Lee-Allen are lower resistivities values over zones with geothermal activity than those observed in the adjacent unaltered sediments. One possible explanation for this is the presence of nearby high TDS groundwaters, which results in lower observed bulk resistivities. Some wells on the margins of Rawhide Flats have chloride values  $> 10,000$  mg/kg.

The observations on HTEM line T49020 are also interesting when compared to well data. Four thermal gradient wells were drilled by the US Navy parallel to this flight line in the late 1970s. Drilled to 150-160 m deep, their bottom-hole temperatures range from 20-26 °C. While these temperatures do not suggest that a hot system lies nearby, their thermal gradients increase steadily to the north from 31.2 °C/km at TG-39, or near background values, to 66.8 °C/km at TG-22 (note that these thermal gradients were calculated for the relatively linear conductive temperature profiles below 30 m, not from surface to bottom hole temperatures). At the north end of this line, and directly over the shallowest low resistivity zone and the embedded resistor, a water well drilled in 1975 to a depth of 24 m reported encountering 100 °C water (NDWR database, Well Log # 16267). This well is labelled as “WW” in this paper but is likely to be poorly located as it is only reported to the nearest  $\frac{1}{4}$ - $\frac{1}{4}$  of one of two possible sections.

Taken together, these observations suggested that the geothermal system may lie southward of Lee Hot springs and the extensive surface mineralization and alteration found there, and that a shallow outflow geometry may be present. This informed the design and planning of a 71-station MT survey, commissioned, and modelled by the BRIDGE project [9] 3D MT Modelling Report, Lee-Allen. The results of that survey provided the first true 3D model at Lee-Allen and have informed the basic geometry of the geothermal conceptual model presented here. It has also offered new constraints on the structural and stratigraphic settings at Lee-Allen.

## Geology

Geologic data for the Lee-Allen geothermal prospect was sourced from the public domain and include geologic maps [77], [81], [82]. Maps by Carlson include reconnaissance 1:50,000 scale mapping of the Eastern Desert Mountains (2017) and detailed 1:24,000 mapping of the Terrill Mountains south of the geothermal prospect area (2018). Detailed mapping by Hinz and others [77]

covers the area surrounding the geothermal prospect area at 1:24,000 scale, including the Blow Sand Mountains, the southern portion of the White Throne Mountains, and the eastern foothills of the Desert Mountains, and a 1:8,000 scale area around the hot springs and sinter outcrops. Detailed geologic mapping on Bombing Range 19, south of the hot springs and east of U.S. Highway 95, is not available. Bombing Range 19 includes the northern extent of Rawhide Flats, the basin south of the geothermal prospect area, and much of the Blow Sand Mountains (Figure 23). Although no new mapping was completed in this study, previous publications provide only brief geology summaries of the stratigraphic and structural framework. Additional detail is provided here to support interpretation of the new geophysical data and conceptual modelling.

#### **4.3.1.1. Geologic Setting**

The Lee-Allen geothermal prospect is located near the northernmost corner of the Walker Lake domain of the Central Walker Lane. The Walker Lane (and eastern California shear zone to the south) is a system of discontinuous strike-slip faults in a ~100 km wide zone in the western Great Basin that accommodates approximately 20% of the dextral motion between the Pacific and North American tectonic plates e.g., [83] and references therein. The Walker Lake domain accommodates 48-100 km of total offset through a series of 5-6 en echelon NW-striking dextral strike-slip faults [78], [84]. In contrast, the Carson domain to the northwest is dominated by ENE-striking faults with sinistral motion associated with block rotations and oroclinal flexure that together accommodate overall dextral strain [82], [85], [86]. To the northeast and east of the Lee-Allen geothermal prospect, generally N- to NNE-striking extensional faulting characteristic of the Basin and Range province dominates.

Southwest of the Lee-Allen geothermal prospect, three of the major dextral strike-slip faults of the Walker Lane terminate in the foothills of the Desert Mountains (Figure 23) [82]. These include the Agai Pah Hills fault (>40 km long), the Gumdrop Hills fault (>50 km long), and the Benton Springs fault (~95 km long) [82], [83]. All of these have Quaternary scarps along their length, with the youngest surface rupture occurring 800 years ago on the Benton Springs fault [87]. The closest Quaternary scarps along these major NW-striking strike-slip faults are along part of the Terrill Mountains, ~16 km SSE of the Lee-Allen geothermal area. In this same area with documented Quaternary faulting, Carlson [82] has inferred cumulative right lateral offset of ~6.3 km based on offset of an early Miocene paleosol that sits between two ignimbrites.

In addition to the major strike-slip faults that have long been recognized across the Walker Lake domain of the Central Walker Lane, a system of smaller magnitude strike-slip faults has been interpreted to extend through the Russell Pass area [77], [78]. The largest of these was interpreted to extend over ~25 km in length and was interpreted based on both gravity data and lateral offset of a series of rhyolite domes by ~5 km across the fault [77], [78]. The south half of this fault forms the boundary between Rawhide Flat and the Blow Sand Mountains and was previously interpreted here based only on interpretations of the gravity data. The north half extends through Russell Pass where it was previously interpreted based on signatures in the gravity data, offset of a series of rhyolite domes, and juxtaposed dip domains of Tertiary strata [77], [78]. This fault runs through the Lee-Allen geothermal area and is informally named the Russell Pass fault in this report. This zone of strike-slip faulting extending through Russell Pass was also previously inferred as the northward extension of the Benton Springs fault, linked by the pull-apart basin that is Rawhide Flat [77], [82].

Numerous NE- to NNE-striking normal faults have been mapped in the Desert Mountains [82], a selection of which are shown in Figure 23. These faults predominantly dip to the NW in the northern Desert Mountains. Adjacent to the termination of the Benton Springs fault, in the

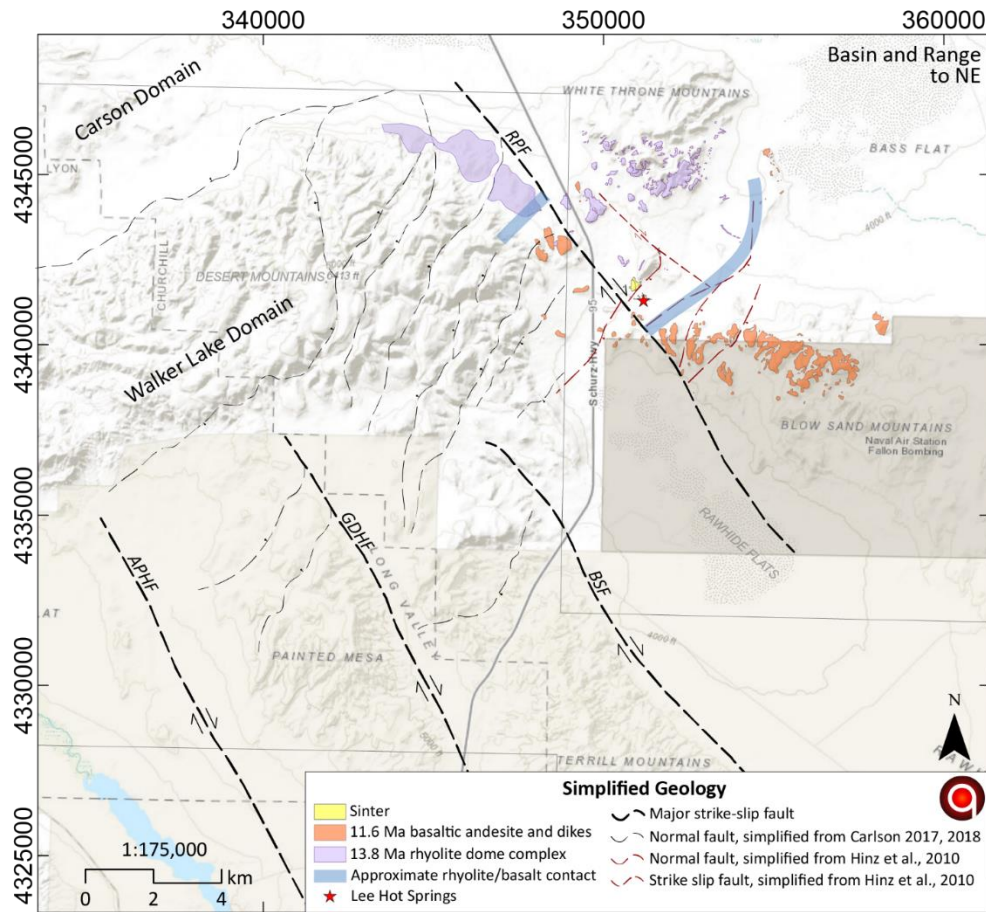


**Figure 23 Simplified regional geologic context of the Lee-Allen prospect area, modified from Carlson (2017, 2018) and Hinz and others [42]. Faults shown on this map vary in certainty of location and exposure. Lee-Allen hot springs are marked by the red star. Note the NNE- and NE-striking normal faults between the NW-striking major strike-slip faults. APHF = Agai Pai Hills Fault, GDHF = Gumdrop Hills Fault, BSF = Benton Springs Fault, RPF = Russell Pass fault. The blue line on the map shows the approximate contact between the 13.8 Ma rhyolite (shown in purple)/11.6 Ma basaltic andesite (shown in orange) that is the basis for inferring ~5 km of dextral offset on the Russell Pass fault.**

southwestern corner of the Desert Mountains, the dominant dip direction of the NE-striking normal faults changes to the southwest. However, the dip direction of the strata in this area does not change, which is not common (typically, strata dip towards the normal fault displacing them). Normal faults mapped to the north of the Russell Pass fault strike NE and dominantly dip to the SE. Although detailed structural relationships between the transform faults and these normal faults are not clear, in several cases the normal faults appear to terminate into the transform faults.

In many areas of western Nevada, Basin and Range extension began before the dextral shear associated with the Walker Lane developed and based on available studies, the Lee-Allen area is likely to have developed this way also. Regional studies in west-central Nevada constrain the onset of Basin and Range extension to ~17-15 Ma in the East Range [88], north of the Lee-Allen area, and ~15-12 Ma in the Wassuk Range area [89], south of the Lee-Allen area. Directly northeast of Lee-

Allen, a 14 Ma north-striking basaltic dike swarm exposed in the Bunejug Mountains and in Rainbow Mountain may correspond to the onset of extension in the Basin and Range [52], [90]. Dextral shear began ~9-10 Ma in the north-central Walker Lane west of Salt Wells [83]. Relatively recent paleomagnetism and geochronology studies in the Carson Domain of the Walker Lane, NW of Lee-Allen support the onset of dextral shear at ~9 Ma [82].

#### 4.3.1.2. Local Stratigraphic Framework

Stratigraphy in the Lee-Allen geothermal prospect area consists of Mesozoic sedimentary and igneous basement rocks, Oligocene to Miocene volcanic and intrusive rocks with interbedded sedimentary deposits, Quaternary surficial deposits including lacustrine, alluvial deposits, playa, eolian, sinter, and tufa deposits [77]. Units from the Miocene volcanic and intrusive rocks as well as Holocene sinter deposits from [77] are shown on the map in Figure 23 to emphasize potential regional offset on the Russell Pass fault. A more complete map of unit distributions can be found in [77], a clip of which is shown in Figure 24. A summary of the major sequences is described below.

8. Mesozoic basement: Mesozoic basement rocks consist of Triassic limestone and phyllite, which crop out in small areas east of the hot springs. The prominent peak just north of the hot springs, informally named Allen Ridge in Hinz and others (2008) and referred as such for this report, is comprised of Jurassic diorite, gabbro, and andesitic dikes. Limited outcrops of Mesozoic basement are found in the foothills of the Terrill Mountains, just west of the Benton Springs fault, and in the southern half of Painted Mesa (Carlson, 2017, 2018). Mesozoic basement is also encountered through most of the wellbore of well 72-33.
9. Oligocene volcanics: Oligocene volcanic rocks are one of the most prevalent Tertiary units found at the surface near the geothermal prospect area; a simplified set of these are shown in Figure 23. These units include a series of five late Oligocene ash-flow tuffs that are locally interspersed with fluvial gravels, mega-breccias, and hornblende-bearing andesitic lavas found in outcrop to the west of Allen Ridge and north of the Blow Sand Mountains. Tuffs within the series include 3 of unknown origin, the Tuff of Campbell Creek (28.8 Ma), and the Nine Hill Tuff (25.3 Ma). The ash-flow tuff series is also overlain by late Oligocene to early Miocene(?) hornblende-bearing andesite lavas found in the same area as the ash-flow tuffs.
10. Miocene volcanic and sedimentary rocks: The Oligocene volcanics are overlain by a sequence of middle to late Miocene volcanic and sedimentary rocks. These include 13.8 Ma rhyolite domes, flows, and associated coarse clastic sedimentary rocks found NW to NE of Allen Ridge, in particular, in the foothills of the Desert and White Throne Mountains. The easternmost Desert Mountains and the top of the Blow Sand Mountains are dominated by outcrops of 11.8 Ma basaltic andesite lavas with interbedded deposits of diatomite and thin fluvial gravels. A younger late Miocene (5.4 Ma) basaltic andesite caps the White Throne Mountains north of Allen Ridge, which also has thin interlayered fluvial and diatomite deposits. The relationship between the 13.8 Ma rhyolite domes and associated units and the 11.8 Ma basaltic andesite provides a possible marker for inferring cumulative offset along dextral faulting, have been highlighted in Figure 23 (yellow), and will be discussed further in the next section.
11. Quaternary surficial deposits: Pleistocene and younger units cover most of the lower elevations in the area near the Lee-Allen geothermal prospect. These include lacustrine units from Lake Lahontan, alluvial fan deposits, active eolian sands, active colluvium, playa deposits, and areas of anthropogenic disturbance (e.g., the landfill north of Allen Ridge).

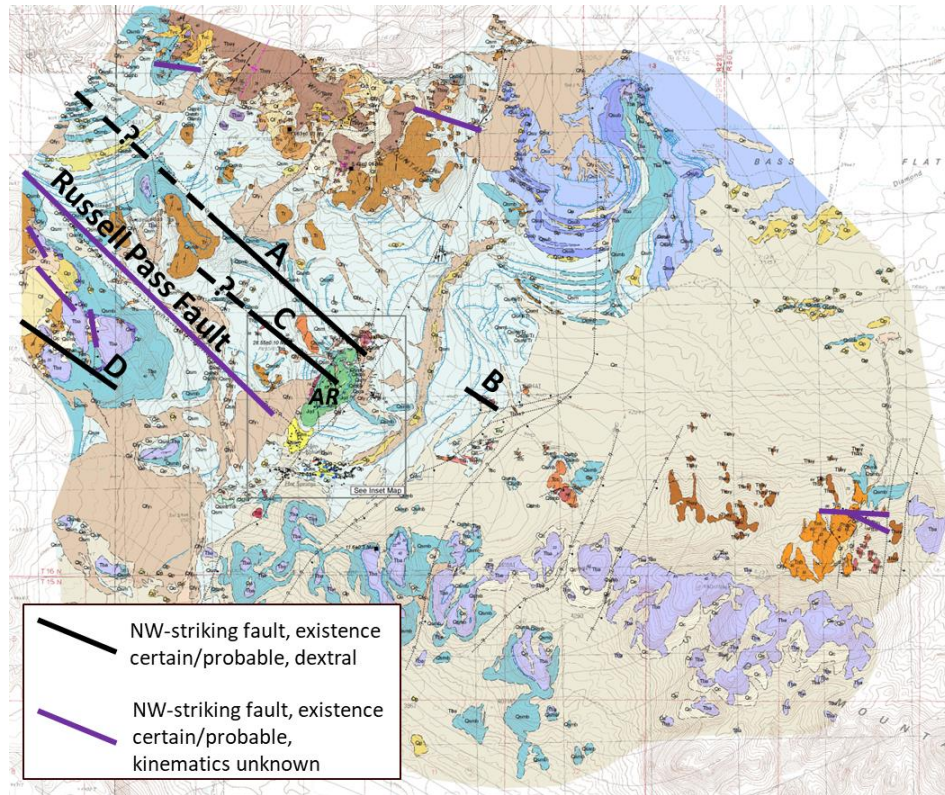


**Figure 24 Geologic map of the Lee-Allen geothermal area from Hinz and others [42] highlighting distribution and kinematic characterization of NW-striking faults. Annotations on top of the map for reference in this report. Black lines over NW-striking faults with inferred stratigraphic offset and/or fault surface data which supports dextral motion. Purple lines over NW-striking faults with stratigraphic offset, but uncertain kinematics (normal vs strike-slip).**

Lacustrine formations include fine grained sediments, tufa, and beach deposits from the Eetza, middle Seho, and upper Seho Allo formations. Some of the lacustrine sediments and tufas have been silicified in the vicinity of Allen Ridge, Allen Springs, and Lee Hot Springs. These sinter deposits are highlighted in Figure 23 and are relatively extensive near the hot springs and at the southern point of Allen Ridge. Another notable outcrop, although less extensive, is located at the northern point of Allen Ridge. Active eolian deposits are even more widespread than the lacustrine deposits and cover much of the area southeast of Allen Ridge. These deposits are how the Blow Sand Mountains gained their name.

#### **4.3.1.3. Local Structural Framework**

Within the geothermal prospect area, the dominant faults mapped in the area are NE-striking, SE-dipping normal faults and NW-striking dextral strike-slip faults. Normal faults mapped in the area are generally NE-striking and SE-dipping. The dominant NE-striking, SE-dipping normal fault in the area cuts along the southeast margin of Allen Ridge and has an estimated stratigraphic throw of ~1 km (Hinz et al., 2008). Given the magnitude of this normal fault and the fact that it extends through the sinter and areas of thermal springs, it is informally named the Lee-Allen fault in this report. Approximately NE-striking, SE-dipping normal faults in the Blow Sand Mountains are

inferred from repeating packages of Oligocene-Miocene ash-flow tuffs with varying dip domains (although the principal dip direction is NW). NE-striking normal faults, most of which dip SE, are also mapped in the southern White Throne Mountains. NE-trending folds are also present in the White Throne Mountains, and it is not clear if these are extensional or due to wrench faulting associated with the Walker Lane. Aside from strike-slip faults described in following paragraphs, mapping of normal faults in the eastern Desert Mountains has not previously been completed in detail as this area sits at the edges of previously published maps [77], [82]. A good characterization of normal fault patterns in this area is not currently available.

Multiple NW-striking faults have been mapped previously in the Lee-Allen area (Figure 24). Where fault surfaces were exposed in bedrock, each exhibited evidence for dextral motion. These faults range in magnitude of offset, strike length, details surface expression, and are described below individually or as groups of fault segments. Of the faults described below, the Russell Pass fault is the largest magnitude in terms of cumulative offset and strike length, and it is possible that all the lesser magnitude strike-slip faults are part of a broader Russell Pass fault zone that extends through the study area.

- **Fault A** is exposed in bedrock to the north and northwest of Allen Ridge and in the Churchill County landfill. The offset on Quaternary-Tertiary stratigraphy in the landfill is dextral-reverse. There are fault blocks north of Allen Ridge containing Oligocene and Miocene volcanic stratigraphy which are offset and juxtaposed with perpendicular strike orientations, supporting dextral, strike-slip motion. Outcrop characteristics support a map-scale fault of at least a few kilometers in length. The landfill and the north end of Allen Ridge are 1.5 km apart, and the fault is projected to connect between these two areas [77]. This fault is projected to extend NW through Russell Pass. To the south, it may terminate into the Lee-Allen fault or it may continue further. There is minor evidence for NW-striking dextral faulting on the SE side of the Lee-Allen fault (Fault B, Figure 24), which may be the SE extension of Fault A, or it is a separate minor fault. No Quaternary fault scarps are noted along Faults A or B.
- **Fault C:** Exposed in Allen Ridge and in low-relief outcrops NW of Allen Ridge. Likely a relatively minor, map-scale fault based on minimal stratigraphic offset. No Quaternary fault scarps are noted along this fault.
- **Russell Pass fault:** An ~25 km-long NW-striking fault was mapped by Hinz and others [77], [78] as concealed and extending through Russell Pass. The inference of this fault was based on apparent offsets in rhyolite domes, differing dip domains of Tertiary strata along and across its length, and interpretations from the gravity data. No fault scarps of any age are noted along the Russell Pass fault. A rough estimate of the apparent offset can be made using the contact of the rhyolite dome sequence and the 11.8 Ma basaltic andesite (shown in blue on Figure 23); this method implies ~5 km of offset between the White Throne and Blow Sand Mountains to the east and the Desert Mountains to the west. The southeast extent of this fault is projected through basalt outcrops in the Blow Sands Mountains. Much of this area is covered with Holocene eolian deposits and late Pleistocene beach gravels. The ridges of basalt that are above the Lake Lahontan high stand are rubbly with poor exposures for determining fault traces. Areas within BR-19 and were not accessible for detailed mapping by [77].
- **Fault D:** Exposed in the foothills of the Desert Mountains SW of the Russell Pass fault, Fault D is based on the juxtaposition of basaltic andesite lavas and sediments with

perpendicular strike and dip orientations. This fault is mapped for ~1 km length at the edge of the map area but may extend for >5 km to the NW, along a contact between basalt and rhyolite. No Quaternary fault scarps are noted along this fault.

- **Other Faults:** Several other NW-striking faults were mapped across the area (purple lines, Figure 24). One of these on the SW side of the Russell Pass fault has a north-facing Quaternary fault scarp. It is unclear if NW-striking faults have pure normal or dextral-normal motion.

Dip domains of lithologic units are dominantly measured in the volcanic and basement rocks and can generally be categorized into two areas, separated by the Russell Pass fault, although additional complexity is present. Miocene units in the eastern Desert Mountains dip between 20-50 degrees to the southeast, which is consistent with the NW dipping normal faults in this area, with an exception where Miocene strata dip SW between Fault D and the Russell Pass fault (Figure 24). In contrast, dips of the units in the White Throne Mountains, Blow Sand Mountains, and near Allen Ridge are on average to the NW, ranging between 20-90°, and there is more variation in strike than in the eastern Desert Mountains. NW dips on the northern side of the Russell Pass fault are consistent with the SE-dipping normal faults in this area. Complexity and variation in strike and dip orientation increases with proximity to the inferred trace of the Russell Pass fault. Strikes near the inferred trace are approximately NW, nearly 90° from those to either side. These significant variations in rock orientations across the Russell Pass fault underscore the potential regional significance of this dextral strike-slip zone.

#### **4.3.1.4. Alteration and Possible Surface Manifestations**

Although it is not clear if any natural thermal springs have been reported in the Lee-Allen prospect area, early reports did note the presence of hot water after shallow digging [74] and extensive Quaternary sinter deposits and evidence of argillic alteration in the Mesozoic basement and Tertiary volcanics are notable indicators of geothermal activity in the recent geologic past. Modern thermal springs include Lee Hot Spring, which is reportedly the boiling (~96 °C at 1220 m elevation) emanation from the earliest known well drilled in 1932, two additional springs mapped in 2008 at 52 °C and 59 °C to the southeast of Lee Hot Springs (~25 and 80 m, respectively) that may also be discharges from shallow wells, and Allen Springs, north-northeast of Lee Hot Springs. Allen Springs is relatively cool at 24-26 °C, but slightly above the groundwater temperature found in shallow well outside of the thermal area (e.g. well DH-1, described in Section 2.4, at 22 °C).

Silicified pluvial Lake Lahontan beach sand sediments are found at both the south and north ends of Allen Ridge, extending about 1.5 km north-south and about 1 km east-west [78]. The NE-SW extent of the sinter is also coincident with the area between the Russell Pass fault and the strike-slip fault A in Figure 24. The elevation at the south end of the ridge spans about 1220 to 1250 masl. At the north end of the ridge, the silicified sediments are at ~1270 to 1280 masl. Lee Hot Springs flows out of the southernmost outcrop of sinter deposits and is actively depositing either silica or calcite today, while Allen Springs flows from sinter at the southern end of Allen Ridge.

Argillic alteration has been observed in the Mesozoic basement that forms Allen Ridge and Tertiary volcanics in the near vicinity. Basement rocks here are pervasively weakly to moderately altered with a likely range of argillic to porphyritic assemblages. Tertiary intrusive and ash-flow tuff units in the immediate surroundings exhibit weak to moderate-intensity alteration, including possible advanced argillic alteration at the north end of Allen ridge. In addition, calcite veins ranging up to 2 m-thick

were observed in Miocene bedrock in the footwall the Lee-Allen fault ~4.5 km NNE of Lee Hot Springs. These veins may be related to relict hydrothermal activity as they are truncated by Quaternary surficial deposits.

### **4.3.2. Wells**

There are several wells in the vicinity of the Lee-Allen geothermal prospect, including shallow test or private wells, temperature gradient holes, and a deep (~915 m) geothermal test well (72-33). Data for the temperature gradient holes and records for several nearby shallow wells are available, but much of the well data for 72-33 remains proprietary and legacy wells dating back to the 1932s are poorly documented. Table 4 shows a summary of the publicly available well data. Temperature-depth plots of the Navy TG wells are shown in Figure 25. Each of these TG wells are shown in cross-section on HTEM line T49020 (Figure 22).

There is historic data for wells drilled between 1932 and 1978 [72], [78]. Miller (1978) details the overall history and findings of some of the wells drilled between 1932 and 1978. The 1932 well was drilled by Bob Lee and Frank Inman to a depth of ~48 m and encountered boiling water and steam. Geyser activity from this well was frequent and reportedly reached hundreds of feet in the air. In 2008, NBMG relogged Lee Hot Springs, reportedly this 1932 well, and found that it was open to a depth of 1.5 meters and had a maximum temperature of 96.6 °C (boiling at this elevation, ~1220 m). Recent estimates of the flow rate were as high as 130 lpm and it is noted that the amount of flow varies throughout the year and from year to year (Hinz and others, unpublished data). A second well was drilled by “Dr. Jacobsen” in 1951 near Allen Springs to a depth of 177 m, which encountered explosive steam pockets, reached a maximum temperature of 88 °C, and flowed at ~3.8 lpm. Between 1953 and 1978 approximately a dozen additional wells were drilled in the area by Ted Ax, who held the water rights to the area at this time. Almost all of these encountered hot water, but details on these wells are scarce. One of these, called “Water Well” or “WW” in the following sections, was drilled in 1975 and has a drilling record in the Nevada Division of Water Resources database (Well Log # 16267). This record indicates the well was drilled to ~17.1 m and encountered boiling water (the maximum temperature recorded is 100 °C, which is above boiling at this elevation). The location of this well is uncertain, given to the nearest quarter-quarter of two possible sections and it is likely that it was drilled near Lee Hot Springs. In this report we have plotted it where it is shown on the NDWR and GBCGE databases. Well casings remain in place for most of these historic wells, which were mapped by GPS by Hinz and others [78]. About half of the wells remain open to the water table and temperature measurements were also collected when mapped.

Original reports and logs for well 72-33 (e.g., mud logs, well completion reports, sundries, well temperature logs, borehole geophysics, and well testing data) are not available publicly. The primary source of information on this well is from [72]. However, it is not clear if the reported data on temperatures and permeability are pieces of drilling data or complete reports, and thus it is safe to assume that the reported data is incomplete. This well encountered boiling water at about 13 m deep and had little reported temperature change for the rest of its depth. The bottom hole temperature is reported at 119 °C, and the well flow peaked at 600 m depth at 1 barrel/minute, or about 160 lpm. It is possible that this flow was related to encountering the Lee-Allen fault. Without more complete data it is unclear how high of temperatures were reached, what depth these were reached, and what the permeability may have been. If the 119 °C temperature is quality data, this can be assumed to be a minimum threshold for a maximum temperature for this well. The limited geology log for this well based on public records indicate that alluvium was encountered from ground surface to either 80 or

250 ft, the result of variations in historical notes provided in online databases by NBMG, and then altered Mesozoic metamorphic rocks to bottom.

In 1979, five temperature gradient holes were drilled on the western edge of Bombing Range 19 to depths of 135-170 m. The northernmost TGH, TGH-22, encountered water and a geochemical sample was taken. Although the maximum temperatures for these are not anomalous (22.4-26.1°C), the temperature gradients for the northernmost wells (TGH-20, 21, and 22) are anomalously high (60.3, 52.5, and 66.8 °C/km, respectively, shown in Figure 25). In addition, these gradients increase northward. The southernmost wells, TGH-39 and 40, have normal temperature gradients of 31.2 and 37.4 °C/km. Although none of these temperature gradient wells are anomalous enough to indicate a geothermal system, the northward warming trend is consistent with the known hot wells

**Table 4 Summary table of available well data at Lee-Allen.**

Well name	Easting (UTM NAD83)	Northing (UTM NAD83)	Date drilled	TD (m)	Water Depth (m)	Max. measured temp. (°C)	Comments
Inman and Lee, 1932	Unknown	Unknown	1932	47.9	Geysered	96.0	Reportedly today's Lee Hot Springs; well 10 of Miller, 1978
72-33	350999	4341380	1/31/78	914.4	~13	119.0	Additional data (temperature surveys, lith logs) collected, but proprietary. Well 3 of Miller, 1978.
TG-39	349988	4334664	11/16/79	169.2	Dry	22.4	Temperature profile data available (Katzenstein and Danti, 1982)
TG-40	351706	4334076	11/17/79	169.2	Dry	22.9	Temperature profile data available (Katzenstein and Danti, 1982)
TG-20	349894	4337256	4/6/79	144.8	Dry	24.4	Temperature profile data available (Katzenstein and Danti, 1982)
TG-21	349858	4335406	4/5/79	134.9	Dry	23.9	Temperature profile data available (Katzenstein and Danti, 1982)
TG-22	349926	4338921	4/10/79	147.8	unknown	26.1	Temperature profile data available (Katzenstein and Danti, 1982)
Jacobsen	350945	4341584	1951	177.0	Flowing	88.0	Lithology data available. Location approximate; drilled near Allen Springs. Encountered "explosive" steam pockets. Well 2 of Miller, 1978.
Water well (WW)	349493	4340370	3/7/75	17.1	No data	100.0	Location uncertain; given to quarter-quarter with 2 possible sections. Possibly drilled near Lee Hot Springs.
Well 1	350980	4341650	1953-1978	6.1	Dry	No data	Lithology data available. Location approximate; drilled near Allen Springs. (Miller, 1978)
Well 4	Approximately located in an area less than 1 km <sup>2</sup> (NW Corner: 350986.624 mE, 4341483.16 mN, NE Corner: 351362.862 mE, 4341483.16 mN, SW Corner: 350986.624 mE, 4341262.497 mN, and SW Corner: 351362.862 mE, 4341262.497 mN).		1953-1978	19.8	19.8	Hot	Lithology data available (Miller,1978)
Well 5			1953-1978	9.1	9.1	Hot	Lithology data available (Miller,1978)
Well 6			1953-1978	10.1	9.1	Hot	Lithology data available (Miller,1978)
Well 7			1953-1978	24.4	7.3	109.0	Lithology data available (Miller,1978)
Well 8			1953-1978	20.4	No data	123.0	Lithology data available (Miller,1978)
Well 9			1953-1978	13.7	13.7	No data	Lithology data available (Miller,1978)
Well 11			1953-1978	8.2	0.9	101.0	Lithology data available (Miller,1978)
Well 12			353279	4342051	1953-1978	41.1	Dry

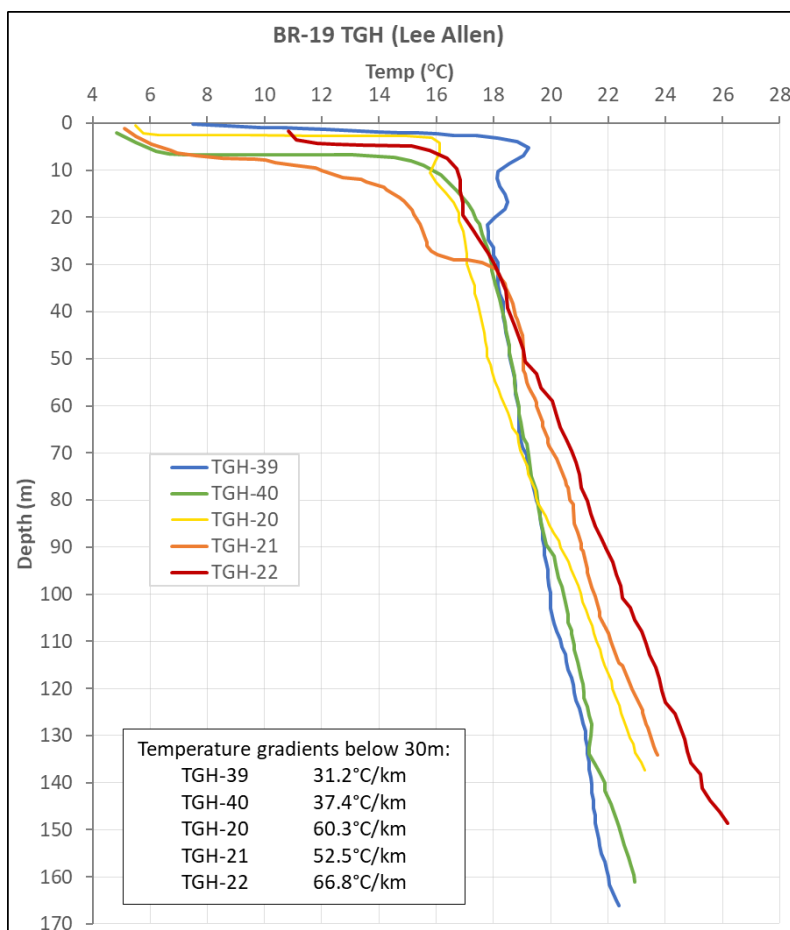


**Figure 25 Temperature-depth plots of the five US Navy thermal gradient holes near HTEM line T49020. Thermal gradients increase to the north.**

to the north. These wells act as a constraint to the south for estimates of the location of the Lee-Allen geothermal system.

### 4.3.3. Fluid Geochemistry

Geochemical analyses of water samples from the area surrounding Lee-Allen were primarily sourced from the Great Basin Center for Geothermal Energy database, with additional samples from [91]. Historical samples were from springs (5 samples), shallow wells (8 samples), and a single sample from the full-size geothermal exploration well 72-33. Springs samples include two samples from Allen Springs, three samples from Stinking Springs, and one sample from Coyote Spring. Shallow well samples include a cold groundwater sample (Well DH-1), a sample from TGH-22, and seven samples from the shallow flowing well(s?) now called Lee Hot Springs.

Analyses from a total of 14 samples were incorporated into a geochemical database. These data were evaluated by calculating charge balances and using typical mixing plots (for example, SiO<sub>2</sub> vs. Cl, Figure 27), trilinear plots (Figure 26, right), and geochemical equilibrium calculations such as geothermometers (Table 5 and Figure 28). Water types were determined by major cation and anion chemistry seen in trilinear diagrams and the relative concentrations of each major analyte (Na, K, Ca, SO<sub>4</sub>, Cl, and HCO<sub>3</sub>) and then evaluated for temperature, TDS, and pH correlations.

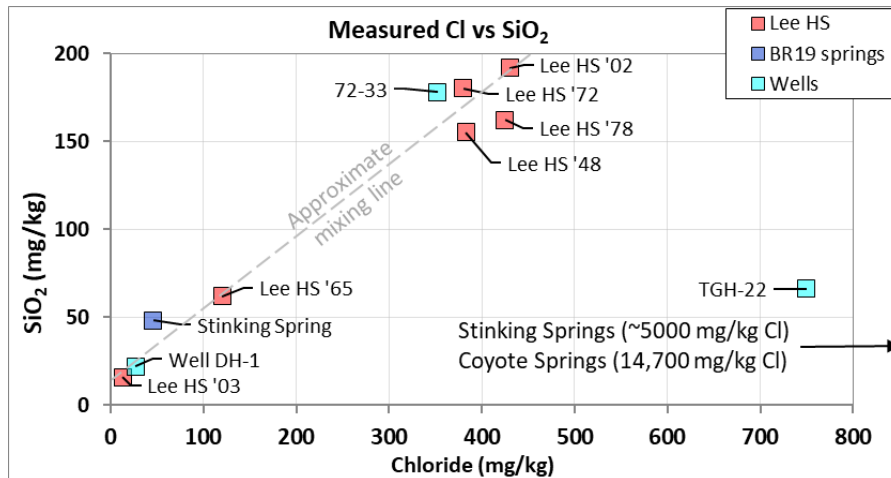


**Figure 26 Chloride vs. SiO<sub>2</sub> for water samples near Lee-Allen. Note that due to the very high salinity of Stinking and Coyote Springs relative to all other waters, they plot far off the x-axis of this chart, despite relatively low SiO<sub>2</sub> concentrations near ~50 mg/kg). This likely indicates that these waters are not related to those near Lee-Allen hot springs.**

Geothermometers were examined for quality, excluding significant outliers and water types for which that geothermometer is not applicable (e.g., those that plot outside of the “partial equilibrium” zone of Figure 28).

Of the available water analyses incorporated into the database, five of them were missing data for major constituents such as bicarbonate (HCO<sub>3</sub>) and in one case, major cations (Na, K, and Ca). Data from the remaining nine samples are generally of good quality with charge balances less than 2.5% with one exception; data from a Lee Hot Spring sample taken in 1978 has anomalously low sulphate that resulted in a charge balance of 18%. Data from this sample (Lee HS '78) were excluded from the anion ternary diagram (Figure 26, top right), but included in the cation ternary (top left) and mixing plot (Figure 27) as it overlaps with two other similar data points from Lee Hot Springs. Evaluation of these data resulted in the conclusions below.

Water types in the Lee-Allen area generally fall into four categories:

- Relatively cool (~28 °C), high TDS (NaCl) (>10,000 mg/kg), slightly alkaline (pH 8-9) Na-Cl and Na-Cl-SO<sub>4</sub> waters from Stinking Springs and Coyote Springs.
- Hot (88-96 °C) and moderately warm (~30 °C), moderate TDS (1200-2500 mg/kg), and neutral pH (7-8) Na-Cl-SO<sub>4</sub> waters from near Lee Hot Springs, including Allen springs, Lee Hot Springs itself, well 72-33, and TGH-22.

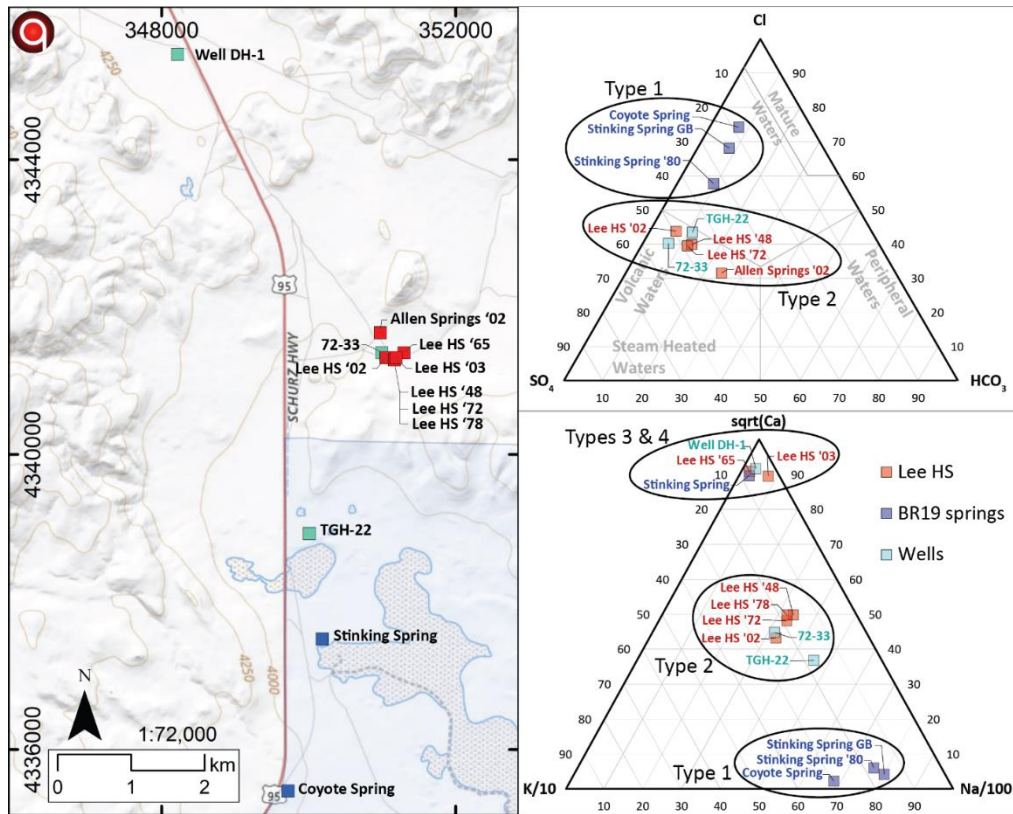


**Figure 27 Map and ternary diagrams of water samples from near Lee-Allen. Above: anion trilinear. Below: cation trilinear. Several samples are missing key anion data and thus are missing from the top trilinear.**

- Hot (91-96 °C), likely mixed low TDS (<500 mg/kg), neutral pH (7-8) Ca-rich waters from near Lee Hot Springs (Lee Hot Springs '65 and '03) with missing key anion data (HCO<sub>3</sub>).
- Relatively cool (22.3-28 °C) waters from near Lee Hot Springs, one sample from Stinking Springs, and Well DH-1, which lack key anion data (HCO<sub>3</sub>) needed to fully evaluate them, but are otherwise likely meteoric waters with high Ca and low Cl.

High TDS NaCl waters are a common indicator of geothermal waters with chemistry indicating significant water-rock interaction enhanced by high temperatures. In contrast, meteoric groundwater is commonly relatively low TDS Ca-HCO<sub>3</sub> waters with relatively high proportions of magnesium (Mg). The category 1, cool, high NaCl waters from Stinking and Coyote Springs may contain a significant amount of geothermal fluid which has cooled, or, more likely, these waters may have high salinity due to interaction with evaporite deposits within the basin sediments (note their location on the map in Figure 26). Waters from the second category (TGH-22 and samples near Lee Hot Springs) have the highest thermal component but may be mixed meteoric waters and geothermal fluids; TGH-22 may also include an additional component of high salinity groundwater such as what

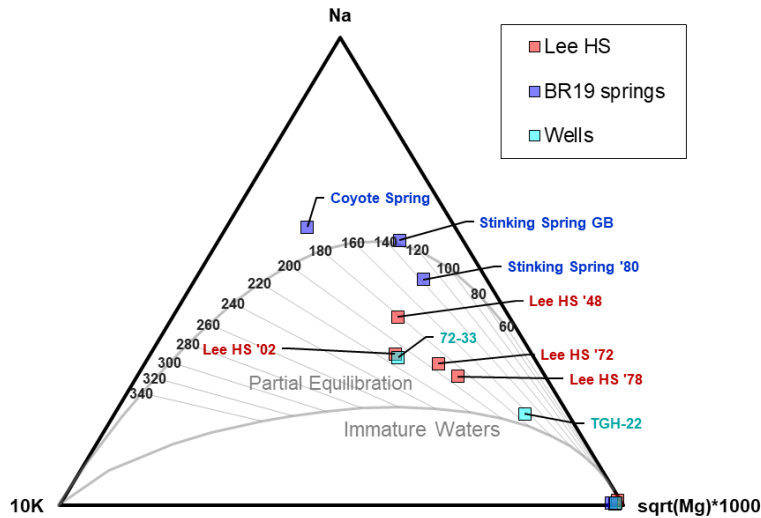


**Figure 28 Giggenbach cation geothermometer trilinear. Note that the samples near Lee-Allen hot springs plot approximately along a 180-200 °C trend, which is relatively consistent with the quartz and average Na/K geothermometer estimates.**

makes up Stinking and Coyote Springs based on its offset from the mixing line in Figure 27. Hot waters from category 3 are low-TDS Lee Hot Spring samples with incomplete analysis that could be conductively heated groundwater (Ca-rich), or thermal waters diluted with condensate (low-Cl); however, the incomplete analyses prevent thorough evaluation. Cool waters from the fourth Ca-rich category are likely to represent meteoric groundwater, but the lack of major constituent data prevents conclusive assessment.

Geothermometers calculated from water chemistry of Lee-Allen samples include reservoir temperature estimations based on equilibrium between aqueous silica and quartz [92] and an average of Na/K geothermometers (averaging 6 Na/K geothermometer equations from the literature). While a glassy, high-silica rhyolite that could influence aqueous silica concentrations (and therefore geothermometer temperature estimates) is present in the area, these Lee-Allen thermal waters are unlikely to have interacted with the rhyolite as it generally crops out to the north and northwest of and of the water sample locations at similar or higher stratigraphic elevations. Geothermometer estimates for samples near the hot springs (samples highlighted in red and well 72-33 in Table 5) range between 112-177 °C (silica) and 146-179 °C (Na/K). The Na-K-Mg chemistry of thermal waters (Figure 28) suggests deep reservoir or upflow temperatures of approximately 180-200 °C. The significant overlap between the silica and Na/K estimates and agreement of the uppermost temperatures increases the confidence that these geothermometer temperatures are representative of the Lee-Allen geothermal system. The water from TGH-22 has a quartz geothermometer temperature of 115 °C and an average Na/K temperature of 130 °C and a slightly lower Na-K-Mg temperature (170 °C, Figure 28). Data from this sample also plot in close proximity to waters from near Lee-Allen, potentially indicating a shared source. However, water from TGH-22 is probably cooler from mixing with more meteoric water and therefore relatively less evolved (Figure 27, Figure 28). Although typically in geothermal areas, high NaCl waters are found to have high thermal components, geothermometer estimates for the high TDS waters from Stinking and Coyote Springs range between 70-115 °C (quartz) and 89-98 °C (Na/K) – lower than the waters near the hot springs. These samples also either plot outside of the partial equilibration zone on the Giggenbach

Na-Mg-K trilinear (Figure 28), or plot on a different (~140 °C) trend from the other Lee-Allen water analyses. The lower geothermometry estimates for these waters supports the hypothesis that Stinking and Coyote Springs are not related to the geothermal system, but instead represent saline groundwater in the basin (and may explain some of the low resistivity signatures discussed further in the geophysics section).

In summary, geochemical data from the Lee-Allen area indicate that waters from the Lee-Allen “hot springs” and the nearby wells (including TGH-22 and 72-33) are likely related to a deep circulation geothermal system, although TGH-22, located south of the other features, may be more mixed with meteoric water and therefore more of an outflow. The upflow of this system may be as high as 180-200 °C based on quartz, Na/K, and Na-Mg-K geothermometry estimates. High TDS springs to the south of these sample locations (Stinking and Coyote Springs) are unlikely to be related to this system and may instead represent saline groundwater in the basin, where the high salinity is due to evaporation or interaction with evaporite deposits.

#### 4.3.4. Geophysics

##### 4.3.4.1. HTEM

HTEM data was collected along seven flight lines over the Lee-Allen prospect (Figure 22). This represents a small subset of the complete HTEM dataset collected for the BRIDGE project, which totals 1,877 line-km of data. HTEM data was contracted through Xcalibur Multiphysics using the HELITEM™ system. This TEM systems consists of a 962 m<sup>2</sup> loop with four turns of wire. A 7.5 Hz, 146 A signal was transmitted to the coil. This lower frequency enhances late-time arrivals and is sensitive to greater depths than higher frequency systems. The receiver employed a central-loop

**Table 5 Water sample temperatures, applicable geothermometers, and notes for samples from the Lee-Allen area. Colors correspond to the sample point colors in the other figures, e.g. red = “spring” samples from near Lee-Allen Hot Springs, light blue = wells, and dark blue = spring samples from Stinking and Coyote Springs.**

Sample Name	Sample Temp. (°C)	Quartz °C (Fournier & Potter, 1982)	Average Na/K °C	Notes
Lee HS '03	96	55	--	No HCO <sub>3</sub> data; Qtz geotherm. estimate less than measured temp. and Na/K not applicable
Lee HS '65	91.1	112	--	No HCO <sub>3</sub> data; Na/K not applicable
Allen Springs '77	26.7	149	152	
Lee HS '48	93	164	146	
Lee HS '78	91	166	156	High charge balance (18%) from low sulphate
Lee HS '72	88	173	158	
72-33	96	173	180	
Lee HS '02	31.6	178	179	
Allen Springs '02	24	--	--	No cation or SiO <sub>2</sub> data
TGH-22	26	115	130	
Stinking Spring GB	28	71	89	
Stinking Spring	28	100	--	No HCO <sub>3</sub> data; Na/K not applicable
Coyote Spring	--	115	--	Plots outside of partial equilibrium zone on Giggenbach trilinear
Stinking Spring '80	--	--	98	Anomalously low SiO <sub>2</sub> ; Na/K not applicable
Well DH-1	22.3	67	--	No HCO <sub>3</sub> data; Na/K not applicable

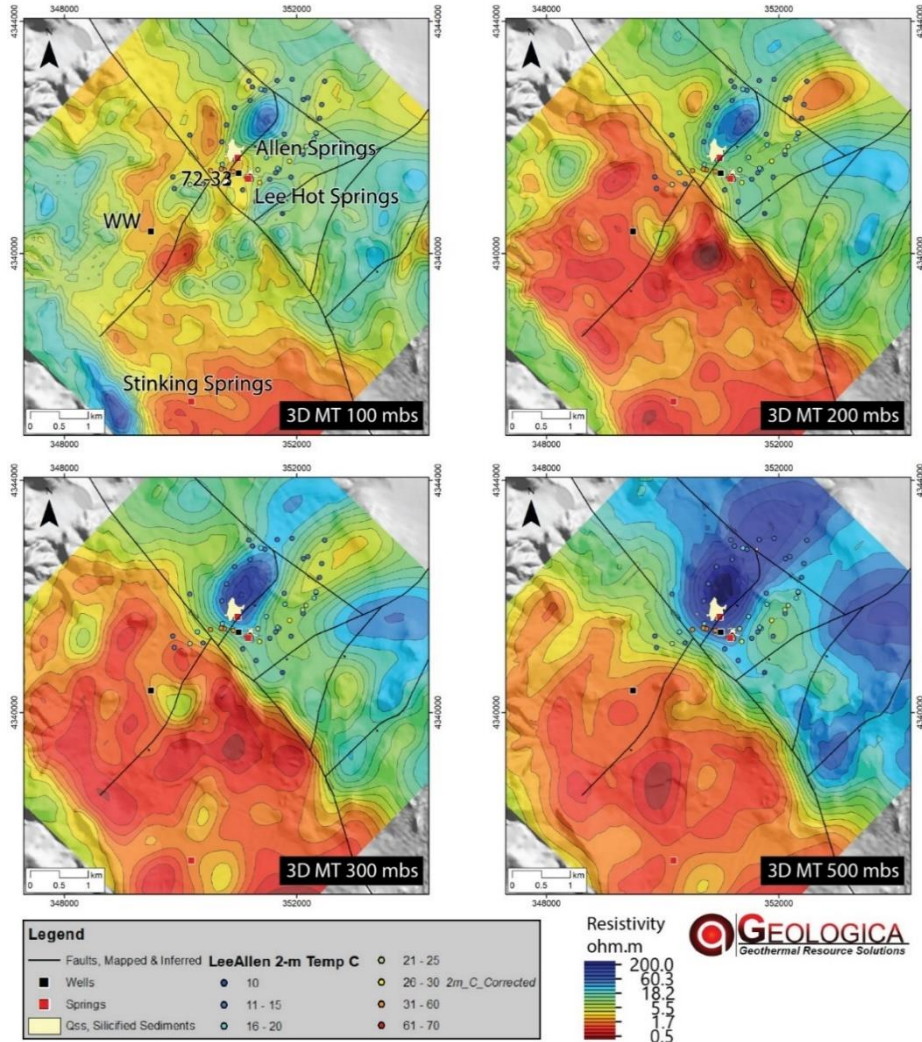


**Figure 29** Depth slices through the 3D MT model at 100, 200, 300 and 500 meters below sea level. Maps include 2-m temperature points, wells, springs, silicified sediments, and an interpreted fault layer that is modified from Hinz et al., 2010a.

design with coils aligned in the X, Y and Z directions. Flight speed averaged 110 km/hr while maintaining a sensor height of ~35 m.

HTEM data were modelled by the USGS using laterally constrained, 1D deterministic inversions ran on the Aarhus Workbench TEM module. The likely depth of investigation was determined, which estimates the depth to which the resistivity structure can be reliably resolved [93]. This is shown in the lower panel Figure 22 as a dashed grey line and a transition to a transparent background. All the HTEM resistivity models over Lee-Allen are shown in the Appendix next to resistivity values from the 3D MT model on the same line.

#### 4.3.4.2. MT

A 71 station MT survey was commissioned by the BRIDGE program with support from Ormat Technologies, the Navy Geothermal Program Office and NAS Fallon (Figure 22, grey triangles).

The survey design was greatly informed by the HTEM results, and the decision was made to move the center of the survey southward from Lee Hot Springs towards the boundary between BLM and BR-19. Some areas of BR-19 could not be accessed due to the risk of unexploded ordinance there. Data were collected by KLM Geoscience using Phoenix RXU-8A receivers, MTU-155 induction coils and refillable Cu-CuSO<sup>4</sup> electrodes. MT sites were left to record overnight, and all sites were recorded simultaneously with a remote reference station maintained ~25 km to the NE. Tipper data were not collected with this dataset.

MT data were modelled in 3D using the RLM-3D inversion program in Geotools software. The model was run on a rotated mesh that accounted for topography and started from a homogeneous 20 Ohm-m. A total of 12 inversions were run to explore the inversion space and arrive at a preferred model. The preferred model shown in this report has an RMS error of 0.81 while using an error floor of 3% on all tensor components. A detailed report on MT data and modelling efforts can be found in [9] **3D MT Modelling Report, Lee-Allen**. Depth slices through the final model are shown with interpreted faults, well data and 2-m temperature probe results in Figure 29. Interpreted fault layer is modified from [77] and described in Geoscientific Interpretations.

#### **4.3.4.3. Gravity**

Existing public gravity datasets were re-gridded for this project and used to inform the structural setting (Figure 30, upper two panels). The datasets that overlap Lee-Allen include [94], data collected by the University of Nevada Reno at Lee-Allen (Hinz et al., 2008), data collected by UNR at Salt Wells and collected by the Navy GPO on BR-19. Some points that appeared to be spurious were removed prior to gridding. The complete Bouguer anomaly (CBA) was produced by using a reduction density of 2.67 g/cc (Figure 30, upper left panel). The horizontal gradient magnitude of the CBA is shown in upper right panel of Figure 30. Interpreted fault layers is modified from Hinz and others [77] and described in Geoscientific Interpretations.

#### **4.3.4.4. Magnetic Data**

Public airborne magnetic data was clipped out of the larger GeoDAWN dataset and re-gridded over the Lee-Allen prospect [16]. These data were collected on a fixed-wing plane with 400 m line spacing and a mean terrain clearance of 200 m. The total magnetic intensity residual was gridded, and to minimize polarity effects, a reduction-to-pole (RTP) transformation was applied to that grid. The RTP is shown in the lower left panel of Figure 30. A pseudo gravity transform was also applied to the data [95], which is a vertical integration (smoothing) technique that shows what the magnetic response would look like if it had the same response as gravity. Here it was used as an intermediate processing step before taking the horizontal gradient magnitude (Figure 30, lower right panel). This workflow allows for horizontal gradient maxima to occur more closely to the edges their respective sources [62]. The interpreted fault layer is modified from [77] and described in Geoscientific Interpretations.

#### **4.3.5. Geoscientific Interpretations**

Geophysical results presented here help inform new insights on the geologic and geothermal setting at Lee-Allen. A significant addition to previous models is evidence of a major NW-SE striking structure, interpreted as a strike-slip fault consistent with Walker Lane tectonics, that bisects the study area (Figure 23, Figure 24, Figure 31). We interpret this feature to represent the RPF, as discussed in Geology, but extended further to the SE than suggested by earlier workers. Evidence of this feature is present in all three geophysical datasets. Despite these observations, there is little

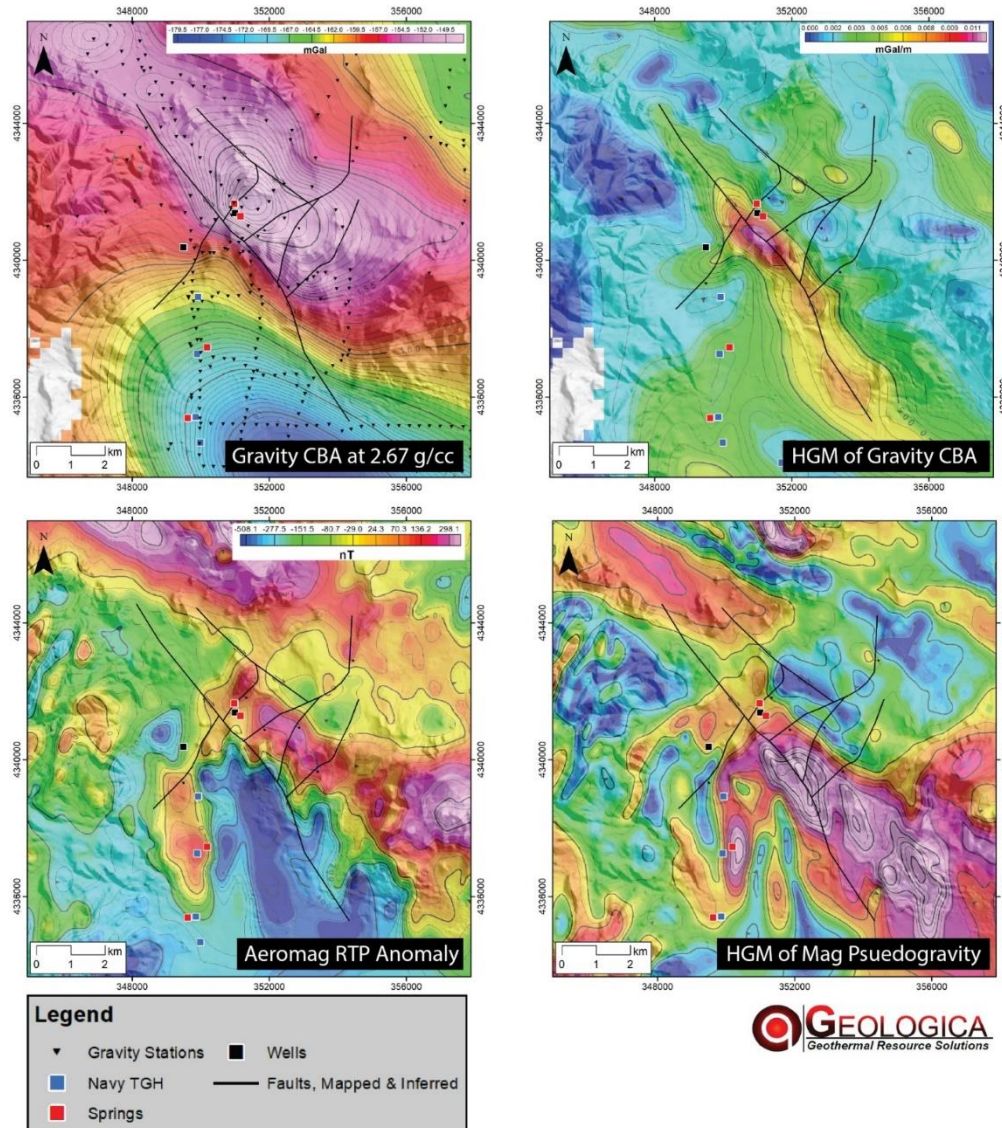


**Figure 30 Gravity and aeromagnetic data over the Lee-Allen Prospect, with springs, wells and interpreted fault layer modified from Hinz and others [42]. Note these maps show a more regional extent than other figures in this report. Upper left: Gravity CBA with gravity station locations (black triangles); upper right: Horizontal gradient magnitude of the CBA; lower left: Reduced-to-pole magnetic anomaly (RTP); lower right: Horizontal gradient magnitude of the pseudo-gravity transform of the aeromagnetic RTP.**

expression of this fault at the surface. This may be exacerbated by the presence of Pleistocene and younger shorelines and wind-blown sands. Figure 31 shows a simplified geologic map from [77] with an updated fault interpretation.

Other inferred faults remain largely unchanged. Neither the resistivity data nor the gravity data seem sensitive to NE-striking structures, such as the Lee-Allen fault, mapped by previous workers. Only the magnetic data suggests a major offset along the NW-SE feature (Figure 30, lower left panel). An apparent right step in this magnetic high lines up approximately with the inferred intersection of the Lee-Allen fault and the RPF.

In cross-sections through the MT model that are perpendicular to the strike-slip fault, a notable thickening of low-resistivity units occurs on the south side (Figure 31, lower panel). These units extend approximately 1 km in depth. This gives the impression of a sedimentary basin opening in this direction. In this case however, we conclude that the units comprising this low resistivity zone are Miocene age and older. Some of the basaltic andesite lava flows (Tba) found on both sides of the strike-slip fault have been dated at  $11.6 \pm 0.3$  mya, but are interlayered with ash flow tuffs, diatomite and fluvial gravels and sands (Hinz et al., 2008). Only a few hundred meters of Quaternary alluvium is expected to be present over Rawhide Flats to the south. Such units are expected to have lower densities and resistivities, and more readily alter in the presence of geothermal fluids and gasses. We conclude, based on the MT and the gravity, that these deposits are significantly thicker to the SW of the RPF. These thicker packages appear to taper off to the NW.

In contrast, sparse outcrops of Mesozoic diorite, limestones, phyllite and chert are found on the north side of the RPF and comprise the basement in this area (Hinz et al., 2008). Such units are expected to have higher density and resistivity values.

Above the cross section in Figure 31 are extracted values from the gravity CBA and the horizontal gradient magnitude of the CBA. The peak value of the horizontal gradient has been picked as the location of the RPF. Here we see that to the north of the strike-slip fault, bulk densities and resistivities are much higher than on the south side of this feature, illustrating a significant change in the rock properties that occur across the RPF at this location.

The cross-section through the MT model in Figure 31 is annotated with geologic interpretations and projected fault planes. The RPF marks a major transition in the resistivity structure. Lee Hot Springs, well 72-33 and virtually all the early drilling occurred in the resistive fault block north of the strike-slip fault, where only a thin veneer of low-resistivity units is found. The Navy TGH wells and well WW are the only wells sited on the south side of the strike-slip fault.

Located approximately 1.5 km south of Lee Hot springs, cross-section CM3 shows a shallow zone of low-resistivity ( $< 2$  Ohm-m) approximately 200-300 m thick, overlying an area of low-to-intermediate resistivity values (2-5 Ohm-m). We interpret this geometry to represent an argillic (smectite) clay cap that overlies a zone of geothermal upflow. The intermediate resistor below the cap is connected to an adjacent shallower embedded resistor (5-10 Ohm-m), first seen in the original HTEM line T49020 and below well WW (as plotted, which may be inaccurate). We interpret this embedded resistor to be a silicified zone that hosts geothermal outflow. This may occur within a more permeable and clay-poor strata such as a fluvial gravel, which would increase its bulk resistivity value.

#### **4.3.6. Conceptual Model**

Below is a list of key conceptual model elements followed by an in-depth discussion:

- Geothermometers estimate a reservoir temperature of 150 °C (P90)-190 °C (P10).
- An argillic clay cap south of the strike-slip fault (RPF) is inferred from resistivity data.
- Historic sinter deposits, extensive silicified sediments, and active thermal anomalies (thermal water discharge and 2-m probe) are present 1.5-2 km north of the interpreted argillic clay cap.

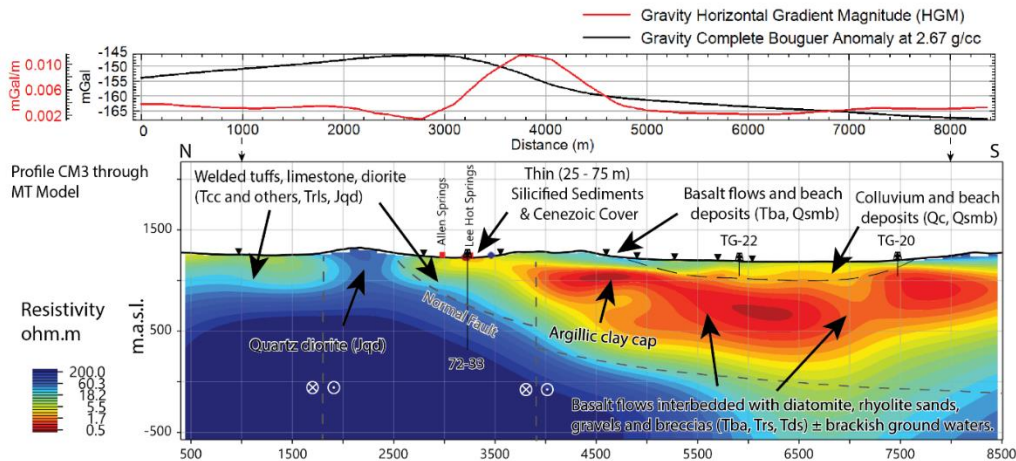
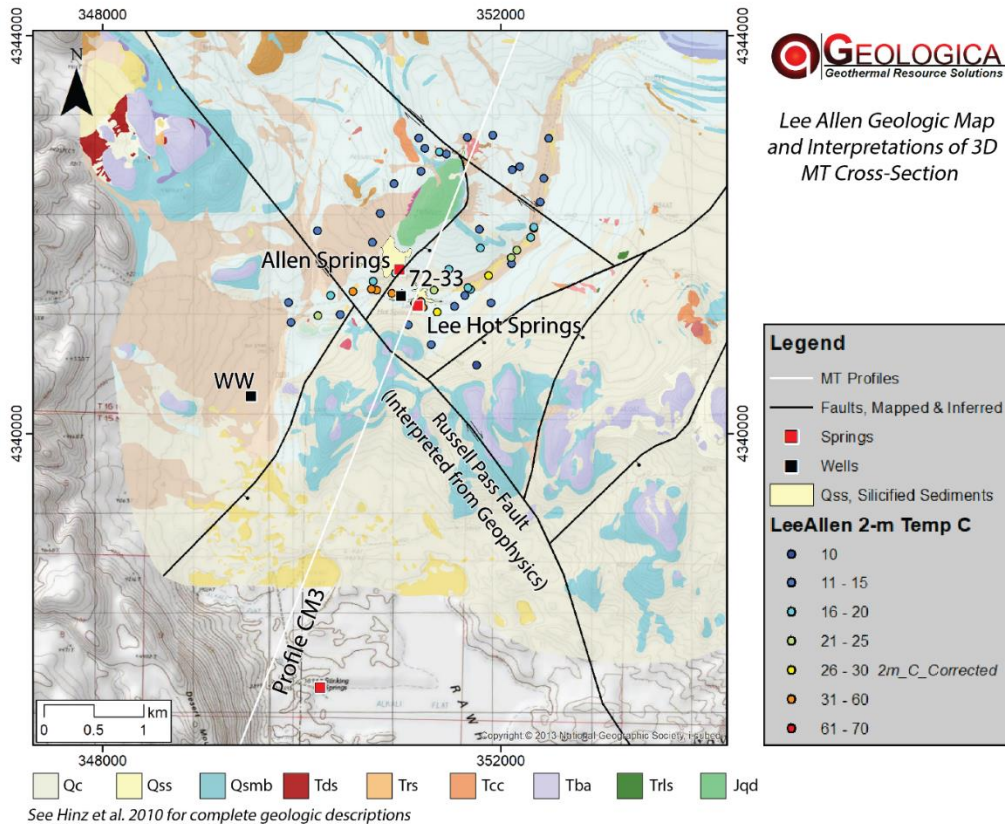


**Figure 31 Geologic interpretations at the Lee-Allen prospect (modified from Hinz et al., 2010a) with 2-meter temperature points, wells, and surface alteration. A NW-striking strike-slip fault (The Russell Pass fault) has been interpreted from Geophysics. Along profile CM3 (white line) a cross-section from the 3D MT model is annotated with geologic interpretations. Above the cross section, values extracted from the gravity CBA and horizontal gradient of the CBA are shown for reference.**

- An embedded resistor within a conductive background adjacent to the clay cap is inferred to be a silicified horizon that hosts geothermal outflow with potentially commercial temperatures.

- The Lee-Allen geothermal system is in a complex structure regime at the intersection of NE-striking normal faults and a NW-striking strike-slip fault, inferred by both geologic mapping and geophysical surveys.
- Despite reports of geysering, steam pockets and other indications of geothermal activity, drilling has yet to discovered deep commercial permeability on the north side of the RPF.

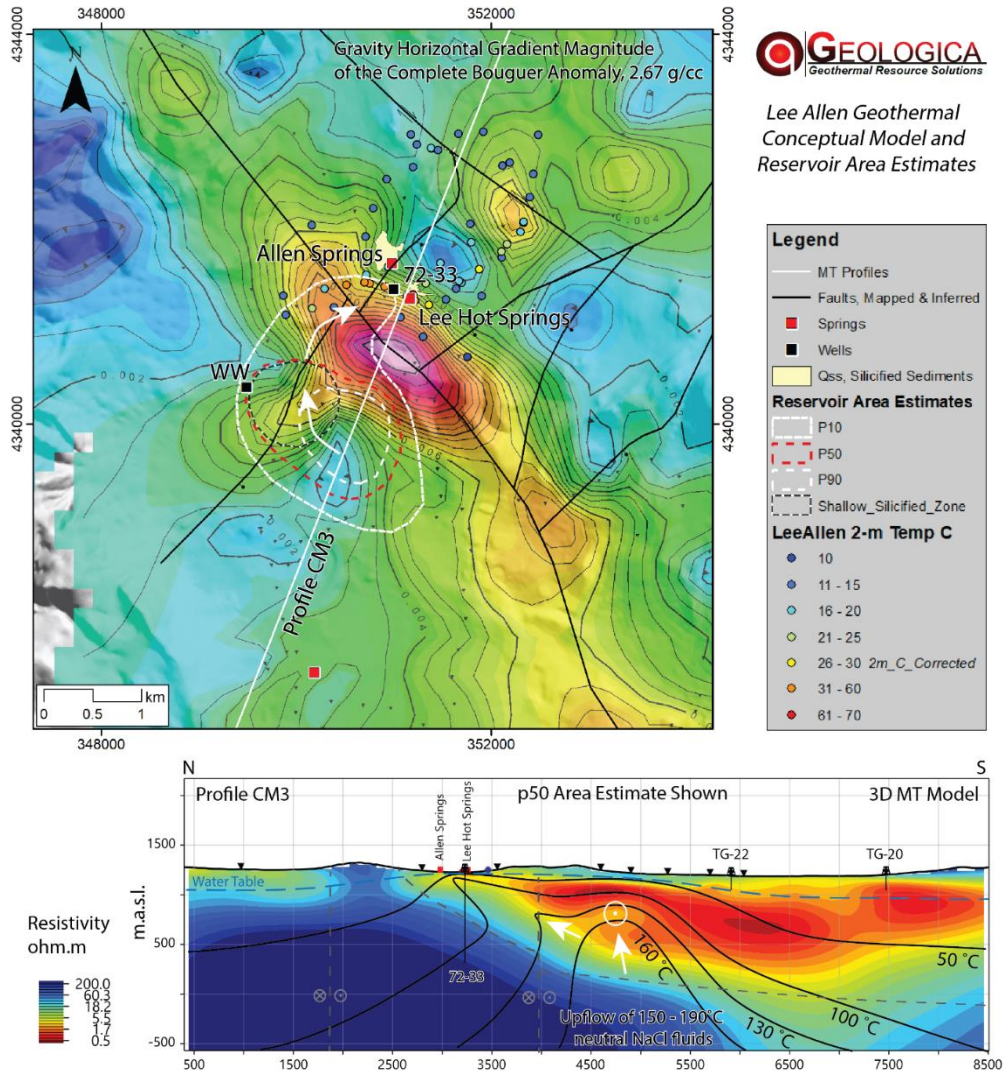
In this section we present a geothermal conceptual model of the system at Lee-Allen, with the intent that it can inform resource-capacity estimations (see Power Capacity Estimates) and future well targeting. This approach of conceptual model building generally follows methods described by Cumming [96], [15]. A key component of conceptual models are estimates of lognormal-distributed reservoir areas, which are shown as P90, P50 and P10 areas in map view. These estimates are guided by a multidisciplinary approach that considers all available geoscientific evidence and are constrained where possible by relevant system analogues from the Basin and Range province and elsewhere.

Figure 32 shows the conceptual model reservoir area estimates in map view as white and red dashed lines. Below this, cross-section CM3 shows inferred isotherms, flow arrows and other conceptual model elements representative of the P50 reservoir estimate. We infer that the upflow zone and most likely location for a 150-190 °C reservoir is hosted below the inferred argillic clay cap on NE-striking, SE-dipping normal faults or within a fractured fault block (bounded by the Lee-Allen fault or other NE faults that remain unobserved). The depth to commercial temperatures and permeability may be as shallow as ~600 m deep. The host rock in the upper portion of the reservoir is likely within Tertiary volcanic rocks that may be interbedded with ash flow tuffs and fluvial sands, gravels and breccias. Diatomite may also be present. Basement rocks likely occur at 800-1200 m deep and may host deeper portions of the system. The argillic clay cap likely acts as a hydrologic barrier, where thermal gradients are conductive throughout before becoming convective below.

**Table 6 Lee-Allen conceptual model estimates of reservoir area and resource temperature.**

Lee-Allen Conceptual Model Distribution Estimate					
		Pessimistic	Middle	Optimistic	
	P99	P90	P50	P10	P01
Reservoir Area (km <sup>2</sup> )	0.4	0.7	1.6	3.5	6.7
Reservoir Temperature (°C)	136	150	169	190	209

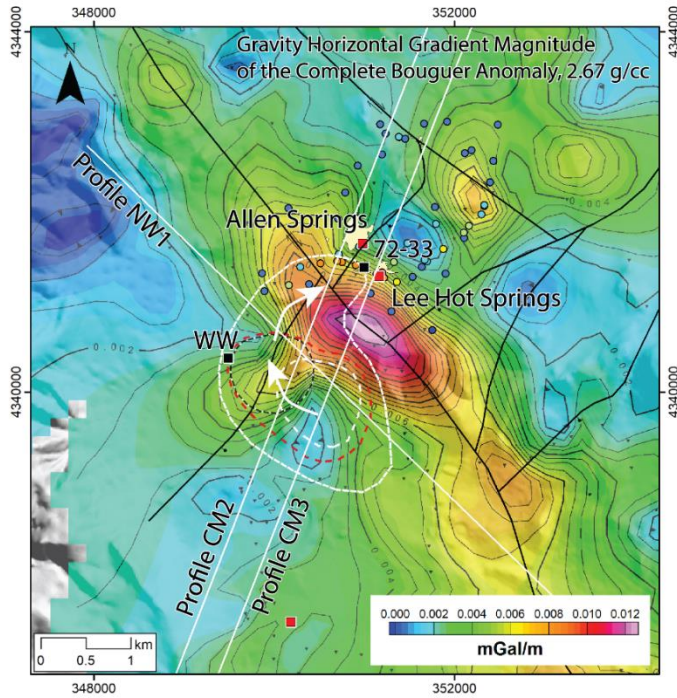
The system at Lee-Allen appears to host a shallow outflow reservoir with a complex 3D geometry. This feature is imaged as the embedded resistor in the MT model and is best seen in the two additional cross sections CM2 and NW1, shown in Figure 33. The embedded resistor is also imaged by HTEM line T49020 (Figure 22) and can be seen prominently in depth-slices through the MT model at 100-300 meters below the surface (Figure 29). This feature is noted graphically in map view with a black dashed circle and referred here as a “shallow silicified zone”. This feature is connected laterally to the inferred upflow zone below the clay cap on section CM3. In some geothermal fields, this type of outflow occurs below thin zones of advanced argillic alteration, but there is no evidence



**Figure 32 Conceptual model figure for Lee-Allen. Reservoir area estimates (P90, P50, P10) are shown in map view on top of the horizontal gradient magnitude of the gravity complete Bouguer anomaly. Inferred isotherms of the P50 conceptual model are shown on the 3D**

that this is occurring at Lee-Allen. Temperatures in the outflow zone at Lee-Allen remain unconstrained but could possibly be high enough to produce power from a binary power plant ( $\geq 130\text{ }^{\circ}\text{C}$ ).

We infer that hot, buoyant geothermal fluids rise under the imaged clay cap, and then move laterally NW and into the silicified zone. This outflow zone likely has a weak connection to Lee Hot Springs, where it rises and passes over to the north side of the strike-slip fault. Note that the 2-m temperatures increase significantly from  $\sim 26\text{ }^{\circ}\text{C}$  to  $\sim 40\text{ }^{\circ}\text{C}$  on the north side of the RPF, which may mark the point where these fluids come nearest to the surface. This flow may be channeled across the RPF by permeability within the crossing Lee-Allen fault. That would help explain losses at  $\sim 600\text{ m}$  deep in 72-33, which may have intersected the fault at that depth. It also explains why there are relic silicified sands found NE of Allen ridge,  $\sim 1.5\text{ km}$  away from the Lee Hot Springs. Some outflow may also flow directly from the upflow zone, along CM3 towards Lee Hot Springs. The



**GEOLOGICA**  
Geothermal Resource Solutions

Lee Allen Geothermal Conceptual Model  
Showing Inferred Outflow Paths

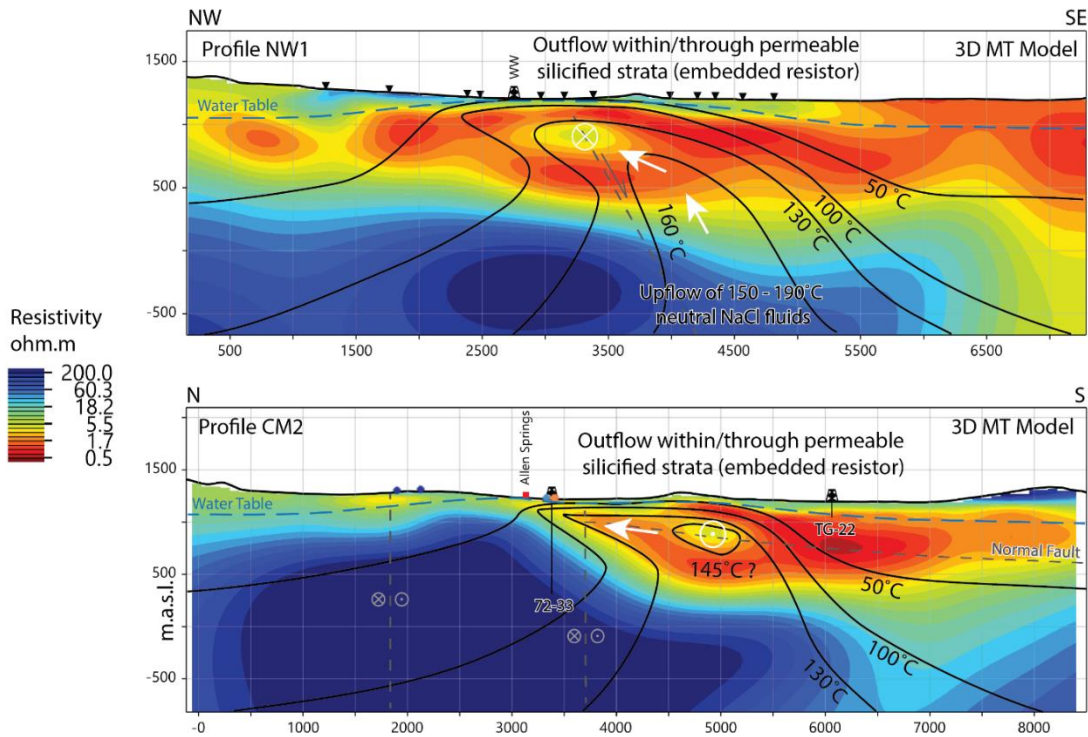
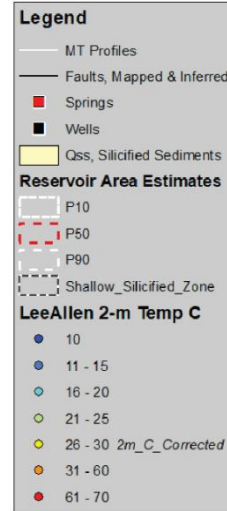


**Figure 33 Lee-Allen conceptual model along profiles CM2 and NW1 that intersect the interpreted outflow path of the geothermal system.**

inferred outflow path is shown with white arrows in the cross-sections in presented in Figure 32 and Figure 33. Note that a white circle with a dot in the middle denotes flow out of the page, and a white circle with a cross inside denotes flow into the page.

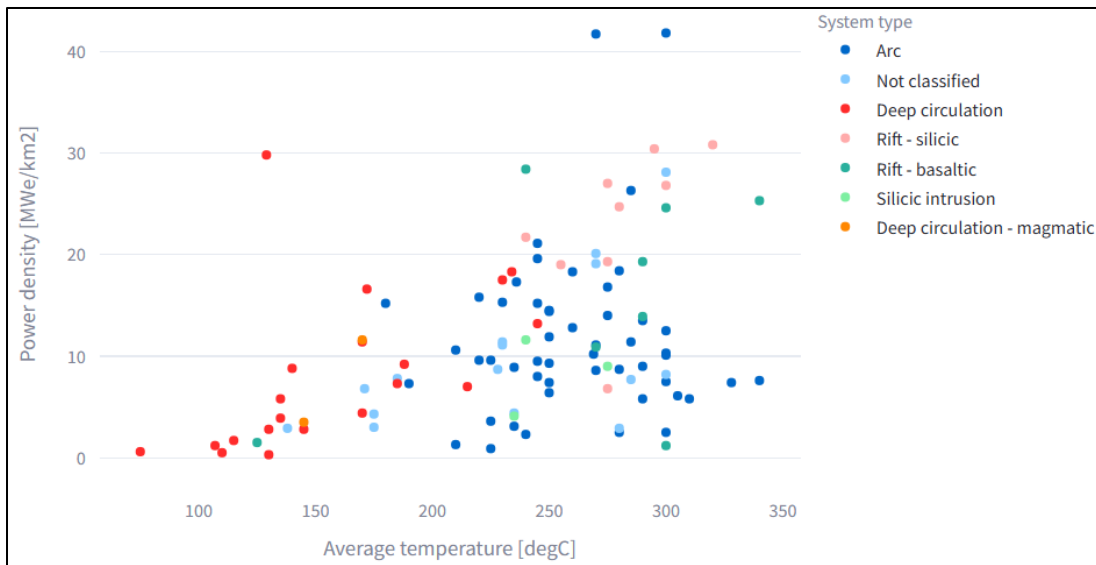


**Figure 34 Analogous Geothermal Fields in terms of power density (MWe/km<sup>2</sup>) and average temperature (°C), based on Wilmarth and others (2020). The red box denotes the range of these parameter applied to Lee-Allen.**

Fields with wells completed in shallow silicified formations that host outflow are fairly common in the Basin and Range and have been used for both production and injection purposes. These are well documented at Don A. Campbell [45], [64], [80] and San Emidio [63], [97], and it likely also occurs at the Brady's, Wabasca and Salt Wells geothermal fields, but are less well documented in these examples.

The nature of the outflow and its possible temperatures factor into the size and geometry of the reservoir area estimates. If the outflow hosts commercial temperatures, it should be considered part of the reservoir, but if not, then it should be excluded. This is addressed by including the entire silicified zone within the P10 (optimistic) and P50 (middle) area estimates but is excluded from the P90 estimates. There is also uncertainty in how far the system may lie to the south as the bottom of the conductor dips in that direction. The Navy well TG-22 offers a constraint in this direction, with its bottom hole temperature suggesting that it is not over the system.

#### 4.3.6.1. System Analogues

There are perhaps no known Basin and Range analogues that are bisected by a Walker Lane strike-slip fault in the manner that Lee-Allen appears to be. The Don A Campbell field, Wabuska and Blue Mountain each are believed to be hosted on displacement transfer zones, where strike-slip faults are linked kinematically to near-perpendicular normal faults [98]. East Hawthorne also appears to be hosted at displacement transfer zone (this report). In these cases, permeability is generally hosted on the normal faults or within silicified stratigraphic horizons.

The San Emidio geothermal system, north of Pyramid Lake in Nevada, is hosted on a major right step in normal faulting, along NE-striking normal faults. Despite the structural differences, it may be a good analogue in terms of the outflow geometry, temperature, size, and shallow stratigraphy. Like many fields in Nevada, the history of San Emidio started with wells drilled into a massive silicified shallow stratigraphy where permeability was easy to find, and temperatures were originally ~130°C. This zone was hinted at by overlying zones of advanced argillic alteration and silicified sediments.

These early efforts supported a small power plant and vegetable drying facility, but owing to the injection design, the resource quickly cooled. Only later was hotter (~150 °C), deep, fracture-hosted permeability discovered that supported a 14.7 MW capacity liquid-cooled power plant that remains online today [99], [97]. In 2023, a second air-cooled 25 MW facility came online with support from additional deep wells along the same major fracture system. One interesting characteristics of this field are that injection goes into a silicified Quaternary alluvial stratigraphy that is <200 m deep. Many of these wells target the same silicified horizons that were originally used for production and rapidly cooled. A second interesting characteristic is that the system hosts a ~5 km long, shallow boiling outflow plume that strikes due-north, parallel to the range front. This outflow path, and other silicified zones here were imaged using MT as embedded resistor similar to the feature at Lee-Allen [63]. One possible explanation for the unique geometry of the outflow at San Emidio is that it is hosted in Quaternary beach deposits and fanglomerates, which have high permeability. At both San Emidio and Lee-Allen, the landscape has been significantly altered by lacustrine deposits, and these features control much of the permeability distribution in the upper few hundred meters.

The geothermal system at Lee-Allen is similarly hosted on NE-striking normal faults, has shallow-to-intermediate outflow that channels towards a silicified horizon, and hosts a complicated outflow geometry where fluids rise and have produced a zone of extensive silicified sediments at the surface. The system at Lee-Allen may be ~10 °C hotter than San Emidio, but smaller in area. The effective proven reservoir area at San Emidio is 2-2.5 km<sup>2</sup> following the recent expansion, with an installed capacity of 39.7 MW.

#### 4.3.7. Power Capacity Estimates

The Power Density (PD) method involves multiplying a lognormal distribution of potentially productive resource area (km<sup>2</sup>) by the likely power density (MWe/km<sup>2</sup>) to yield a probabilistic estimate of resource capacity (P10, P50, P90; Cumming, 2016). The resource area estimates of 0.7 – 3.5 km<sup>2</sup> were derived from the key conceptual model elements. The power density was constrained using the net power generation per reservoir area (km<sup>2</sup>) of developed resources that are analogues for Lee-Allen (Figure 34) [100]. The power density range used is 5 - 15 MWe/km<sup>2</sup> and is based on developed analogue geothermal resources that have a similar temperature regime and have similar geologic properties. Using these areas and power density, the P50 capacity is estimated at 14 MWe net (Table 7).

**Table 7: Power capacity estimates for Lee-Allen**

Probability (%)	Reservoir Temperature (°C)	Resource Area (km <sup>2</sup> )	Power Density (Mwe/km <sup>2</sup> )	MWe Net
90	150	0.7	5	5
50	169	1.6	9	14
10	190	3.5	15	36
			<i>Mean</i>	<b>18</b>

#### 4.3.8. Recommendations for Future Work

The current state of exploration surface studies at the Lee-Allen prospect is relatively mature, and additional work may not advance the conceptual model significantly. One exception is the gravity

data, which is sparse SW of the RPF. A high-resolution gravity survey with <400 m station spacing on a regular grid may be able to better characterize the crossing NE-striking normal faults that are proposed to host upflow of the system here. A second exception is additional geologic mapping of bedrock exposures in the NE Desert Mountains, to both characterize dip domains and the distribution and characteristics of normal faulting SE of the Russell Pass fault zone.

The Lee-Allen prospect is at a point where some form of exploration drilling is the most effective next step to advance understanding of the system. This may include some form of lower cost drilling such as thermal gradient or core drilling. Such drilling would take care to note this history of artesian wells here, and the likely presence of a shallow boiling aquifer. Early objectives of this drilling would be to verify the temperatures, permeability, and nature of the silicified outflow zone, which may be capable of producing commercial temperatures or could make for an effective injection target. Drilling near the center of the P90 reservoir area estimate could constrain the nature of the inferred clay cap, possible reservoir temperatures, provide information on the nature of the reservoir rock type and may characterize controlling faults, should they exist.

The location of this prospect, which appears to straddle BLM and DoD lands may provide an additional barrier to development. It is difficult to imagine how the prospect could be fully developed without involving some land on each side. The status of the DoD lands as an active bombing range with unexploded ordinance obviously complicates the matter further. The best path to development for Lee-Allen may be through a collaboration between private and government agencies.

## **4.4. East Hawthorne Prospect**

### **4.4.1. Background**

The hidden geothermal system at East Hawthorne lies along the western and northwestern edges of the Garfield Hills, near the town of Hawthorne, NV. The system was first identified by [101] following a 2-meter temperature probe survey that discovered elevated temperatures to the southwest of the Garfield Hills. This was followed up with the drilling test hole HHT-2 (Figure 35), which encountered 60 °C fluids at 122 m deep, and experienced severe drilling losses. The geothermal gradient at HHT-2 is approximately 300 °C/km, more than an order of magnitude above background gradients.

In 2008 the Navy's Geothermal Program Office (GPO) initiated an exploration campaign that examined the geothermal resources across the Hawthorne Ammunition Depot lands. This effort included a large 2-m probe survey across the southern part of Walker Lake basin. The results of which expanded the anomaly in East Hawthorne previously discovered by [101] to the north, and discovered a zone with temperatures 2-8 °C above background [35]. These zones are contoured in Figure 35. Overall, this work revealed a shallow temperature anomaly ~8 km in length. Additional surface studies were conducted in 2009 including geologic mapping, geochemistry, geophysics and 3D modelling [102], [103], [104], [105], [106], [107]. These efforts culminated in a temperature gradient drilling program on both sides of the Walker Lake Basin, which delineated a large area in East Hawthorne with elevated temperatures and thermal gradients. In 2010, deep slim well HAD-1 was drilled just north of where the highest 2-m probe temperatures were observed and recorded 98.9 °C fluids and drilling losses at contact between smectite clay altered alluvium and quartz diorite. This contact was interpreted as a fault, based on the lithologic log, loss zones, the temperature profile, and thin section analyses [47], alternatively, this could be a depositional contact. Temperatures rolled over sharply, however, indicating that hot shallow fluids are moving laterally here. To date, no quality fluid chemistry samples of has been collected at East Hawthorne and thus aspects like geothermometry remain undetermined.

The BRIDGE Project took up investigation of the geothermal system at East Hawthorne in 2022. These efforts kicked off with an HTEM survey over East Hawthorne, collected along a 1 km spaced grid of survey lines. This was followed up with a 61-station MT survey over the same area (Figure 35). Results of these datasets are summarized by Sewell and others [10] and [9] East Hawthorne 2D Gravity Modeling Report. This was followed up by a novel joint-inversion of the two datasets was used to build a 3D resistivity volume over the prospect [9] East Hawthorne 3D MT + HTEM Joint Inversion Modelling Report. The BRIDGE project has since worked to develop a geothermal conceptual model on the prospect and recommendations for future exploration drilling targets. Those results are presented in this report.

### **4.4.2. Geology**

In this section, the geologic setting and local stratigraphic and structural framework of the East Hawthorne geothermal area are summarized to provide background for key geologic conceptual model elements. The map data is primarily from Hinz and others [103], [108].

#### **4.4.2.1. Geologic Setting**

The East Hawthorne geothermal area is located along the western margin of the Walker Lake domain of the Walker Lane fault system within the Basin and Range province [83]. This area has been subjected to extension associated with Basin and Range extension and strike-slip faulting

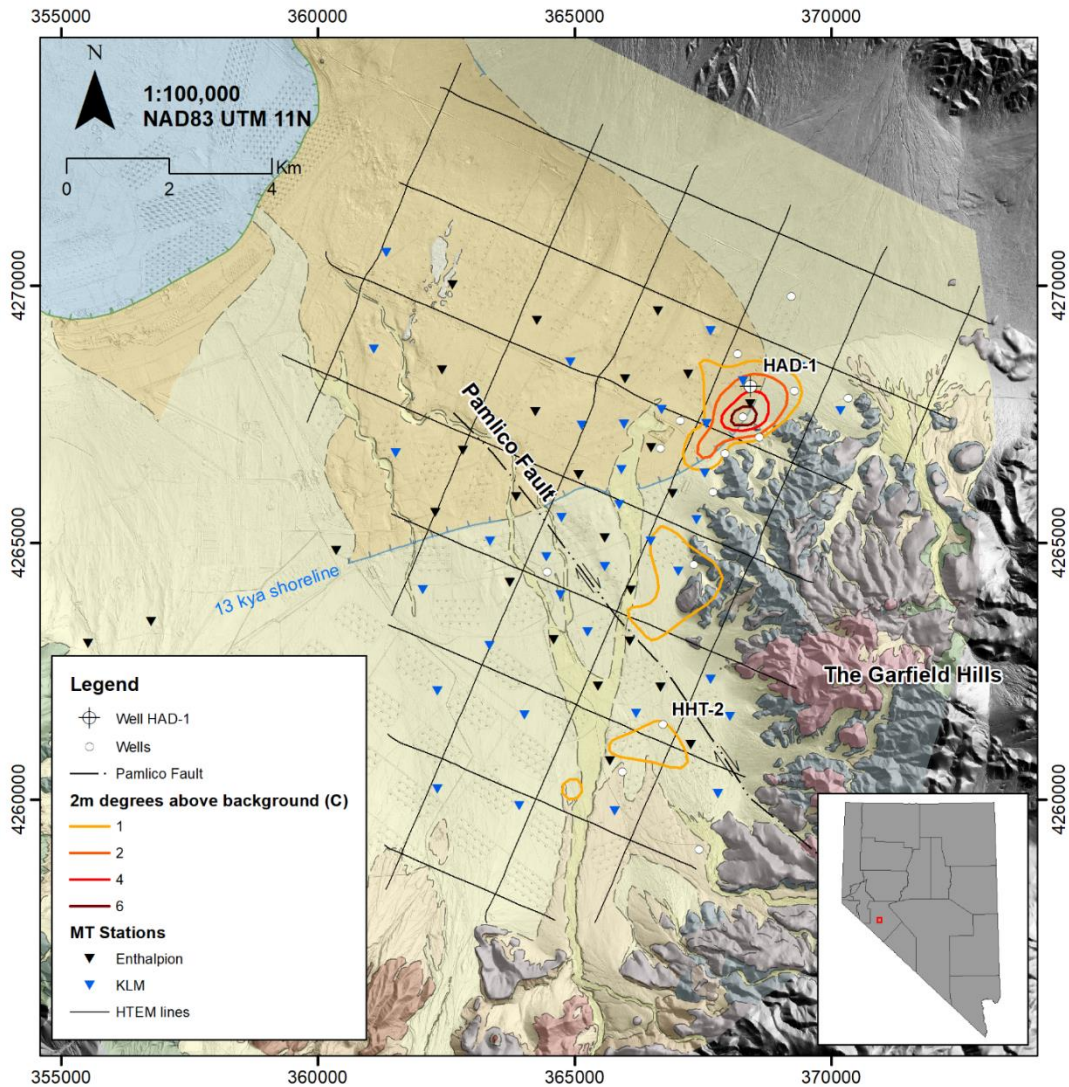


**Figure 35 Overview map of East Hawthorne study area. Geologic map simplified from Hinz and others (2010c). Map includes wells (white circles), MT stations (black and blue triangles), HTEM flight lines and contours of the 2-meter temperature probe degrees above background.**

associated with the Walker Lane. Locally, the East Hawthorne geothermal area sits along the southeast part of the Walker Lake basin, which is a west-tilted half graben bound on the west by the active Wassuk Range-front fault system (Figure 36, Figure 37). To the north and east of the East Hawthorne geothermal area are major NW-striking dextral faults of the Central Walker Lane. To the south of the East Hawthorne geothermal area are major ENE-striking sinistral faults associated with the Mina Deflection part of the Walker Lane.

In the region around the East Hawthorne geothermal area, extension associated with the Basin and Range began prior to the onset of development of strike-slip faulting associated with the Walker Lane. The Wassuk Range records rapid extension between 15 and 12 Ma with a second stage of extension beginning at ~4-3 Ma. Dextral shear associated with the Walker Lane migrated through the region between ~10 to 6 Ma with the largest magnitude strike-slip faults developing to the east of Walker Lake basin [83], [109]. Kinematically linked with normal faults, the dextral faults locally

reorganized concurrent with the renewed extension ~4-3 Ma [89], [109], [110], and synchronous with a pulse of activities documented along the Sierra Nevada frontal fault system at ~3 Ma (e.g., [111]).

#### 4.4.2.2. Local Stratigraphic Framework

The stratigraphic framework of the East Hawthorne geothermal area consists of Cenozoic volcanic and sedimentary rocks that rest unconformably on Mesozoic basement. The Cenozoic strata range 0 to 0.25 km-thick across the northwestern Garfield Hills and estimated 1.5 to 2 km-thick in the south-central part of Walker Lake basin west of the East Hawthorne geothermal area, based on 3D seismic, gravity, and well data (Figure 36) [103] and unpublished geochronology data, [112]. Four primary sequences of Cenozoic strata were distinguished across the southern part of the Walker Lake basin include from oldest to youngest [103]. Each of these four sequences are described below, including their likely distribution specific to the East Hawthorne geothermal area.

12. *Middle Miocene andesite lavas*: Porphyritic andesite lavas rest unconformably on Mesozoic basement in the southern and central parts of the Wassuk Range. Based on regional mapping, early Miocene fluvial gravels may locally be present along the base of these lavas, filling paleo-river channels [108]. The age of this sequence of andesite laves ranges from ~15 to 16.2 Ma [113] and places it just prior to onset of Basin and Range extension in this region. Although widespread in the Wassuk Range and in the Singatse Range farther west, it is unknown how extensive it is across the floor of the Walker Lake basin. There are small outcrops of this andesite in fault blocks immediately west of the primary active Wassuk Range-front fault trace (Figure 37). This andesite was not encountered in the slim wells HWAAD #2 and #3 in the West Hawthorne geothermal area, however these may have missed the andesite based on the geometry of the extensional fault blocks as interpreted by Ayling and Hinz [112]. Based on interpretation of 3D reflection seismic, ~0.5 km of andesite was interpreted at the base of the Tertiary strata in the southern half of the 3D reflection seismic data [103]. Porphyritic andesite is exposed in the axis of a faulted anticline in the southernmost part of the Walker Lake basin (Figure 37) where it likely sits underneath the Wassuk Group of fluvial-lacustrine sediments. The andesite is not exposed in the Garfield Hills and either was never deposited or was eroded prior to deposition of younger Tertiary strata. Based on geologic cross-section development (Figure 37), [108] interpreted the andesite extending under younger sediments in the subsurface in the East Hawthorne geothermal area, however, there are no local drilling data or map data that proves middle Miocene sits at the base of the Tertiary section in this area.

*Wassuk Group - Late to middle Miocene fluvial and lacustrine sediments*: The Wassuk Group [113], [114], [115], [116] consists of syntectonic fluvial-lacustrine sediments that consist of alternating sequences of conglomerate, sandstone, thin non-welded tuffs, and siltstone. Some of the siltstone contains abundant lenses of gypsum. These sediments are exposed in the Wassuk Range north of Walker Lake [113], along the southern margin of the Walker Lake basin (Figure 37), and between late Miocene lavas and Mesozoic basement in parts of the Garfield Hills. Locally, this unit contains coarse, angular, breccia that may be the result of major landslide collapse along major fault systems active at the time. This unit has been estimated to range from ~12 to 7 Ma, and has been documented to be 600-900 m in thickness north of Walker Lake and west of the Wassuk Range by [109]. Unpublished geochronology data from Hinz and others from tephtras interlayered in the Wassuk Group sediments in the southern part of the Walker Lake basin are ~9.5 Ma. Exposed thicknesses of this group of sediments reaches ~100 m-thick in the southern part of the Walker

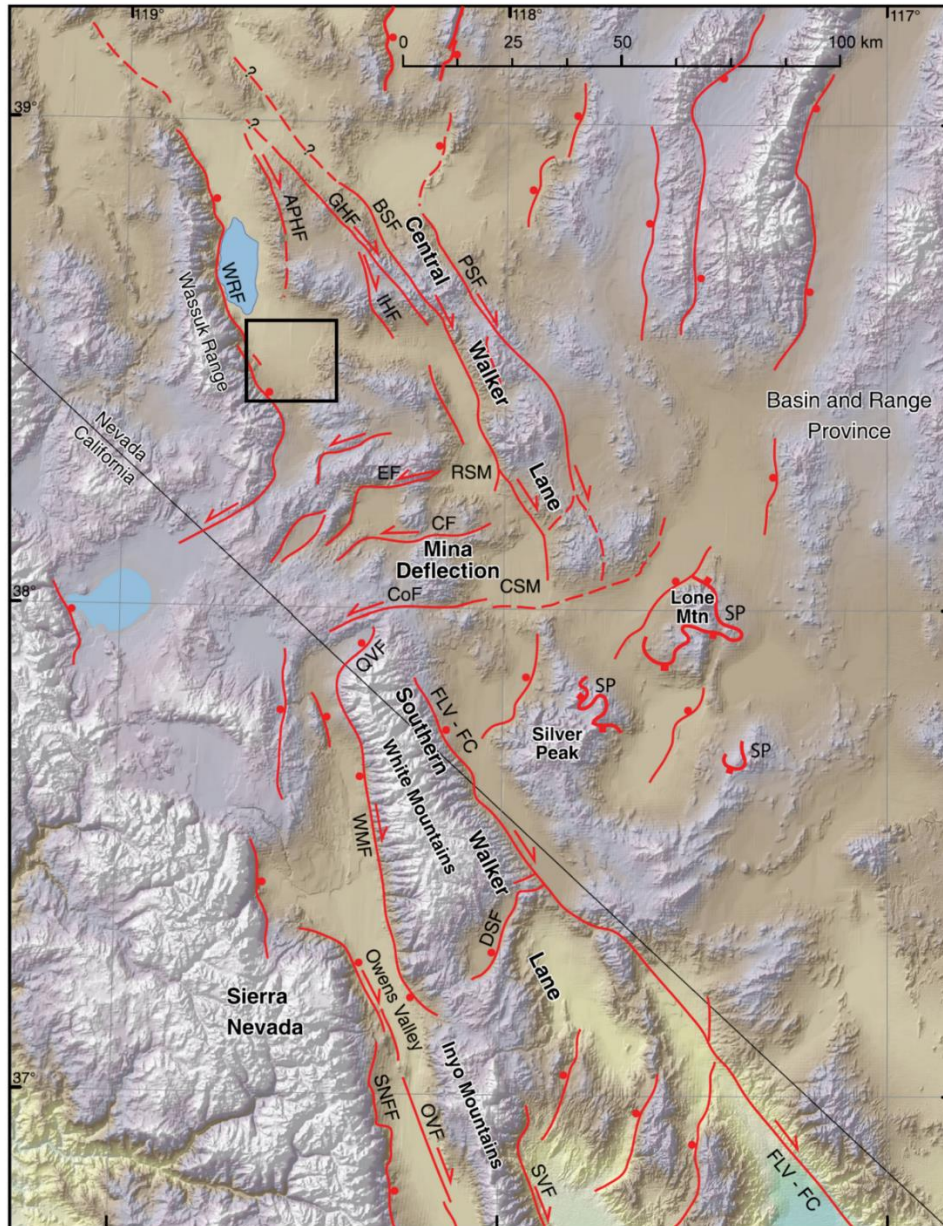


**Figure 36 Map from Faulds and Henry (2008) showing location of the East Hawthorne geothermal area (black box) relative to major active faults and Walker Lane structural domains.**

Lake basin, however, the base of these sediments is not exposed in the middle of the basin. The Wassuk Group sediments do thin eastward and pinch out under the overlying late Miocene sediments in the Garfield Hills. In the NW Garfield Hills, adjacent to the East Hawthorne geothermal area, the Wassuk Group (Ts and Tdm, Figure 37) fill small channels under the overlying lavas and make up of very minor component of the subaerial Tertiary strata exposed at the surface.

13. *Late Miocene basaltic andesite lavas and Mio-Pliocene(?) rhyolite domes*: Basaltic andesite lavas that have been dated at 7.8 Ma in the southern part of the Walker Lake basin (Hinz, unpublished data) and ~7 Ma norther of Walker Lake [113]. Surpluss and others [109] reports that these lavas rest along an angular unconformity with the Wassuk Group norther of Walker Lake,

however, south of Walker Lake, these lavas rest conformably on the Wassuk Group sediments and may be interlayered with upper-most Wassuk Group sediments in the Garfield Hills (Figure 37). These lavas reach about 100 m thick and are relatively widespread across the Garfield Hills (Tba). Outcrops of basaltic andesite locally rest on Mesozoic metamorphic basement directly adjacent to the East Hawthorne geothermal area. Many of the outcrops along the edge of the basin dip west  $\sim 20\text{-}25^\circ$  into the Walker Lake basin adjacent to well HHT-2, and dip NW  $\sim 30^\circ$  into the basin adjacent to well HAD-1. Locally, rhyolite domes (Tri) rest directly on the basaltic andesite lavas and reach up to  $\sim 300\text{-m}$  thick. These are not dated, and dips are generally conformable with the underlying basaltic andesite lavas. It is likely that rhyolite domes and basaltic andesite lavas are concealed beneath Pliocene to present basin fill sediments in parts of the East Hawthorne geothermal area.

14. *Pliocene to recent basin fill sediments:* Poorly to unconsolidated lacustrine and fluvial deposits are the dominant map unit exposed at the surface across the core of the East Hawthorne geothermal area. The thickness of the post 7 Ma sediments ranges up to at least  $\sim 100$  m thick based on drilling data. The distribution of Quaternary surficial deposits relative to fingers of bedrock exposure extending into the basin supports that if this margin of the basin is tectonically active, the slip rates are relatively low.

The Mesozoic basement exposed in the Garfield Hills consists of metavolcanics and metasediments, locally intruded by granitoid plutons (Figure 37). The metamorphic strata lithologies include basalt, volcanoclastic sandstone, rhyolite lavas and breccia, and limestone. Much of the metamorphic strata are moderate to intensely altered by relict Mesozoic magmatism. One pluton is exposed at the surface and another was intersected by well HAD-1 [47]. Detailed structural and stratigraphic mapping within the metamorphic rocks in the NW Garfield Hills has not been published (or completed?) in previous studies. Of the map data collected by [108], the formation dips within the metamorphic strata in the NW end of the Garfield Hills strikes NE with mostly  $20^\circ$  to  $70^\circ$  SE dips.

#### 4.4.2.3. Local Structural Framework

The Walker Lake basin is inferred to be a half-graben [103], bound on its western side by the Wassuk Range-front fault. Based on the distribution of tilted Miocene lavas in the Garfield Hills, the East Hawthorne geothermal area resides a short distance west of the hinge line that defines the eastern extent of the Walker Lake basin half graben. The northwest part of the Garfield Hills is intersected by a combination of NNW- to NNE-striking normal faults, NW-striking dextral and dextral-normal faults, NE to ENE-striking sinistral, sinistral-normal(?) and/or sinistral-reverse(?) faults, and folds that are dominantly ENE-trending. Several NE- to ENE-striking faults are high angle and are associated with stratigraphic offsets consistent with left-lateral motion. Although most of these NE- to ENE-striking faults are shown sinistral-normal or normal, some field observations support reverse motion on some ENE-striking faults and thus more of these may have reverse offset rather than normal offset. Reverse offset would be consistent with the sense of NNW-SSE oriented shortening accommodated by the folds.

Many of these faults have  $\sim 10$  to  $100$  m of stratigraphic offset. At least one can be inferred to extend into the basin based on gravity data and has previously been called the Pamlico Fault (Figure 37) [103]. An outcrop with exposed strands of the Pamlico Fault is shown in Figure 38.

Relative to the western and central parts of the Walker Lake basin the faults that have been mapped adjacent to the East Hawthorne geothermal area are not associated with many well-defined Quaternary fault scarps. A few of the ENE-striking sinistral faults were noted to be associated with possible Quaternary fault scarps during previous mapping [103] and unpublished data. Review of

Lidar data supports the field observations; however, the faults have not been revisited to reconfirm initial observations in combination with the Lidar data. At least one of the N-striking, E-dipping normal faults is associated with a likely fault scarp based on Hinz (unpublished data), and this is exposed just east of the published map area (Figure 37) [108].

There is no clear cross-cutting pattern between the dextral faults, normal faults, sinistral faults, and the folds. The ~7 Ma basaltic andesite lavas are folded the same degree as the underlying Wassuk Group sediments, supporting most of the folding begin in the Pliocene. The combination of NW-striking dextral faults, ENE-striking sinistral faults, ENE-trending folds, and ~N-striking normal faults supports overall ~N-S shortening and ~E-W extension. It is possible that all of these groups of structures remain relatively active in this area today and may reflect overall deformation patterns across the Garfield Hills.

The Garfield Hills is bound by the ~20 km-long, Holocene active, NW-striking, dextral Whiskey Flat fault along the southeast side, and is bound by the ~25 km-long, Holocene active, ENE-striking, sinistral Rattlesnake Flat fault along the south side. This combination of faults within the Garfield Hills near the East Hawthorne geothermal area, and the major faults the bound the area, supports that the Garfield Hills sits within a transitional area between the Mina deflection and Walker Lake regions of the Walker Lane as defined by others e.g., [83].

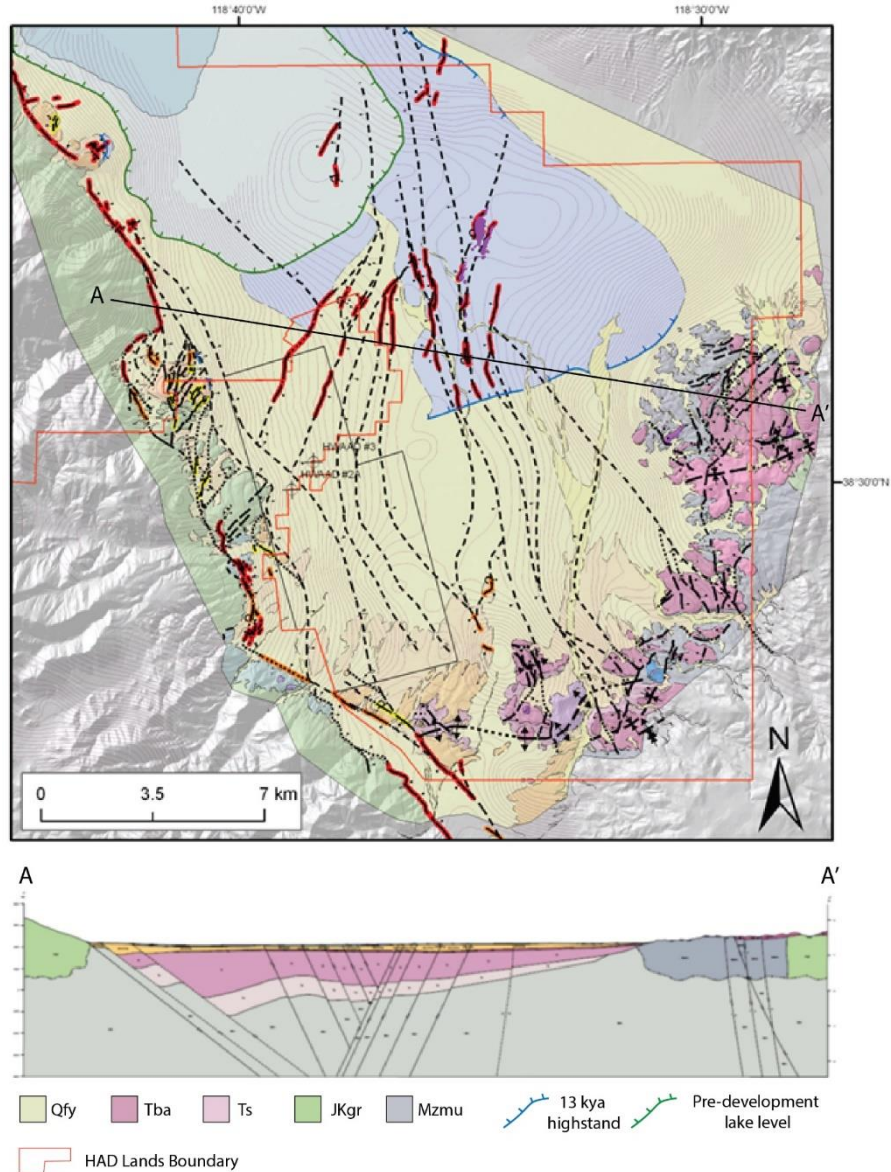


**Figure 37: Map and cross-section from Hinze and others (2010a): Semi-transparent geologic map draped over shaded relief image. Faults: highlighted red, Holocene; highlighted orange, Pleistocene; highlighted yellow, Quaternary undivided; dashed, inferred from subsurface and geophysical data.**

The Mesozoic basement is locally highly faulted and folded, with deformation predating Tertiary tectonic activity. These details are mostly not captured with existing mapping for areas of Mesozoic metamorphic or granitic basement within the study area.

#### **4.4.2.4. Alteration and Possible Surface Manifestations**

In the Garfield Hills, flanking the East Hawthorne geothermal area, Mesozoic metamorphic strata are mostly moderately altered with mixed clay to phyllic-propylitic alteration, including areas of pervasive silicification. This alteration is interpreted to be the result of alteration and mineralization halos around Mesozoic plutons. The Tertiary volcanic and sedimentary strata and Quaternary

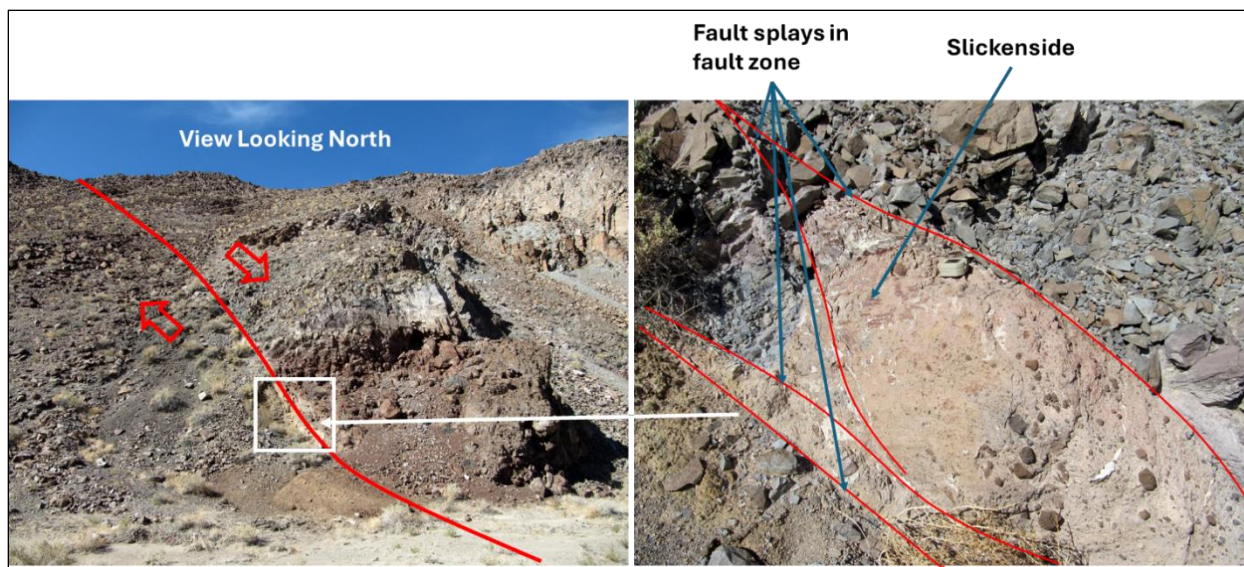


**Figure 38** Field photos of the Pamlico fault in the Garfield Hills.

surficial deposits that overlie the Mesozoic basement rocks are unaltered in and around the East Hawthorne geothermal area [103].

There are no known thermal springs or areas of warm or steaming ground within the Walker Lake basin. The only surface manifestations possibly related to geothermal activity in the southern part of the Walker Lake basin were observed in the form of massive tufa heads and colonies related to paleo-springs [103]. Exposures up to 8 m-thick of tufa were mapped coincident with Holocene fault scarps (Figure 37). These are located ~5 km NW from the primary East Hawthorne geothermal area and if related to geothermal activity, they may not be connected to the East Hawthorne system.

#### 4.4.2.5. Remaining Geologic Mapping Gaps

- The lithologic units in the Mesozoic metamorphic basement can be mapped out in detail (basalt, rhyolite, volcanoclastic sediments, limestone). This may provide additional details on Tertiary fault extent, geometry, and sense of motion, including if ENE-striking faults are normal-oblique or reverse-oblique, or both.
- Most of the Mesozoic metamorphic rocks are highly altered and the Tertiary volcanics and sediments are not altered. If some of the Tertiary volcanics and/or sediments in the northwest end of the Garfield Hills are highly altered, it is possible that these could have been misidentified as Mesozoic rather than Tertiary by previous mapping efforts [103].
- Field reconnaissance of possible Quaternary active faults in the northwest Garfield Hills to confirm fault recency and sense of motion (Figure 38).

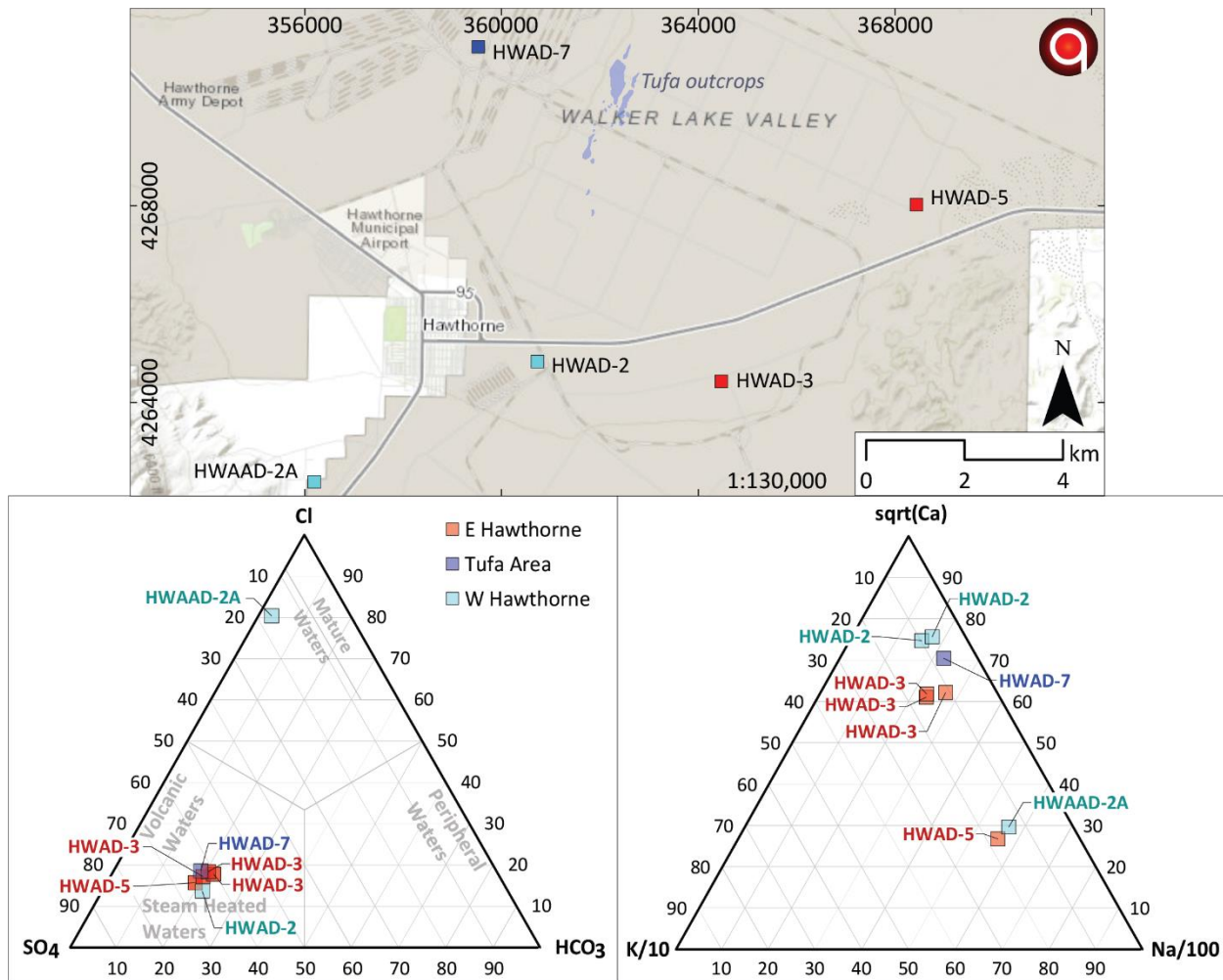


**Figure 39** Map (above), anion trilinear (bottom left), and cation trilinear (bottom right) for water samples from near the tufa outcrops in the central part of the valley, East Hawthorne, and samples from two select wells in West Hawthorne for comparison.

#### 4.4.3. Fluid Geochemistry

Geochemical analyses of waters samples for the East Hawthorne geothermal prospect area were sourced from the great Basin Center for Geothermal Energy database and a single sample collected by the BRIDGE project. All samples included here were collected from wells, generally classified into three different geographic areas: East Hawthorne, West Hawthorne, and the area in the central part of the valley near mapped tufa deposits. Analytical data from 4 samples from two wells in East Hawthorne, one complete analysis from a well near the tufa deposits were considered. Analyses of three additional samples from two wells in West Hawthorne, a separate geothermal system recognized by Ayling and Hinz [112], were also included for comparison. Incomplete analyses from an additional 88 samples from 22 wells near the tufa deposits were also considered in our evaluation but are not shown as they appear similar to the one complete sample from the tufa area (HWAD-7).

Analyses from a total of 96 samples were incorporated into a geochemical database and evaluated for completeness and quality. These data were evaluated by calculating charge balances and using mixing plots, trilinear plots (Figure 39), and geochemical equilibrium calculations such as

geothermometers (Table 8 and Figure 40). Water types were determined by major cation and anion chemistry seen in trilinear diagrams and the relative concentrations of each major analyte (Na, K, Ca, SO<sub>4</sub>, Cl, and HCO<sub>3</sub>) and then evaluated for temperature, TDS, and pH correlations. Geothermometers were examined for consistency, excluding significant outliers and water types for which that geothermometer is not applicable (e.g., those that plot outside of the “partial equilibrium” zone of Figure 40).

Of the total 96 samples added to the database for East Hawthorne, only 7 have complete data. These include two samples from West Hawthorne included for comparison, from wells HWAAD-2 and HWAAD-2A, four samples from East Hawthorne from wells HWAD-3 (3 samples) and HWAD-5 (one sample), and a single sample from the tufa area, HWAD-7. A second sample from HWAD-2 includes data for major anions (HCO<sub>3</sub>, SO<sub>4</sub>, and Cl) and some major cations (Ca and Mg but not Na or K). The remaining 88 samples, from near the outcrops of tufa, have major cation data (Na, K, Ca, and Mg) but lack any major anion data and therefore cannot be evaluated for quality. Charge balance percentages for samples with complete data are below 4% and most are below 2%, indicating relatively high-quality data. However, the sample that BRIDGE collected from HWAD-5, despite a charge balance of 1.56% indicating a good analysis, may not be a representative sample of the water sampled by the well. Despite attempts to stimulate and flow the well via air lift, little flow was recovered. Due to the low flow rate, it is not certain that a clean, representative sample was recovered.

Evaluation of the available geochemical data in the vicinity of East Hawthorne indicate that there are approximately three water types in the area:

15. Moderately high TDS (4300 mg/kg), neutral pH, high temperature (115 °C), NaCl water from well HWAAD-2A in West Hawthorne.
16. Moderate TDS (926 mg/kg), slightly alkaline (9.37 pH), warm (41 °C), NaSO<sub>4</sub> water from HWAD-5.
17. And likely moderate to moderately high TDS (600-900 and possibly >900), neutral (7-8 pH), and cool to warm (21-40 °C) Ca-SO<sub>4</sub> waters from the tufa area (HWAD-7), West Hawthorne (HWAD-2), and East Hawthorne (HWAD-3).

The neutral, high temperature, NaCl water from HWAAD-2A has typical geothermal water chemistry indicative of water-rock interaction facilitated by high temperatures (Figure 39). This

**Table 8: Select water sample temperatures, applicable geothermometers, and notes for waters samples from the Hawthorne Valley. Table colors correspond to the colors used in other figures in this section; red is East Hawthorne, light blue is West Hawthorne, and dark blue is the Tufa Area.**

Sample Name	Max. measured BHT (°C)	Sample Temp. (°C)	Quartz °C (Fournier & Potter, 1982)	Average Na/K (°C)	Na-K-Mg trilinear (°C)	Notes
HWAD-5	90	41.0	21	--	--	Well sampled during air lift; limited sample quality. Qtz temp. estimate lower than sample temp.
HWAD-3	40.8	34.0	106	--	--	Water immature; Na/K not applicable
HWAD-3	40.8	37.2	107	--	--	Water immature; Na/K not applicable
HWAD-3	40.8	40.8	106	--	--	Water immature; Na/K not applicable
HWAD-2	27.5	27.5	110	--	--	Water immature; Na/K not applicable
HWAD-2	27.5	27.5	110	--	--	Water immature; Na/K not applicable
HWAAD-2A	115.3	115.1	94	101	~140	Mature NaCl water from W Hawthorne
HWAD-7	unk.	21.0	155	118	~160	Likely conductively heated groundwater

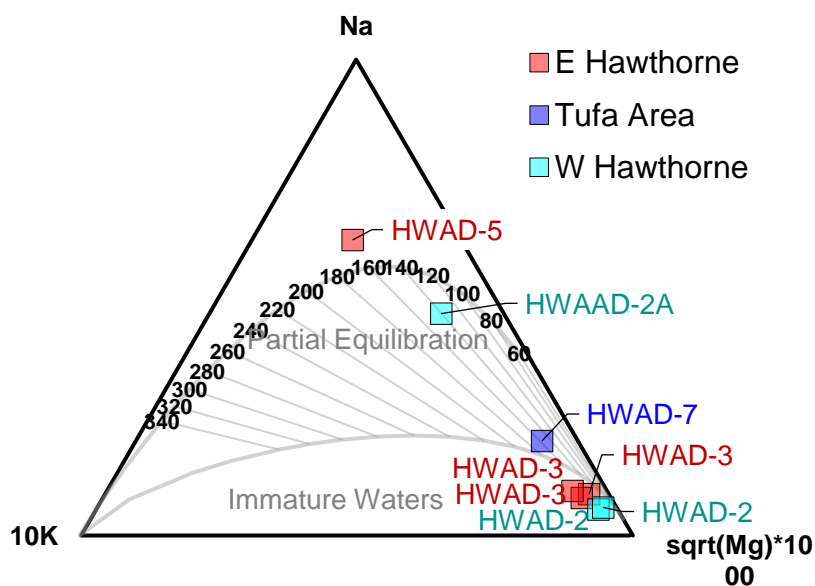


**Figure 40 Giggenbach cation geothermometer trilinear for samples in the Hawthorne area. Note that HWAD-5 plots outside of the partial equilibration zone and the majority of other samples plot in the “immature waters” zone.**

sample, collected by Ayling and Hinz [112]), was included as a representative of the geothermal system in West Hawthorne for comparison to East Hawthorne water samples. The second water type, from HWAD-5, plots closely with the  $\text{CaSO}_4$  waters of the third type on the anion trilinear (Figure 39, bottom left), but plots closely with the geothermal NaCl water from HWAAD-2A on the cation trilinear (Figure 39, bottom right), which may suggest similar mineral equilibrium but cations by themselves don't indicate geothermal fluids.. The remaining type of water, the  $\text{Ca-SO}_4$  waters, include samples from HWAD-3 (East Hawthorne), HWAD-2 (West Hawthorne), and the wells near the tufa outcrops (represented by HWAD-7, the only complete analysis from this area). Waters of the  $\text{Ca-SO}_4$  type appear to mainly represent shallow groundwater influenced by evaporite deposits in the basin rather than waters with a geothermal influence.

Geothermometer temperatures calculated from the Hawthorne water chemistry are limited. Reservoir estimations based on equilibrium between aqueous silica and quartz [92] and an average of Na/K geothermometers (averaging 6 Na/K geothermometer equations from the literature) are calculated, however, the cation geothermometers are only applicable for water chemistry within the partial equilibrium zone of Figure 40. Values for the samples for which the geothermometer is applicable as well as sample notes and sampling temperatures are shown in Table 8; none of the samples with chemistry within the partial equilibrium space of Figure 40 are within East Hawthorne area. Because the application of geothermometers for East Hawthorne is limited to silica geothermometers for HWAD-3 and HWAD-5, the estimated reservoir temperatures range from 21-107 °C. However, it is worth noting that the sample from HWAD-5 (21 °C) may not be representative and the samples from HWAD-3 (106-107 °C) are likely to represent shallow, conductively heated groundwater rather than waters from a geothermal system. As a result of these uncertainties, these data place very limited constraints on our understanding of temperatures at the East Hawthorne geothermal system.

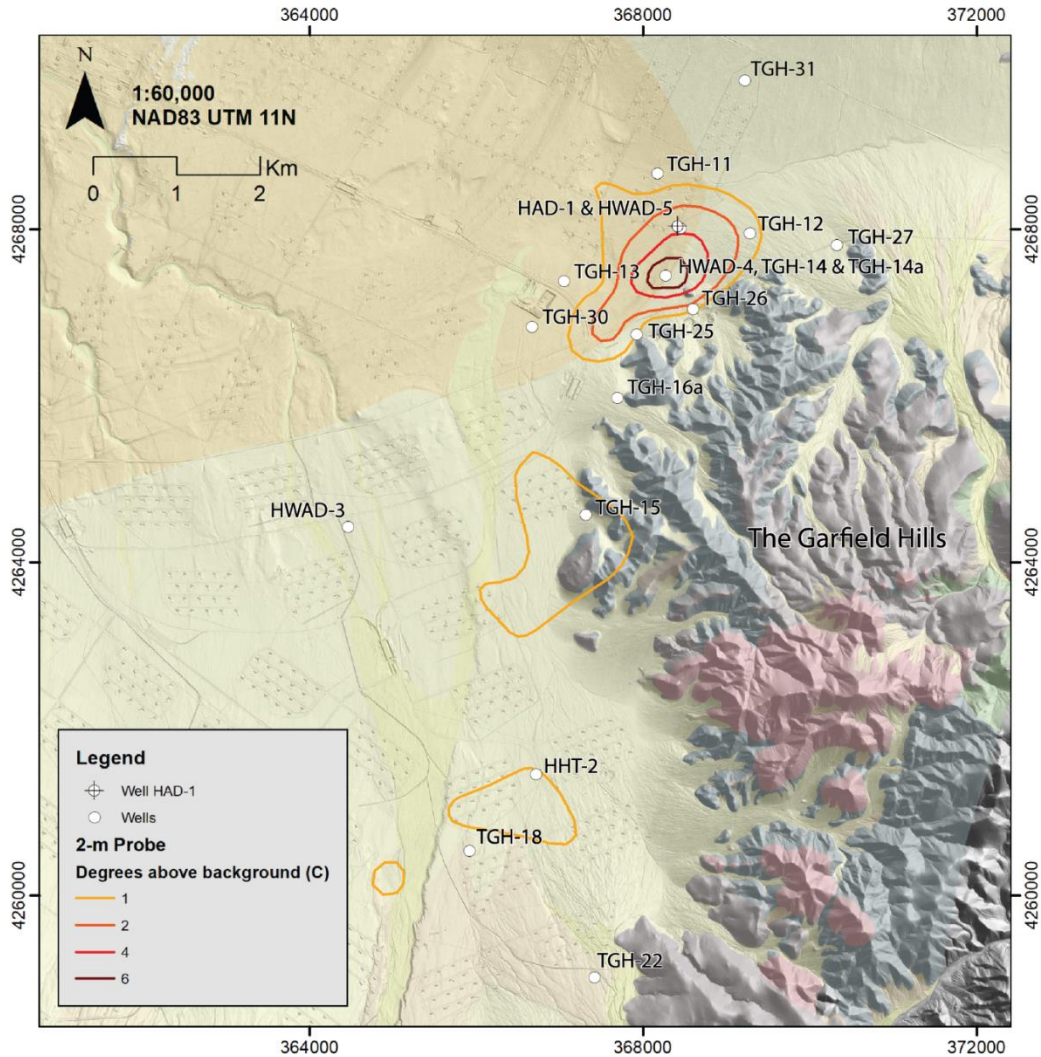


**Figure 41 Exploration wells drilled to date at the East Hawthorne geothermal prospect. 2-m degrees above background (DAB) is contoured, and geologic units are shown from Hinz and others (2010a). The background hill shade is from LiDAR and shows the locations of HAD infrastructure.**

Geothermometers for the select samples from West Hawthorne that were included for comparison include silica geothermometers for samples from HWAD-2 and both silica and cation geothermometers for HWAAD-2A. HWAD-2 has a silica geothermometer of 110 °C, while HWAAD-2A, as a mature NaCl water, has a silica geothermometer of 94 °C, and average Na/K geothermometer of 101 °C, and plots on the 140 °C trend on the Na-K-Mg trilinear. Waters from HWAD-2 are, however, similar to those from HWAD-3 and likely to represent conductively heated groundwater. In contrast, geothermometers from HWAAD-2A are more likely to be representative of the temperature of the geothermal system in West Hawthorne.

Waters sampled near the tufa outcrops are all likely to be conductively heated groundwater and are represented by HWAD-7; as such the geothermometer temperatures here should be considered with skepticism. HWAD-7 has a relatively cool sampling temperature of 21°C, but the silica geothermometer temperature is 155 °C, the average Na/K geothermometer temperature is 118 °C,

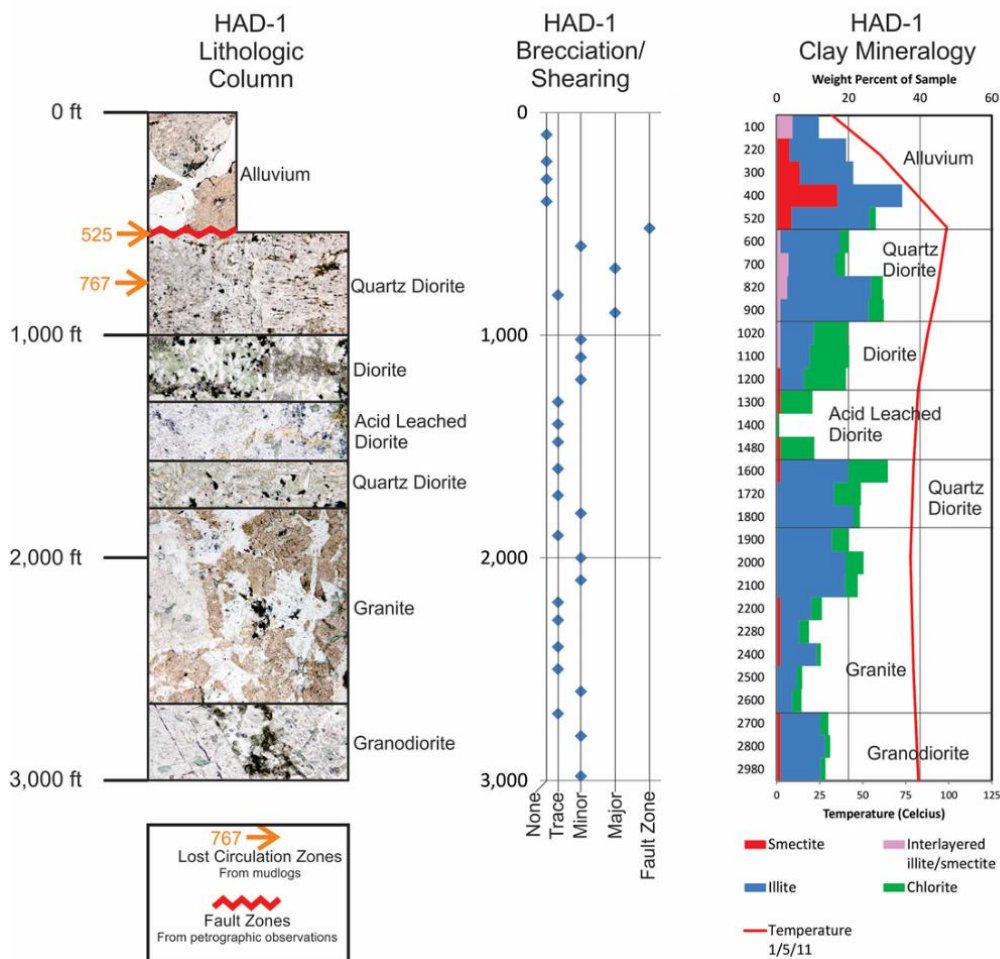


**Figure 42 Select well data observed from cuttings at well HAD-1. Left column: geology, inferred faults and lost circulation zones. Middle column: Qualitative degree of brecciation/shearing. Right column: Clay mineralogy from XRD, with equilibrated well temperature (red line). Figure includes content from Blake and others (2017) and Sewell and others (2023).**

and it plots on the 160 °C trend in Figure 40. If, perhaps, the waters in the tufa area are from outflow related to a geothermal system in either West or East Hawthorne, these values may have some meaning. However, as the geochemistry of the HWAD-7 sample indicates, this water is likely to be shallow groundwater influenced by evaporite deposits and there is little evidence to suggest a connection using the currently available dataset.

In summary, the geochemical data from East Hawthorne and the vicinity, including West Hawthorne and the area near the tufa deposits, provide limited information about a potential geothermal system at East Hawthorne. Most of the water samples are representative of shallow, possibly conductively heated groundwater that has interacted with evaporite deposits in the basin sediments. The exceptions to this are HWAAD-2A, which likely represents a mature NaCl geothermal fluid from the West Hawthorne geothermal system and is an outlier in the Hawthorne basin, and HWAD-5, which resembles HWAAD-2A in cations but the Ca-SO<sub>4</sub> groundwater samples in anions. Unfortunately, limited number of samples from East Hawthorne are unlikely to offer

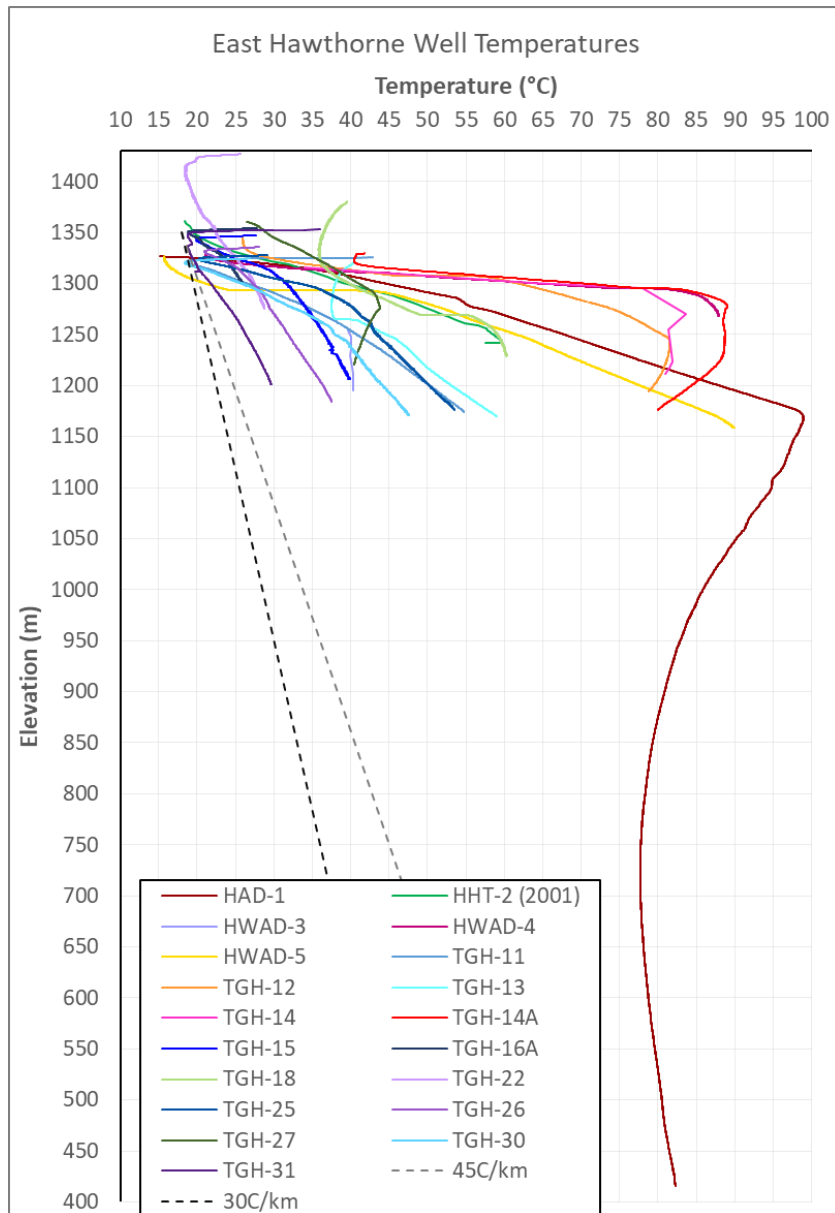


**Figure 43 Temperature-depth plots for East Hawthorne wells. 30 °C/km and 45 °C/km gradients are shown as black and grey dashed lines, as a reference to potential background values here.**

temperature constraints on this geothermal system due to 1) the immature nature of samples from HWAD-3; 2) the problematic low silica concentration, low Cl and relatively high Na in the sample from HWAD-5; and 3) HWAD-5 sample plots outside equilibrium in the Giggenbach trilinear (Figure 40). Should it be possible, additional sampling of available wells in the East Hawthorne area, such as the slim well HAD-1 (discussed further in the well section), HWAD-5, or future TGH drilled in the area, should be conducted for complete analysis to constrain the likely temperature of the East Hawthorne geothermal system based on geothermometers or the chemistry of the reservoir.

#### 4.4.4. Wells

Wells drilled to date at East Hawthorne are shown in map view in Figure 41. Equilibrated temperature-depth plots for each available well are shown Figure 43. The history of well drilling for

**Table 9 Well summary table for East Hawthorne**

Well ID	Longitude (NAD83)	Latitude (NAD83)	TD (m)	Date drilled	Max Temp. (°C)	Relevant Notes
HAD-1	-118.509644	38.550792	912.1	9/17/2010	99.0	Lithology data is available
HHT-2	-118.52825	38.491528	122.5	1982	59.9	
HWAD-3	-118.554657	38.517919	137.8	1952	40.8	- Alternate names: HAAD-3 and NAD-3 - A 2nd HWAD-3 was drilled in ~2010 in West Hawthorne.
HWAD-4	-118.51155	38.545681	>61.94	2010	88.0	An older HWAD-4 (previously called NAD-4) is in West Hawthorne
HWAD-5	-118.509631	38.550792	>168.99	2010	90.0	An older HWAD-5 (previously called NAD-5) is in West Hawthorne
TGH-11	-118.5130005	38.5567017	152.1	5/5/2010	54.8	
TGH-12	-118.500078	38.550383	151.7	5/18/2010	81.5	
TGH-13	-118.526001	38.544899	151.5	5/5/2010	59.0	
TGH-14	-118.5110016	38.5457993	152.4	2010	83.7	
TGH-14A	-118.51075	38.545689	153.7	5/20/2010	89.0	
TGH-15	-118.5220032	38.5196991	140.9	2010	39.8	
TGH-16A	-118.5179977	38.5323982	55.7	2010	26.0	
TGH-18	-118.5370026	38.4831009	151.4	2010	60.4	
TGH-22	-118.5199966	38.4696007	151.8	2010	28.8	
TGH-25	-118.5149994	38.5391998	152.2	2010	53.5	
TGH-26	-118.5080032	38.542099	152.7	2010	37.5	
TGH-27	-118.487999	38.5493011	151.5	2010	43.8	
TGH-30	-118.5299988	38.5399017	154.0	2010	47.6	
TGH-31	-118.5009995	38.5668983	152.4	2010	29.6	

East Hawthorne, including timelines and types of wells is listed below. The detailed findings from these wells are listed in the subsequent paragraphs.

- Pre-1981: Water wells (HWAD-3)
- 1981, Geothermal exploration (HHT-2)
- 2010, Geothermal exploration with TGH and slim well drilling (HWAD-4, HWAD-5, HAD-1, and TGH-series)

Well HAWD-3 is a water supply well for the ammunition depot and was first named HAAP-3. It was later renamed as NAD-3 and then renamed again as HAWD-3. It is unknown when it was drilled and is possibly anywhere from the 1930s when the ammunition depot was first established up until 1952 when there is the first recorded geochemistry sample collected (GDA, 1981). During sampling in 2001, the well flowed at 650 gallons per minute [117], however it is not clear under what conditions the well was flowed (e.g., pumped, artesian, etc.). The well was previously flowed by pumping in December 1980 and then a temperature survey was run immediately following flow and a maximum downhole measurement on December 4, 1980, of 40.3 °C at 138 m depth. Water table depth is unknown for this well.

HHT-2 was drilled in 1981 as a temperature gradient hole and was drilled into basin fill sediments without reaching volcanic or other rocks. The basin fill sediments contained abundant clay in the lower half of the well with clay was reported to range from 5 to 70% based on visual estimate and was encountered from ~60 to 120 m depth [101]. The well was completed with 3” pipe, capped at the bottom so it could be filled with water for subsequent temperature surveys, however it was noted in the first surveys that the tubing leaked, and water was only encountered 103 m depth in the 120 m deep well [101]. Trexler and others [101] only collected a temperature log in the part of the water well with water, over a 17 m interval. In the most recent temperature survey in October 2001, the water level inside the 3” tubing was intersected at 106 m depth [117]. The temperature log in 2001 acquired temperature data from ground surface to TD and showed a conductive temperature profile, ranging from 18 °C at the surface to ~60 °C at ~120 m depth.

Sixteen TGH wells were drilled at East Hawthorne in 2010 under direction of the Navy GPO to depths as great as 169 m. Three of these (HWAD-4, TGH14, and TGH-14a) were drilled on the same well pad and thus there are 14 separate TGH locations. The purpose of the TGHs was to explore the 2m thermal anomaly defined in 2009 and that built on a previous 2m survey and anomalously warm wells in East Hawthorne (HAWD-3 and HHT-2). These wells were such that two wells were drilled ~1-2 km south of HHT-2 and the rest were drilled ~3-6 km north of HHT-2 and targeted relative to a 2m temperature peak anomaly at the NW end of the Garfield Hills.

These TGH wells encountered maximum temperatures ranging from near 30 to 90 °C. All the temperature gradients are greater than ~80 °C/km which is above background for most of the Basin and Range (e.g., average is about 45 °C/km with some basins 50 to 55 °C/km), and thus the edges of shallow thermal anomaly at East Hawthorne were not defined. Wells with the coolest gradients include TGH-22 and TGH-31 which are at the south and north ends of the area covered by TGHs, so it is possible that the edge of the thermal anomaly is not far beyond these locations.

At the south end of the East Hawthorne area, TGH-18 encountered similar conditions to HHT-2. Based on correlating the water table from HHT-2, it looks like TGH-18 encountered a 60 °C aquifer. TGH-22 is ~2 km SE of TGH-18 and was drilled ~50 m higher elevation than TGH-18 and did not reach the water table. The gradient is slightly anomalous, but cooler than HHT-2 and TGH-22 and only reaches ~29 °C at ~147 m depth.

In the areas north of HHT-2, all the wells likely intersected the water table and encountered variable conductive gradients within the water table. Three of the wells or well clusters (e.g., HWAD-4, TGH-14, and TGH-14a) encountered reversals, supporting the existence of a shallow thermal outflow aquifer at or near the top of the water table. TGH-14a, sited at the location of the highest 2-m temperatures, encountered a maximum temperature of  $\sim 83$  °C and a temperature reversal at 1275 meters above sea level (masl). At a similar elevation, TGH-27 encountered a reversal with a maximum temperature of  $\sim 44$  °C, located  $\sim 2$  km east of TGH-14a. TGH-12 located between and slightly north of TGH-14a and TGH-27 also encountered a reversal with a maximum temperature of  $\sim 79$  °C, but at slightly lower elevation of 1240 masl. The highest temperature of the TGHs was in HWAD-5, located  $<1$  km north of TGH-14a with a maximum temperature of  $\sim 90$  °C at 1160 masl and a smooth conductive gradient to TD. This maximum temperature in HWAD-5 was about 115 m lower elevation than the reversal in TGH-14a.

Following TGH drilling program in 2010, slim well HAD-1 was drilled to 914 m deep just to the north of TGH-14a in late 2010. HAD-1 encountered 98.9 °C fluids at 167 m deep (1165 masl) at a contact between alluvium and quartz diorite (Figure 42). Drilling losses also occurred at this depth, and again at 234 m deep [47], [118]. It is not clear from these results if hot fluids are rising along this fault zone, or if they are flowing laterally along a depositional contact. XRD analysis of cuttings at HAD-1 confirmed that smectite clay alteration was present in the alluvial section above the fault zone. Below this, the alteration regime switches to chlorite and mixed-layer clays, interpreted as relict alteration. The smectite clay zones that overlie the near-boiling outflow were shown to correlate with zones of low resistivity imaged by the HTEM survey [10]. Hence, the shallow regions of low resistivity imaged here are confirmed to be of geothermal origin.

#### **4.4.5. Geophysics**

##### **4.4.5.1. Gravity and Magnetics**

Gravity data were compiled from the open-source dataset described by Ponce [94] and from two separate deployments collected by the U.S. Navy in 2001 and 2009 [119]. For this project, data were re-merged from the original files, terrain corrections were re-calculated digitally using LiDAR data, and the results were reduced to the complete Bouguer anomaly (CBA) using standard methods [120]. After editing some spurious points, a total of 998 gravity stations covers the southern portion of the Walker Lake Basin. The CBA, along with its horizontal gradient magnitude (HGM) and first vertical derivative (1VD) are shown in panels A-C of Figure 44.

Aeromagnetic data was clipped out of the GeoDAWN dataset collected by the USGS [16]. In this region, line spacing is 400 m and the mean terrain clearance was 237 m above ground. Flight lines were oriented east-west. The reduced-to-pole magnetic residual (RTP) is shown in panel D of Figure 44.

Gravity data were forward modelled along two profiles, “CM1” and “CM2”, which are roughly perpendicular to gravity contours. A version of the gravity data reduced at 2.67 g/cc was used for modelling purposes. Modelling was performed using the GM-SYS program within Oasis Montaj software. This program calculates the gravity forward response based on the methods of [60]. On each line, very limited well data were used to constrain the depth of basement, and the 3D MT model was used as a backdrop to inform a joint interpretation. The density of alluvium increased slightly with depth and the basement is modelled at 2.67 g/cc. The objective of this model was to quantify the depth to dense basement rocks, and to estimate fault offsets on the Pamlico and NE-striking normal fault(s) that parallels the Garfield Hills. Extracted horizons from these models are

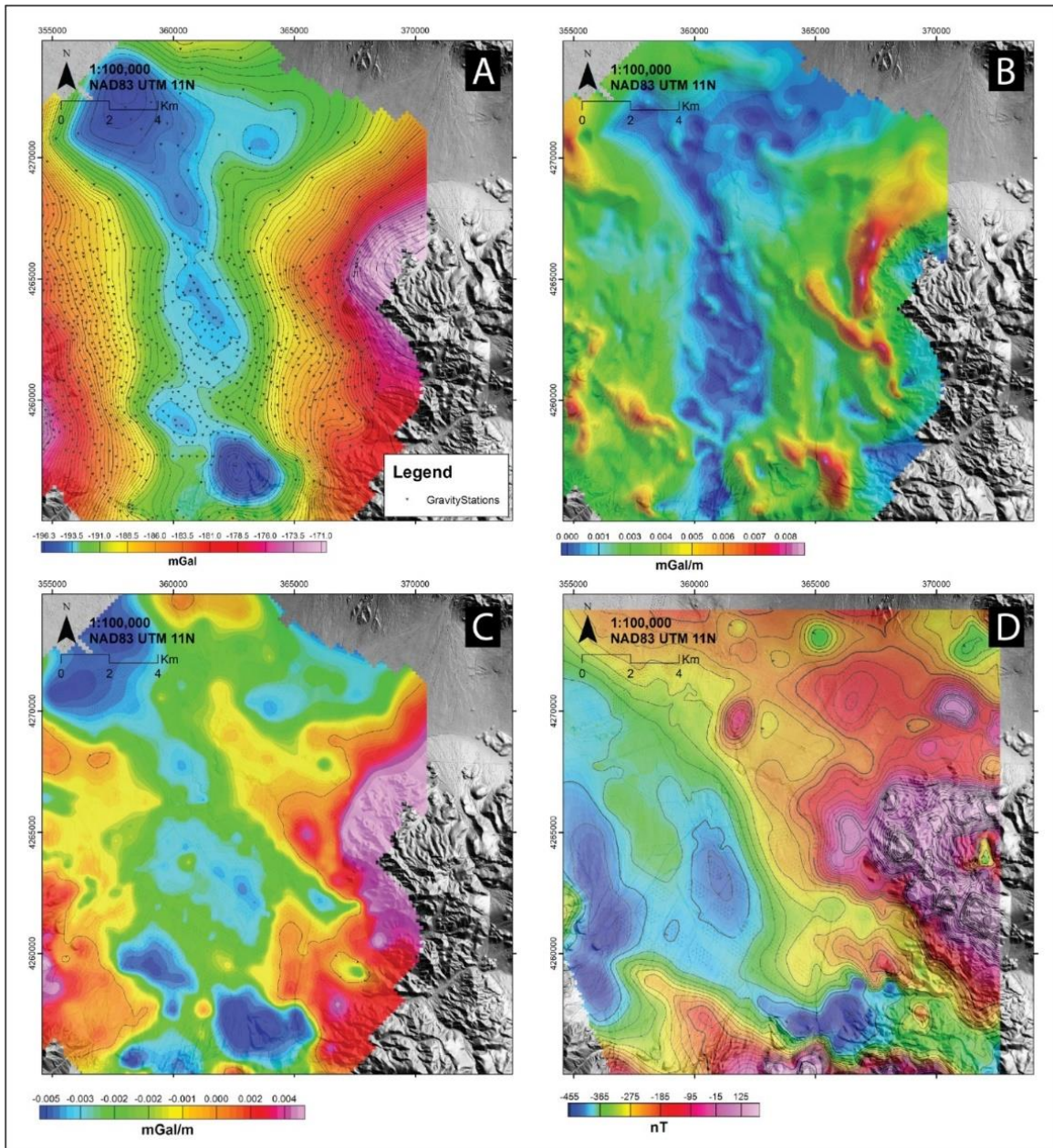


**Figure 44 Gravity and magnetic data over East Hawthorne. Panel A: Complete Bouguer anomaly (CBA) reduced at 2.45 g/cc and gridded at 150 m, with gravity station locations shown as small triangles. Panel B: Horizontal gradient (HGM) magnitude of the CBA. Panel C: First vertical derivative (1VD) of the CBA. Panel D: Reduced-to-pole magnetic anomaly (RTP) from the GeoDAWN dataset (Glen & Earney, 2024).**

shown in Figure 47. These modelling efforts are described in more detail by [9] Hawthorne 2D Gravity Modelling Report.

#### 4.4.5.2. HTEM

HTEM data were collected along 1,877 line-km in the western Basin and Range. 2 km line spacing was considered adequate for prospecting purposes and enabled a large area to be surveyed for reasonable cost. One downside to the large line spacing is that the results cannot be contoured in

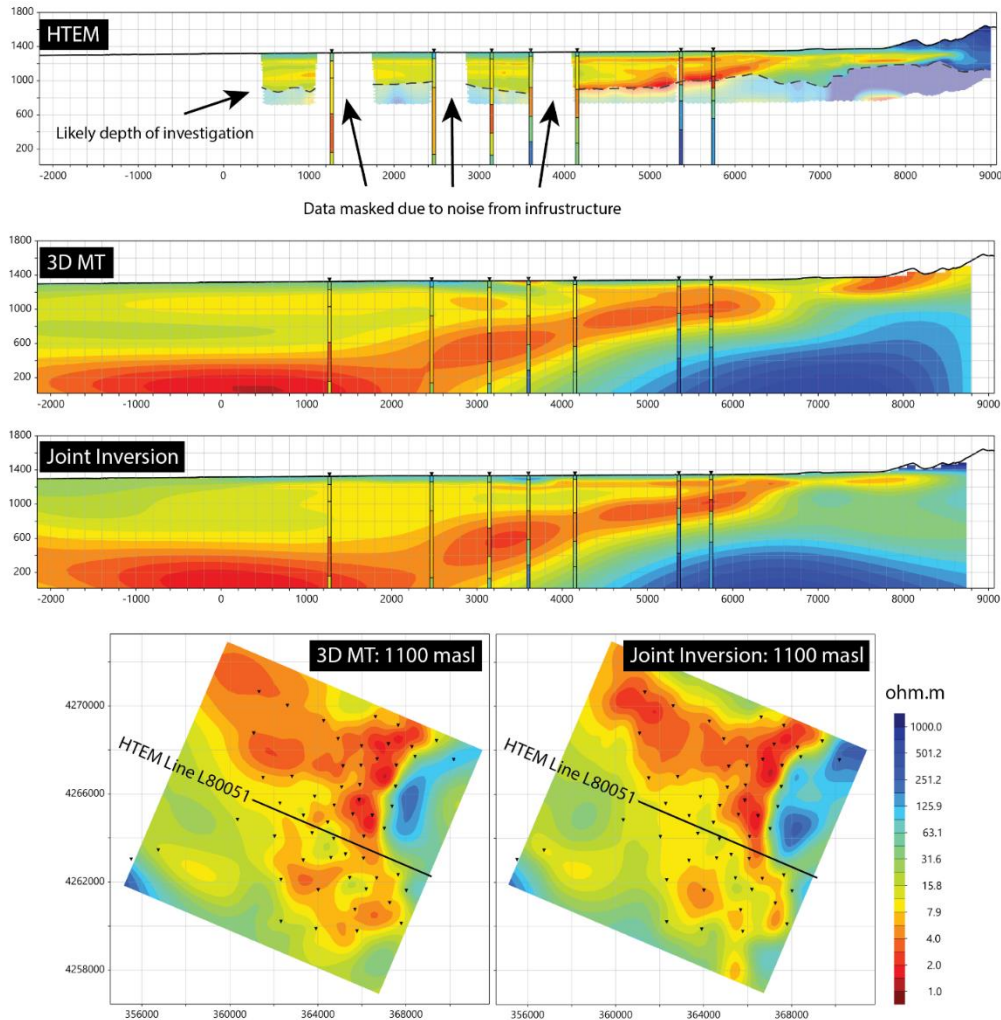


**Figure 45 A comparison of the modelled resistivity results from 1D inversions of HTEM data, a 3D MT inversion, and a fully 3D joint inversion of MT and HTEM data.**

plan-view without severely aliasing features. Lines were chosen to be perpendicular to structures. In the East Hawthorne area only, tie-lines were spaced equally at 2 km (Figure 35).

HTEM data were contracted through Xcalibur Multiphysics using their HELITEM™ system. This system deployed a 962 m<sup>2</sup> loop with four turns of wire. A 7.5 Hz, 146 A current with 50% duty cycle was transmitted to the coil. Returns were measured in 25 time-gates at a central-loop, multicoil (X, Y, Z) receiver. An independent magnetometer was also deployed just aft of the receiver coil. Flight speed averaged 110 km/h with an average sensor height of 35 m.

Laterally constrained, 1D deterministic inversions of the HTEM data were carried out by the USGS using the Aarhus Workbench Airborne TEM module. The depth of investigation was determined, which is an estimate of the depth at which the modelled results can resolve the resistivity structure given local signal and noise levels [93]. This is shown in the HTEM figures in this report as a

transition from opaque to transparent color scales. Note that this depth is variable and dependent on the overlying resistivity values. In areas with near surface conductors, the depth of investigation is decreased.

In many areas at East Hawthorne, noise from anthropogenic sources such as railways, ammunition bunkers, power lines and buried utilities caused problems with the results. These issues are generally easy to identify and present themselves as localized early-time transients in the receiving coil. Care was taken to edit these points prior to modelling, which results in blank strips in some of the models (see Figure 45 for examples of these blank strips). Induced-polarization (IP) effects are also present in the data, which can occur in strong central-loop TEM systems. This effect causes rapid decay of transient voltages followed by a polarity reversal [121].

#### **4.4.5.3. MT**

MT data were collected in two phases. In the first phase, Enthelption Energy collected 26 sites in 2022 using customized 32-bit receivers, custom magnetic field sensors and PbCl non-polarizable electrodes. Each station recorded vertical magnetic data. Stations were left to record for two nights each and recorded simultaneously with two sets of remote reference coils at distant locations. A ‘far’ remote was operated in northwestern Oregon, and a ‘local’ remote was installed approximately 70 km east of the survey center. All data were processed using dual-remote references, which is an approach designed to reduce the impact of geomagnetically induced currents in grounded power transmission lines. The contractor noted, however, that there was little evidence of bias in the results due to these sources. Final transfer functions include MT responses from 440 Hz-0.00055 Hz. In a second phase, KLM Geoscience was commissioned to add 35 MT locations to the original grid, reducing the station spacing to ~800 m. KLM deployed Phoenix RXU-8A receivers, MTC-155 broadband magnetic sensors and Cu-CuSO<sub>4</sub> porous pot electrodes. Vertical magnetic data was not collected. Each station collected data overnight and each were recorded simultaneously to a single remote reference station located 20 km to the east of the survey grid. Final transfer functions include MT responses from 10,000 Hz-0.001 Hz.

#### **4.4.5.4. Full 3D HTEM – MT Joint Inversion**

An initial 3D resistivity model was created for East Hawthorne using only the MT data, which enabled a direct comparison with the HTEM results [11]. This MT-only model was used as a starting point for a single-domain, joint inversion of both the MT and HTEM datasets, which resulted in improved resolution in the near surface, and removal of some near-surface artefacts [9] 3D MT + HTEM Joint Inversion Modelling Report, East Hawthorne. A side-by-side comparison of the resistivity results from the HTEM data, 3D MT model, and the final 3D HTEM-MT joint inversion is shown in Figure 45.

The initial 3D MT model was constructed using the RLM-3D inversion code and Geotools software. The inversion was performed on a rotated mesh that aligned with the HTEM flight lines and was approximately perpendicular to structures. The mesh accounted for topography and the starting model for the inversion was assigned a homogeneous value of 20 Ohm-m. A total of eight inversions were ran to explore the inversion space, achieve an acceptable RMS error data fit, and determine suitable inversion parameters.

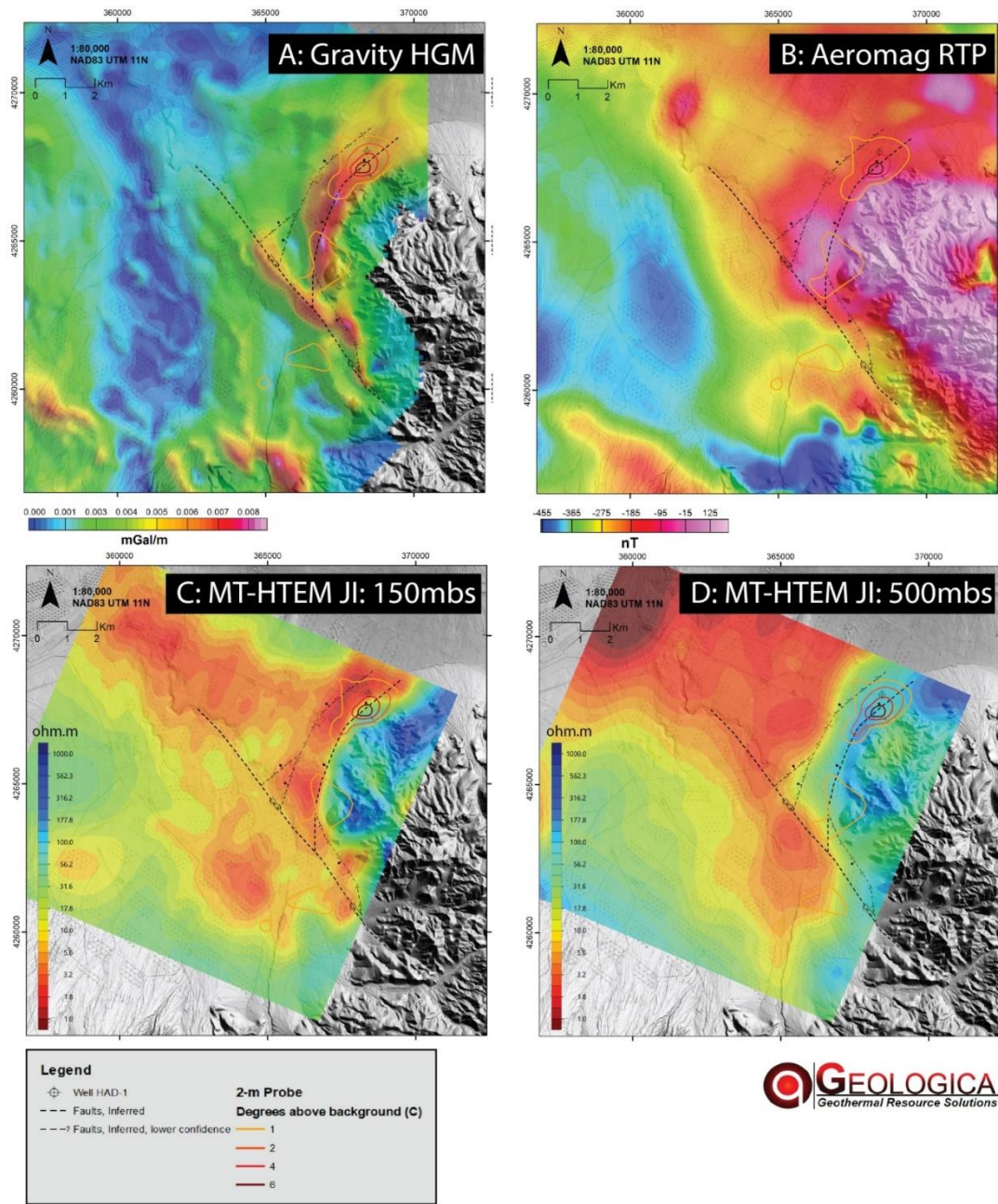
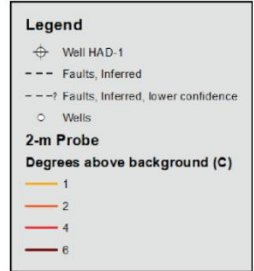
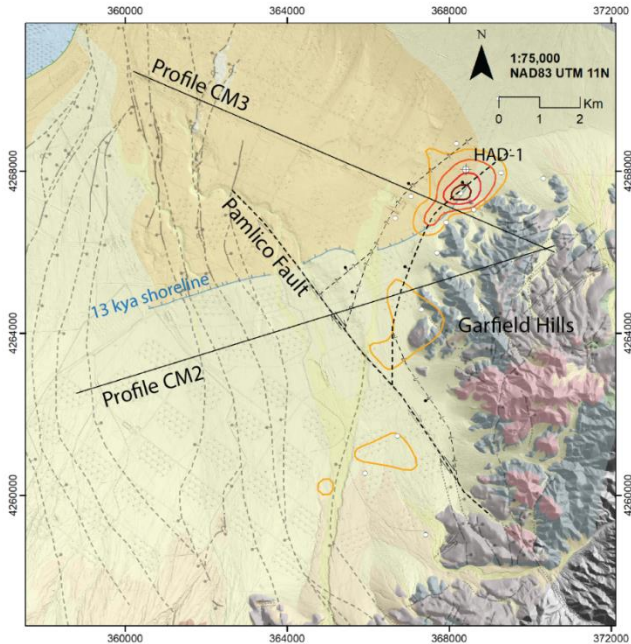


**Figure 46 Structural interpretation shown on different geophysical data layers. Panel A: HGM of the gravity CBA. Panel B: Reduced-to-pole aeromagnetic data. Panels C and D: Depth slices through the joint inversion resistivity models at 150 and 500 meters below surface, respectively.**

A new workflow was then applied to generate a joint inversion of the MT and HTEM datasets. HTEM data were edited and handled locally using Viridien’s Otze Airborne Tool. The inversions were run on the Viridien Cloud, using RLM-3D inversion code for the MT data, and the Otze modelling tool for the HTEM data. Staff from Viridien helped guide the workflow during this effort.

East Hawthorne joint-interpretation  
of geological, gravity, magnetic  
and MT data



Pamlico fault and faults inferred from this study shown in black. Additional faults from Hinz et al. (2010b) are shown in grey. All faults are shown as dashed black lines in section view.

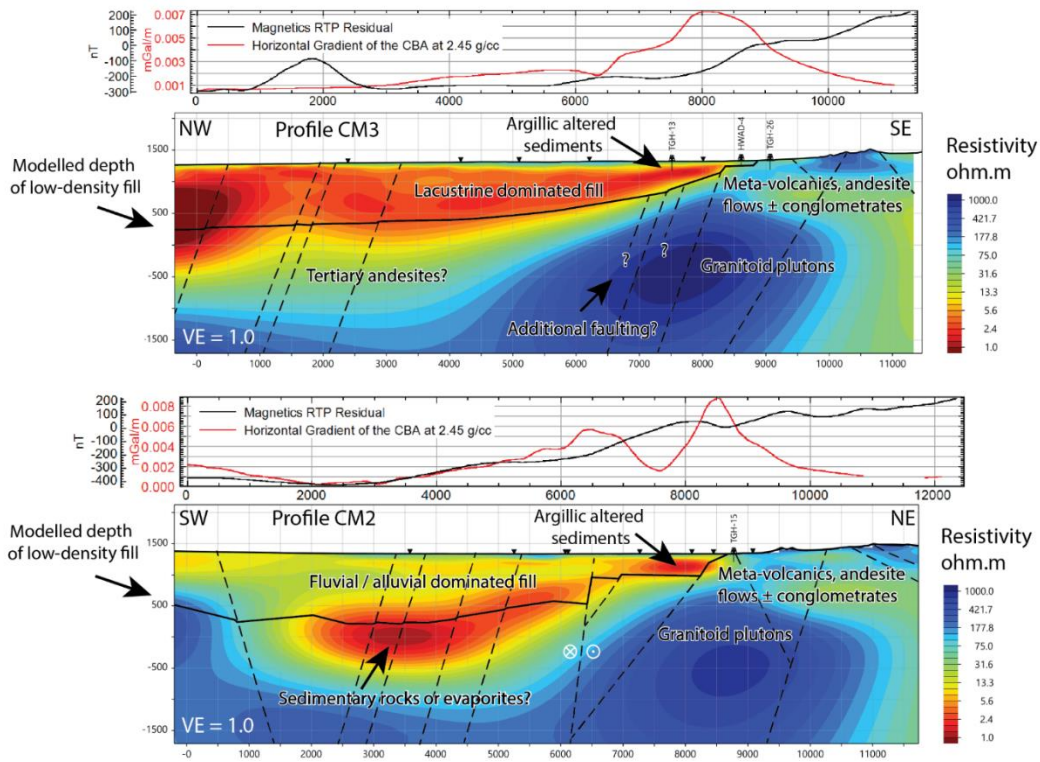


**Figure 47 Geologic Interpretations of East Hawthorne using geological, gravity, magnetic and MT data. Along each profile, magnetic data and the horizontal gradient magnitude of the gravity have been extracted and are shown above slices through the 3D MT-HTeM joint inversion resistivity model.**

The 3D MT model was first used to ‘paint’ resistivity values onto a finer mesh which then acted as a starting model for the joint inversions. The initial 3D MT model had 1.2 million cells, whereas the joint inversion mesh had 2.6 million cells and finer discretization. A first joint inversion was run for

50 iterations on the full MT dataset and using only the WNW-ESE HTEM flight lines. This first run employed a 2D forward solver for the HTEM data. The results of this 3D/2D joint inversion were then used as the starting model for a final, fully 3D/3D joint inversion that included all the HTEM flight lines and used a full 3D forward solver for the HTEM data. The final 3D/3D inversion ran for 13 iterations. The final RMS error data fit for the joint inversion was 1.07 for MT while using a 3% error floor on all components of the impedance tensor  $\mathbf{Z}$ . RMS error data fit was 0.92 for the HTEM data while applying a 5% relative and 2% absolute error floor.

Additional depth slices and cross-sections through the resistivity model are shown in Appendix 2.

#### **4.4.6. Geologic Interpretations**

Combined results from the geophysical data, geologic map and available well data enable new insights on geologic interpretations of East Hawthorne. In this section we present a simplified structural model for the geothermal system at East Hawthorne and a joint interpretation of the resistivity model that honors these other data.

An inferred fault map is shown in Figure 46. The HGM of the gravity CBA (Figure 46, panel A) shows two strong and nearly perpendicular gradients, which we interpret as relatively larger magnitude faults, corresponding to abrupt changes in thicknesses of basin fill deposits. Similar conclusions can be drawn from the magnetic data (panel B) and the resistivity volume (panels C and D), which shows that at 150 mbs, a shallow low-resistivity feature is present at the junction of these two fault zones. At 500 mbs, a resistive corner is embedded into a conductive background, also giving the appearance of a fault intersection here. Elevated values are seen in both the gravity residual (Figure 46, panel C) and the RTP magnetics at this location, suggesting the presence of a buried and structurally high bench where the two fault zones meet.

An alternative geologic interpretation for the NNE gravity gradient high is that it is not caused by a concealed normal fault, but by a stratigraphic feature instead. The ~7 Ma basalt in the NW Garfield Hills dips consistently ~20 to 35° N to NW and is repeated by SE dipping faults. A ~20 to 35° N to NW dipping contact between Mesozoic basement and low-density sediments flanking the NW side of the Garfield Hills could explain some of the gravity gradient and the deepening of low-resistivity units seen in the resistivity model. Thus, no W- to NW-dipping normal faults would be needed to extend around the NW edge of the Garfield Hills. However, given that this gravity gradient on this edge of the Garfield Hills is the largest in the entire dataset, and that analysis by Blake and others [47] suggests a fault contact in HAD-1 at this location, normal faulting seems like the most plausible explanation.

Geologic interpretations using normal faults rather than depositional contacts are shown along cross sections CM2 and CM3 in Figure 47. Along each section, the depth of low-density basin fill is estimated by forward modelling the gravity data. Resistivity values have been extracted along these profiles to enable a joint interpretation. Data profiles above each section show extracted values from the HGM of the gravity and the RTP magnetics. Note that the peak gravity HGM values occur directly over faults with large offsets. Faults from Hinz and others [103] and those inferred from this report are shown in both the map of Figure 47 and in each cross section. It should be noted that none of the mid-basin faults are required to fit the gravity data. Only the Pamlico fault and the NE striking, NW dipping normal fault nearest to the Garfield Hills supports sharp relief in the depth to basement to fit the gravity data. Elsewhere, a gently-dipping basement contact fits the data well. Approximately 450 m of offset is modelled on the Pamlico fault on section CM2. An additional 200

– 400 m of offset is modelled on the NE normal fault on this same profile, although some of that offset may be dip-slope and not caused by faulting.

The depth to basement is less well constrained on section CM3, since the gravity station spacing is larger here at roughly 1 km (Figure 44, Panel A). This survey geometry creates a large but more diffuse gravity gradient, which is best fit by a gently dipping basement contact. This zone could host multiple parallel normal fault strands or even antithetic faults without being detected by the current data. The more westward of the two NE-striking normal faults is therefore more diagrammatic and meant to convey the possibility of additional faulting here. There is evidence that the more eastward NE striking normal fault was intersected by HAD-1 just north of cross section CM3.

The overall structural interpretation suggest that East Hawthorne hosts a displacement transfer zone [9] 3D MT + HTEM Joint Inversion Modelling Report, East Hawthorne, in which strike-slip faulting is kinematically linked to one or more near-perpendicular normal faults. This type of structural setting has been identified as favorable for hosting geothermal systems and epithermal mineral deposits [3], [50]. Large uncertainties remain possible with this fault geometry, however. The NE fault is only poorly constrained by gravity data, as are fine details at the intersection of the normal fault(s) and the Pamlico fault. Regardless of the details, it seems likely that the intersection hosts a complicated damage zone.

Some aspects of the stratigraphy may also be inferred from the resistivity model. The northern cross-section CM3 passes over the 13 kya high stand of Lake Lahontan, placing the bulk of the profile over some thickness of lacustrine sediments. On this section, a ~1 km thick section has resistivities < 5 Ohm-m and correlates well with the modelled depth of basin fill. On CM2 however, the sedimentary package above the depth of basement is more resistive at 7-30 Ohm-m, and this section does not pass over evidence of paleo lake deposits. We infer that the nature of these unconsolidated units differs, with those on section CM3 being dominated by fine-grained and clay-rich lacustrine sediments, whereas CM2 lies over coarser alluvial and fluvial units instead.

Below the depth of basin fill, section CM3 suggests a ~1 km thick wedge of intermediate resistivities before seeing >200 Ohm-m basement at ~1 km below sea level. This may represent thick sequences of Tertiary andesites, which are mapped by [103] in the Garfield Hills, and were included in 2D forward gravity models made by [107]. However, this unit has not been encountered by any wells.

Unique to section CM2, a deep low-resistivity feature (1-5 Ohm-m) is found below the modelled depth of basement. The cause is unknown, but it may be due to older sedimentary or evaporite units that are localized to this zone or have been eroded away from the adjacent ranges. Another factor may be the presence of deep sedimentary brines that can have exceptionally high TDS levels.

The Garfield Hills are comprised of meta-volcanics, andesite flows and conglomerates, with one granitic pluton identified there [103] (Hinz et al., 2010b). This is consistent with modelled resistivity values of 30 – 100 Ohm-m in the upper 500 - 1000 m. Below this, both cross-sections show a highly resistive body (>200 Ohm-m) that merges with the basement. We infer that this represents a granitoid pluton at depth.

As mentioned previously, shallow zones of low resistivity near the edge of the Garfield Hills correlate spatially with smectite clay alteration and elevated temperatures, and are hence related to the geothermal system (Sewell et al., 2023). We presume that all the shallow low-resistivity zones that about the Garfield Hills are caused by the geothermal system or its outflow in some way. Along section CM3, and above the highest 2-m temperature anomaly, a 1.3 – 3 Ohm-m zone lies perched atop the basement contact. On this section, this zone does not stand out significantly from the low-

resistivity lacustrine-dominated fill further out in the basin. This is common issue when interpreting geothermal signatures next to low-resistivity playas or lakebeds; a similar example from Dixie Valley can be found in Delwiche and others [69]. On section Conceptual Model 2, however, a shallow low-resistivity zone, 1.4-4 Ohm-m, stands out in stark contrast to the adjacent and more resistive sediments.

#### 4.4.7. Conceptual Model

In this section, we present two geothermal conceptual models of the system at East Hawthorne, with the intent that they might guide future well targeting efforts. This approach of conceptual model building generally follows methods described by Cumming [15], [96]. A key component of conceptual models are estimates of lognormal-distributed reservoir areas, which are shown as P90, P50 (median) and P10 areas in map view. These estimates are guided by a multidisciplinary approach that considers all available geoscientific evidence and are constrained where possible by relevant system analogues from the Basin and Range province and elsewhere.

The available data appears to support at least two options of where the geothermal upflow and reservoir might be found. These are based on two interpretations of the loss zone and thermal roll-over observed in well HAD-1. “Model 1” assumes that these fluids are outflow, coming from the SSW, and flowing along-strike with faults and permeable stratigraphy’s. “Model 2” assumes that fluids are rising along the fault that HAD-1 intersected, and the well was simply targeted too far up-dip to intersect the resource. It remains possible, of course, that the actual system may be a hybrid of the two options shown here.

There are few constraints on the potential reservoir temperatures at East Hawthorne, since no reliable or representative geochemistry samples have been collected here. However, given the elevated thermal gradients and temperatures that occur over a wide area, the apparently extensive near-surface alteration of sediments, and inferred outflow paths that are several km in length, the geothermal system here bears the hallmarks of a power-capable system. The presence of near-boiling outflow is not diagnostic of reservoir temperatures, since near-surface temperatures generally follow the boiling-point-with-depth curve. In other words, reservoirs ranging from 100-300 °C or higher would all generate ~100 °C outflow along the water table. Given system analogues for East Hawthorne, we estimate that reservoir temps fall into the range of 135-190 °C, and are more likely to be between 150-165 °C. Since temperatures remain largely unconstrained and we present two competing conceptual models, we have chosen to not present power capacity estimates at this time.

##### 4.4.7.1. Conceptual Model 1

Figure 48 shows a set of panels that describe Model 1. The upper panel shows the reservoir area estimates in map view, with wells, the fault model, 2-m temperatures, outflow arrows and cross-

**Table 10 East Hawthorne conceptual model estimates of reservoir area and temperature.**

<i>East Hawthorne Conceptual Model Distribution Estimates</i>						
			Pessimistic	Middle	Optimistic	
		P99	P90	P50	P10	P01
<b>Model 1</b>	Reservoir Area (km <sup>2</sup> )	0.3	0.6	1.4	3	5.7
<b>Model 2</b>	Reservoir Area (km <sup>2</sup> )	0.3	0.5	1.2	2.8	5.6
<b>1 &amp; 2</b>	Reservoir Temperature (°C)	120	135	156	180	202

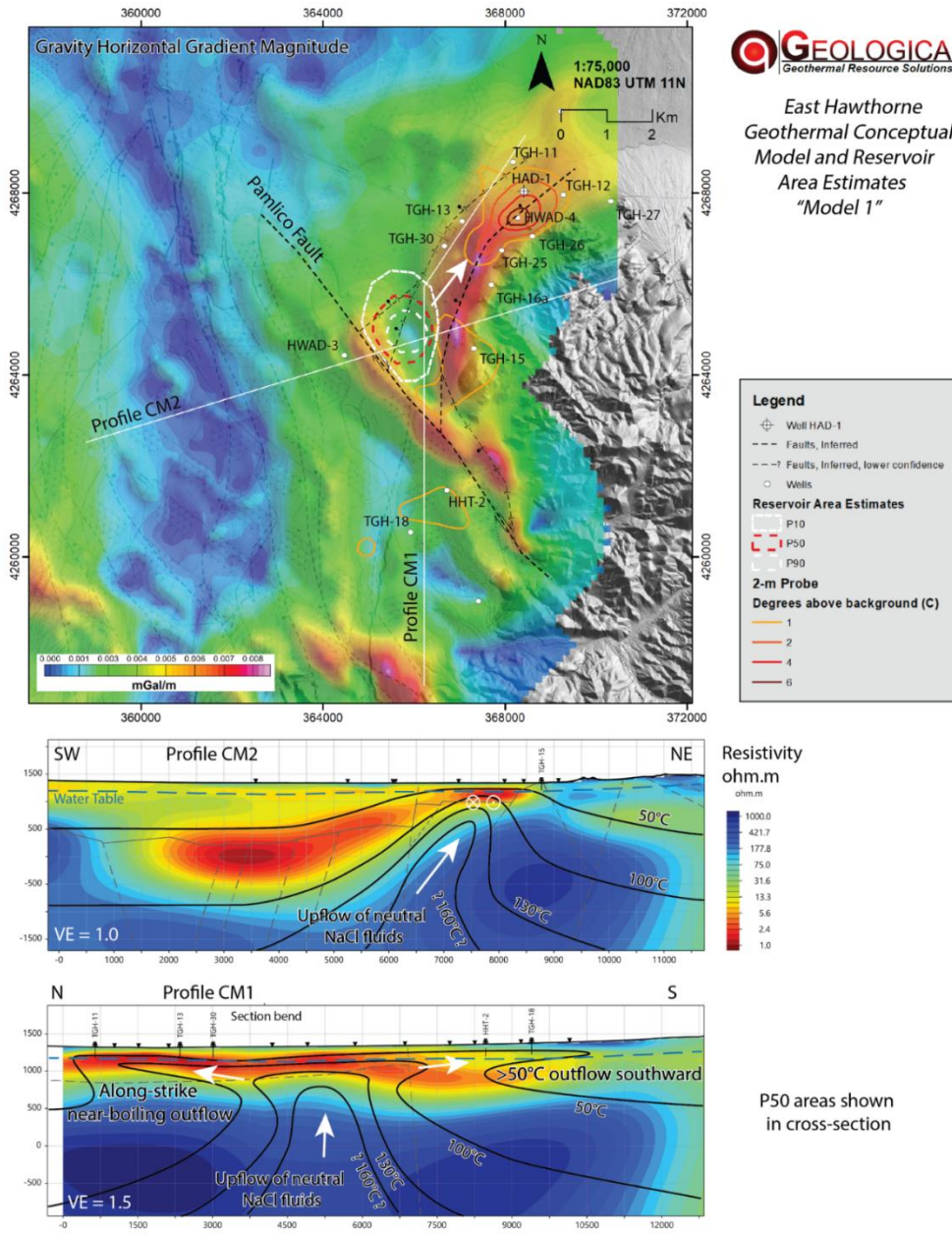
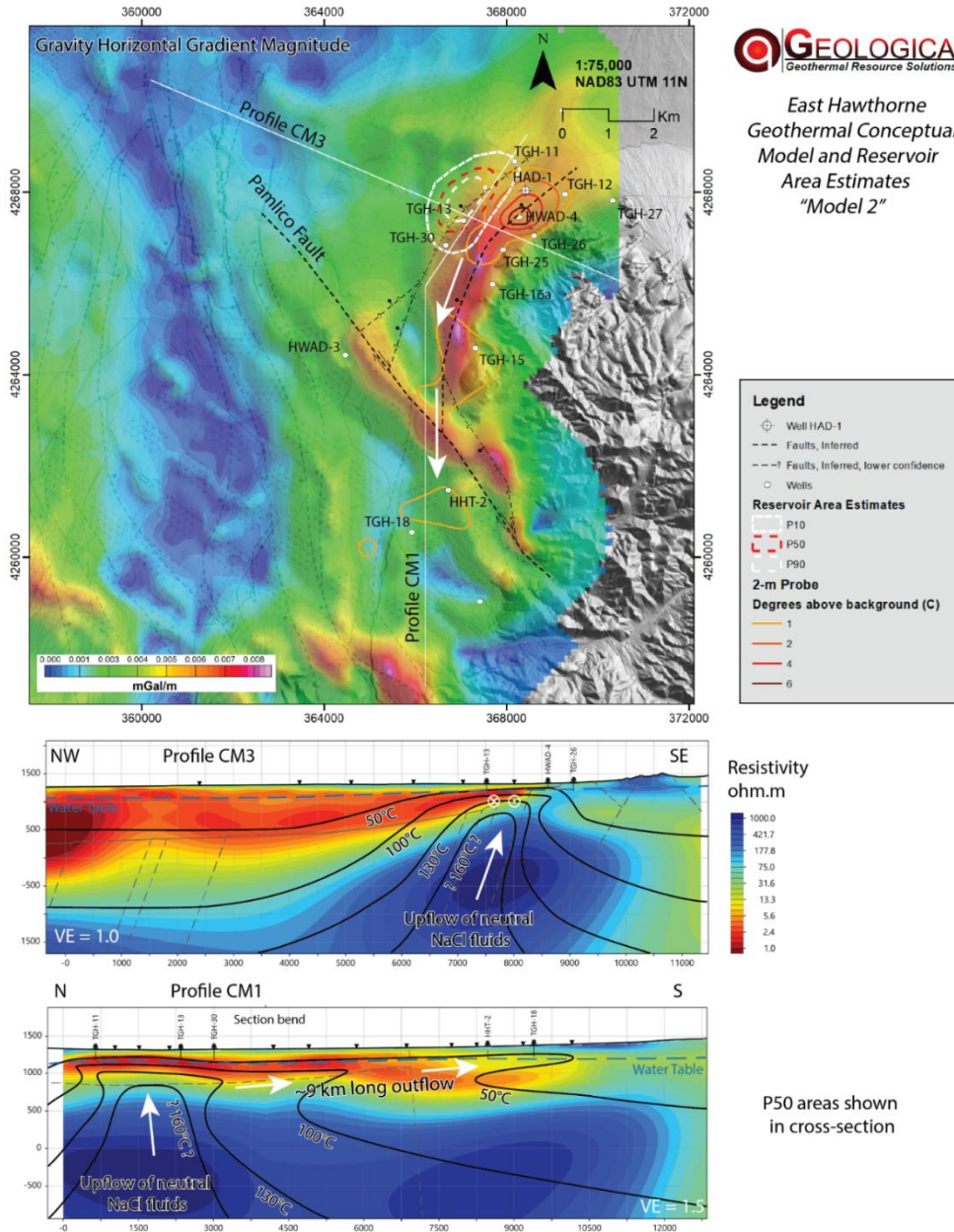


**Figure 48 Conceptual Model 1, with upflow hosted near the intersection of the Pamlico Fault and inferred NNE-striking, NW-dipping normal faults.**

section locations, all on the gravity HGM map layer. Below the map, isotherms representative of the P50 reservoir area are drawn on the resistivity volume on sections Conceptual Model 1 and Conceptual Model 2. In this model, we infer that upflow is hosted on NE-striking normal faults that occur within a complex damage zone near the intersection of the Pamlico fault. Upflow may be hosted on a single fault, be more broadly distributed in a damaged fault block, or be hosted along multiple parallel structures. From this location, a near-boiling plume of outflow is directed along-strike to the NNE, and toward the zone with the highest 2-m temperature anomaly. Outflow is not necessarily hosted in a fault zone but may be channeled through permeable unconsolidated



sediments such as fanglomerates or coarse-grained beach deposits. We note that the 13 kya high-stand perfectly bisects the 2-m temperature anomaly, which may not be a coincidence. A second lower-temperature outflow is directed southward towards wells HHT-2 and TGH-18, both of which encounter >50 °C temperatures and high thermal gradients, but do not roll over. Each outflow path appears to be 3-4 km in length.

Smectite clay, argillic-altered, unconsolidated sediments lie both over the top of the system near the fault intersection, and along the NNE outflow path. Lower temperatures on the southward outflow

path may limit the degree of alteration seen there. Over the reservoir these altered sediments may act as a hydrologic barrier, forming a cap over the system. It is common in the Basin and Range for the most intense alteration to occur within unconsolidated sediments above a geothermal system, which can alter to clays more readily than more competent rocks.

#### **4.4.7.2. Conceptual Model 2**

Figure 49 shows an alternate Model 2, with similar data layers as Figure 48. In this end-member model, we infer that the near-boiling fluids encountered by HAD-1 were rising along the NE-striking, NW-dipping normal fault near that location. Where these fluids encounter unconsolidated sediments, they have formed an intense smectite-clay altered cap over the system. The upflow may occur on this single near-range front fault, or it may flow up a series of subparallel structures that remain poorly characterized. Under this model, we infer that a ~9 km long plume of outflow emanates from the system and flows first SSW, following along-strike with structures, before turning south and reaching wells HHT-2 and TGH-18. This outflow path would explain the extension of the ~1 °C above background 2-m temperature probe anomalies. The length of this outflow would be exceptional but not unheard of in the Basin and Range province.

Model 2 lacks a well-defined favorable structural setting that typically host geothermal systems and epithermal mineral deposits in the Basin and Range, as described by [50]. If there are concealed NE-striking, NW-dipping normal faults as proposed, they appear to lack elements that would enhance their permeability such as a fault intersection, bend, relay-ramp, etc. Such structures may yet exist, but cannot be imaged by the current gravity dataset given the coarse station spacing here.

#### **4.4.7.3. System Analogues**

Producing fields in the Basin and Range that share similar structural characteristics as East Hawthorne include Don A. Campbell, Wabuska and Blue Mountain, each of which are categorized as being hosted on a displacement transfer zone [50]. Not surprisingly, many of these systems are in the Walker Lane or are adjacent to it, where strike-slip faulting is more common. A few notable prospects that are believed to be hosted on displacement transfer zones include South Gabbs [40] and Rhodes Marsh. Each of these systems may provide a decent analogue to East Hawthorne.

Both end member conceptual models presented here propose that the system hosts a robust sub-lateral outflow covering an extensive area. Model 1 proposes two 3-4 km long outflow plumes, and Model 2 proposes a single ~9 km long outflow plume. This unique geometry warrants some examination with analogue systems. The longest known outflow in the Basin and Range arguably occurs at the Salt Wells Field, NV, where shallow wells < 153 m deep, 2-m temperatures and hot springs cover 12 km in length [51]. The Desert Queen prospect in Hot Springs Mountains has a 6 km long, ~1.5 km wide 2-m temperature anomaly interpreted as outflow [43]. The San Emidio producing field has a well characterized, along-strike outflow plume 5 – 6 km in length [63] that has recently served as an injection target. The geothermal system at Gerlach hosts a network of near-boiling springs spanning a 2.7 km distance, yet the upflow has never been found. At other fields which do not have well characterized

**Table 11 Recommended exploration drilling targets at East Hawthorne**

<b>Well</b>	<b>Easting</b>	<b>Northing</b>	<b>Elevation (m)</b>	<b>Minimum Depth (m)</b>	<b>Rationale</b>
A	367250	4268016	1322	304.8	Target conceptual model 2 inferred up flow.
B	367161	4266421	1331	304.8	Target and characterize inferred outflow path common to both models
C	365859	4264912	1338	304.8	Target conceptual model 1 inferred up flow.
<i>NAD-83 UTM 11 north</i>					

outflow plumes, it is still common to see wells with shallow temperature profiles that roll over, implying at least localized outflow. This casual study suggests that most outflow plumes in the Basin and Range are likely < 5-6 km in length, with only exceptional systems hosting longer plumes.

Another option for East Hawthorne is that it hosts two separate systems. Other geothermal areas in the Basin and Range are as close as 5 km, such as Bradys and Desert Peak, Desert Peak and Desert Queen, and Humboldt House and Star Peak. In these areas, shallow thermal anomalies can abut each other providing an option for early-stage exploration interpretations of a single geothermal system.

#### **4.4.8. Recommendations for Future Work**

Surface studies at East Hawthorne are fairly complete, with a few notable areas where improvements could be made that would help refine the conceptual model(s). Demonstrating that Model 1, Model 2 or that another model is valid will ultimately require exploration drilling. A short list of recommended studies is below, followed by a description of and rationale for a proposed TGH drilling campaign.

1. Geochemistry is lacking from wells at East Hawthorne, making it difficult to estimate reservoir temperatures through geothermometry. Some attempts to recover fluids from the existing wells have been made but are suspected to be contaminated.
2. Additional geologic mapping in the Garfield Hills, as discussed in section 3.2.5.
3. An in-fill gravity survey along the northwestern margin of the Garfield Hills, reducing station spacing there to ≤400 m and enabling better characterization of the inferred hidden faulting there.
4. A 3-well thermal gradient drilling campaign, described in Table 11 and Figure 50.

Thermal gradient drilling is an effective and comparatively low-cost method to locate and characterize the thermal geometry of a geothermal system. In addition to their low costs, they are simpler to permit under a categorical exclusion (CX) and so are ideal for early-stage exploration. The results can be difficult to interpret in the presence of outflow, however, especially if the wells are not deep enough to see a thermal roll-over. TG wells drilled in 2010 had a maximum planned depth of 152.4 m (500 ft), and only a few were able to image a shallow rollover (Figure 43, TGH-14, TGH-14a, TGH-12). These wells were not deep enough to see the outflow at the location of HAD-1, and none were able to provide a thermal gradient below the rollover point. Other wells encountered

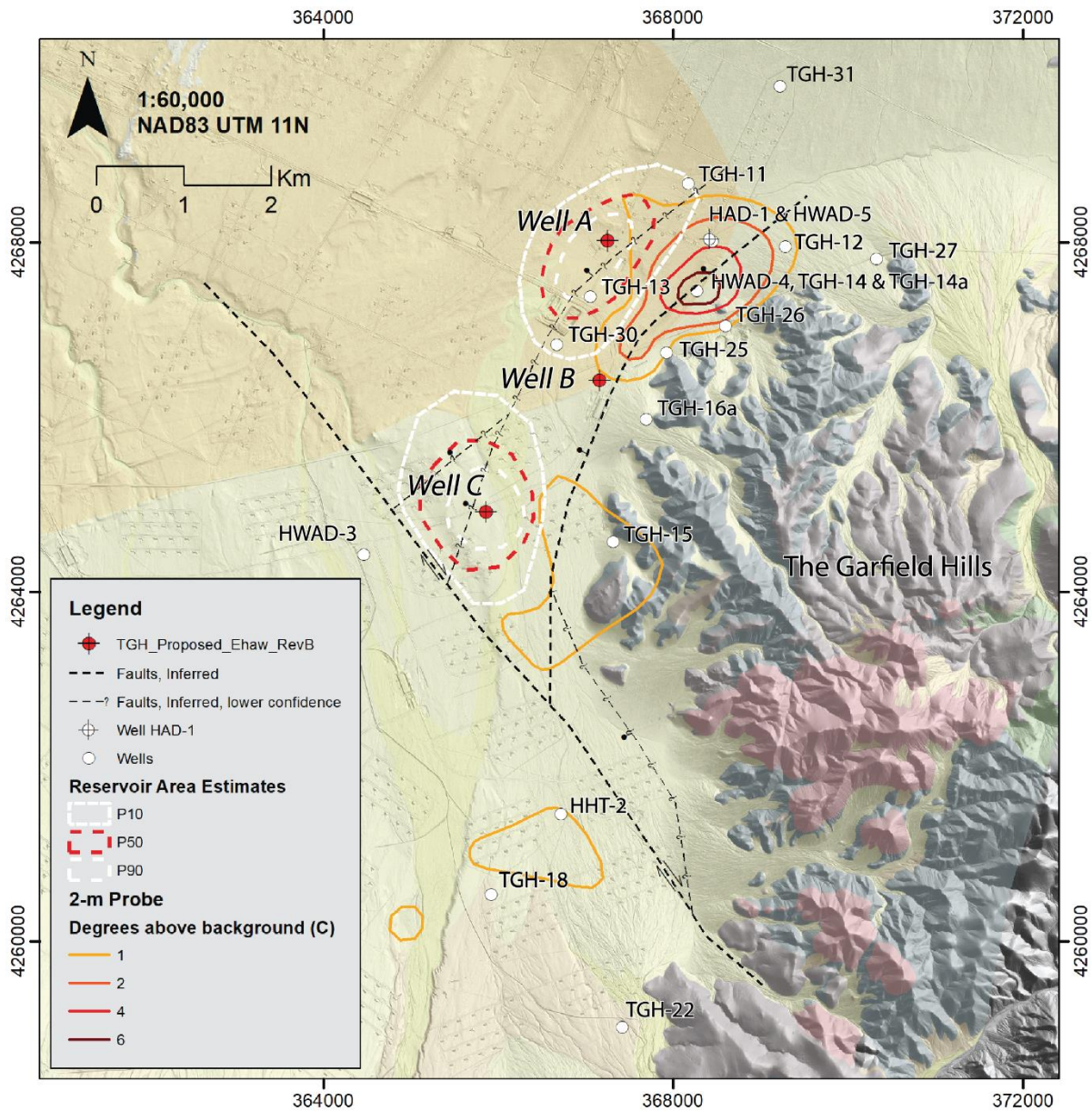


**Figure 50 Proposed TGH well target locations, with existing wells, relevant components of the fault model, 2-m temperature anomalies and reservoir area estimates for Models 1 and 2.**

promising linear gradients, but it remains unclear if a rollover lies deeper below them (Figure 43, TGH-25, TGH-11, TGH-13, TGH-18). We recommend drilling three additional and deeper TGH wells at East Hawthorne, based on the analysis and conceptual models presented here (Table 11 and Figure 50). Each well would have a minimum depth of 304.8 m (1,000 ft).

TGH wells A and C are located within the P90 reservoir area estimates of the conceptual models 1 and 2, respectfully. These targets are chosen to see elevated linear thermal gradients that are expected over a an upflow zone. Each of these wells penetrate thick sections of low-resistivity quaternary alluvium, which may host a sealing clay cap over these systems. TGH well B is chosen to

target the inferred outflow zone that is common to both models. These observations could help determine the direction and geometry of the outflow (by comparison with other wells that see rollovers). This well is placed just outside of the 2-m temperature probe anomaly.

After drilling the three TGH wells and addressing the other recommendations, the conceptual model(s) should be revised with the new observations. Hopefully following these steps, a clearer path towards development of a power generating facility at East Hawthorne can emerge.

#### 4.5. Geothermal Exploration Data and Data Products

The Basin & Range Investigation for Developing Geothermal Energy (BRIDGE) Project data deliverables include a wide variety of geophysical and geologic datasets and modeled results spread over several geothermal prospects. New geophysical data was collected by professional contractors and modelled by the USGS and by Geologica Geothermal Group. Several legacy datasets were also used and are included here for completeness. 2-meter data was collected by the Navy Geothermal Program Office. Each dataset is unique. These datasets are available on the Geothermal Data Repository (GDR) at <https://gdr.openei.org/submissions/1682>. Please refer to the main README (also available in Appendix D) and individual dataset README files found in each data directory for more details.

#### 4.6. Conference Proceedings

The following list captures BRIDGE conference papers. This does not include the numerous oral and poster presentations given by the BRIDGE team over the course of this project.

Downs, C., Schwering, P., Sewell, S., Winn, C., Hinz, N., Zimmerman, J., Blake, K., Sabin, A., Lopeman, J., Milton, A., Siler, D., & Cumming, W., (2023). Development of the Prospect Portfolio and Initial Surface Exploration Studies in the Basin & Range Investigations for Developing Geothermal Energy (BRIDGE) Project. GRC Transactions, Vol. 47.

Folsom, M., Winn, C., Zimmerman, J., Blake, J., Sabin, A., Downs, C., Sewell, S., Kraal, K., Nale, S., Huang, W., Milton, A., Schwering, P. (2024). An Early-Stage Exploration Update on the Grover Point Blind Geothermal System in Dixie Valley, Nevada. PROCEEDINGS, 49th Workshop on Geothermal Reservoir Engineering, Stanford University, Stanford, California. SGP-TR-227.

Folsom, M., Sewell, S., Cumming, W., Zimmerman, J., Sabin, A., Downs, C., Hinz, N., Winn, C., Seiderman, B., & Schwering, P. (2024). A Direct Comparison of Resistivity Models from Helicopter Transient Electromagnetic and Magnetotelluric Datasets Collected over a Blind Geothermal System in East Hawthorne, Nevada, USA. Geothermal Resources Council Transactions, 48.

Kraal, K., Lindsey, C., Zimmerman, J., Sladek, C., & Burgess, Q., (2024). Development of shallow (2-m) temperature survey standard operating procedures and interpretation workbook. PROCEEDINGS, 49th Workshop on Geothermal Reservoir Engineering, Stanford University, Stanford, California. SGP-TR-227.

Kraal, K.O., & Schwering, P.C., (2024). Remote Sensing Case Studies for Detection and Interpretation of Geothermal Surface Materials for Geothermal Exploration in the Basin and Range, Nevada, USA. GRC Transactions, Vol. 48.

Kraal, K., Folsom, M., Winn, C., Delwiche, B., Feucht, D., Sewell, S., Downs, C., Hinz, N., & Cumming, W. (in prep). Petrologic Validation of Exploration Geophysical Anomalies Utilizing Drill Core and Cuttings from the Don A. Campbell Geothermal System, Nevada, USA. PROCEEDINGS, 50th Workshop on Geothermal Reservoir Engineering, Stanford University, Stanford, California, February 10-12, 2025, SGP-TR-229.

Schwering, P., Lowry, T., Hinz, N., Matson, G., Sabin, A., Blake, K., Zimmerman, J., Sewell, S., & Cumming, W., (2022). The BRIDGE Project – Hidden Systems Reconnaissance in Western Nevada. GRC Transactions, Vol. 46.

Sewell, S., Cumming, W., Schwering, P., Hinz, P., Downs, C., Zimmerman, J., Bedrosian, P., Robinson, B., Murray, D., & Schlutz, A., (2023). Using helicopter time-domain electromagnetic (HTEM) resistivity surveys with supporting geoscience data to target temperature gradient wells and discover hidden geothermal systems in the US Basin and Range. GRC Transactions, Vol. 47.

## REFERENCES

- [1] M. F. Coolbaugh, G. L. Raines, R. E. Zehner, L. Shevenell, and C. F. Williams, “Prediction and discovery of new geothermal resources in the Great Basin: Multiple evidence of a large undiscovered resource base,” in *Geothermal Resources Council Transactions*, 2006, pp. 867–873.
- [2] P. F. Dobson, “A review of exploration methods for discovering hidden geothermal systems,” in *Geothermal Resources Council Transactions*, 2016, pp. 695–706.
- [3] J. Faulds and N. Hinz, “Favorable tectonic and structural settings of geothermal systems in the Great Basin region, western USA: Proxies for discovering blind geothermal systems,” in *Proceedings*, Melbourne, Australia, 2015. [Online]. Available: <https://www.osti.gov/biblio/1724082>
- [4] N. H. Hinz, M. F. Coolbaugh, J. E. Faulds, D. L. Siler, and G. Dering, “Building the Next Generation of Regional Geothermal Potential Maps: Examples from the Great Basin Region, Western USA,” in *Proceedings World Geothermal Congress 2015*, Melbourne, Australia, 2015.
- [5] J. Faulds, J. Craig, M. Coolbaugh, N. Hinz, J. Glen, and S. Deoreo, “Searching for Blind Geothermal Systems Utilizing Play Fairway Analysis, western Nevada,” *GRC Bulletin*, vol. 47, 2018.
- [6] D. L. Siler *et al.*, “Play-fairway analysis for geothermal resources and exploration risk in the Modoc Plateau region,” *Geothermics*, vol. 69, pp. 15–33, 2017.
- [7] B. Ayling *et al.*, “INGENIOUS - Great Basin Regional Dataset Compilation.” GBCGE, NBMG, UNR, Jun. 30, 2022. doi: 10.15121/1881483.
- [8] J. Faulds *et al.*, “Preliminary Report on Applications of Machine Learning Techniques to the Nevada Geothermal Play Fairway Analysis,” in *Proceedings 45th Workshop on Geothermal Reservoir Engineering*, Stanford, CA, 2020, pp. 229–34.
- [9] P. Schwering *et al.*, “Basin and Range Investigation for Developing Geothermal Energy: Exploration Data.” Sandia National Laboratories, Jan. 03, 2022. [Online]. Available: <https://gdr.openei.org/submissions/>
- [10] S. Sewell *et al.*, “Using Helicopter Time-Domain Electromagnetic (HELITEM) Resistivity Surveys with Supporting Geoscience Data to Target Temperature Gradient Wells and Discover Hidden Geothermal Systems in the US Basin and Range,” in *Geothermal Resources Council Transactions*, Davis, California: Geothermal Rising, 2023, pp. 1934–1948.
- [11] M. Folsom *et al.*, “A Direct Comparison of Resistivity Models from Helicopter Transient Electromagnetic and Magnetotelluric Datasets Collected over a Blind Geothermal System in East Hawthorne, Nevada, USA,” in *Geothermal Resources Council Transactions*, 2024.
- [12] M. Folsom *et al.*, “An Early-Stage Exploration Update on the Grover Point Blind Geothermal System in Dixie Valley, Nevada: Highlights of Geophysics Results and Conceptual Modeling,” in *Proceedings*, Stanford, CA, 2024.
- [13] G. W. Lederer *et al.*, “Annual review 2023: Critical minerals,” *Mining Engineering*, vol. 76, no. 5, pp. 29–42, 2024.
- [14] M. Gehringer and V. Loksha, “Geothermal handbook : planning and financing power generation (English),” World Bank Group, Washington, D.C., ESMAP technical report 002/12, 2012. [Online]. Available: <http://documents.worldbank.org/curated/en/396091468330258187/Geothermal-handbook-planning-and-financing-power-generation>
- [15] W. Cumming, “Geothermal Resource Conceptual Models Using Surface Exploration Data,” in *PROCEEDINGS, Thirty-Fourth Workshop on Geothermal Reservoir Engineering*, Stanford, CA, 2009.

- [16] J. M. Glen and T. E. Earney, “GeoDAWN: Airborne magnetic and radiometric surveys of the northwestern Great Basin, Nevada and California.” U.S. Geological Survey, 2024. doi: 10.5066/P93LGLVQ.
- [17] M. F. Coolbaugh, C. Sladek, J. E. Faulds, R. E. Zehner, and G. L. Oppliger, “Use of rapid temperature measurements at a 2-meter depth to augment deeper temperature gradient drilling,” in *PROCEEDINGS*, Stanford, CA, 2007.
- [18] L. Lévy *et al.*, “The role of smectites in the electrical conductivity of active hydrothermal systems: electrical properties of core samples from Krafla volcano, Iceland,” *Geophysical Journal International*, vol. 215, no. 3, pp. 1558–1582, 2018.
- [19] Y. Qi and Y. Wu, “Electrical conductivity of clayey rocks and soils: A non-linear model,” *Geophysical Research Letters*, vol. 49, no. 10, p. e2021GL097408, 2022.
- [20] M. Folsom, J. Lopeman, D. Perkin, and M. Sophy, “Imaging Shallow Outflow Alteration to Locate Productive Faults in Ormat’s Brady’s and Desert Peak Fields Using CSAMT,” in *PROCEEDINGS*, 2018.
- [21] D. L. Siler *et al.*, “The geologic framework of the Fallon FORGE site,” in *Geothermal Resources Council Transactions*, 2016, pp. 573–584.
- [22] G. Ussher, C. Harvey, R. Johnstone, and E. Anderson, “Understanding the resistivities observed in geothermal systems,” in *Proceedings*, Kyushu Japan, 2000, pp. 1915–1920.
- [23] G. Hodges, T. Chen, and R. van Buren, “HELITEM detects the Lalor VMS deposit,” *Exploration Geophysics*, vol. 47, no. 4, pp. 285–289, 2016.
- [24] H. Gibson, B. Delwiche, D. FitzGerald, S. Wieberg, J. Mims, and P. Berardelli, “Demonstration of new geophysical methods for geothermal exploration-the technology explained,” in *Proceedings of the World Geothermal Congress, Melbourne, Australia*, 2015. [Online]. Available: <https://pangea.stanford.edu/ERE/db/WGC/papers/WGC/2015/13094.pdf>
- [25] J. Hope, J. Feijth, S. Mulè, S. Machida, and J. Kuwamura, “Using HeliFALCON airborne gravity gradiometer and HELITEM electromagnetic and magnetic data for geothermal exploration,” in *Proceedings*, Tokyo, Japan: Society of Exploration Geophysicists and Society of Exploration ..., 2015, pp. 248–251.
- [26] H. Ishikawa *et al.*, “Targeting Geothermal Exploration Using Airborne Multi-geophysics, Kutcharo Caldera, Teshikaga Area,” *Natural Resources Research*, vol. 30, no. 4, pp. 2957–2968, Aug. 2021, doi: 10.1007/s11053-020-09704-5.
- [27] 千葉昭彦, 亀山正義, 毛利拓治, 代田敦, 石川弘真, and 近持雅春, “日本の地熱資源ポテンシャル調査への空中物理探査の適用性,” *物理探査*, vol. 70, pp. 96–109, 2017.
- [28] H. Huang and D. C. Fraser, “The differential parameter method for multifrequency airborne resistivity mapping,” *Geophysics*, vol. 61, no. 1, pp. 100–109, 1996.
- [29] G. H. Olmsted, “Use of temperature surveys at a depth of 1 meter in geothermal exploration in Nevada,” Report 1044B, 1977. doi: 10.3133/pp1044B.
- [30] A. Lang, J. Deymonaz, and H. Pilkington, “Comparative studies of geothermal surveys in 3-meter and temperature-gradient holes,” in *Geothermal Resources Council Transactions*, AMAX Exploration Inc., Golden, CO, 1982.
- [31] D. T. Trexler, T. Flynn, B. A. Koenig, E. J. Bell, and G. Ghusn, “Low-to-Moderate-Temperature Geothermal Resource Assessment for Nevada: Area Specific Studies, Pumpernickel Valley, Carlin and Moana. Final Report June 1, 1981-July 31, 1982,” University of Nevada Reno, Reno, NV, Report DOE/NV/10220-1, Jan. 1982. doi: 10.2172/5167530.
- [32] C. Sladek, M. F. Coolbaugh, and R. E. Zehner, “Development of 2-meter soil temperature probes and results of temperature survey conducted at Desert Peak, Nevada, USA,” in *Geothermal Resources Council Transactions*, 2007, pp. 363–368.

- [33] C. Kratt, M. Coolbaugh, C. Sladek, R. Zehner, R. Penfield, and B. Delwiche, “A new gold pan for the west: discovering blind geothermal systems with shallow temperature surveys,” in *Geothermal Resources Council Transactions*, 2008, pp. 153–158.
- [34] C. Kratt, M. Coolbaugh, B. Peppin, and C. Sladek, “Identification of a new blind geothermal system with hyperspectral remote sensing and shallow temperature measurements at Columbus Salt Marsh, Esmeralda County, Nevada,” in *Geothermal Resources Council Transactions*, 2009, pp. 481–485.
- [35] C. Kratt, C. Sladek, M. Coolbaugh, and others, “Boom and bust with the latest 2 m temperature surveys: Dead Horse Wells, Hawthorne Army Depot, Terraced Hills, and other areas in Nevada,” in *Geothermal Resources Council Transactions*, 2010, pp. 567–574.
- [36] J. Skord, P. H. Cashman, M. Coolbaugh, and N. Hinz, “Mapping hydrothermal upwelling and outflow zones: preliminary results from two-meter temperature data and geologic analysis at Lee Allen Springs and Salt Wells Basin,” in *Geothermal Resources Council Transactions*, 2011, pp. 1017–1021.
- [37] J. Skord, C. Sladek, M. Coolbaugh, P. Cashman, M. Lazaro, and C. Kratt, “Two-meter temperature surveys for geothermal exploration project at NAS Fallon,” in *Geothermal Resources Council Transactions*, 2011, pp. 1023–1027.
- [38] L. A. LeSchack and J. E. Lewis, “Geothermal prospecting with Shallo-Temp surveys,” *Geophysics*, vol. 48, no. 7, pp. 825–1018, Feb. 2012, doi: 10.1190/1.1441523.
- [39] R. E. Zehner, K. N. Tullar, and E. Rutledge, “Effectiveness of 2-meter and geoprobe shallow temperature surveys in early stage geothermal exploration,” in *Geothermal Resources Council Transactions*, 2012, pp. 835–841.
- [40] J. W. Craig *et al.*, “Discovery and analysis of a blind geothermal system in southeastern Gabbs Valley, western Nevada, USA,” *Geothermics*, vol. 97, p. 102177, Dec. 2021, doi: 10.1016/j.geothermics.2021.102177.
- [41] J. Zimmerman, K. Blake, S. Nale, A. Sabin, and W.-C. Huang, “Evaluation of 2-Meter Temperature Surveys from the Coso Geothermal Field, CA,” in *Geothermal Resources Council Transactions*, Geothermal Rising, 2023, pp. 1651–1670. Accessed: Dec. 21, 2024. [Online]. Available: <https://www.geothermal-library.org/index.php?mode=pubs&action=view&record=1034794>
- [42] K. O. Kraal, J. Zimmerman, and C. Lindsey, “Review of shallow (2-m) temperature surveys for geothermal exploration and resource conceptual modeling in the Basin and Range region, USA,” 2024.
- [43] M. Coolbaugh, C. Sladek, R. Zehner, and C. Kratt, “Shallow temperature surveys for geothermal exploration in the Great Basin, USA, and estimation of shallow aquifer heat loss,” in *Geothermal Resource Council Transactions*, 2014, pp. 115–122.
- [44] K. O. Kraal, C. Lindsey, J. Zimmerman, C. Sladek, and Q. Burgess, “Development of shallow (2-m) temperature survey standard operating procedures and interpretation workbook,” in *PROCEEDINGS*, Stanford, CA, 2024.
- [45] R. Orenstein and B. Delwiche, “The Don A. Campbell Geothermal Project,” in *Geothermal Resources Council Transactions*, 2014, pp. 91–97.
- [46] J. F. Payne, “Characterization of a blind geothermal prospect through LiDAR analysis and shallow temperature survey, Gabbs Valley, Nye and Mineral Co., NV,” University of Nevada, Reno, 2013.
- [47] K. Blake *et al.*, “Hawthorne Army Depot: Update of geothermal exploration and direct use applications,” in *Geothermal Resources Council Transactions*, 2017.

- [48] D. D. Blackwell, R. P. Smith, and M. C. Richards, “Exploration and Development at Dixie Valley, Nevada: Summary of DOE Studies,” in *PROCEEDINGS*, Stanford, CA, 2007.
- [49] M. F. Coolbaugh *et al.*, “Geothermal potential map of the Great Basin region, western United States,” Nevada Bureau of Mines and Geology, 2005.
- [50] J. Faulds, M. F. Coolbaugh, and N. H. Hinz, *Inventory of Structural Setting for Active Geothermal Systems and Late Miocene (~ 8 MA) to Quaternary Epithermal Mineral Deposits in the Basin and Range Province of Nevada*. Nevada Bureau of Mines and Geology, 2021.
- [51] N. H. Hinz, J. E. Faulds, and M. F. Coolbaugh, “Association of fault terminations with fluid flow in the Salt Wells geothermal field, Nevada, USA,” in *Geothermal Resources Council Transactions*, 2014, pp. 3–10.
- [52] J. W. Bell, S. J. Caskey, and P. K. House, “Geologic Map of the Lahontan Mountains Quadrangle, Churchill County, Nevada,” Nevada Bureau of Mines and Geology, 2010.
- [53] C. Kreemer, W. C. Hammond, G. Blewitt, A. A. Holland, and R. A. Bennett, “A geodetic strain rate model for the Pacific-North American plate boundary, western United States,” in *EGU General Assembly Conference Abstracts*, 2012, p. 6785.
- [54] W. C. Hammond, C. Kreemer, and G. Blewitt, “Exploring the relationship between geothermal resources and geodetically inferred faults slip rates in the Great Basin,” in *GRC Transactions*, 2007, pp. 391–395.
- [55] S. Alm, “A Geological and Geophysical Investigation into the Evolution and Potential Exploitation of a Geothermal Resource at the Dixie Valley Training Range, Naval Air Station Fallon,.” University of Kansas, 2016. [Online]. Available: <https://api.semanticscholar.org/CorpusID:133153612>
- [56] B. Delwiche, B. Peters, M. Sophy, C. Smith, and J. O’Brien, “Successful Deployment of a Multi-Crossing Directional Drilling Method at Ormat’s New Tungsten Mountain Geothermal Field in Churchill County, Nevada,” in *PROCEEDINGS*, Stanford, CA, 2018.
- [57] R. Fournier and A. Truesdell, “An empirical Na K Ca geothermometer for natural waters,” *Geochimica et Cosmochimica acta*, vol. 37, no. 5, pp. 1255–1275, 1973.
- [58] C. Sladek and M. Coolbaugh, “Development of online map of 2 meter temperatures and methods for normalizing 2 meter temperature data for comparison and initial analysis,” in *Geothermal Resources Council Transactions*, 2013, pp. 333–336.
- [59] Water Resources Division, “Aeromagnetic map of the Clan Alpine Mountains, west-central Nevada,” Report 85–752, 1985. doi: 10.3133/ofr85752.
- [60] M. Talwani, J. L. Worzel, and M. Landisman, “Rapid gravity computations for two-dimensional bodies with application to the Mendocino submarine fracture zone,” *Journal of Geophysical Research*, vol. 64, no. 1, pp. 49–59, 1959.
- [61] L. Cordell, “Sedimentary facies and gravity anomaly across master faults of the Rio Grande rift in New Mexico,” *Geology*, vol. 7, no. 4, pp. 201–205, 1979.
- [62] L. Cordell and V. Grauch, “Mapping basement magnetization zones from aeromagnetic data in the San Juan Basin, New Mexico,” in *The Utility of Regional Gravity and Magnetic Anomaly Maps*, Society of Exploration Geophysicists, 1985, pp. 181–197.
- [63] M. Folsom, R. Libbey, D. Feucht, I. Warren, and S. Garanzini, “Geophysical observations and integrated conceptual models of the San Emidio geothermal field, Nevada,” in *PROCEEDINGS*, Stanford, CA, 2020.
- [64] C. Winn *et al.*, “Lost Circulation in a Hydrothermally Cemented Basin-Fill Reservoir: Don A. Campbell Geothermal Field, Nevada,.” Sandia National Lab.(SNL-NM), Albuquerque, NM (United States), 2021.

- [65] J. W. Hedenquist, A. Arribas R., and E. Gonzalez-Urien, “Exploration for Epithermal Gold Deposits,” in *Gold in 2000*, vol. 13, S. G. Hagemann and P. E. Brown, Eds., Society of Economic Geologists, 2000, p. 0. doi: 10.5382/Rev.13.07.
- [66] V. J. S. Grauch, “High-resolution aeromagnetic survey to image shallow faults, Dixie Valley geothermal field, Nevada,” Report 2002–384, 2002. doi: 10.3133/ofr02384.
- [67] V. J. S. Grauch, M. R. Hudson, and S. A. Minor, “Aeromagnetic expression of faults that offset basin fill, Albuquerque basin, New Mexico,” *GEOPHYSICS*, vol. 66, no. 3, pp. 707–720, May 2001, doi: 10.1190/1.1444961.
- [68] S. Soengkono, “Airborne Magnetic Surveys to Investigate High Temperature Geothermal Reservoirs,” in *Advances in Geothermal Energy*, B. I. Ismail, Ed., Rijeka: IntechOpen, 2016. doi: 10.5772/61651.
- [69] B. Delwiche, R. Libbey, M. Folsom, A. Johnson, J. Murphy, and R. Zuza, “Exploration History and Conceptual Model of the Dixie Meadows Geothermal Field, Nevada, USA,” in *Proceedings*, Beijing, China, Sep. 2023.
- [70] W. Cumming and R. Mackie, “Resistivity imaging of geothermal resources using 1D, 2D and 3D MT inversion and TDEM static shift correction illustrated by a Glass Mountain case history,” in *Proceedings World Geothermal Congress*, Bali, Indonesia, 2010, pp. 25–29.
- [71] I. C. Russell, *Geological history of Lake Lahontan, a Quaternary lake of northwestern Nevada*. in Monographs of the United States Geological Survey. 11, no. xiv, 288 p. Washington: Govt. print. off., 1885. [Online]. Available: <https://catalog.hathitrust.org/Record/009788953>
- [72] D. W. Miller, “Hydrogeologic analysis of shallow hole temperatures at Allen Springs and Lee Hot Springs, Churchill County, Nevada,” PhD Thesis, University of Nevada, Reno, 1978.
- [73] E. Mlawsky and B. Ayling, “GBCGE Subsurface Database Explorer and APIs.” NBMG; GBCGE; UNR, Mar. 16, 2020. doi: 10.15121/1987556.
- [74] J. W. Merrit, “The geology of a portion of the Desert Mountains, Nevada,” Northwestern University, 1912.
- [75] P. A. Glancy and T. Katzer, “Water-resources appraisal of the Carson River basin, western Nevada,” US Geological Survey, 1975.
- [76] R. H. Mariner, J. B. Rapp, L. M. Willey, and T. S. Presser, “The chemical composition and estimated minimum thermal reservoir temperatures of the principal hot springs of northern and central Nevada,” Report 74–1066, 1974. doi: 10.3133/ofr741066.
- [77] N. H. Hinz, J. Faulds, and G. Oppliger, “Preliminary geologic map of the Lee-Allen geothermal area,” Nevada Bureau of Mines and Geology, 2010.
- [78] N. H. Hinz, J. E. Faulds, and G. L. Oppliger, “Structural controls of Lee-Allen Hot Springs, southern Churchill County, western Nevada: A small pull-apart in the dextral shear zone of the Walker Lane,” in *Geothermal Resources Council Transactions*, 2008, pp. 285–290.
- [79] J. Skord, “Implications of shallow temperature and soil gas surveys at Lee-Allen geothermal system, Churchill County, Nevada,” in *Geothermal Resources Council Transactions*, 2013, pp. 37–40.
- [80] K. Kraal *et al.*, “Petrologic Validation of Exploration Geophysical Anomalies Utilizing Drill Core and Cuttings from the Don A. Campbell Geothermal System, Nevada, USA,” in *PROCEEDINGS*, in SGP-TR-229. Stanford, CA, in prep.
- [81] C. Carlson, “Geologic map of the Terrill Mountains quadrangle,” Nevada Bureau of Mines and Geology, 2018.
- [82] C. W. Carlson, “Kinematics and transfer mechanisms of strain accommodation at the transition between the Northern and Central Walker Lane, Western Nevada,” PhD Thesis, University of Nevada, Reno, 2017.
- [83] J. Faulds, C. D. Henry, J. Spencer, and S. Titley, “Tectonic influences on the spatial and temporal evolution of the Walker Lane: An incipient transform fault along the evolving

- Pacific–North American plate boundary,” *Ores and orogenesis: Circum-Pacific tectonics, geologic evolution, and ore deposits: Arizona Geological Society Digest*, vol. 22, pp. 437–470, 2008.
- [84] R. F. Hardyman and J. S. Oldow, “Tertiary tectonic framework and Cenozoic history of the central Walker Lane, Nevada,” in *Geology and ore Deposits of the Great Basin*, vol. 1, G. Raines, R. Lisle, R. Schafer, and W. Wilkinson, Eds., in Geological Society of Nevada Symposium Proceedings, vol. 1, Reno, Nevada, Geological Society of Nevada Symposium Proceedings, 1991, pp. 279–301.
- [85] P. H. Cashman and S. A. Fontaine, “Strain partitioning in the northern Walker Lane, western Nevada and northeastern California,” *Tectonophysics*, vol. 326, no. 1–2, pp. 111–130, 2000.
- [86] J. E. Faulds and M. Perkins, “Evidence for dextral shear along the western margin of the Carson Sink: The missing link between the central and northern Walker Lane, western Nevada,” in *Geological Society of America Abstracts with Programs*, 2007, p. 15.
- [87] S. G. Wesnousky, “Active faulting in the Walker Lane,” *Tectonics*, vol. 24, no. 3, 2005.
- [88] J. Fosdick and J. Colgan, “Miocene extension in the East Range, Nevada: A two-stage history of normal faulting in the northern Basin and Range,” *Geological Society of America Bulletin*, vol. 120, no. 9–10, pp. 1198–1213, 2008.
- [89] D. F. Stockli, B. E. Surpless, T. A. Dumitru, and K. A. Farley, “Thermochronological constraints on the timing and magnitude of Miocene and Pliocene extension in the central Wassuk Range, western Nevada,” *Tectonics*, vol. 21, no. 4, pp. 10–1, 2002.
- [90] N. H. Hinz, J. E. Faulds, and J. W. Bell, “Preliminary geologic map of the Bunejug Mountains Quadrangle, Churchill County, Nevada,” Nevada Bureau of Mines and Geology, 2011.
- [91] J. Whelan, C. Halsey, and B. Jackson, “Geothermal evaluation of Range Bravo 19, Naval Air Station, Fallon, Nevada,” in *Geothermal Resources Council Transactions*, Naval Weapons Center, China Lake, CA, 1980.
- [92] R. O. Fournier and I. I. Potter, “A revised and expanded silica (quartz) geothermometer,” *Bulletin of Geothermal Resources Council*, vol. 11, pp. 3–12, 1982.
- [93] A. Vest Christiansen and E. Auken, “A global measure for depth of investigation,” *Geophysics*, vol. 77, no. 4, pp. WB171–WB177, 2012.
- [94] D. Ponce, “Gravity data of Nevada: US Geological Survey Digital Data Series DDS-42.” US Geological Survey, Denver, CO, 1997.
- [95] V. Baranov, “A new method for interpretation of aeromagnetic maps: pseudo-gravimetric anomalies,” *Geophysics*, vol. 22, no. 2, pp. 359–382, 1957.
- [96] W. Cumming, “Resource conceptual models of volcano-hosted geothermal reservoirs for exploration well targeting and resource capacity assessment: Construction, pitfalls and challenges,” in *Geothermal Resource Council Transactions*, 2016, pp. 623–638.
- [97] S. Matlick, “San Emidio Geothermal System,” Empire, Nevada, Field Guide, 1995.
- [98] J. Faulds *et al.*, “Discovering Blind Geothermal Systems in the Great Basin Region: An Integrated Geologic and Geophysical Approach for Establishing Geothermal Play Fairways: All Phases,” Univ. of Nevada, Reno, NV (United States); ATLAS Geosciences, Inc., Reno, NV ..., DOE-UNR-06731-01, 2021.
- [99] G. T. Rhodes, “Structural controls of the San Emidio geothermal system, northwestern Nevada,” University of Nevada, Reno, 2011.
- [100] M. Wilmarth, J. Stimac, and G. Ganefianto, “Power density in geothermal fields, 2020 update,” in *Proceedings*, 2020, pp. 1–8.
- [101] D. T. Trexler, B. A. Koeing, T. Flynn, J. L. Bruce, and G. Ghush Jr, “Low-to-moderate temperature geothermal resource assessment for Nevada: Area specific studies, final report for the period June 1, 1980-August 30, 1981,” Nevada Bureau of Mines and Geology, University of Nevada, Reno, NV, DOE/NV/10039-3, 1981.

- [102] J. W. Bell and N. Hinz, “Young Walker Basin faults provide new insights into structural relations controlling geothermal potential at the Hawthorne army weapons depot, central Nevada,” in *Geothermal Resources Council Transactions*, 2010, pp. 751–754.
- [103] N. H. Hinz, J. E. Faulds, I. Moeck, J. W. Bell, and J. S. Oldow, “Structural controls of three blind geothermal resources at the Hawthorne Ammunition Depot, west-central Nevada,” in *Geothermal Resources Council Transactions*, 2010, pp. 785–790.
- [104] M. Lazaro *et al.*, “United States Department of the Navy geothermal exploration leading to shallow and intermediate/deep drilling at Hawthorne ammunition depot, Hawthorne, NV,” in *Geothermal Resources Council Transactions*, 2010, pp. 595–598.
- [105] R. Penfield, L. Shevenell, L. Garside, and R. Zehner, “Nevada Geothermal Resources,” Nevada Bureau of Mines and Geology, 2010. Accessed: Dec. 16, 2024. [Online]. Available: <https://pubs.nbmng.unr.edu/product-p/m161.htm>
- [106] I. Moeck, N. Hinz, J. Faulds, J. Bell, A. Kell-Hills, and J. Louie, “3D geological mapping as a new method in geothermal exploration: a case study from central Nevada,” in *Geothermal Resources Council Transactions*, 2010, pp. 807–812.
- [107] J. Shoffner, Y. Li, N. Hinz, A. Sabin, M. Lazaro, and S. Alm, “Understanding fault characteristics and sediment depth for geothermal exploration using 3D gravity inversion in Walker Valley, Nevada,” in *Geothermal Resources Council Transactions*, 2010, pp. 633–636.
- [108] N. H. Hinz, J. W. Bell, and J. E. Faulds, “Preliminary geologic map of the Hawthorne geothermal area, Mineral County, Nevada,” Navy Geothermal Program Office, 2010.
- [109] B. E. Surpless, D. F. Stockli, T. A. Dumitru, and E. L. Miller, “Two-phase westward encroachment of Basin and Range extension into the northern Sierra Nevada,” *Tectonics*, vol. 21, no. 1, pp. 2–1, 2002.
- [110] J. S. Oldow, J. W. Geissman, and D. F. Stockli, “Evolution and strain reorganization within late Neogene structural stepovers linking the central Walker Lane and northern Eastern California shear zone, western Great Basin,” *International Geology Review*, vol. 50, no. 3, pp. 270–290, 2008.
- [111] C. D. Henry and M. E. Perkins, “Sierra Nevada–Basin and Range transition near Reno, Nevada: two-stage development at 12 and 3 Ma,” *Geology*, vol. 29, no. 8, pp. 719–722, 2001.
- [112] B. F. Ayling and N. H. Hinz, “Developing a conceptual model and power capacity estimates for a low-temperature geothermal prospect with two chemically and thermally distinct reservoir compartments, Hawthorne, Nevada, USA,” *Geothermics*, vol. 87, p. 101870, 2020.
- [113] B. Surpless, “A structural, magmatic, and thermochronological study of the central Wassuk Range, western Nevada,” PhD Thesis, Stanford University, Stanford, CA, 1999.
- [114] D. I. Axelrod, *Mio-Pliocene floras from west-central Nevada*, vol. 33. University of California Press, 1956.
- [115] C. M. Gilbert and M. W. Reynolds, “Character and chronology of basin development, western margin of the Basin and Range province,” *Geological Society of America Bulletin*, vol. 84, no. 8, pp. 2489–2510, 1973.
- [116] J. L. McIntyre, “Late Cenozoic structure of the Central Wassuk Range, Mineral County, Nevada,” M.S. Thesis, Oregon State University, 1990.
- [117] A. Katzenstein, S. Bjornstad, and D. Meade, “Geothermal Resource Evaluation of the Hawthorne Army Ammunition Depot (HWAD), Hawthorne, NV,” Internal Navy GPO Technical Report, 2002.
- [118] D. Meade *et al.*, “Results of the US Navy Geothermal Program Office 2010 Drilling Project at Hawthorne Army Depot, Nevada,” in *Geothermal Resources Council Transactions*, 2011, pp. 193–195.
- [119] J. Shoffner, L. Y., A. Sabin, and M. Lazaro, “Understanding the Utility of Gravity and Gravity Gradiometry for Geothermal Exploration in the Southern Walker Lake Basin, Nevada,” in

- Geothermal Resources Council Transactions*, Davis, California: Geothermal Resources Council, 2011, pp. 1747–1751.
- [120] W. J. Hinze *et al.*, “New standards for reducing gravity data: The North American gravity database,” *Geophysics*, vol. 70, no. 4, pp. J25–J32, 2005.
- [121] H. El-Kaliouby, “Extracting IP parameters from TEM data,” in *Handbook of Geophysical Exploration: Seismic Exploration*, vol. 30, Elsevier, 2001, pp. 307–326.
- [122] C. D. Henry, *Geologic map of the Bell Canyon quadrangle, western Nevada*. in Field Studies, no. 11c. United States Geological Survey, 1996.
- [123] C. D. Henry, “Geologic map of the Bell Canyon quadrangle, western Nevada,” 1996. Accessed: Dec. 16, 2024. [Online]. Available: <https://pubs.nbmng.unr.edu/product-p/fs011c.htm>
- [124] D. Blankenship, “Fallon FORGE: Well Data, Geophysical Data, and Geologic Maps.” Sandia National Laboratories, Mar. 31, 2016. doi: 10.15121/1287550.
- [125] K. O. Kraal, B. F. Ayling, K. Blake, L. Hackett, T. S. P. Perdana, and R. Stacey, “Linkages between hydrothermal alteration, natural fractures, and permeability: Integration of borehole data for reservoir characterization at the Fallon FORGE EGS site, Nevada, USA,” *Geothermics*, vol. 89, p. 101946, 2021.
- [126] J. B. Witter, J. M. Glen, D. L. Siler, and D. Fournier, “2D and 3D Potential field mapping and modelling at the Fallon FORGE site, Nevada, USA,” in *Geothermal Resources Council Transactions*, 2018, p. 21.
- [127] EDCON-PRJ, Inc., “Aeromagnetic Survey of South Dixie Valley.” U.S. Navy Geothermal Program Office, 2012.
- [128] S. Alm, J. D. Walker, and K. Blake, “Structural Complexity of the Pirouette Mountain and Elevenmile Canyon Geothermal Systems,” in *Geothermal Resources Council Transactions*, 2016, pp. 433–438.
- [129] D. John, “Geologic map of the Pirouette Mountain quadrangle,” 1995.
- [130] D. A. John, “Geology of the Wonder Mountain quadrangle,” Citeseer, 1997.
- [131] D. A. John, J. P. Colgan, M. E. Berry, C. D. Henry, and N. J. Silberling, “Geologic map of the southern Stillwater Range, Nevada,” Reston VA, Report 3521, 2024. doi: 10.3133/sim3521.
- [132] J. Unruh, B. Gray, K. Christopherson, S. Pullammanappallil, S. Alm, and K. Blake, “Seismic Reflection and Magnetotelluric Imaging of Southwestern Dixie Valley Basin, Nevada,” in *Geothermal Resources Council Transactions*, 2016, pp. 455–461.
- [133] D. A. John and N. J. Silberling, “Geologic map of the La Plata Canyon quadrangle, Churchill County, Nevada,” United States Geological Survey, 1994.
- [134] J. I. Satterfield, “Geologic map of the southern Sand Springs Range,” Nevada Bureau of Mines and Geology, 2002.
- [135] E. B. Ekren and F. M. Byers Jr., “Geologic map of the Mount Annie NE, Mount Annie, Ramsey Spring, and Mount Annie SE quadrangles, Mineral and Nye counties, Nevada,” Report 1579, 1986. doi: 10.3133/i1579.
- [136] T. Earney *et al.*, “Geophysical Investigations of a Blind Geothermal System in Southern Gabbs Valley, Nevada,” in *Geothermal Resources Council Transactions*, Nevada Bureau of Mines and Geology, University of Nevada, Reno, 2018.
- [137] C. J. Vitaliano and E. Callaghan, “Geology of the Paradise Peak Quadrangle,” United States Geological Survey, 1963.
- [138] E. B. Ekren and F. M. Byers Jr., “Geologic map of the Gabbs Mountain, Mount Ferguson, Luning, and Sunrise Flat quadrangles, Mineral and Nye Counties, Nevada,” Report 1577, 1985. doi: 10.3133/i1577.

- [139] E. B. Ekren and F. M. Byers Jr., “Geologic map of the Murphys Well, Pilot Cone, Copper Mountain, and Poinsettia Spring quadrangles, Mineral County, Nevada,” Report 1576, 1986. doi: 10.3133/i1576.
- [140] C. D. Henry, J. W. Bell, D. A. John, and J. P. Colgan, “Preliminary Geologic Map of the West Gate Quadrangle, Churchill County, Nevada,” United States Geological Survey.
- [141] J. N. Louie and S. K. Pullammappallil, “Hawthorne 3-D Seismic GIS Interpretation,” U.S. Navy Geothermal Programs Office, Technical Report, 2009.
- [142] J. Shoffner, Y. Li, N. Hinz, A. Sabin, M. Lazaro, and S. Alm, “Understanding fault characteristics and sediment depth for geothermal exploration using 3D gravity inversion in Walker Valley, Nevada,” *Geothermal Resource Council*, vol. 34, pp. 633–636, 2010.

## APPENDIX A. HTEM AND 3D MT RESISTIVITY MODEL FOR LEE-ALLEN

This section presents the modelled resistivity results for both the HTEM and MT datasets. A separate and complete modelling report of the MT dataset is described by [9].

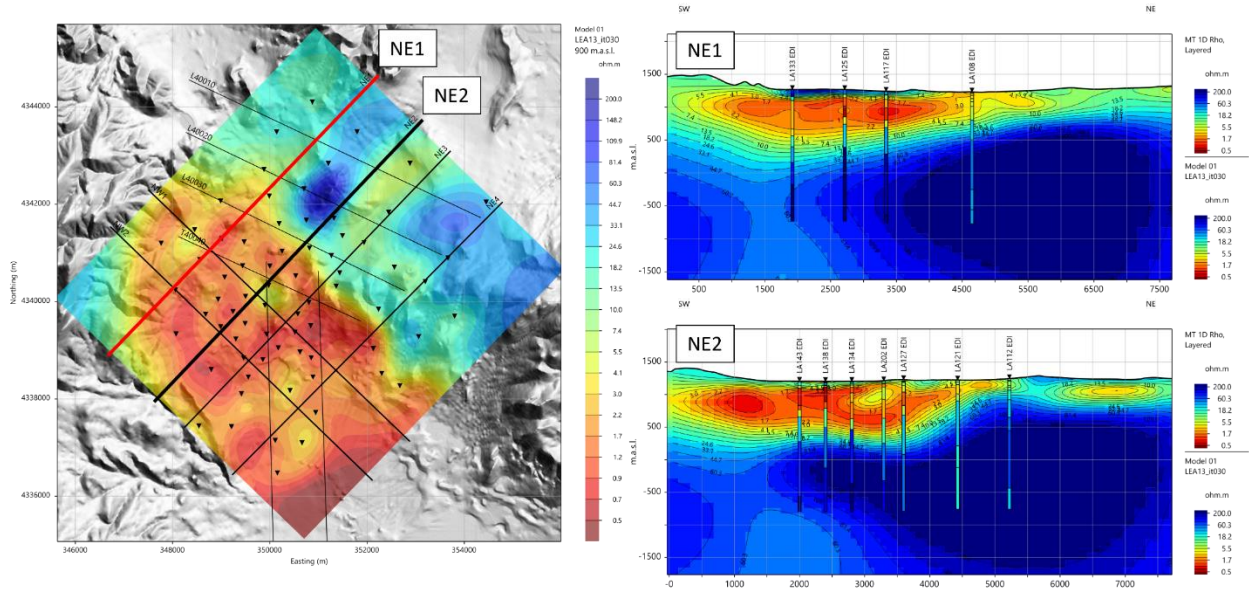
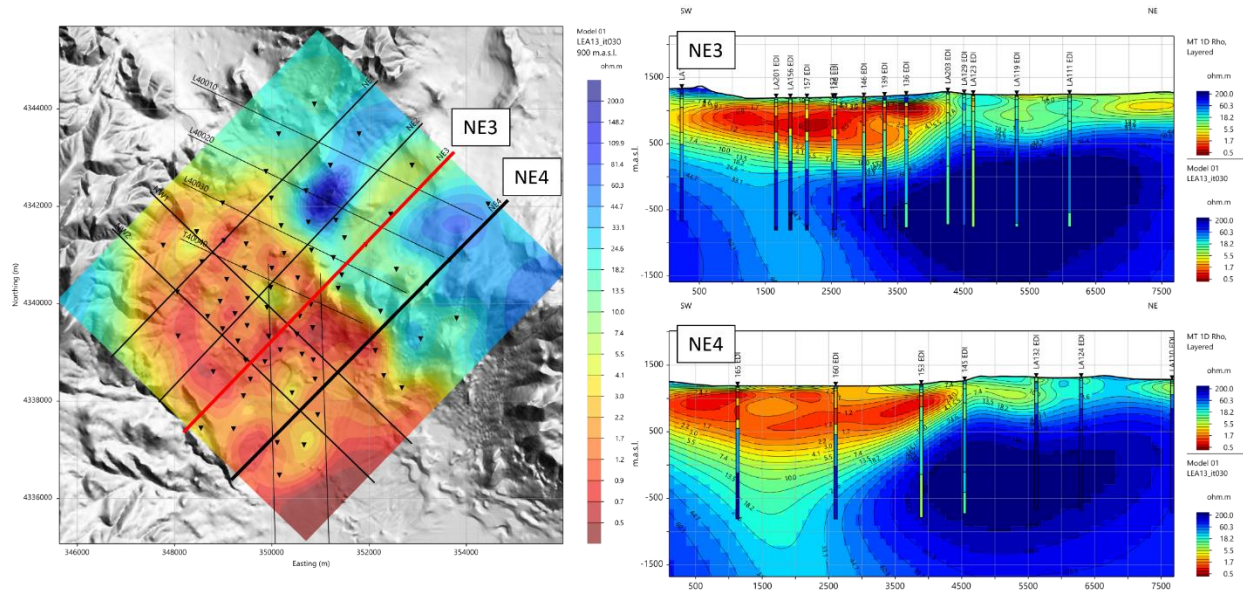
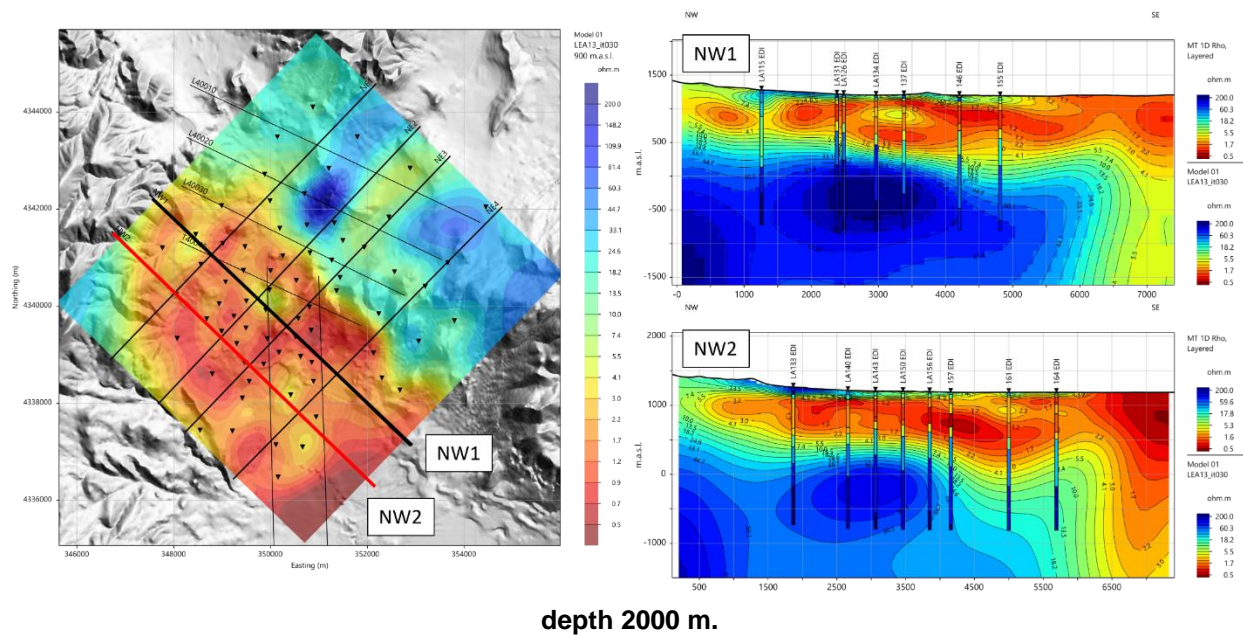


Figure 51: Cross sections NE1 and NE2 through the 3D MT resistivity model. Layered 1D models of the MT data are shown as model bars on top of the 3D model, and are cut off at an arbitrary depth 2000 m.



**Figure 52: Cross sections NE3 and NE4 through the 3D MT resistivity model. Layered 1D models of the MT data are shown as model bars on top of the 3D model, and are cut off at an arbitrary**



depth 2000 m.

**Figure 53: Cross sections NW1 and NW2 through the 3D MT resistivity model. Layered 1D models of the MT data are shown as model bars on top of the 3D model, and are cut off at an arbitrary depth 2000 m.**

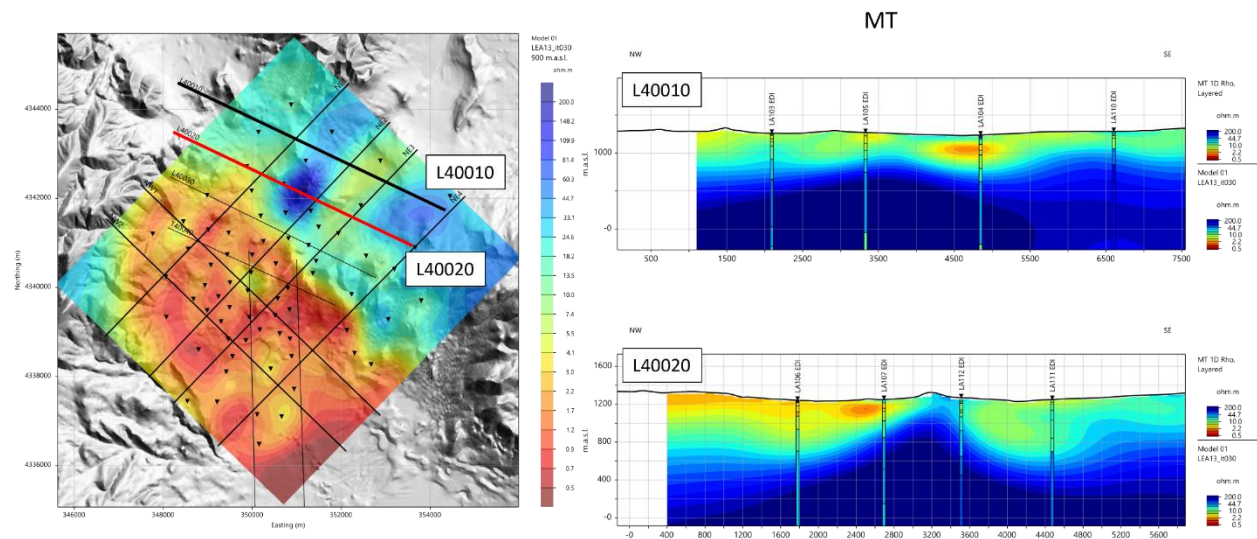
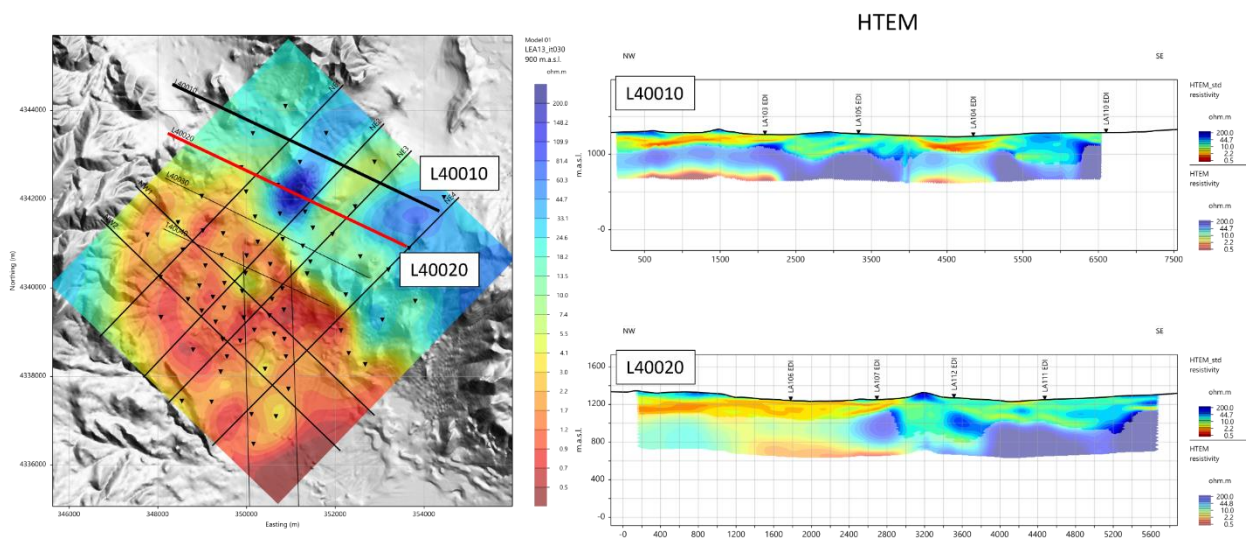


**Figure 54** Cross sections along HTEM flight lines L40010 and L40020 through the 3D MT resistivity model. Layered 1D models of the MT data are shown as model bars on top of the 3D model.



*HTEM transitions to a transparent background below the likely depth-of-investigation*

**Figure 55** Resistivity models for HTEM flight lines L40010 and L40020. The transition to a transparent background denotes the likely depth of investigation, which is variable. MT stations are shown at black triangles for reference.

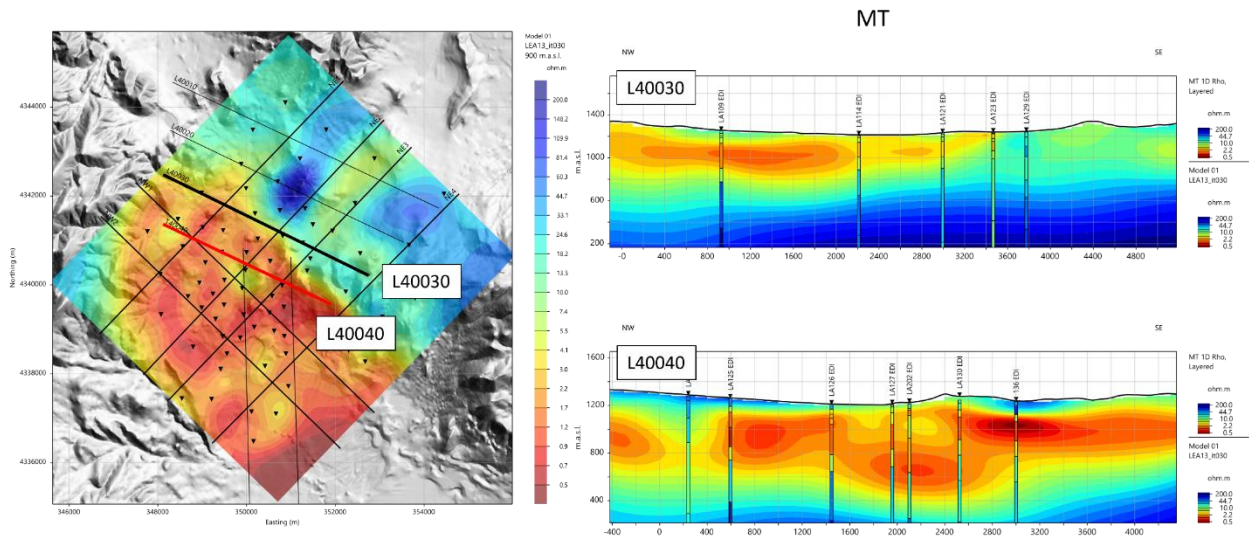
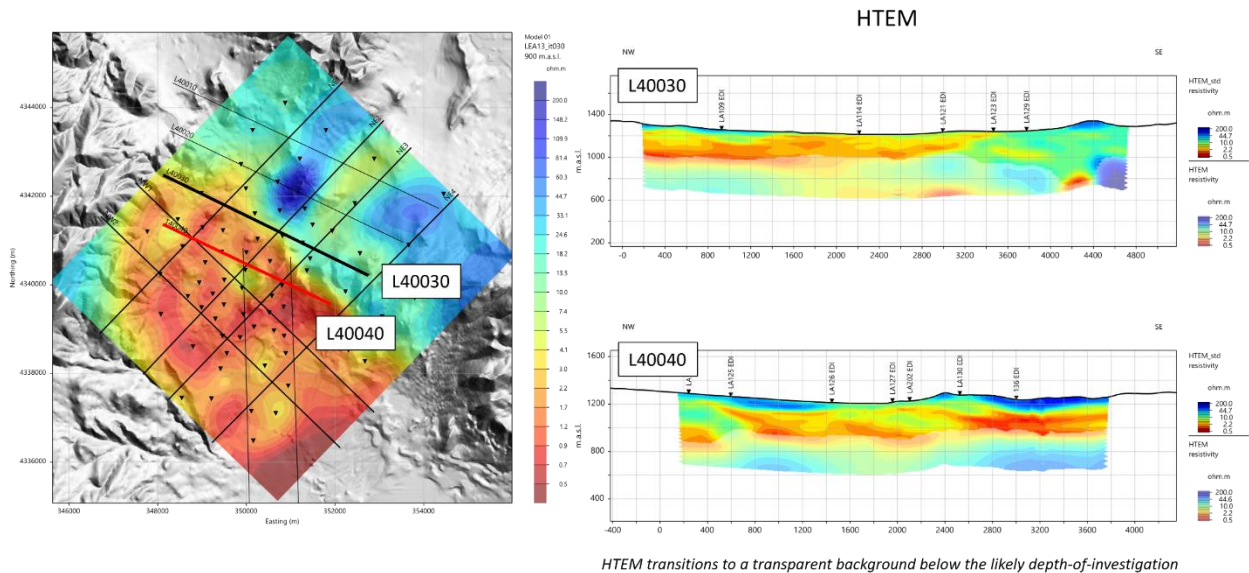


**Figure 56** Cross sections along HTEM flight lines L40030 and L40040 through the 3D MT resistivity model. Layered 1D models of the MT data are shown as model bars on top of the 3D model.



*HTEM transitions to a transparent background below the likely depth-of-investigation*

**Figure 57** Resistivity models for HTEM flight lines L40030 and L40040. The transition to a transparent background denotes the likely depth of investigation, which is variable. MT stations are shown at black triangles for reference.

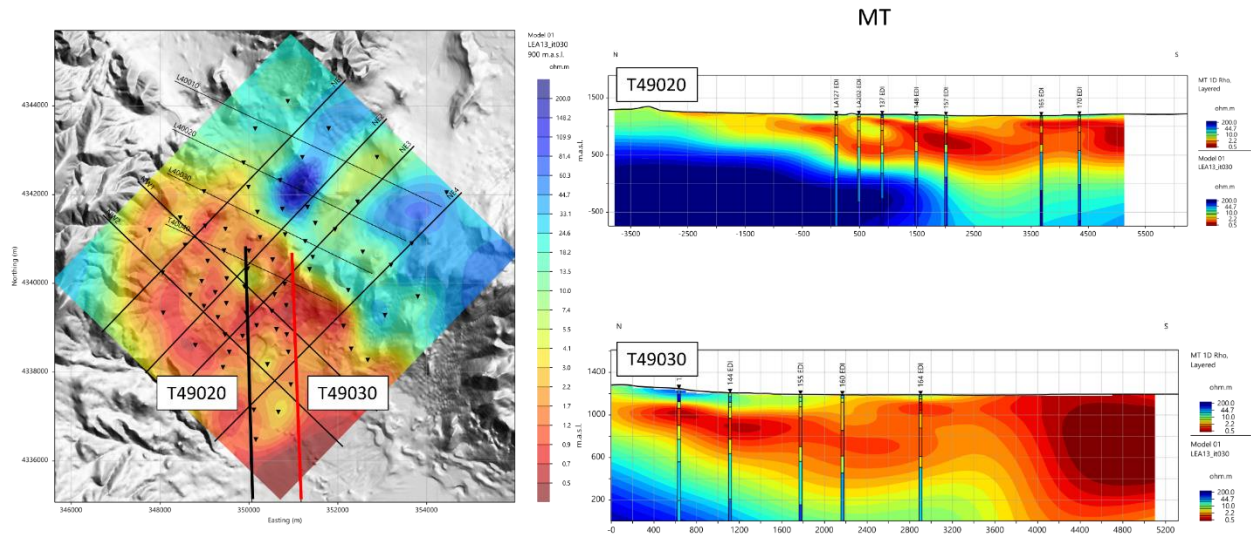


**Figure 58** Cross sections along HTEM flight lines L49020 and L49030 through the 3D MT resistivity model. Layered 1D models of the MT data are shown as model bars on top of the 3D model.

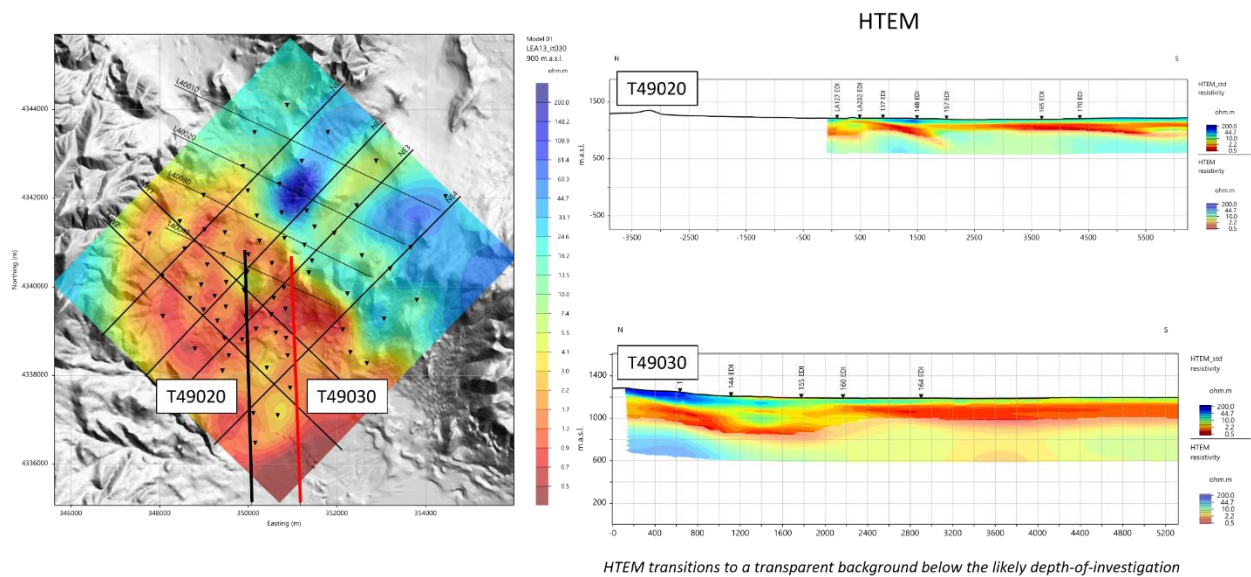


**Figure 59** Resistivity models for HTEM flight lines L49020 and L49030. The transition to a transparent background denotes the likely depth of investigation, which is variable. MT stations are shown at black triangles for reference.

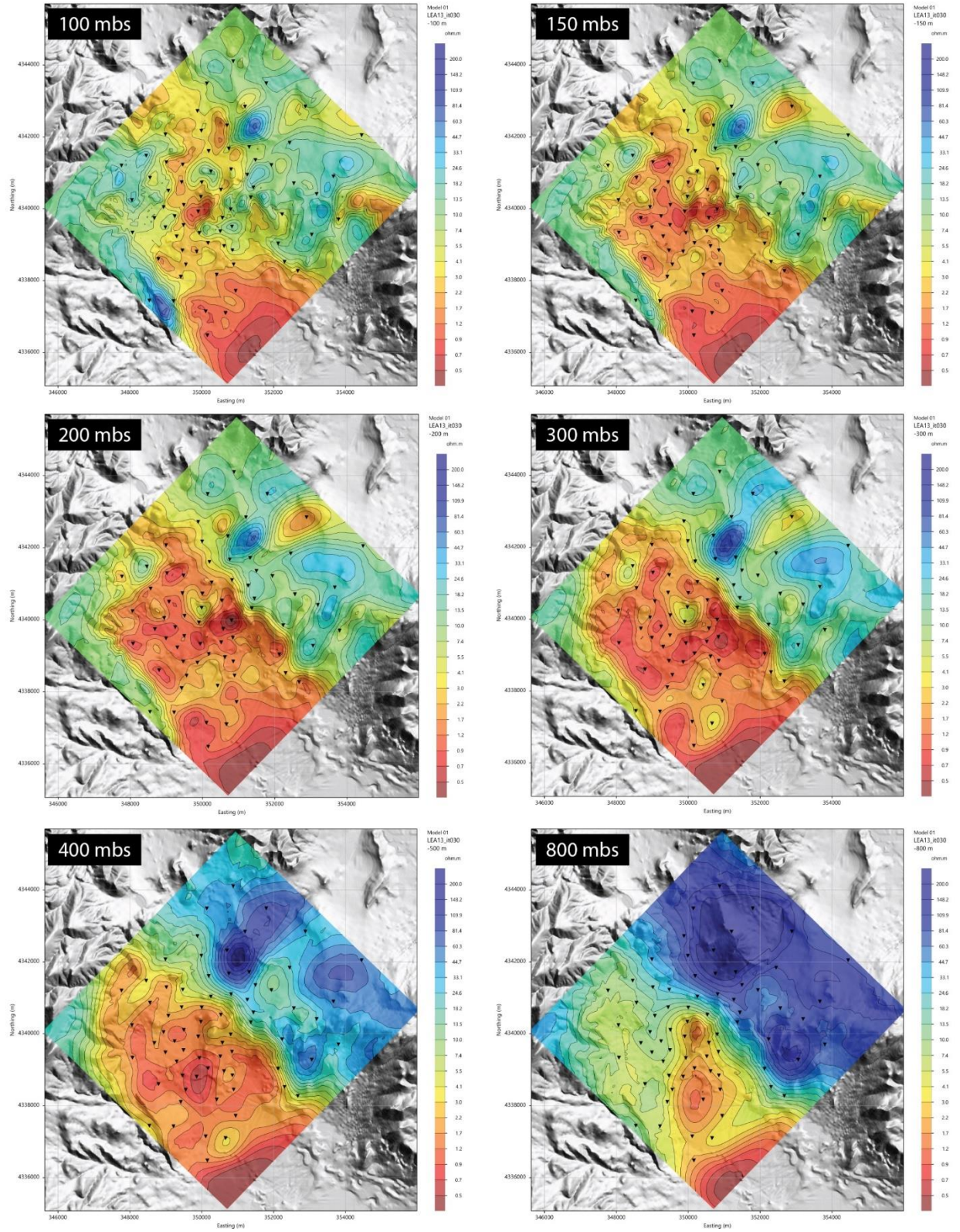


**Figure 60** Depth slices through the 3D MT model at 100, 150, 200, 300 400 and 800 meters below surface. MT station locations are shown as black triangles for reference.

## APPENDIX B. 3D JOINT INVERSION RESISTIVITY MODEL AT EAST HAWTHORNE (HTEM + MT)

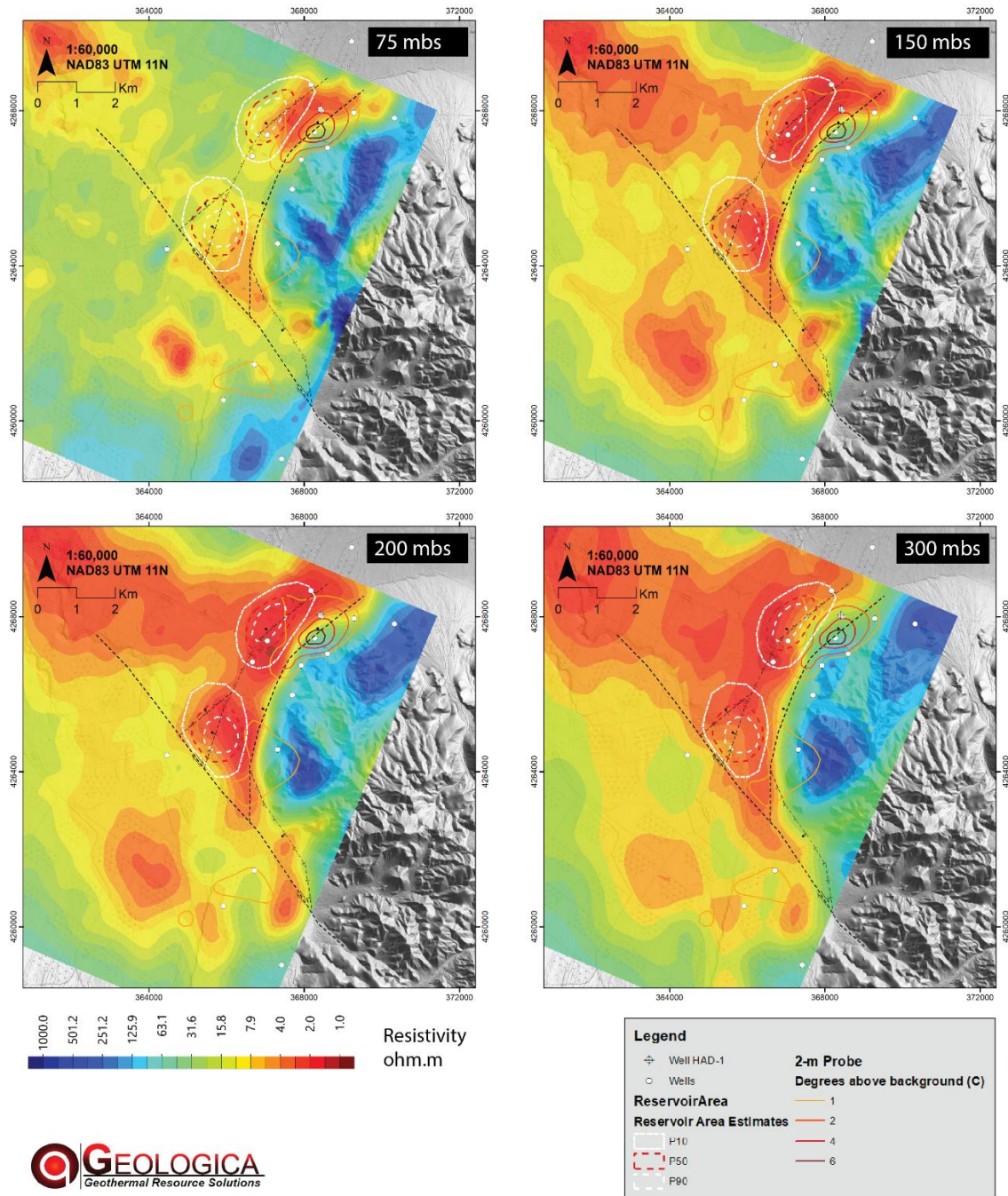


Figure 61 Depth slices through the 3D joint inversion resistivity model (HTEM + MT) at 75, 150, 200 and 300 meters below surface. Each map includes key interpreted fault layer, wells, 2-m temperature contours and reservoir area estimates for Model 1 and Model 2, as discussed in the text.

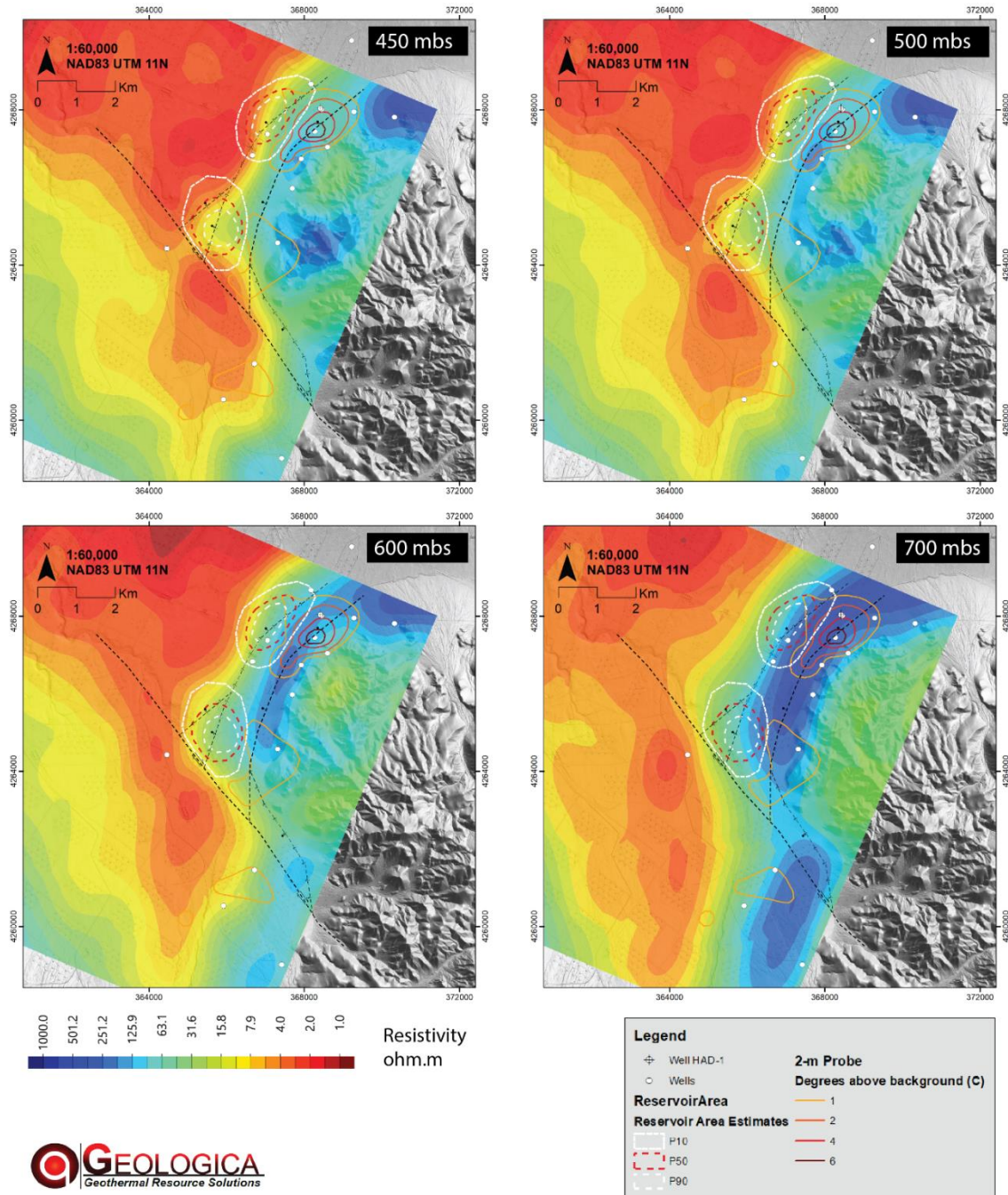
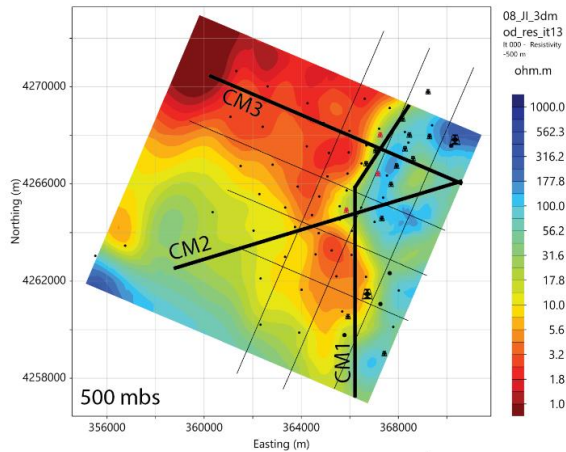
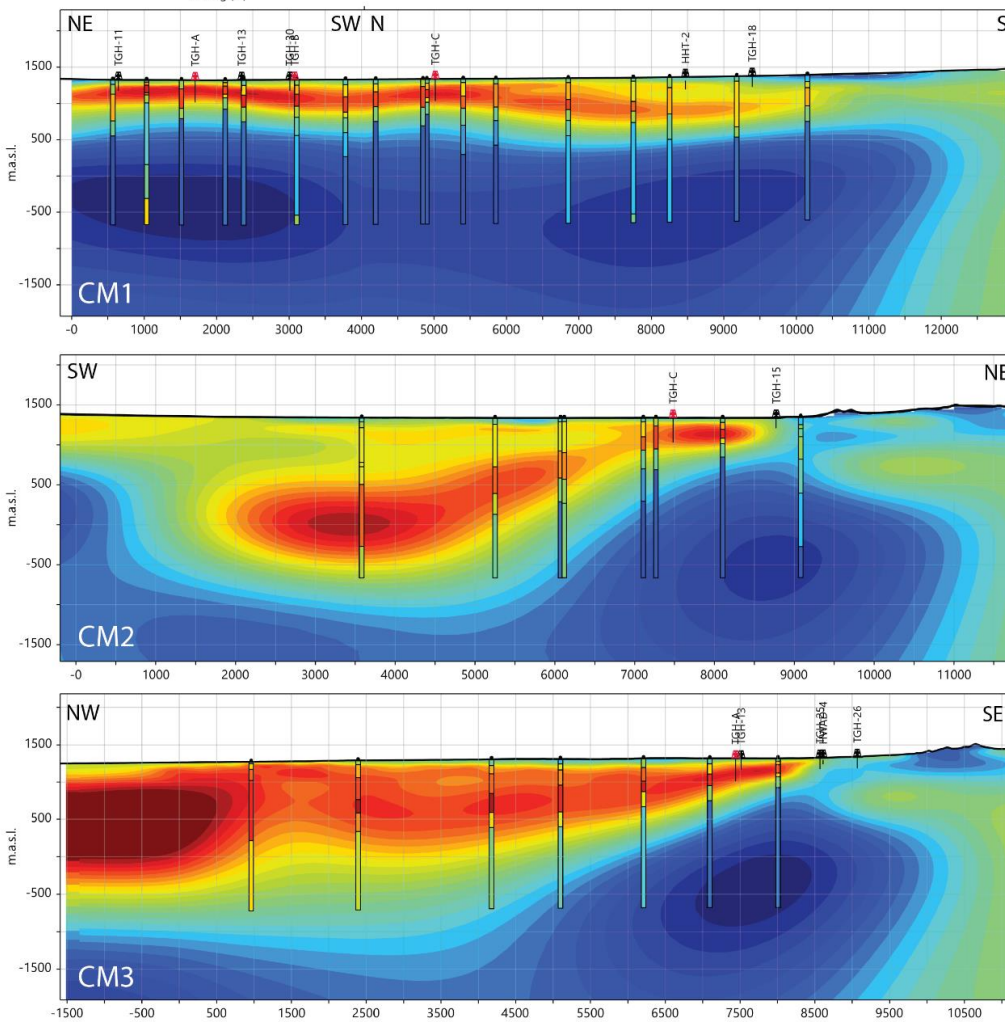


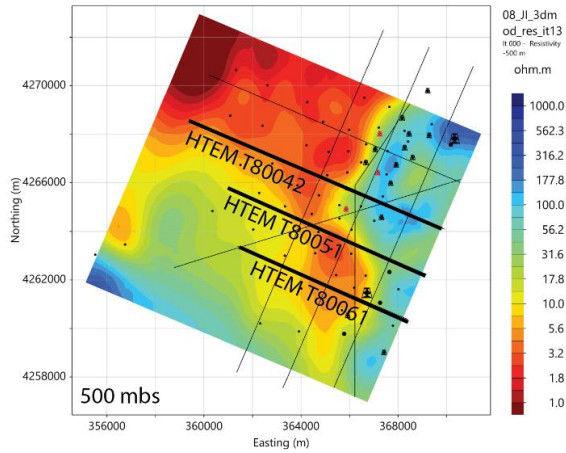
Figure 62 Depth slices through the 3D joint inversion resistivity model (HTEM + MT) at 450, 500, 600 and 700 meters below surface. Each map includes key interpreted fault layer, wells, 2-m temperature contours and reservoir area estimates for Model 1 and Model 2, as discussed in the text.



### 3D Joint Inversion Model Cross-Sections (HTEM + MT)



**Figure 63** Cross-sections through the 3D joint inversion model. Each section includes wells (existing = black, proposed = red), MT stations (small black circles) and 1D layered models of the MT shown as model bars. 1D models are arbitrarily clipped at 2 km deep and may include portions of data that are not 1D in nature.



## 3D Joint Inversion Model Cross-Sections (HTEM + MT)

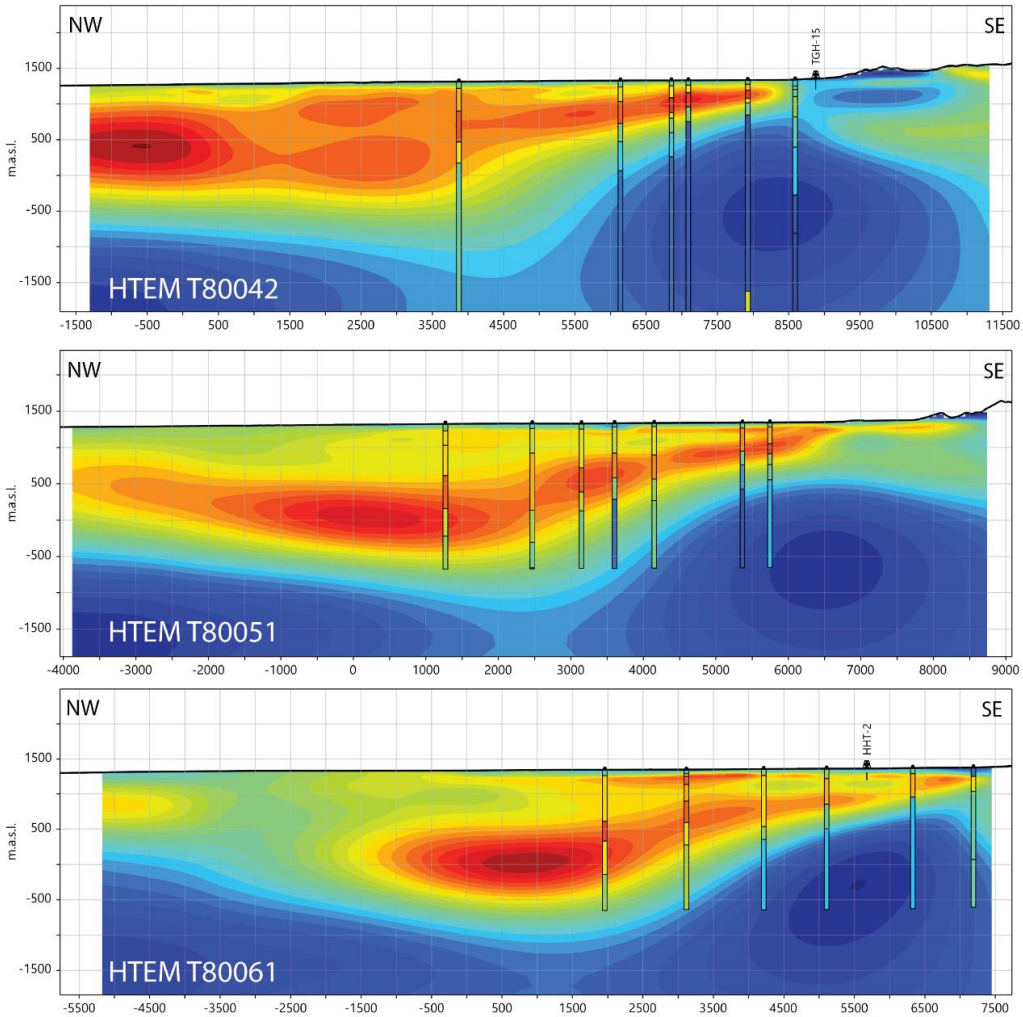
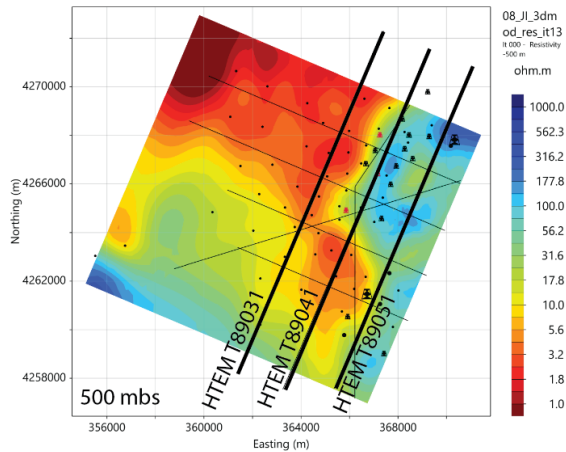


**Figure 64** Cross-sections through the 3D joint inversion model. Each section includes wells (existing = black, proposed = red), MT stations (small black circles) and 1D layered models of the MT shown as model bars. 1D models are arbitrarily clipped at 2 km deep and may include portions of data that are not 1D in nature.



### 3D Joint Inversion Model Cross-Sections (HTEM + MT)

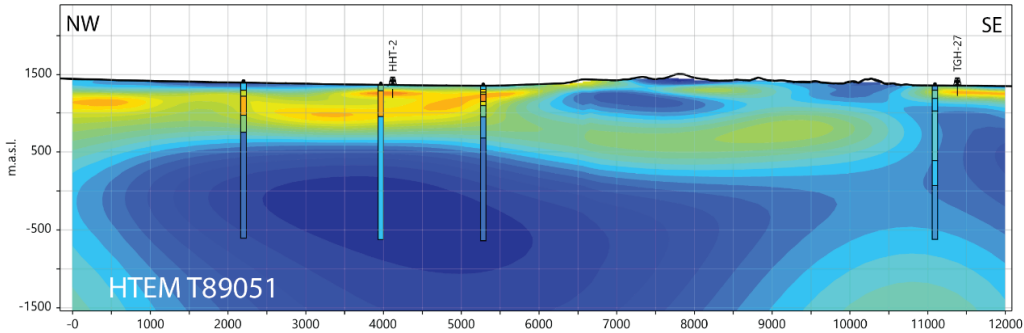
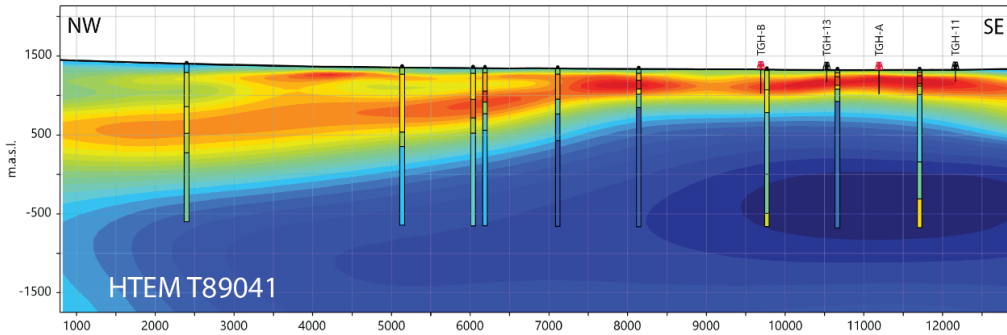
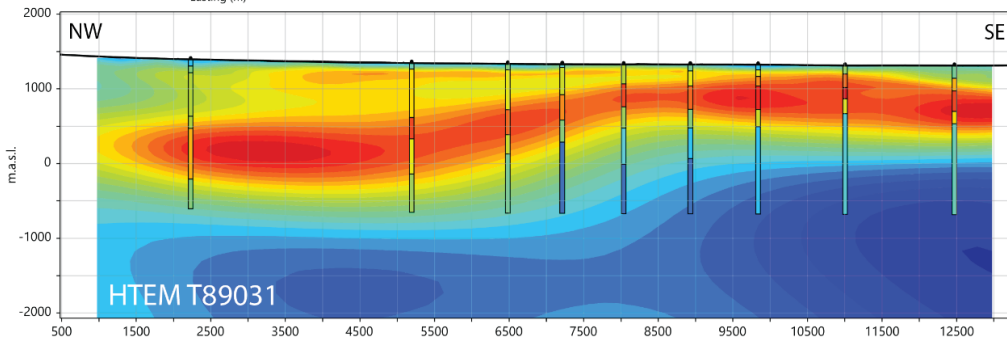


**Figure 65** Cross-sections through the 3D joint inversion model. Each section includes wells (existing = black, proposed = red), MT stations (small black circles) and 1D layered models of the MT shown as model bars. 1D models are arbitrarily clipped at 2 km deep and may include portions of data that are not 1D in nature.

## APPENDIX C. PUBLIC DATA COMPILATION

Basin	Prospect	Available data	Data type	Citation
Bell Flat Valley	Bell Flat	1:24k Geologic mapping	Geologic map	[122]
			Geologic map	[123]
Carson Sink	Lee Allen	1:24k Geologic mapping, 2m, TGH, exploration wells, geochemistry, gravity, magnetics	Geologic map	[77]
			2m	[79]
			TGH	GPO internal report, SMU
			exploration wells	GBCGE, NBMG
			geochemistry	GBCGE
			gravity	[78]
			mag	[78]
	BR-16 North	1:24k Geologic mapping, 2m, TGH (gradient only), magnetics, gravity	Geologic map	Bell and Faulds 2010 (unpublished)
			2m	UNR 2010, Navy GPO personal comm.
			TGH	[117], SMU
			mag	UNR 2010, unpublished
			gravity	UNR 2010, unpublished
	BR-16 South	1:24k Geologic mapping, 2m, single TGH (gradient only), magnetics, gravity		*same as BR-16 North
	Salt Wells	1:24k Geologic mapping, 2m, TGH, production wells	Geologic map	[51], [90]
			2m	[17], [37]
			TGH	SMU, GBCGE
			Production wells	GBCGE
	Carson Lake/Fallon	1:24k Geologic mapping, 2m, TGH, deep wells, geochemistry, gravity	Geologic map	[52], [90]
			2m	[124], Navy GPO internal report
			TGH	[124], SMU
			Deep wells	[124], [125]
			geochemistry	GBCGE
			gravity/mag	[124], [126]
Dixie Valley	Grover Point	TGH, nearby geochemistry (cold wells), magnetics	TGH	SMU
			geochemistry	GBCGE
			mag	[127]

Basin	Prospect	Available data	Data type	Citation
	Chalk Mountain	1:24k Fault mapping, 2m, ~3 TGH, gravity, magnetics	Fault mapping	[128]
			2m	[37]
			TGH	Hunt 99, SMU
			gravity	[55]
			mag	[127]
	The Bend	2m, ~TGH, gravity	2m	[37]
			TGH	Hunt 99, SMU
			gravity	[55]
	Pirouette Mountain	1:24k Geologic mapping, 2m, TGH, single geochemistry, deep well, gravity, magnetics, MT, seismic	Geologic map	[128], [129], [130], [131]
			2m	[36]
			TGH	Hunt 99, SMU
			geochemistry	GBCGE
			Deep wells	GBCGE, NBMG
			gravity	[55]
			mag	[127]
			MT	[132], CGG
	Elevenmile Canyon	1:24k Geologic mapping, 2m, TGH, gravity, magnetics, MT, seismic	Geologic map	[128], [129], [133]
			2m	[36]
			TGH	Hunt 99, SMU
			gravity	[55]
			Mag	[127]
MT			[132], CGG	
seismic			[132], CGG	
Fairview Valley	Bell Flat Hot Spring	1:24k Geologic mapping (limited coverage), TGH (GPO)	Geologic map	[123]
			TGH	SMU, Navy GPO
	Big Kasock	1:24k Geologic mapping (limited coverage), TGH	Geologic map	[134]
			TGH	SMU, GPO
	Labou Flat	Gravity, shallow cold well	gravity	[55]
			well data	GBCGE
Gabbs Valley	Rawhide Hot Springs	1:24k, 1:48k Geologic mapping, 2m, geochemistry, gravity	Geologic map	[46], [135]
			2m	[33]
			gravity	NV regional
			geochemistry	GBCGE

Basin	Prospect	Available data	Data type	Citation
	North Gabbs	1:24k Geologic mapping (partial coverage), 2m, TGH, single warm well)	Geologic map	[46], [135]
			2m	[33]
			TGH	SMU
			well data	GBCGE, NWIS
	Kaiser	1:24k, 1:48k Geologic mapping, TGH	Geologic map	[46], [135]
			TGH	SMU
	Cobble Cuesta	1:24k, 1:48k Geologic mapping, 2m, TGH, gravity	Geologic map	[46], [135]
			2m	[46]
			TGH	SMU
			gravity	[136]
	Dead Cow Splay	1:48k Geologic mapping, sparse gravity	Geologic map	[135]
			gravity	NV regional
	Town of Gabbs	1:48k Geologic mapping, hot shallow wells, geochemistry	Geologic map	[137]
			well data	GBCGE, NWIS
			geochemistry	GBCGE
	Gene Sawyer	1:24k Geologic mapping, single warm shallow well, geochemistry	Geologic map	[137]
			well data	GBCGE, NWIS
			geochemistry	GBCGE
	Finger Rock	1:24k Geologic mapping, sparse gravity, partial coverage magnetics	Geologic map	[135], [138]
			gravity	[136]
			mag	[136]
Benton Springs	1:24k Geologic mapping, sparse gravity	Geologic map	[135], [138]	
		gravity	[136]	
Don A. Campbell	1:24k Geologic mapping, 2m, geochemistry, deep wells	Geologic map	[139]	
		2m	[35]	
		geochemistry	GBCGE	
		Deep wells	GBCGE, NBMG	
Petrified Springs	1:24k Geologic mapping, 2m, TG, MT, gravity, magnetics	Geologic map	[40]	
		2m	[40]	
		TGH	[40], SMU	
		MT	[136]	
		gravity	[136]	
		mag	[136]	
Middlegate Valley	Middlegate	1:24k Geologic mapping (partial coverage), gravity (partial coverage)	Geologic map	[140]
			gravity	[55]

Basin	Prospect	Available data	Data type	Citation
Walker Lake Valley	East Hawthorne	1:24k Geologic mapping, 2m, TGH, sparse gravity	Geologic map	[108]
			2m	[35]
			TGH	[104]
			deep well	[47], [104]
			gravity	[119]
	West Hawthorne	1:24k Geologic mapping, 2m, TGH, geochemistry, gravity, 3D seismic	Geologic map	[108]
			2m	[35]
			TGH	[104]
			well data	GBCGE, NWIS
			geochemistry	[112], GBCGE
			gravity	[119]
			3D seismic	[141]

## APPENDIX D. DATA REPOSITORY SUMMARY

Table 12 Summary of BRIDGE published data.

Modality	Whole data set	Split by prospect
HTEM	X	
MT		X
Gravity		X
Regridded Legacy Magnetics		X
Geologic Mapping		X
LiDAR analysis		X
2-m	X	X
Geochemistry	X	X
Hyperspectral (airborne/hand sample)		X

The BRIDGE data and data products included here were collected and are organized on a per-prospect basis, except for the regional-scale HTEM survey. The outline below reflects the file structure found in the BRIDGE Geothermal Data Repository data submission (<https://gdr.openei.org/submissions/1682>).

1. HTEM
  - a. Data in .txt and .gdb formats
  - b. Metadata
  - c. Xcalibur acquisition report
  - d. GALEI inversion results
  - e. Aarhus Workbench inversion results and supporting files (by USGS – preferred)
2. 2-Meter Temperature Surveys (Combined)
  - a. Shapefile and data table for 2-m points collected by the Navy GPO for the Bridge Project. These files contain data relevant to the following fields: East Hawthorne, Grover Point, Dead Cow Splay (Gabbs Valley), Kaiser (Gabbs Valley) and Bell Flat.
3. Leapfrog
  - a. Pirouette Mtn Leapfrog model
    - i. LF model
    - ii. Input files for TGH
  - b. Elevenmile Canyon Leapfrog model
    - i. LF model
    - ii. Input files for TGH and wells
4. GIS and geology
  - a. Map package (MPK) for ArcGIS (ArcMap and ArcPro) containing shapefiles and symbolization of MT stations, gravity stations, geochemistry samples, all LiDAR fault picks (covering the southern half of Dixie Valley, Fairview Valley, Bell Flat, Gabbs Valley, Lee Allen, and Walker Lake Valley), and dip direction indicators for

LiDAR fault picks. Note that LiDAR fault picks have only been field verified in Dixie Valley and Gabbs Valley.

- b. Shapefiles covering entire BRIDGE study area (no layer files for symbology)
  - i. 2m stations
  - ii. Geochemistry samples
  - iii. HTEM lines
  - iv. MT stations
  - v. Gravity stations
  - vi. LiDAR fault picks
  - vii. LiDAR fault dip directions (fault balls)
  - viii. Airborne hyperspectral mineral classification (RS\_Minerals)
5. Geochemistry
  - a. All BRIDGE geochemistry data in .csv and .xlsx formats
6. Bell Flat
  - a. GIS and geology (shapefiles)
    - i. LiDAR fault picks
    - ii. LiDAR fault dip directions (fault balls)
    - iii. Gravity stations
    - iv. 2m survey
    - v. Remote Sensing Minerals (AVIRIS-c interpretation)
  - b. 2-meter temperature survey
    - i. Data in .csv format
  - c. Gravity survey
    - i. Data in .csv and .gdb formats
    - ii. Magee Geophysical acquisition report
    - iii. Maps of the complete Bouguer anomaly and derivative products
  - d. Aeromagnetic data, extracted from the GeoDAWN dataset [16]
    - i. Data in Oasis Montaj format (.gdb)
    - ii. Maps of the magnetic data and derivative products in .png and .geotiff formats
  - e. Airborne hyperspectral mineral classification
  - f. An informal geophysics sketchbook presentation that shows gravity, magnetic, 2m-temperature, LiDAR fault scarps and HTEM resistivity data correlate with one another.
7. East Hawthorne
  - a. GIS and geology (shapefiles)
    - i. LiDAR fault picks
    - ii. LiDAR fault dip directions (fault balls)
    - iii. Gravity stations
    - iv. MT stations
    - v. 2m survey
    - vi. Remote Sensing Minerals (AVIRIS-c interpretation)
  - b. 2-meter temperature survey
    - i. Data in .csv format

- c. Aeromagnetic data, extracted from the GeoDAWN dataset [16]
    - i. Data in Oasis Montaj format (.gdb)
    - ii. Maps of the magnetic data and derivative products in .png, .geotiff and as packed Geosoft maps
    - iii. A brief summary report
  - d. Gravity data: Three merged datasets originally published by [142]
    - i. Reprocessing project
      - 1. Merged, reprocessed gravity data in .csv and .gdb formats
      - 2. Geosoft project file
      - 3. A brief reprocessing report
      - 4. Maps of the complete Bouguer anomaly and derivative products in .png, .geotiff and as packed Geosoft maps
      - 5. Down-sampled LiDAR digital elevation model used in terrain corrections
    - ii. 2D gravity modeling
      - 1. Two 2D gravity & magnetic models in gmsys format
      - 2. Images of the model results
      - 3. Vertical section grids of the model results
      - 4. A brief modeling report with comparisons to the 3D MT model
  - e. Magnetotellurics
    - i. Data
      - 1. MT Data in processed .edi format and as raw time series. Formats differ slightly between data collected by Enthalpion and KLM Geoscience.
      - 2. Acquisition reports for both Enthalpion and KLM geoscience MT surveys
    - ii. Single-domain 3D MT modeling project
      - 1. A detailed 3D MT modeling report. Most figures in this report are available as separate .png images
      - 2. 3D MT model as .out file, .xyzv file, UBC format and as a Geotools results packet
      - 3. Metadata files for the inversion parameters and model performance
    - iii. Joint-inversion 3D MT & HTEM modeling Project
      - 1. A detailed modeling report. Most figures in this report are available as separate .png images
      - 2. 3D joint-inversion results model as .out file, .xyzv file and in UBC format.
      - 3. Metadata files for the inversion parameters and model performance
  - f. Airborne hyperspectral mineral classification
8. Gabbs Valley
- a. GIS and geology (shapefiles)
    - i. LiDAR fault picks
    - ii. LiDAR fault dip directions (fault balls)
    - iii. MT stations

- iv. 2m survey
    - v. Remote Sensing Minerals (AVIRIS-c interpretation)
    - vi. Brief field visit summary (.docx format)
  - b. 2-meter temperature survey
    - i. Data in .csv format
    - ii. Two main surveys: Kaiser and Dead Cow Splay
  - c. Aeromagnetic data
    - i. Data in Oasis Montaj format (.gdb)
    - ii. Maps of the magnetic data and derivative products in .png, .geotiff and as packed Geosoft maps
    - iii. A brief summary report
  - d. Magnetotellurics
    - i. Data
      - 1. Processed MT data in .edi format and as raw time series (Phoenix format)
      - 2. KLM Geoscience acquisition report
    - ii. Preliminary 3D MT Model
      - 1. A brief modeling report
      - 2. 3D MT model as a .out file
      - 3. Metadata files for the inversion parameters and model performance
  - e. Airborne hyperspectral mineral classification
- 9. Grover Point
  - a. GIS and geology (shapefiles)
    - i. LiDAR fault picks
    - ii. LiDAR fault dip directions (fault balls)
    - iii. Gravity stations
    - iv. MT stations
    - v. 2m survey
    - vi. Geochemistry samples
    - vii. Remote Sensing Minerals (AVIRIS-c interpretation)
  - b. 2-meter temperature survey
    - i. Data in .csv format
  - c. Legacy aeromagnetic data that was re-gridded by Edcon-PRJ in 2012. See [55].
    - i. Edcon-PRJ Acquisition and processing report
    - ii. Original grid files produced by Edcon-PRJ of merged dataset
    - iii. New maps produced for the BRIDGE Project over Grover Point in .geopdf, .geotiff and .png format
  - d. Gravity
    - i. Original contractor deliverables from Zonge International, including:
      - 1. Acquisition report,
      - 2. data in .gdb and .csv formats
      - 3. Maps of the CBA and select derivatives in .png, .geotiff and packed Geosoft formats

- ii. An alternate set of gridded maps of the CBA and derivative products in .geopdf, .geotiff and .png formats
  - e. Magnetotellurics
    - i. Processed MT data in .edi format and as raw time series (Phoenix format)
    - ii. KLM Geoscience Acquisition report
    - iii. 3D MT model in .out file format
    - iv. 3D MT modeling report
  - f. Geologic mapping
    - i. Complete geologic map as PDFs in two plates
      - 1. “GroverPoint\_GeoMap\_Layout”
      - 2. “GroverPoint\_GeoMap\_TempData\_GeoPDF”
    - ii. ArcPro Map Package (MPKX.)
      - 1. “GroverPoint\_GeologicMap\_BRIDGE\_2024”
    - iii. Linework data as “GroverPoint\_GeoLines.shp” includes:
      - 1. Contacts
      - 2. Faults
    - iv. Paleo shoreline data as “GroverPoint\_LithologyPolygons.shp”
    - v. Point data as .shp files including
      - 1. GroverPoint\_Attitudes.shp
      - 2. GroverPoint\_FaultBallsandBars.shp
      - 3. GroverPoint\_GeoLines.shp
  - g. Airborne hyperspectral mineral classification
- 10. Lee Allen
  - a. GIS and geology (shapefiles)
    - i. LiDAR fault picks
    - ii. LiDAR fault dip directions (fault balls)
    - iii. MT stations
    - iv. Remote Sensing Minerals (AVIRIS-c interpretation)
    - v. Remote Sensing Field Validation
  - b. Aeromagnetics, extracted from the GeoDAWN dataset [16]
    - i. Data in Oasis Montaj format (.gdb)
    - ii. Maps of the magnetic data and derivative products in .png and .geotiff formats
  - c. Gravity
    - i. Legacy gravity data, which had been merged from four different public datasets was re-gridded for analysis by the BRIDGE Project. The data has been compiled into a single .gdb file, and used to make maps the CBA and select derivatives. These are provided in .png and .geotiff formats.
  - d. Magnetotellurics
    - i. Data
      - 1. MT Data in processed .edi format and as raw time series (Phoenix format).
      - 2. Two KLM geoscience acquisition reports. This data was collected over the course of two mobilizations in the summer of 2024.

- ii. 3D MT modeling project
  - 1. A detailed 3D MT modeling report. Most figures in this report are available as separate .png images
  - 2. 3D MT model as .out file, .xyzv file and as UBC format.
  - 3. Metadata files for the inversion parameters and model performance
- e. Laboratory Infrared Spectroscopy data
  - i. Raw data (text)
  - ii. Interpretation spreadsheet (.csv)
- f. Airborne hyperspectral mineral classification

## DISTRIBUTION

### Email—Internal

Name	Org.	Sandia Email Address
Giorgia Bettin	8916	gbettin@sandia.gov
Technical Library	1911	<a href="mailto:sanddocs@sandia.gov">sanddocs@sandia.gov</a>

### Email—External

Name	Company Email Address	Company Name
Michael Weathers	michael.weathers@ee.doe.gov	DOE GTO
Nicholas Hinz	nhinz@geologica.net	Geologica Geothermal Group

### Hardcopy—Internal

Number of Copies	Name	Org.	Mailstop

### Hardcopy—External

Number of Copies	Name	Company Name and Company Mailing Address

This page left blank



Sandia  
National  
Laboratories

Sandia National Laboratories is a multimission laboratory managed and operated by National Technology & Engineering Solutions of Sandia LLC, a wholly owned subsidiary of Honeywell International Inc. for the U.S. Department of Energy's National Nuclear Security Administration under contract DE-NA0003525.